

# Nano Studies

11

2015

# NANO STUDIES

11

2015

# Nano Studies, 2015, 11

UDG [53 + 54 + 620.22] (051.2)  
N – 21

**Nano Studies** is a biannual scientific journal published in Georgia.

**Nano Studies'** topics of interest include Nanoscience and Nanotechnology, and related problems of Physics, Chemistry and Materials Science.

**Nano Studies** publish following categories of scientific articles: research papers, communications, reviews and discussions.

**Nano Studies** publish scientific articles in English and also in Georgian and in Russian.

Summaries of all the articles of **Nano Studies** are referred in **Georgian Abstracts Journal** and are accessible in **Tech Inform** (Georgia's Central Institute for Scientific and Technical Information) database: <http://www.tech.caucasus.net>

Full-texts of articles published in **Nano Studies** are free-accessible at the journal's web-site: [www.NanoStudies.org](http://www.NanoStudies.org)

Editor & Publisher:	<b>Levan Chkhartishvili</b>
Editorial Assistant:	<b>Tamar Berberashvili</b>
Address of Editorial Office:	<b>Department of Engineering Physics Georgian Technical University Campus 4, Room 307 77 Merab Kostava Avenue Tbilisi, 0175, Georgia <a href="http://www.NanoStudies.org">www.NanoStudies.org</a></b>

E-mail:	<b><a href="mailto:chkharti2003@yahoo.com">chkharti2003@yahoo.com</a></b>
Phone:	<b>995 322 37 19 42</b>
Mobile:	<b>995 599 34 07 36</b>

© Authors of articles, 2015

Publishing House **Nekeri**

ISSN 1987 – 8826

CONTENTS

Professor Raphael Chikovani – 85

Scientist, Educator, Great Personality – *in Georgian*

Administration of the Georgian Technical University

Engineering Academy of Georgia

Editorial Board of the Journal 'Georgian Engineering News'

Georgian Society of Science History

Faculty of Informatics & Control Systems (GTU)

Department of Engineering Physics (GTU) ..... 7-10

Proceedings of the ICANM 2015: International Conference & Exhibition on  
Advanced & Nano Materials (August 10–12, 2015, Ottawa, Ontario, Canada)

Fabrication and characterization of SS316L

–Al<sub>2</sub>O<sub>3</sub> composites for wear applications

C. Kuforiji, M. Nganbe ..... 11-18

Numerical simulation of droplet breakup,  
splitting and sorting in microfluidic device

T. Chekifi, B. Dennai, R. Khelifaoui ..... 19-28

Dipole moment of quasi-planar boron clusters

R. Becker, L. Chkhartishvili ..... 29-48

Poly(glycerol-succinate) oligoesters as bio-based surfactants  
for stability of o / w emulsion formulated with rice bran oil

V. Aomchad, J. Singkhonrat ..... 49-56

Facile preparation of P3HT–ZnO heterostructure:

Structural and spectroscopic properties

G. L. Kabongo, G. H. Mhlongo,

B. M. Mothudi, M. S. Dhlamini ..... 57-62

In-plane shear deformability of out-of-autoclave  
prepregs under double-diaphragm vacuum compaction

H. A. Alshahrani, M. H. Hojjati ..... 63-68

Development of thermoplastic starch  
nanocomposites for wet conditions

M. Oishi, Ch. Dal Castel,

R. Park, B. Wolff, L. Simon ..... 69-74



## Contents.

---

Production of ultrafine-grained titanium by industrial caliber rolling G. Krállics, J. Gubicza, Z. Bezii .....	75-86
Nanocrystalline hardystonite synthesized by solid state process as a novel bioceramic for medical purposes; preparation and characterization E. Karamian, H. Gheisari .....	87-94
Nano / micro fibrous gelatin–PLA yarns fabrication and characterization for biomedical applications N. Movagatian, A. Hadjizadeh, M. Latifi .....	95-102
<b>Regular Papers</b>	
Investigation of the optical absorption spectra of thin epitaxial lead selenide layers approaching the nanoscale thickness A. M. Pashaev, O. I. Davarashvili, M. I. Erukashvili, Z. G. Akhvlediani, L. P. Bychkova, V. P. Zlomanov .....	103-110
Volume of intersection of six spheres: A special case of practical interest L. Chkhartishvili, S. G. Narasimhan .....	111-126
Morphological studies of bismuth nanostructures prepared by hydrothermal microwave heating O. V. Kharissova, M. Osorio, B. I. Kharisov.....	127-142
Consideration of the problem of absorption of some chemical elements by the cells of alga <i>Spirulina platensis</i> on the basis of the results of short-time experiments – <i>in Georgian</i> N. Kuchava.....	143-150
Mechanical durability of TmSe, TmS and LaBi thin films – <i>in Russian</i> Z. U. Jabua, A. V. Gigineishvili .....	151-154
Management of occupational radiation exposure in Georgia G. Nabakhtiani, I. Giorgadze, K. Gorgadze, Sh. Khizanishvili.....	155-160
Statement of boundary conditions of equation for magnetic fluid including nanoparticles K. Kotetishvili, E. Iordanishvili, G. Chikhladze.....	161-162

A new mechanism of “anomalies” of phenomena related to atomic displacements in nanomaterials A. Gerasimov, G. Chiradze, M. Vepkhvadze, T. Ratiani .....	163-172
Insertion of liquid Bi and Hg into one-dimensional channels of zeolite NaM – <i>in Russian</i> A. A. Kapanadze, G. D. Tabatadze, M. S. Taktakishvili.....	173-176
The spatially separated process of the formation of nanosized iron–oxygen structures on the steel surface contacting with water dispersion medium O. M. Lavrynenko.....	177-190
The state-of-the-art chemical analytical method for detection of sodium azide by <sup>14</sup> N NMR spectroscopy T. Chachibaia, M. M. Pastor .....	191-200
Some optical methods of detecting pathogenic nano-bio-particles K. Kapanadze, G. Kakabadze, V. Kvintradze .....	201-206
The uptake of Cr(III) in the presence of Mn(II) during growth of <i>Arthrobacter</i> species E. Gelagutashvili, A. Rcheulishvili.....	207-210
Material absorbing thermal and resonance neutrons – <i>in Russian</i> N. V. Bagdavadze, A. V. Rustambekov, T. I. Zedginidze, T. G. Petriashvili .....	211-214

#### Science History Pages

On history of expanding Universe theory – <i>in Russian</i> J. Tsertsvadze .....	215-224
Passion after the Jubilee – <i>in Georgian</i> V. Kvatchadze .....	225-228

#### Chronicle

2nd International Conference “Modern Technologies & Methods of Inorganic Materials Science” – <i>in Georgian</i> O. Tsagareishvili .....	229-232
---	---------

## Contents.

---

ICANM 2015: International Conference & Exhibition  
on Advanced & Nano Materials – *in Georgian*

**L. Chkhartishvili**.....233-236

**მეცნიერი, აღმზრდელი, დიდებული პიროვნება**

ცნობილი ქართველი მეცნიერი, საზოგადო მოღვაწე, ტექნიკის მეცნიერებათა დოქტორი, საქართველოს ტექნიკური უნივერსიტეტის პროფესორი, საქართველოს საინჟინრო აკადემიის აკადემიკოსი, ოპტიკისა და ფოტონიკის საერთაშორისო საზოგადოების საქართველოს ეროვნული კომიტეტის თავმჯდომარე, მეცნიერების ისტორიის საქართველოს საზოგადოების პრეზიდენტი რაფიელ ჩიქოვანი 85 წლის შესრულდა.



მაღალი ერუდიცია, შრომისმოყვარეობა, პრინციპულობა, პატიოსნება, თავმდაბლობა, დიდი ორგანიზატორული ნიჭი, პერსპექტივის აღლო, ყურადღებიანი და უაღრესად გულისხმიერი დამოკიდებულება ადამიანებისადმი – ამ პირადმა თვისებებმა საყოველთაო პატივისცემა და ავტორიტეტი მოუპოვა რაფიელ ჩიქოვანს.

რაფიელ ჩიქოვანი დაიბადა 1930 წლის 29 ნოემბერს დაბა ცაგერში მოსამსახურის ოჯახში. 1937 წელს შევიდა ცაგერის საშუალო სკოლაში, ხოლო 1948 წელს ოქროს მედლით დაამთავრა თბილისის ვაჟთა მე-7 სკოლა. 1953 წელს წარჩინებით დაამთავრა თბილისის სახელმწიფო უნივერსიტეტის ფიზიკის ფაკულტეტი. 1963 – 1965 წლებში იგი მოსკოვშია, საკავშირო მეცნიერებათა აკადემიის რადიოფიზიკისა და ელექტრონიკის ინსტიტუტში. 1965 წელს, თბილისში ნახევარგამტარული ხელსაწყოების ფიზიკის სამეცნიერო-კვლევითი საკავშირო ინსტიტუტის გახსნასთან დაკავშირებით, ის გამოიძახეს და დანიშნეს დირექტორის მოადგილედ სამეცნიერო მუშაობის დარგში. რაფიელ ჩიქოვანის უშუალო ხელმძღვანელობით ინსტიტუტში შეიქმნა ნახევარგამტარული ოპტოელექტრონიკის მიმართულება. 1973 წელს ჩამოყალიბდა სამეცნიერო-კვლევითი ინსტიტუტი “მიონი” ქარხნითურთ და რაფიელ ჩიქოვანი დაინიშნა დირექტორის მოადგილედ. 1977 – 1984 წლებში კი იგი იყო სამეცნიერო-კვლევითი ინსტიტუტის “მიონი” და მისი ქარხნის დირექტორი.

ამ პერიოდში “მიონმა” მნიშვნელოვან სამეცნიერო და საწარმოო წარმატებებს მიაღწია: გაიზარდა საწარმოს ტექნიკური დონე; შეიქმნა ქარხნის ფილიალები თელავსა და წალკაში; დამუშავდა და წარმოებაში დაინერგა ახალი მიკროელექტრონული ხელსაწყოები; შესრულდა სამუშაოების სრული ციკლი ოპტოელექტრონიკის მასალების კვლევიდან დაწყებული და ხელსაწყოების შექმნითა და მათი წარმოებაში დანერგვით დამთავრებული; დაიწყო მიკროელექტრონული და ოპტოელექტრონული ხელსაწყოების სერიული გამოშვება საბჭოთა კავშირის მასშტაბით, აგრეთვე, მათი

ექსპორტი საზღვარგარეთის ქვეყნებში; აშენდა საცხოვრებელი სახლები “მიონის” თანამშრომლებისათვის, ახალგაზრდული ბანაკი, პროფილაქტორიუმი, ბაკურიანის დასასვენებელი ბაზა და სხვ. “მიონი” საქართველოს ერთ-ერთ უდიდეს და დიდმნიშვნელოვან ორგანიზაციად გადაიქცა.

რაფიელ ჩიქოვანმა 1970 წელს დაიცვა დისერტაცია ფიზიკა-მათემატიკის მეცნიერებათა კანდიდატის, ხოლო 1998 წელს ტექნიკის მეცნიერებათა დოქტორის სამეცნიერო ხარისხების მოსაპოვებლად. 1973 წელს საკავშირო უმაღლესი საატესტაციო კომისიის მიერ მას მინიჭებული აქვს უფროსი მეცნიერ-თანამშრომლის წოდება. 1992 წელს ის აირჩიეს საქართველოს საინჟინრო აკადემიის წევრ-კორესპონდენტად, ხოლო 1996 წელს – ამ აკადემიის ნამდვილ წევრად.

1980 წელს ოპტოელექტრონული ხელსაწყოების დამუშავებისა და შექმნისათვის თანამშრომელთა ჯგუფს რაფიელ ჩიქოვანის ხელმძღვანელობით მიენიჭა საქართველოს სახელმწიფო პრემია მეცნიერებისა და ტექნიკის დარგში.

სხვადასხვა წლებში იგი იყო საკავშირო მეცნიერებათა აკადემიის სექციებთან არსებული ჰეტეროსტრუქტურებისა და ნახევარგამტარული ლუმინოფორების საბჭოების წევრი.



რაფიელ ჩიქოვანის სამეცნიერო ინტერესების სფეროს წარმოადგენს ნახევარგამტარების ფიზიკა, განსაკუთრებით ნახევარგამტარული ოპტოელექტრონიკა. მისი სამეცნიერო მოღვაწეობა მჭიდროდ არის დაკავშირებული სხვადასხვა მნიშვნელოვანი კვლევითი ცენტრის მეცნიერებთან. იგი თავისი დაუცხრომელი საქმიანობით ახალ-ახალ თაოსნობათა ორგანიზატორია, რომელთა განხორციელებისთვის ახალგაზრდული ენერჯითა და შემართებით იღწვის. მას გამოქვეყნებული აქვს 150-ზე მეტი სამეცნიერო ნაშრომი და 5 სახელმძღვანელო, მიღებული აქვს 12 საავტორო მოწმობა და 19 პატენტი. საზოგადოებისათვის კარგადაა ცნობილი მისი პუბლიკაციები საქართველოში მიკროელექტრონიკის განვითარების შესახებ. განსაკუთრებით აღსანიშნავია მისი აქტიური ცხოვრებისეული პოზიცია ჩვენი ქვეყნისათვის სხვადასხვა მტკივნეული საკითხის მიმართ.

გარდა უშუალოდ მეცნიერული საქმიანობისა, მრავალია სხვა ისეთი საქმეც, რომლის განხორციელებაშიც რაფიელ ჩიქოვანს ფასდაუდებელი წვლილი მიუძღვის: თბილისის სახელმწიფო უნივერსიტეტში ნახევარგამტარების ფიზიკის პრობლემური ლაბორატორიის შექმნა; თბილისის სახელმწიფო უნივერსიტეტსა და საქართველოს



ტექნიკურ უნივერსიტეტში ნახევარგამტარული მიკროელექტრონიკის კათედრების ორგანიზება; სტუ-ის ფიზიკის დარგის სადისერტაციო საბჭოში ნახევარგამტარების ფიზიკის სპეციალობის ჩამოყალიბება და საბჭოს შემდგომი ფუნქციონირება; სტუ-ში მიკროელექტრონიკის სამეცნიერო-საინჟინრო ცენტრის შექმნა და ხელმძღვანელობა; საქართველოს ფიზიკოსთა საზოგადოების შექმნა; ოპტიკისა და ფოტონიკის საერთაშორისო საზოგადოების (SPIE) საქართველოს ეროვნული კომიტეტის შექმნა და ხელმძღვანელობა; მეცნიერების ისტორიის საქართველოს საზოგადოების აღორძინება და რამდენიმე, მათ შორის საერთაშორისო, კონფერენციისა და სემინარის ორგანიზება (საერთაშორისო სამეცნიერო კონფერენციის “მეცნიერება და რელიგია” ჩატარება, იუნესკოს მიერ გამოცხადებული ფიზიკის წლისადმი (2005) მიძღვნილი კონფერენციის ორგანიზება, იუნესკოს გადაწყვეტილებით დაწესებული მეცნიერების დღისადმი მიძღვნილი საზეიმო სხდომების ჩატარება ყოველწლიურად, უნიკალური წიგნის “ბაგრატიონების სამეცნიერო და კულტურული მოღვაწეობა” მომზადება და გამოცემა, მრავალი კრებულის გამოცემა ქართველი მეცნიერების მოღვაწეობისა და სახელის უკვდავსაყოფად, ტექნიკური მეცნიერებების მთავალი პრიორიტეტების განსაზღვრა და სხვ.).



2004 წელს რაფიელ ჩიქოვანი დაინიშნა საერთაშორისო ბიოგრაფიული საზოგადოების (კემბრიჯი, ინგლისი) გენერალური დირექტორის მოადგილედ საქართველოში. მისი სახელი შეტანილია ისეთ ბიოგრაფიულ გამოცემებში, როგორცაა: “21-ე საუკუნის 2000 გამოჩენილი ინტელექტუალი” (2005, კემბრიჯი), “საერთაშორისო ბიოგრაფიული ცენტრის გენერალური დირექტორის მოადგილეები” (2005, კემბრიჯი). “საქართველო: დრო, ადამიანები” (2004, თბილისი).

რაფიელ ჩიქოვანი უმაღლესი სკოლის სასწავლო პროცესის ორგანიზატორი და აღიარებული პედაგოგია. 1989 – 2004 წლებში იგი იყო საინჟინრო ფიზიკის ფაკულტეტის დეკანი, სტუ-ის ფუნდამენტურ მეცნიერებათა სასწავლო-სამეცნიერო კომპლექსის ხელმძღვანელი, ფუნდამენტურ მეცნიერებათა სასწავლო-სამეცნიერო ინსტიტუტის დირექტორი, ფიზიკა-ტექნიკისა და ელექტრონიკის ფაკულტეტის დეკანი. საერთო ჯამში რაფიელ ჩიქოვანს აქვს პედაგოგიური მოღვაწეობის 49 წლის სტაჟი. იგი სხვადასხვა დროს თსუ-სა და სტუ-ში კითხულობდა და ამჟამადაც კითხულობს ლექციების კურსს ფიზიკისა და ტექნიკის სხვადასხვა სპეციალობაში.

რაფიელ ჩიქოვანისათვის გასაკუთრებულად მნიშვნელოვანია მისი მშობლიური მხარე – ლეჩხუმი. ეს დიდი სიყვარული სათანადოდ დაუფასა მისმა მშობლიურმა ხალხმა – 2014 წელს იქნა არჩეული ლეჩხუმის საპატიო მოქალაქედ.



სამაგალითოა რაფიელ ჩიქოვანის დამოკიდებულება თანამშრომლებთან და სტუდენტებთან. იგი არის პრინციპული, მომთხოვნის, სამართლიანი, გულისხმიერი, არაჩვეულებრივად კეთილმოსურნე და მზრუნველი, სპეტაკი პიროვნება.



საამაყო, რომ იგი მზრუნველობას და სიყვარულს არ აკლებს თავის ოჯახს – შესანიშნავ მეუღლეს ეკა მაჩაბელს, სამ სამაგალითო შვილს და რვა შვილიშვილს.

ვუსურვებთ ბატონ რაფიელს ჯანმრთელობას და დიდხანს სიცოცხლეს, რათა ჩვეული ენერგიით, ხალისით, დაუშრეტელი შრომისუნარიანობით და ღრმა ინტელექტით ემსახუროს თავის ქვეყანასა და ხალხს.

*საქართველოს ტექნიკური უნივერსიტეტის რექტორატი  
საქართველოს საინჟინრო აკადემია  
ჟურნალის "საქართველოს საინჟინრო სიახლენი" რედაქცია  
მეცნიერების ისტორიის საქართველოს საზოგადოება  
სტუ-ის ინფორმატიკისა და მართვის სისტემების ფაკულტეტი  
სტუ-ის საინჟინრო ფიზიკის დეპარტამენტი*

2015 წლის 11 ნოემბერი

FABRICATION AND CHARACTERIZATION OF SS316L  
–Al<sub>2</sub>O<sub>3</sub> COMPOSITES FOR WEAR APPLICATIONS

C. Kuforiji, M. Nganbe

University of Ottawa  
Department of Mechanical Engineering  
Ottawa, Canada  
ckufo091@uottawa.ca

Accepted October 19, 2015

**Abstract**

The low cost and excellent mechanical properties of steel and alumina make them outstanding candidates for fabricating composites for highly demanding wear applications. Therefore, SS316L-Al<sub>2</sub>O<sub>3</sub> composites were fabricated using mechanical alloying and powder metallurgy. The microstructure, hardness and abrasive wear behavior were investigated. The final composites consisted of 1-3 μm alumina particles homogeneously dispersed in the SS316L matrix. The porosity, hardness and wear rate were 5.3 vol. %, 1085 HV and 0.004 mm<sup>3</sup> / m, respectively. Compared to SS316L reference steel, the composites showed 9 times increase in hardness and 7.3 times decrease in wear rate. However, they exhibited 5.7 times higher wear rate compared to WC–Co due to lower ceramic content and higher porosity. Improved densification using hot isostatic pressing may result in substantial further improvement. It is concluded that the addition of Al<sub>2</sub>O<sub>3</sub> particles, together with optimized powder metallurgy processing can produce low cost steel based composites with excellent wear resistance.

**1. Introduction**

Increasing the wear resistance and the lifespan of wear components would contribute to reducing maintenance and wear damage costs and ultimately to increasing the equipment efficiency. Ceramic–metal composites are known as excellent candidates to meet this challenge. Machines, equipment and other devices that are designed or adopted for activities such as drilling, cutting, digging, crushing and grinding are subject to harsh application conditions. They are exposed to direct contact with abrasives that are entrapped between the components during operation resulting in 50 % of components failing by wear [1 – 4]. As a result, machines, pumps and other equipment used in such environment can fail prematurely leading to short lifecycles, increased maintenance and replacement costs in addition to loss of revenue in downtime. Therefore, mining components must possess high hardness to prevent wear, excellent hot strength to prevent distortion, sufficient toughness to prevent cracking due to impact, and fatigue strength to prevent failure due to vibrations.

WC–Co is commonly used as a highly wear resistant material in cutting tools, drilling and mining equipment because of its exceptional combination of strength, hardness and wear resistance [5, 6]. However, its toughness and impact resistance are often limited. Therefore,



steel components are generally preferred for heavy wear applications such as mining due to their higher toughness and impact resistance.

The presented research focuses on the fabrication of SS316L-Al<sub>2</sub>O<sub>3</sub> composites using the powder metallurgy route. SS316L and Al<sub>2</sub>O<sub>3</sub> are widely available at low cost making them viable for potential industrial use.

### 2. Methodology

SS316L steel and Al<sub>2</sub>O<sub>3</sub> composite powders were mechanically alloyed using a custom made attritor mill. Steel and alumina initial powders were 44 and 27 μm in size, respectively. The powder-to-powder weight ratio was 1 : 1 while the ball-to-powder ratio was 10 : 1. Mechanical alloying was performed wet at 720 and 800 rpm milling speeds till a homogeneous distribution of the reinforcement in the matrix was attained. Ethanol was used as milling aid and the alloyed powders were dried for 24 h in air. The produced SS316L-Al<sub>2</sub>O<sub>3</sub> composite powders were uniaxially pressed in a cylindrical die at compaction pressures ranging between 662 and 863 MPa. Pressureless sintering was performed in a vacuum furnace under argon atmosphere. A heating rate of 12 °C / min was used and the samples were maintained at 1400 °C for one hour. The sintered samples were furnace cooled. The bulk density was determined using the Archimedes principle according to ASTM B311-93 and distilled water. The percentage relative density was obtained by comparing the bulk density to the theoretical density. Microstructural characterization was carried out using a Clemex optical (OM) and a Carl Zeiss scanning electron (SEM) microscopy.

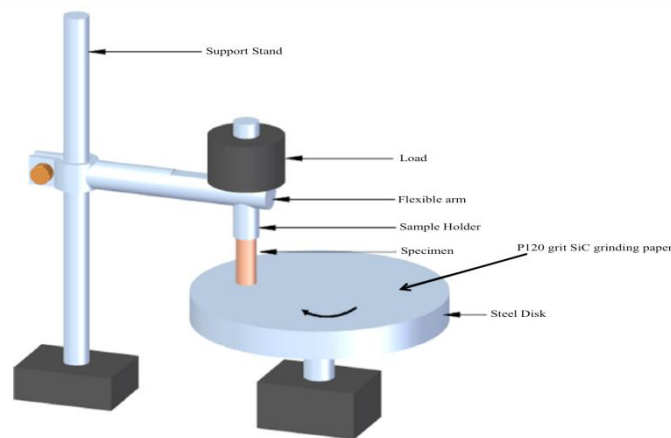


**Figure 1.** Schematic illustration of the pin-on-disk wear test apparatus [7].

Vickers hardness tests were conducted using a Wilson Beuhler machine and the wear behavior was investigated using a custom made pin-on-disk testing machine as seen in **Figure 1** according to ASTM G132. The pin samples were made to slide against a P120 grit SiC abrasive disk with a linear velocity of 1 m/s and a load of 2 N over a 3000 m distance. The pins were thoroughly cleaned with alcohol and weighed using an electric scale of accuracy ± 0.1 mg to determine the weight loss. The wear coefficient was calculated using the Archard wear Eq. (1) [8]:

$$Q = \frac{KW}{H}, \quad (1)$$

where  $Q$  is the volume loss per unit sliding distance,  $K$  is the wear coefficient,  $W$  is the load and  $H$  is the hardness of the pin.

### 3. Results and discussion

Two sets of SS316L–Al<sub>2</sub>O<sub>3</sub> composites were successfully fabricated as summarized in Table 1.

**Table 1.** Summary of fabrication parameters for SS316L–Al<sub>2</sub>O<sub>3</sub> composites.

Composites	Vol. fraction Al <sub>2</sub> O <sub>3</sub> (%)	Milling speed (rpm.)	Milling duration (hrs.)	Compaction pressure (MPa)	Sinter holding time (mins.)	Sinter temperature (°C)	Sinter atmosphere	Furnace heating rate (°C/min)	Cooling	Particle size (µm)
SET1	67	720	30	794.4	60	1400	Argon	12	Furnace cooling	1-3
SET2	67	800	20	794.4	60	1400	Argon	12	Furnace cooling	1-3

#### 3.1. Microstructure

Figures 2a – d show the microstructural evolution during compaction and sintering. Overall, SET1 samples showed a finer grain structure as well as a more homogeneous distribution of Al<sub>2</sub>O<sub>3</sub> particles in the steel matrix, which altogether are known to result in composites with improved mechanical properties for low temperature applications [9 – 11].

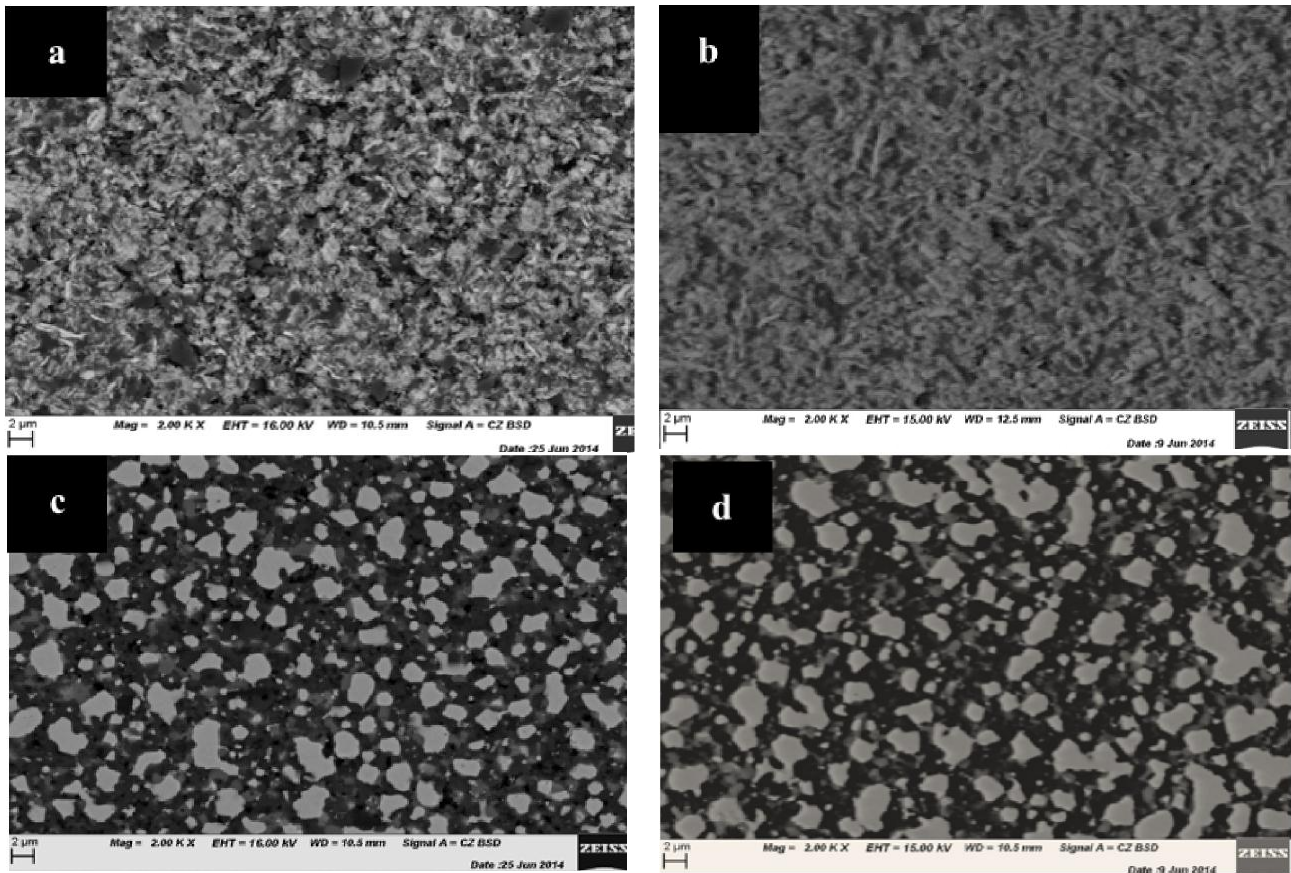


**Figure 2.** Micrographs of SS316L–Al<sub>2</sub>O<sub>3</sub> composites: a) SEM micrograph of a SET1 green; b) SEM micrograph of a SET2 green; c) SEM micrograph of sintered SET1 composite; d) SEM micrograph of sintered SET2 composite.

### 3.2. Densification and hardness

Figure 3 shows that as the compaction pressure increases, the green and sinter hardness first increases and then decreases with the peak hardness achieved at the optimum compaction pressure of 794.4 MPa. The lower speed milling at 720 rpm together with the longer milling duration in SET1 produces finer Al<sub>2</sub>O<sub>3</sub> particles in the steel matrix. This results in the observed increased hardness approximately 1.5 times higher than SET2 samples.

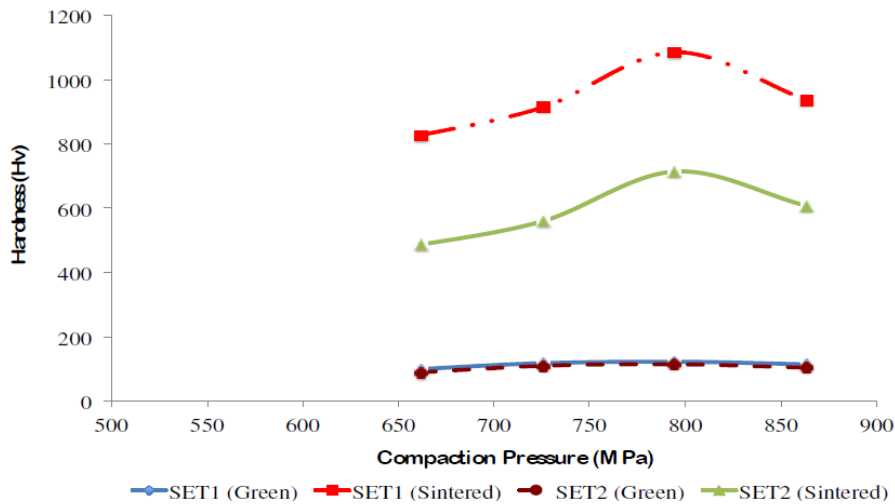


Figure 3. Variation of green and sinter hardness of SS316–Al<sub>2</sub>O<sub>3</sub> composites as a function of compaction pressure, milling parameters and sinter conditions.

All sintered samples showed a lower porosity than the green compacts, which illustrates the success of the sinter process. As can be seen in Figure 4, milling at 720 rpm produces the lowest porosity. Also, the samples compacted at the optimum pressure of 794.4 MPa showed the lowest sinter porosity of 5.3 %. The porosity decreases up to the peak density due to more advanced closing of gaps between individual powder particles. Beyond the densification peak, further increase in pressure leads to cracking resulting in a decrease in density.

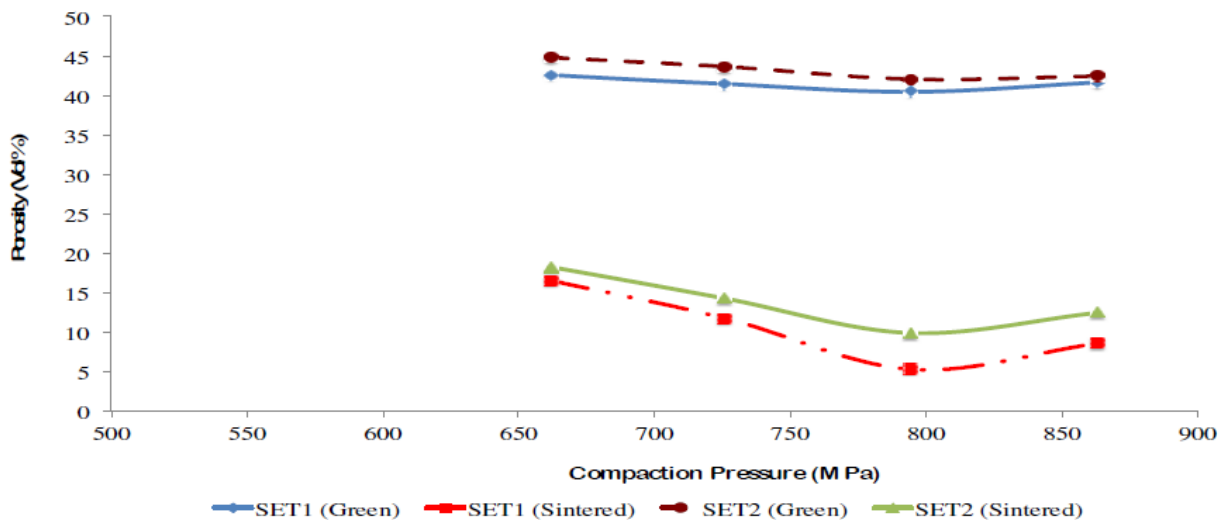
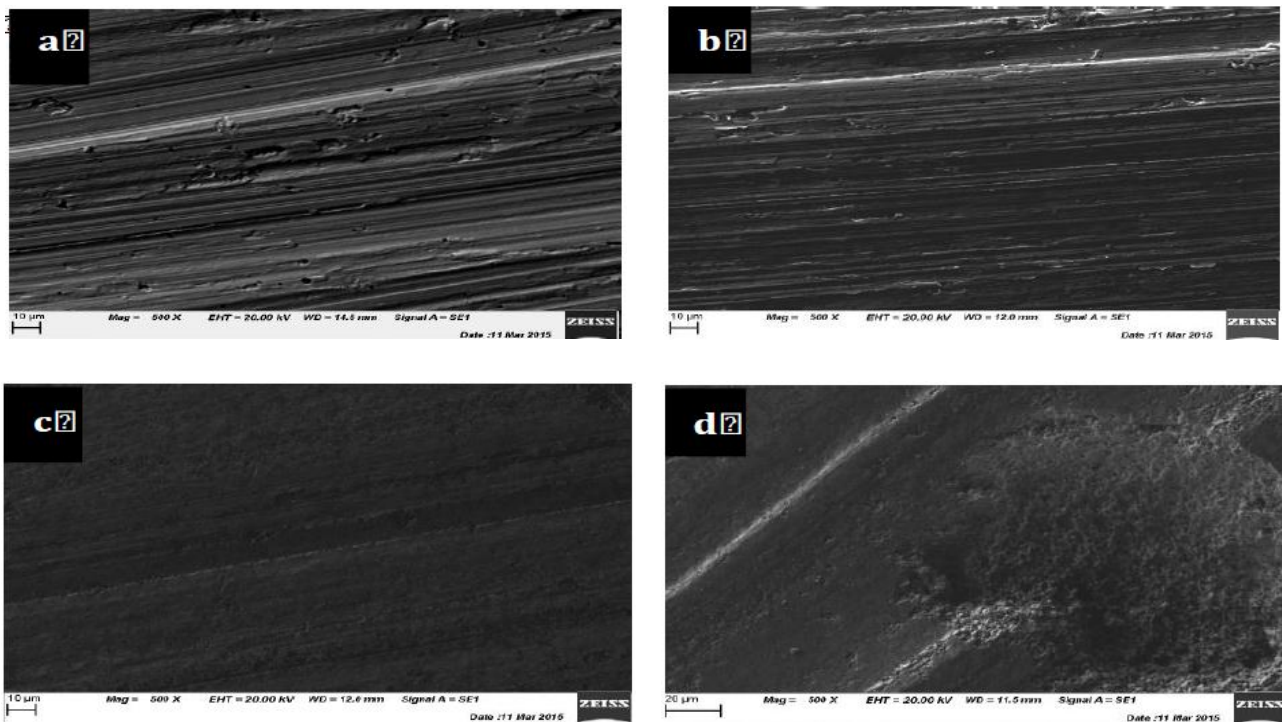


Figure 4. Porosity of green and sintered SS316L–Al<sub>2</sub>O<sub>3</sub> composites as a function of compaction pressure, milling speed and sinter conditions.

### 3.3. Wear behavior

The SEM images in **Figure 5** show scars on composite surfaces following wear testing. The composite wear primarily takes place by slow micro-cutting (see **Figures 5c** and **d**) in contrast to rapid wear of unreinforced steel as illustrated by the deep grooves in **Figures 5a** and **b**. The higher wear resistance of steel-alumina composites is due to their much higher hardness that efficiently limits plug-in of the SiC abrasive particles [12]. **Figure 5d** illustrates occasional dimples observed on some worn composite surfaces as a result of dislodging of some alumina particles or inclusion during wear testing.



**Figure 5.** SEM images of worn sample surfaces: a) Fabricated SS316L; b) Commercial SS316; c) SET1 composite; d) SET2 composite.

**Figures 6** and **7** show the comparative plot of the wear rates and hardness of the existing materials and fabricated composites (SET1 and SET2). The SET1 and SET2 composites have measured hardness values of 1085.2 and 714.3 HV with wear rates of 0.004 and 0.011 mm<sup>3</sup>/m, respectively, compared to commercial SS316 with a hardness of 140 HV, a wear rate of 0.0195 mm<sup>3</sup>/m, and unreinforced SS316L with a hardness of 121 HV and a wear rate of 0.0288 mm<sup>3</sup>/m as seen in **Figures 6** and **7**. The higher wear rates of unreinforced steel (commercial 316 and fabricated SS316L) are due to their lower hardness compared to the SiC abrasives used for wear testing with a hardness of 2500 HV. The abrasives can therefore remove materials more rapidly from the wear surface [11] by deep plug-in and rapid micro-cutting [12]. The substantially higher wear resistance of the composite is due to the added Al<sub>2</sub>O<sub>3</sub> particles and the resulting higher hardness [13], which limit plug-in and micro-cutting [14]. However, compared to commercial 90WC–10Co, 5.7 and 15.7 times higher volume loss was measured for SET1 and SET2 over a sliding distance of 3000 m, respectively. This corresponds to an increase in wear

rate by 93.6 to 83 % for SET2 and SET1, respectively. This can be rationalized by the two major differences: First, the used  $\text{Al}_2\text{O}_3$  particle content of 50 wt. % is much lower than the 90 wt. % WC content in 90WC-10Co. Second, the remaining porosity of 5.3 % or higher observed in the fabricated  $\text{Al}_2\text{O}_3$ -steel composites is much higher than in conventional WC-Co composites. Therefore, it can be expected that more advanced processes such as hot pressing or hot isostatic pressing may further substantially improve the density, the hardness and the wear resistance of the  $\text{Al}_2\text{O}_3$ -steel composites.

The relationship between the hardness and the wear rate is nonlinear [15]. The wear resistance depends on both the hardness and the toughness. As an increase in hardness mostly leads to some reduction in toughness, an optimum balance must be obtained to prevent the material from either being too soft or too brittle.

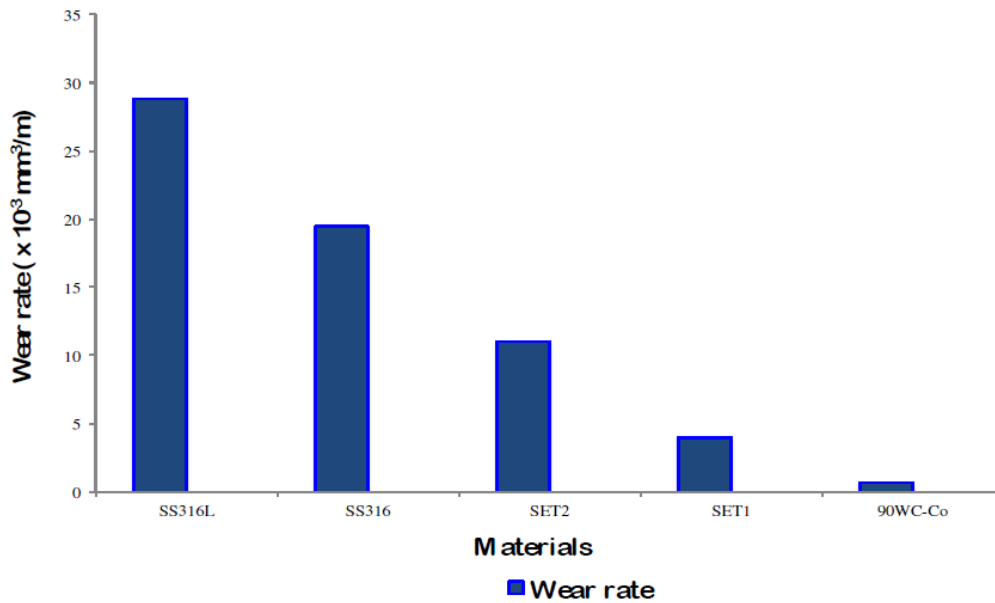


**Figure 6.** Comparative plot of wear rate of fabricated unreinforced SS316L, commercial SS316, fabricated SS316L- $\text{Al}_2\text{O}_3$  composites (SET1 and SET2) and 90WC-Co composites.

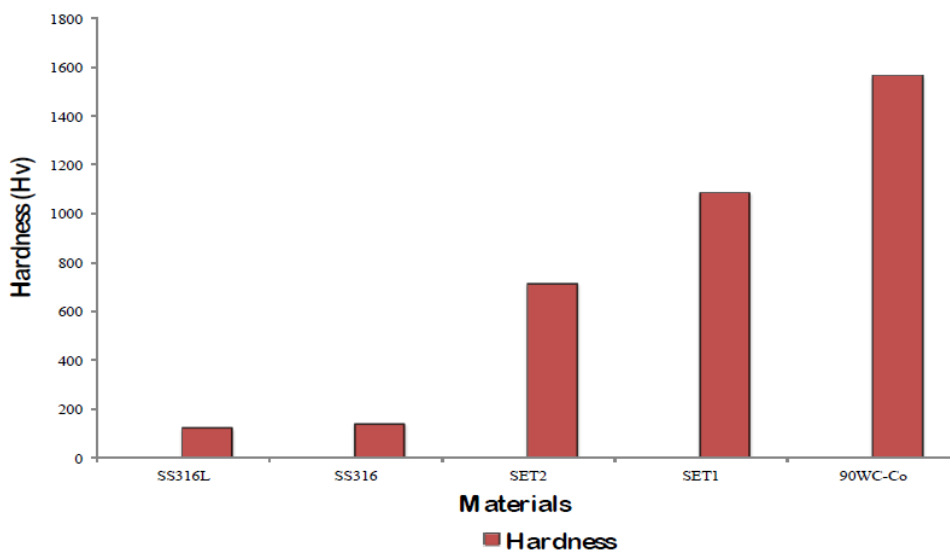


**Figure 7.** Comparative plot of hardness of fabricated unreinforced SS316L, commercial SS316, fabricated SS316L- $\text{Al}_2\text{O}_3$  composites (SET1 and SET2) and 90WC-Co composites.



#### 4. Conclusions

50 wt. % Al<sub>2</sub>O<sub>3</sub> and 50 wt. % SS316L steel composites are successfully fabricated using the conventional powder metallurgy technique. The lower milling speed of 720 rpm combined with a longer milling duration of 30 h is more appropriate for the mechanical alloying of SS316L–Al<sub>2</sub>O<sub>3</sub> composite powder. The compaction pressure of 794.4 MPa yielded the lowest porosity, highest hardness and wear resistance. The sinter temperature of 1400 °C in an argon environment produced good densification, hardness and wear resistance. The addition of 50 wt. % alumina particles led to up to 86 % reduction in wear rate resulting in up to 7.3 times decrease in volume loss compared to unreinforced SS316L. Due to the remaining porosity and lower ceramic content however, commercial 90WC–Co composites showed about 5.7 times lower wear rate compared to the best SS316L–Al<sub>2</sub>O<sub>3</sub> composite samples fabricated so far. Therefore, higher Al<sub>2</sub>O<sub>3</sub> contents as well as better densification by hot pressing or hot isostatic pressing are expected to further substantially improve the wear resistance of SS316L–Al<sub>2</sub>O<sub>3</sub> composite properties.

#### References

1. K. H. Zum Gahr. *Microstructure and Wear of Materials*. 1987, Amsterdam, The Netherlands Elsevier Sci. Publ. B.V., 10.
2. J. Pirso, S. Letunovič, M. Viljus. Friction and wear behavior of cemented carbides. *J. Wear*, 2004, 257, 3-4, 257-265.
3. G. W. Stachowiak, A. W. Batchelor. *Engineering Tribology* (3rd Ed.). 2006, Burlington, Butterworth–Heinemann.
4. M. Petrica, E. Badisch, T. Peinsitt. Abrasive wear mechanisms and their relation to rock properties. *J. Wear*, 2013, 308, 1-2, 86-94.
5. G. Gille, B. Szesny, K. Dreyer, H. van den Berg, J. Schmidt, T. Gestrich, G. Leitner. Submicron and ultrafine grained hardmetals for microdrills and metal cutting inserts. *Int. J. Ref. Met. & Hard Mater.*, 2002, 20, 1, 3-22.
6. K. Konopka. Novel ceramic–metal composites with metal phase from micro- to nanosize. *Solid State Phen.*, 2004, 101, 139-142.
7. S. C. Vettivel, N. Selvakumar, R. Narayanasamy, N. Leema. Numerical modeling, prediction of Cu–W nano powder composite in dry sliding wear condition using response surface methodology. *Mater. & Des.*, 2013, 50, 977-996.
8. J. F. Archard. Contact and rubbing of flat surfaces. *J. Appl. Phys.*, 1953, 24, 8, 981-988.
9. F. E. H. Müller, M. Nganbe, H. J. Klauß, M. Heilmaier. Monotonic and cyclic high temperature deformation behavior of the ODS nickel-base superalloy PM 1000. *J. Adv. Mater.*, 2000, 32, 9-20.
10. J. B. Fogagnolo, F. Velasco, M. H. Robert, J. M. Torralba. Effect of mechanical alloying on the morphology, microstructure and properties of aluminium matrix composite powders. *Mater. Sci. & Eng. A*, 2003, 342, 131-143.
11. M. Nganbe, M. Heilmaier. Dependence of mechanical strength on grain structure in the  $\gamma'$  and oxide dispersion strengthened nickel base superalloy PM 3030. *Zeitschrift fuer Metallkunde*, 2005, 96, 625-631.

12. M. Vardavoulias, M. Jeandin, F. Velasco, J. M. Torralba. Dry Sliding Wear mechanism for p / m austenitic stainless steels and their composites containing Al<sub>2</sub>O<sub>3</sub> and Y<sub>2</sub>O<sub>3</sub> particles. *Tribol. Int.*, 1996, 29, 6, 499-506.
13. M. Chmielewski, K. Pietrzak, W. Włosiński. Properties of sintered Al<sub>2</sub>O<sub>3</sub>-Cr Composites depending on the method of preparation of the powder mixture. *Sci. Sinter.*, 2006, 38, 231-238.
14. M. Imbaby, K. Jiang. Net shape fabrication of stainless steel-alumina composite micro parts. *J. Micromech. & Microeng.*, 2009, 19, 045018.
15. L. Huei-Long, L. Wun-Hwa, S. L.-I. Chan. Abrasive wear of powder metallurgy al alloy 6061-SiC particle composites. *J. Wear*, 1992, 159, 2, 223-231.

NUMERICAL SIMULATION OF DROPLET BREAKUP,  
SPLITTING AND SORTING IN MICROFLUIDIC DEVICE

T. Chekifi, B. Dennai, R. Khelifaoui

University Tahri Mohammed Bechar Bechar  
Laboratory ENERGARID  
Bechar, Algeria  
chekifi.tawfiq@gmail.com

Accepted October 19, 2015

**Abstract**

Droplet in microfluidic is applied to lab-on-a-chip devices for biomedical testing and synthesis, droplets of water-in-oil are produced by flow focusing technique; an obstacle configuration is used to split the droplet. The finite volume numerical method was applied to solve the Navier–Stokes equations in conjunction with the Volume of Fluid (VOF) approach for interface tracking of the commercial code FLUENT. Numerical simulations were carried out for different flow conditions. The effects of some parameters on the droplet motion were investigated to find the optimal conditions for droplet breakup. The numerical results show that the main channel width, the surface tension, the contact angle and the capillary number of continuous phase play an important role on the droplet generation. The computation also demonstrates that an obstacle configuration can be used to split droplet, where the latter are sorted in the end of the main channel. It also demonstrates that the volume of fluid method is an effective way to simulate the generation of droplets in flow focusing configuration.

**Nomenclature**

f: frequency (Hz)	$\mu$ : dynamic viscosity (kg / m · s)
u: velocity (m / s)	$\alpha$ : phase fraction (%)
u <sub>c</sub> : continuous phase velocity (m / s)	$\sigma$ : the surface tension coefficient (N / m)
u <sub>d</sub> : dispersed phase velocity (m / s)	$\tau$ : time (s)
n: unit vector normal to the interface	W: width of the main channel
$\kappa$ : curvature of the interface	W <sub>c</sub> : width of continuous phase inlet
F: the surface tension force	W <sub>d</sub> : width of continuous phase inlet
W: width (mm)	$\rho_c$ : continuous phase density
$\rho$ : density (kg / m <sup>3</sup> )	$\rho_d$ : dispersed phase density

**1. Introduction**

Over the last few decades, modeling immiscible fluids such as oil and water have been a classical research topic. Droplet-based microfluidics presents a unique platform for mixing, reaction, separation, dispersion of drops and numerous other functions [1, 2]. Droplet-based



microfluidics is of great interest for biological research, chemical synthesis, drug delivery and medical diagnostics.

Droplet-based microfluidics refers to devices and methods for controlling the fluid flows in length scales smaller than one millimeter. Monodisperse droplets in microfluidic devices have been generated using different microchannel configurations such as T-junction [3, 4], flow focusing [5], or co-flowing [6]. In microfluidics, controlling droplet size is a core technique not only for producing highly monodisperse emulsions [7], but also for using the droplet itself as a tool for manifold purposes [8, 9]. As for droplet breakup, Link et al. introduced two methods to reduce droplet size using T-junction or a square obstruction deposited in the center of the channel [10]. As these methods are passive ways in droplet manipulation, it provides a way of reducing droplet size in a rapid process with a narrow size distribution. As this is an effective process to reduce the droplet size, it is worthwhile to get physical insights through numerical analysis on the relevant droplet flows in microfluidics [11].

In recent studies, unlike relatively simple geometries such as T-junctions [12, 13] or flow focusing devices [14, 15], novel designs have been developed for improved manipulation of droplets. Lee et al. [16] presented a one-step method for size control and sorting of droplets in a modified flow focusing geometry with a moving wall technique operated by pressure inlets. Also, in a cross-shaped channel, droplet generation by a thread breakup due to pressure inlets at both sides was shown with a surface treatment technique [17]. Droplet fusion devices were also proposed using a hydrodynamic trap at a wide cross channel [18, 19], at a tapered channel [20], at a fluid resistance in straight channels [21], and an array of pillar elements [22]. As mentioned previously, an obstruction in microchannel can also be utilized to reduce the droplet size [10]. Menech [23] was performed numerical analysis to figure out the droplet breakup process and optimize the geometry configuration for the process. In which, the author suggested T-junction channel using a phase-field method to compute droplet breakup, Carlson et al. [24] extended the phase field method to simulation of droplet motion in a Y-junction channel. Their results showed that the tip of the junction affected the droplet deformation, and the droplet breakup or non-breakup regime depended on the capillary number and droplet size. The droplet breakup by a circular cylinder in a microchannel was computed by Chung et al. [25] using a front tracking method, in which the droplet shape was represented by the moving front elements. Their numerical results showed that the split droplets merged in the rear side of the obstacle when the capillary number was not large.

Although various studies on the generation of droplets in T-junction and flow focusing devices have been carried out, a fundamental understanding of the flow physics that account for the effect of the geometry of the devices is still missing. In addition, simulation of two immiscible phases flow in complex geometry is a challenging work [26].

Computational fluid dynamics (CFD) studies allow for broad parametric variations that are hard to study experimentally. CFD also provides detailed information on flow details such as pressures and velocities that are difficult to measure experimentally, and can thus provide mechanistic insights needed to check various hypotheses. Recently, the volume of fluids method has been proved to be a powerful method to simulate droplet dynamics [27]. In this method, the interface is given implicitly by a color function, which is defined as the volume fraction of one of the fluids within each cell. From this function, a reconstruction of the interface is made and the interface is then propagated implicitly by updating the color function. VOF methods are conservative and can deal with topological changes of the interface. However,

VOF methods cannot accurately compute several important properties, such as curvature and the normal to the interface. Moreover, a high order of accuracy is hard to achieve because of the discontinuities in the color function [27].

Motivated by the previous work [26] and [28], using a VOF method, we perform a two-dimensional numerical CFD study of droplet breakup, splitting and sorting, in the present study we suggest device that allows droplet breakup in flow focusing configuration, splitting and sorting. In this microsystem, the effect of main channel size and capillary number on the droplet dynamics is investigated. In previous numerical works [26, 29, 30], surface tension plays a significant role on the droplet deformation in confined microchannel flows. In the same manner, by testing a several values between both phases, we expect that this parameter affects the droplet dispersion in the microchannel. In which, the effects of inertia and gravity in the volume does not play an important role with respect to the macroscopic scale. We also study the droplet breakup as function of the capillary number and the main channel size to find the optimal conditions for droplet detachment. In our model, we investigate the droplet splitting and sorting by size in the end of the main channel by the use of an obstacle. The frequency of droplet generation and droplet sorting is also considered. Finally, we suggest useful ideas for manipulating droplets in microchannel flows.

## 2. Description of the system and geometries

The physics to be simulated involves droplet breakup by flow focusing technique. Three sizes of the main channel are evaluated to produce water-in-oil droplet. There are two oil inlets, one water inlet and one outlet in. All the micro- channels are 5 mm long. The description of the geometries is presented in **Figure 1**. Due to the existence of the obstacle, two sub-channels are formed in the end of main channel.

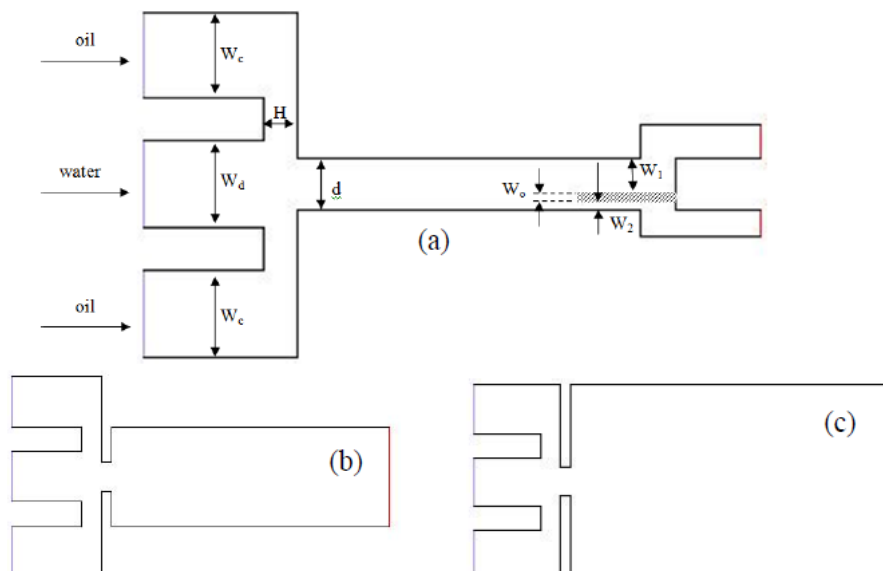


**Figure 1.** (a): Schematic of flow focusing configuration.  $W_c = W_d = 2$ . An orifice with width  $d = 1.2$  is placed at a distance  $H = 0.8$  downstream of three coaxial streams. The main channel width is varied (a):  $W = 1.2$ , (b):  $W = 4$  and (c):  $W = 8$ .  $W_o = 0.16$ , sub-channel1:  $W_1 = 0.8$ , sub-channel 2:  $W_2 = 0.24$ . The total length of the configuration is 12. (All the numbers are in mm).

In our system, the droplet is generated by the flow focusing, which has been widely used for generating highly spherical droplet [31 – 33]. **Figure 1** shows the flow focusing geometry implemented into a microfluidic device. In this structure, the dispersed phase flows in the middle of the channel, while the continuous phase flows through upper and lower channels. The continuous phase and dispersed phase penetrate into the downstream channel, and the continuous phase exerts pressure and stress which force the dispersed phase into a narrow thread. The dispersed phase breaks inside or downstream of the orifice, then the droplet is generated at the end of the flow stream where the neck forms.

The surface tension term reflects the interfacial force between the discrete liquid (droplet) and the continuous liquid. The interaction (attraction or repulsion) between droplets results from the continuous liquid flow which is affected by the interfacial forces existing at each droplet surface.

### 3. Numerical approach

The segregated solver for an unsteady laminar flow was used in CFD, the volume of fluid method was performed to track the interface between water droplet and the continuous phase. The VOF model is a surface-tracking technique that is useful when studying the position of the interface between two immiscible fluids. A single set of momentum equations is shared by the fluids, and the volume fraction of each of the fluids in each computational cell is tracked throughout the domain. The VOF model uses phase averaging to define the amount of continuous and dispersed phase in each cell. A variable,  $\alpha$ , was defined as [29, 30]:

$\alpha = 1 \Rightarrow$  when the cell is 100 % filled with continuous phase

$\alpha = 0 \Rightarrow$  when the cell is 100 % filled with dispersed phase

$0 < \alpha < 1 \Rightarrow$  when the cell contains an interface between the two phases

The density  $\rho$ , and viscosity  $\mu$ , for both phases (water and oil) can be calculated using a linear dependence:

The subscript 1 is chosen for the continuous liquid (primary) phase, while the subscript 2 for the discrete phase (microdrops)

$$\rho = \rho_1 \alpha + \rho_2 (1 - \alpha), \quad (1)$$

$$\mu = \mu_1 \alpha + \mu_2 (1 - \alpha). \quad (2)$$

There are several different VOF algorithms with different accuracies and complexities in CFD. The geometric reconstruction scheme used in this study is based on the work of Youngs (1982) [33] and further described by Rudman (1997) [34]. This scheme permits a piecewise-linear approach, which assumes that the interface has a linear slope within each cell, and the position of the interface is calculated from the volume fraction and their derivatives in the cell. The solutions of the velocity field and pressure are calculated using a body-force-weighted discretization scheme for the pressure, the Pressure-Implicit with Splitting of Operators (PISO) scheme for the pressure velocity.

The body-force-weighted scheme is used since it works well with the VOF model, and the PISO scheme is chosen to improve the efficiency of the calculation of the momentum balance after the pressure correction equation is solved. The CFD software was used to simulate the flow of oil microdrops sorting. The governing equations are the mass conservation equation for each phase and the momentum equation:

$$\partial_t C + \vec{u} \nabla C = 0, \quad (3)$$

where the velocity is given by  $u$ . In addition, a single momentum equation is used for the mixture of two-phase-fluid.

The momentum equation hence is described by

$$\partial_t(\rho u) + \nabla \cdot (\rho u u) + \nabla u \cdot \nabla[\mu] = -\nabla P + F, \quad (4)$$

where  $F$  is the surface tension  $F = \sigma(x)n$  force,  $P$  is the curvature of the interface and  $n$  is a unit vector normal to the interface.  $\sigma$  is the surface tension coefficient.

#### 4. Droplet simulation and parameters

FLUENT 6.3 in CFD software was used to model droplet formation in the microfluidic by flow focusing configuration (see **Figure 1**). The volume of fluid (VOF) model in three-dimensional form was used, which enables capturing and tracking the precise location of the interface between the fluids. The VOF method operates under the principle that the two or more fluids are not interpenetrating. The flows are taken to be two-dimensional and laminar. In the simulations, a constant velocity boundary scheme proposed by Zou & He [32] is imposed on both water and oil inlet and the pressure of outlet is the same as the atmospheric pressure. At the position where the fluid meets the solid walls, half-way bounce-back boundary scheme is applied to achieve the non-slip velocity condition at the solid walls. The viscosities of both liquids water and gasoil are respectively defined as  $\mu_w = 0.001$  and  $\mu_o = 0.003 \text{ kg / m} \cdot \text{s}$ . An equilibrium contact angle  $\theta = 60^\circ$  were prescribed. This contact angle is used to correct the surface normal in the vicinity of the wall, and therefore adjusts the curvature of the interface and the surface tension calculation near the wall [35]. The second-order upwind scheme is used for discretization of the momentum equation. The PISO scheme is taken as the pressure-velocity coupling scheme, while the PRESTO! is taken as the pressure discretization scheme. The geometric reconstruction scheme is used for interpolation of the interface geometry. It is able to form mono-dispersed droplets by this way due to the different surface tensions of two fluids.

The computations were run for a large number of time steps ( $10^{-5}$ ) to generate a database from which statistically converged mean and perturbation flow quantities could be extracted. The convergence limit was set to a residual sum of  $10^{-3}$  for the continuity and velocity components. These results are discussed in the following sections.

The requirement to successfully follow of droplets behavior leads to very large numbers of grid cells when uniform meshes are used. Three intervals mesh sizes were tested to obtain grid independent solutions ( $h = 0.06, 0.08$  and  $0.10 \mu\text{m}$ ). The relative difference of droplet volumes and interface shapes between successive mesh sizes is observed to be small as the mesh size decreases. Therefore, our simulations in this study are done with  $h = 1 \mu\text{m}$  to save computing time without losing the accuracy of the numerical results.

##### 4.1. The main channel width effects

To test whether the confinement of geometry plays an important role in the breakup of plugs, we first perform computations to investigate the effect of the main channel width on the droplet flow regime. In the simulations, to single out the geometrical parameter, the inlet flow velocity of both phases is ( $u_d = u_c = 0.2 \text{ m / s}$ ), the densities of both fluids are  $\rho_c = 830$  and  $\rho_d = 998.2 \text{ kg / m}^3$ . the results for three configuration are presented in the **Figure 2**.

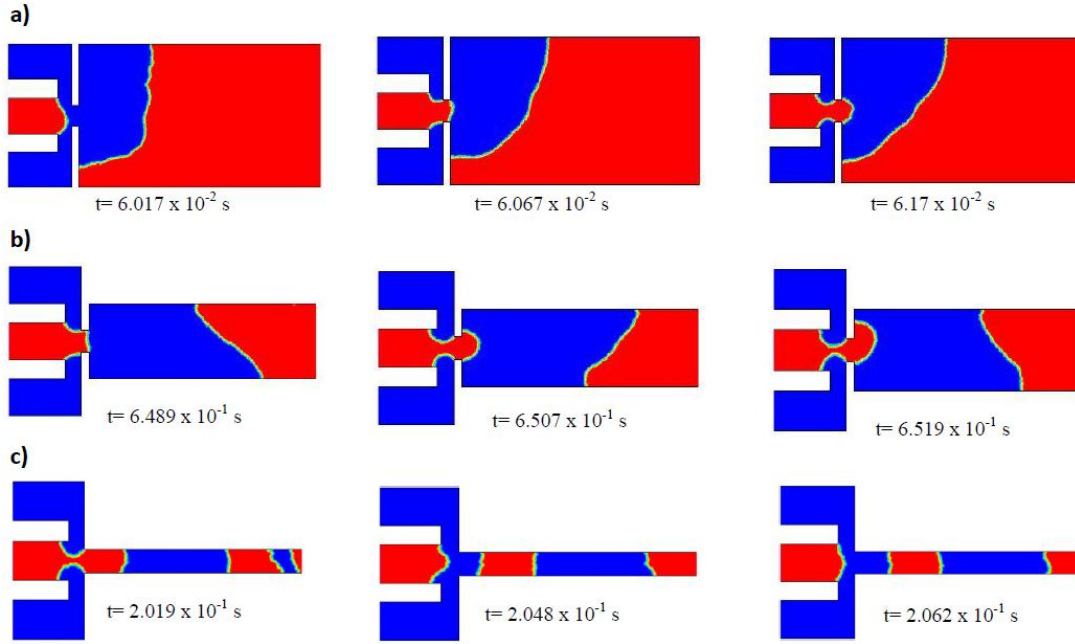


**Figure 2.** The droplet generation at  $u_d/u_c = 1$  ( $u_d = u_c = 0.2$  m / s) for three different widths of main channel. (a)  $W=8$ mm, b)  $W=4$ mm and c)  $W=1.2$ mm.

The geometry effect, i.e., the width of the main channel ( $W$ ) plays an important role in the flow dispersion in the main channel **Figure 2**, at the same conditions for large main channel the flow is observed in thread regime due to the accumulation of generated droplets, which are flow with low velocity **Figures 2a** and **b**, where droplet emerging is occurred. For the smallest model **Figure 2c**, no emerging is observed, because droplets flow with high velocities. Therefore, the flow pattern is clearly observed with high dispersion. For the next sections, we use the smallest model with main channel width = 1.2 mm.

#### 4.2. Surface tension effect

For two phase flows in microchannels, the surface tension forces play an important role in determining the dynamics of droplets, whereas gravitational forces are generally less important, we investigate the influence of surface tension coefficient on the droplet flow regime.

In this subsection, we use water as the dispersed phase and oil as the continuous phase, and observe flow regime, which depends on the surface tension coefficient. The densities of the continuous and dispersed phase are assumed respectively  $\rho_c = 830$  and  $\rho_d = 998.2$  kg / m<sup>3</sup>. The channel surface is hydrophobic, i.e., the contact angle between dispersed phase and the channel surface is  $\theta = 0^\circ$ . It is shown in **Figure 3** that for capillary numbers which define flows in the jetting to dripping regime through numerical simulations, and quantify the results in terms of the “stable” droplet formation regime in a microchannel. for a given inlet velocity of both phases ( $u = 0.2$  m / s) As shown in **Figure 3**, three typical flow patterns are identified for different surface tension at a fixed capillary number ( $Ca = 3.43 \cdot 10^{-2}$ ). For low  $\sigma$ , thread regime of dispersed phase is clearly observed, as we increase  $\sigma$ , the thread becomes unstable after a distance of laminar flow  $\sigma = 0.01$  N / m, for higher surface tension  $\sigma = 20$  N / m, droplet are formed with high dispersion due to the squeezing mechanism. For the next simulations, we use  $\sigma=20$ N/m to generate mono dispersed droplet.

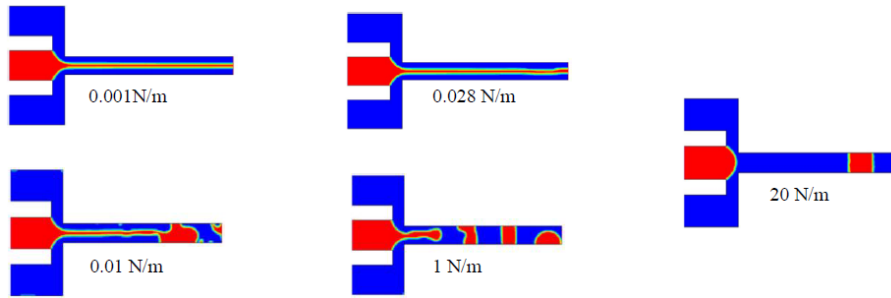


**Figure 3.** Droplet flow regimes as a function of the surface tension ( $\sigma$ ) for  $u_c / u_d=1$  ( $u_c = u_d = 0.2 \text{ m / s}$ ) for the small model.

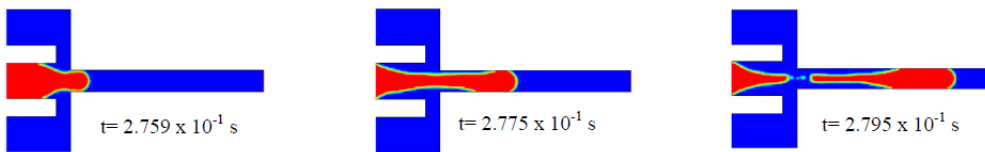
### 4.3. Contact angle effect

Wetting properties are usually characterized by the contact angle on a surface. Young's law provides the relation between interfacial tensions and contact angle. For a water droplet on a surface, surrounded by oil, the equilibrium contact angle is [36]:

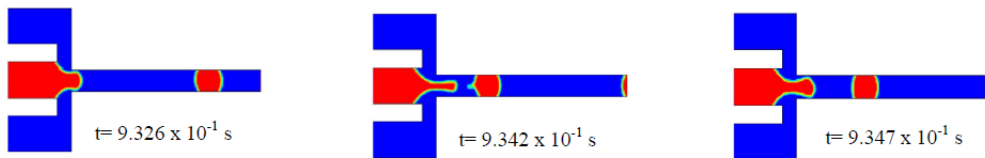
$$\cos(\theta) = \frac{\sigma_{oil,wall} - \sigma_{water,wall}}{\sigma_{oil,water}}$$

where  $\sigma_{oil,wall}$  is the interfacial tension of oil with the wall surface, water, wall is the interfacial tension of water with the wall surface, and  $\sigma_{oil,water}$  is the interfacial tension of the oil with water.

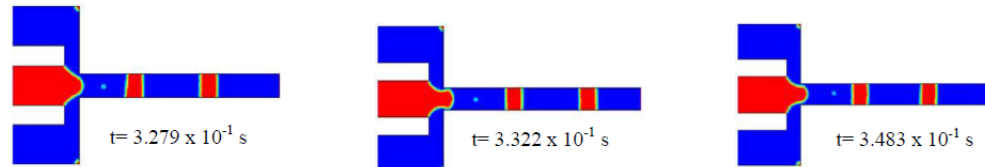
a)  $\Theta=0^\circ$



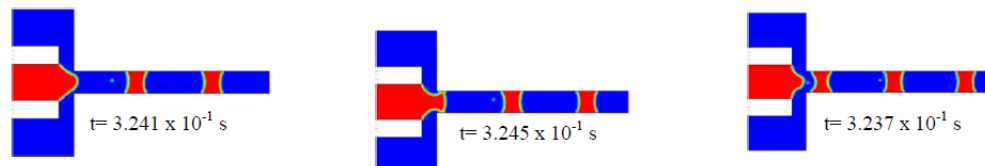
b)  $\Theta=60^\circ$



c)  $\Theta=90^\circ$



d)  $\Theta=120^\circ$



e)  $\Theta=180^\circ$

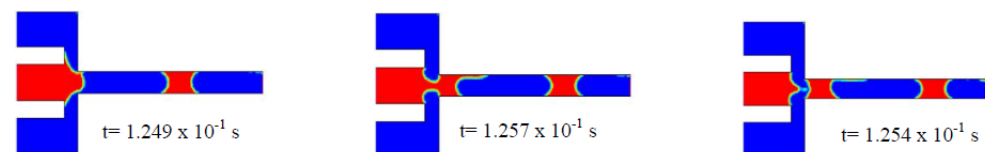


**Figure 4.** Droplet (water-in-oil) flow pattern as a function of contact angle at  $Ca = 0.053$  ( $u_c = 0.5 \text{ m / s}$  and  $u_d = 0.3 \text{ m / s}$ ) and  $\sigma = 10 \text{ N / m}$ .



A constant contact angle associated to a non slip condition was imposed at the contact point between the gas–liquid interface and the walls defining our structure. The corresponding numerical procedure is described in detail in Dupont and Legendre [20]. The result of the droplet flow pattern as function of contact angle is presented in the **Figure 4**.

The wetting properties of the fluids relative to the channel walls, more specifically the contact angle, have also been shown to affect the two-phase flow patterns in microchannels [41]. In order to determine the influence of the contact angles on droplet shape, different values of the contact angles ( $\Theta = 0, 60, 90, 120$  and  $180^\circ$ ) are tested by keeping the same conditions to find the optimum contact angle to obtain spherical form of droplet. It is clearly observed that the droplet takes a shape for each contact angle. For  $\Theta = 0^\circ$ , elongated droplet are observed with low production frequency, whereas the rest of contact angle the geometrical form is smaller. For  $\Theta = 90^\circ$ , the droplet takes uniform rectangular shape with high production frequency compared of  $\Theta = 0^\circ$ . For both  $\Theta = 120^\circ$  and  $\Theta = 180^\circ$  droplets take concaved shape in its extremity. The contact angle of  $60^\circ$  is the optimum condition for droplet flow pattern; which is used for the next sections. The droplet are taken uniform spherical shape.

### 5. Droplet splitting and sorting

Numerical simulations of droplet breakup and splitting are performed using VOF method, droplet of water-in-oil are generated by flow focusing configuration, The simplest droplet sorting techniques require no detection or switching mechanisms, but instead rely on creative device geometry that allows the separation of droplets by size. By simply creating an obstacle geometry in which the daughter channels had different widths, droplets were induced to sort into one of the channels (**Figure 5**). The split daughter droplets pass the sub-channels, while the bigger split daughter droplets pass the sub-channels 2. When a droplet collides with the obstacle, it splits into the obstacle-wall gaps (or sub-channels). The split portions of droplet leave out the sub-channels to the outlet of microsystem.

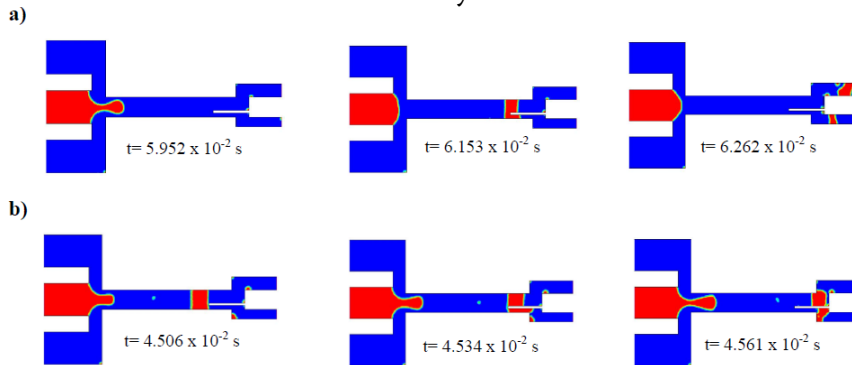


**Figure 5.** Droplet breakup, splitting and sorting for two different capillary numbers:

a)  $u_c = 1$  m / s,  $u_d = 0.1$  m / s,  $Ca = 5.36 \cdot 10^{-2}$  and b)  $u_c = 0.5$  m / s,  $u_d = 0.3$  m / s,  $Ca = 6.64 \cdot 10^{-2}$ .

**Figure 5** shows the droplet motion. A convergence test for grid resolutions is first conducted for droplet breakup by the use of a quadrature obstacle. Water-in-oil droplet are generated by flow focusing configuration, splitting of droplet is performed by thinner obstacle at the end of the main channel, for both capillary numbers ( $Ca = 5.36 \cdot 10^{-2}$  and  $6.64 \cdot 10^{-2}$ ). We observe for in three successive moments that the split daughter droplets pass the sub-channels without re-merging unlike; our numerical simulations are in good agreement with previous works of [2] and [37]. It is also seen from **Figure 5b** that the droplet volume fraction is higher for higher capillary number **Figure 4b**, as we demonstrated in the previous section. Due to

difference of both sub-channel widths, the bigger split daughter droplets pass the sub-channels 1, while the smaller split daughter droplets pass the sub-channels 2.

The present computations demonstrate that an inclined obstacle can be used as an effective method for droplet splitting with even-sized daughter droplets.

## 6. Conclusions

Droplet generation in flow focusing configuration, splitting and sorting were investigated numerically by using the VOF method of the commercial code FLUENT. Various parameters which affect the generation of the droplets, including capillary number, geometry of configuration, surface tension and contact angle are systematically analyzed. It shows that the droplet breakup depends on fluid properties such as capillary number, surface tension and the main channel width. We also find that the flow focusing configuration with the smaller main channel width likely to generate stable droplet. The capillary number is an important parameter to define the droplet length and droplet generation frequency. The increase of this parameter leads to the increase of droplet frequency, while it conducts to small droplet length. The numerical simulations of droplet breakup also showed that the obstacle configuration is effective for droplet splitting and sorting, where, daughter split droplet are sorted into smaller droplet that passed through small sub-channel and the bigger passed the bigger sub-channel. We hope this numerical study helps understanding the underlying physics on the droplet dynamics as well as designing the complicated flows in future microfluidic applications.

## Acknowledgment

The authors wish to acknowledge ENERGARID laboratory, especially the group of integral system control.

## References

1. M. A. Burns, C. H. Mastrangelo, T. S. Sammarco, F. P. Man, J. R. Webster, B. N. Johnson, B. Foerster, D. Jones, Y. Fields, A. R. Kaiser, D. T. Burke. Microfabricated structures for integrated DNA analysis. *Proc. Natl. Acad. Sci. USA*, 1996, 93, 11, 5556-5561.
2. U. Lehmann, S. Hadjidj, V. K. Parashar, C. Vandevyver, A. Rida, M. A. M. Gijs. Two-dimensional magnetic manipulation of microdroplets on a chip as a platform for bioanalytical applications. *Sens. & Actuat. B*, 2006, 117, 2, 457-463.
3. P. Garstecki, M. J. Fuerstman, H. A. Stone, G. M. Whitesides. Formation of droplets and bubbles in a microfluidic T-junction – Scaling and mechanism of break-up. *Lab Chip*, 2006, 6, 3, 437- 446.
4. J. H. Xu, S. W. Li, J. Tân, Y. J. Wang, G. S. Luo. Preparation of highly monodisperse droplet in a T-junction microfluidic device. *AIChE J.*, 2006, 52, 9, 3005-3010.
5. N. T. Nguyen, T. H. Ting, Y. F. Yap, T. N. Wong, J. C. K. Chai, W. L. Ong, J. Zhou, S. H. Tan, L. Yobas. Thermally mediated droplet formation in microchannels. *Appl. Phys. Lett.*, 2007, 91, 084102.
6. J. H. Xu, S. W. Li, W. J. Lan, G. S. Luo. Microfluidic approach for rapid interfacial tension measurement. *Langmuir*, 2008, 24, 19, 11287-11292.
7. L. Y. Chu, A. S. Utada, R. K. Shah, J. W. Kim, D. A. Weitz. Controllable monodisperse multiple emulsions. *Angew. Chem. Int. Ed.*, 2007, 46, 8970-8974.
8. S. Y. Teh, R. Lin, L. H. Hung, A. P. Lee. Droplet microfluidics. *Lab. Chip*, 2008, 8, 198-220.
9. G. M. Whitesides. The origins and the future of microfluidics, *Nature*, 2006, 442, 368-373.
10. D. R. Link, S. L. Anna, D. A. Weitz, H. A. Stone. Geometrically mediated breakup of drops in microfluidic devices. *Phys. Rev. Lett.*, 2004, 92, 054503.
11. Ch. K. Chung, K. H. Ahn, S. J. Lee. Numerical study on the dynamics of droplet passing through a cylinder obstruction in confined microchannel flow. *J. Non-Newtonian Fluid Mech.*, 2009, 162, 38-44.



12. T. Thorsen, R. W. Roberts, F. H. Arnold, S. R. Quake. Dynamic pattern formation in a vesicle-generating microfluidic device. *Phys. Rev. Lett.*, 2001, 86, 4163-4166.
13. C. Priest, S. Herminghaus, R. Seemann. Generation of monodisperse gel emulsions in a microfluidic device. *Appl. Phys. Lett.*, 2006, 88, 024106.
14. S. L. Anna, N. Bontoux, H. A. Stone. Formation of dispersions using “flowfocusing” in microchannels. *Appl. Phys. Lett.*, 2003, 82, 364-366.
15. S. L. Anna, H. C. Mayer. Microscale tipstreaming in a microfluidic flow focusing device. *Phys. Fluids*, 2006, 18, 121512.
16. C.-Y. Lee, Y.-H. Lin, G.-B. Lee. A droplet-based microfluidic system capable of droplet formation and manipulation. *Microfluid. & Nanofluid.*, 2009, 6, 599-610.
17. Y. C. Su, L. W. Lin. Geometry and surface-assisted micro flow discretization. *J. Micromech. & Microeng.*, 2006, 16, 1884-1890.
18. Y. C. Tan, Y. L. Ho, A. P. Lee. Droplet coalescence by geometrically mediated flow in microfluidic channels. *Microfluid. & Nanofluid.*, 2007, 3, 495-499.
19. Y. C. Tan, J. S. Fisher, A. I. Lee, V. Cristini, A. P. Lee. Design of microfluidic channel geometries for the control of droplet volume, chemical concentration, and sorting, *Lab. Chip.*, 2004, 4, 292-298.
20. L. H. Hung, K. M. Choi, W. Y. Tseng, Y. C. Tan, K. J. Shea, A. P. Lee. Alternating droplet generation and controlled dynamic droplet fusion in microfluidic device for CdS nanoparticle synthesis. *Lab. Chip.*, 2006, 6, 174-178.
21. J. M. Kohler, T. Henkel, A. Grodrian, T. Kirner, M. Roth, K. Martin, J. Metze. Digital reaction technology by micro segmented flow—components, concepts and applications. *Chem. Eng. J.*, 2004, 101, 201-216.
22. X. Niu, S. Gulati, J. B. Edel, A. J. de Mello. Pillar-induced droplet merging in microfluidic circuits. *Lab. Chip.*, 2008, 8, 1837-1841.
23. D. E. Menech. Modeling of droplet breakup in a microfluidic T-shaped junction with a phase-field model. *Phys. Rev. E*, 2006, 73, 031505.
24. A. Carlson, M. Do-Quang, G. Amberg. Droplet dynamics in a bifurcating channel. *Int. J. Multiphase Flow*, 2010, 36, 397-405.
25. C. Chung, M. Lee, K. A. Char, K. H. Ahn, S. J. Lee. Droplet dynamics passing through obstructions in confined microchannel flow. *Microfluid. & Nanofluid*, 2010, 9, 1151-1163.
26. Y. Shi, G. H. Tang, H. H. Xia. Lattice Boltzmann simulation of droplet formation in T-junction and flow focusing devices. *Computers & Fluids*, 2014, 90, 155-163.
27. B. A. Nichita, I. Zun, J. R. Thome. A VOF method coupled with a dynamic contact angle model for simulation of two-phase flows with partial wetting. In: 7th Int. Conf. Multiphase Flow. 2010, Tampa, ICMF.
28. J. Lee, W. Lee, G. Son. Numerical study of droplet breakup and merging in a microfluidic channel. *J. Mech. Sci. & Technol.*, 2013, 27, 6, 1693-1699.
29. S. L. Anna, N. Bontoux, H. A. Stone. Formation of dispersions using flow focusing in microchannels. *Appl. Phys. Lett.*, 2003, 82, 364-366.
30. T. Anna, T. Gun, T. Christian. CFD modelling of drop formation in a liquid-liquid system. In: 6th Int. Conf. Multiphase Flow. 2007, Leipzig, ICMF.
31. B. D. Hamlington, B. Steinhaus, J. J. Feng, D. Link, M. J. Shelley, A. Q. Shen. Liquid crystal droplet production in a microfluidic device. *Liq. Cryst.*, 2007, 34, 861-870.
32. Q. S. Zou, X. Y. He. On pressure and velocity boundary conditions for the lattice Boltzmann BGK model. *Phys. Fluids*, 1997, 9, 1591-1598.
33. D. L. Youngs. Time-dependent multi-material flow with large fluid distortion. In: *Numerical Methods for Fluid Dynamics*. 1982, Wiley, 273-285.
34. M. Rudman. Volume-tracking methods for interfacial flow calculations. *Int. J. Numer. Meth. Fluids*, 1997, 24, 671-691.
35. D. A. Hoang, L. M. Portela, Ch. R. Kleijn. Numerical study on droplet breakup in a microfluidic T-junction. *J. Fluid Mech. R*, 2013, 717, 4, 1-11.
36. H. H. Liu, A. J. Valocchi, Q. J. Kang. Pore-scale simulation of high-density-ratio multiphase flows in porous media using lattice Boltzmann method. *Comput. Phys.*, 2010, 229, 8045-8063.
37. W. Lee, G. Son. Numerical study of obstacle configuration for droplet splitting in a microchannel. *Computers & Fluids*, 2013, 84, 351-358.

## DIPOLE MOMENT OF QUASI-PLANAR BORON CLUSTERS

R. Becker<sup>1</sup>, L. Chkhartishvili<sup>2,3</sup>

<sup>1</sup> Cluster Sciences Research Institute  
Boron Cluster Metamaterials  
Ipswich, MA, USA  
ionsourcerer@mac.com

<sup>2</sup> Department of Engineering Physics  
Georgian Technical University  
Tbilisi, Georgia  
chkharti2003@yahoo.com

<sup>3</sup> Laboratory for Boron & Powdered Composite Materials  
F. Tavadze Institute of Metallurgy & Materials Science  
Tbilisi, Georgia

Accepted October 19, 2015

### Abstract

Boron crystallizes in complex structures containing several non-equivalent atomic sites with different coordination numbers. Shifting of the electron density towards to the highly-coordinated atoms yields the palpable polarization of all-boron lattices, in general unexpected in elemental crystals. Same effect has to be inherent of boron clusters as well. We have experimental evidences that boron vapor consists of small clusters  $B_n$ , which are known to exhibit (quasi)planar structures (for number of boron atoms  $n$  not more than  $\sim 15$ ). For all ground-state isomers of them we have estimated effective atomic charges and for asymmetric species – dipole moment as well. Binding energies per atom of (quasi)planar boron clusters, theoretically determined from the B–B interatomic pair potential, have been refined taking into account the obtained polarity of a part of B–B bonds.

### Instead of introduction – An overview

The role of boron in forming of the various structural phases, it is incommensurable of its abundance great. Understanding of the diversity of boron structures reduces to the electronic structure of an isolated boron atom. In multi-atomic networks, by the adding an electron the valence shell configuration peculiar to the free B atom  $2s^2 2p$  transforms at first in the energetically more favorable configuration  $2s^2 2p^2$ , which then tends to most stable one  $2s 2p^3$ . Thus, boron is distinct electron-acceptor and, consequently, all-boron structures have to be electron-deficient. It is a reason why all the boron crystalline modifications exhibit complex – clustered structures. For them, the icosahedron  $B_{12}$  with 12 boron atoms at vertices serves as a main structural motif.

Since carbon nanosystems were discovered, it has triggered interest in other materials, including bare boron, which may also exhibit nanostructures. Boron-based nanomaterials are both of great academic and technological interests [1]. Due to its rich chemistry, boron is a natural choice for constructing nanosystems like the clusters, nanotubes, nanowires, etc. Relatively recently they were actually synthesized.

A boron atom of the given icosahedron is bonded with 5 neighboring atoms and, usually, is linked with an atom of the neighboring icosahedron. It explains why the average coordination number of atomic sites in all the solid-state forms of boron is almost 6. But, a free regular icosahedron  $B_{12}$  still remains electron-deficient: it needs 2 extra electrons to fill all the MOs (molecular orbitals). In boron crystals and amorphous boron, electron-deficiency is compensated by the presence of intrinsic point defects and / or certain impurity atoms in very high concentrations. In addition to solid-state modifications, constructed from full and fused icosahedra, elemental boron forms diboron molecule  $B_2$  and molecular clusters  $B_n$ ,  $n > 2$ . At relatively low  $n$  these clusters are (quasi)planar, but at sufficiently high  $n$  they can take polyhedral, nearly spherical, cage-like shapes and, in particular, icosahedral shape if dangling bonds at boron atoms are saturated by hydrogen or other foreign atoms. Thus, most boron atoms should be surrounded by 6 nearest neighbors, i.e. have 5 intra- plus 1 inter-icosahedral bonds. Alternatively, this circumstance leads to the possibility of synthesizing the fragments of (quasi)planar nanosheets in form of surfaces with triangular 6-coordinated 2D lattices, which can be wrapped into nanotubes. Present 'Introduction' might be considered as a brief overview of the last decades' achievements in an important field of nano-structured boron – boron clusters.

As it is known, clusters as systems of a finite number of bound atoms are physical objects occupying an intermediate position between atomic particles (atoms and molecules) and macroscopic atomic systems (solids and liquids). One of the most interesting features of elemental boron is the occurrence of highly symmetric icosahedral clusters. However, the 5-fold symmetry does not lend  $B_{12}$  clusters to construct ideal 3D periodic frameworks, and various degrees of compromise in the pattern of icosahedral linkage give rise to the observed proliferation of boron polymorphs. Then, in bare boron structures most of the atoms usually are members of almost regular atomic triangles. This circumstance leads to possibility of the boron-based nanomaterials in form of (quasi)planar or convex boron surfaces with triangular 2D lattices. The rich chemistry of boron also is dominated by 3D cage structures. Consequently, it is important to gain deep insight in boron clusters – “building blocks” of nanoboron.

According to the mass-spectrometric analysis [2] of the boron cluster ions from the high-purity (99.99995 % B) target-source in process of growing of amorphous boron films, there are some peaks corresponding to the interval from  $B_2^+$  to  $B_8^+$ .

Let start with diboron molecule  $B_2$ , the simplest boron cluster. The Douglas–Herzberg transition, observed [3] in the optical absorption spectrum of  $B_2$ , indicated that its ground electronic state is of  $\Sigma$ -type. In the other hand, the molecule  $B_2$  was not observed via ESR (electron spin resonance), what was interpreted as support for the  $^3\Sigma_g^-$  ground state rather than  $^5\Sigma_u^-$  favored by ab initio calculations. Further more accurate CI (configuration interaction) calculation established [4] that the ground electronic state of  $B_2$  indeed is of  $^3\Sigma_g^-$  symmetry, and Douglas–Herzberg emission system is due to the transitions from the second  $^3\Sigma_u^-$  state to the  $X^3\Sigma_g^-$ . Hyperfine coupling constants for the ground electronic state  $^3\Sigma_g^-$  of the  $B_2$  molecule were computed [5] using correlation procedures based on spin-unrestricted wave functions. As for

the potential curves, transition energies, and spectroscopic constants of several low-lying electronic states of the molecular ion  $B_2^+$  and part of doubly excited states of  $B_2$  were given in [6]. At the first time, a theoretical study of the IPs (ionization potentials) of the  $B_2$  molecule was performed in [7]. An ab initio MO-study [8] of  $B_2$  and  $B_2^+$  determined the dissociation energy of the  $^3\Sigma_g^-$  ground state of  $B_2$  as 2.71 eV, and the adiabatic IPs to states  $^2\Sigma_g^+$  and  $^2\Pi_u$  of  $B_2^+$  as 8.99 and 9.27 eV, respectively. The singlet, triplet, and quintet states of  $B_2$  below about  $45000\text{ cm}^{-1}$  were studied at the multi-reference CI level of the theory in an atomic natural orbital basis set [9]. The dissociation energy for the  $X^3\Sigma_g^-$  state was computed to be 2.78 eV and estimated as 2.85 eV in the complete-CI limit. Calculations of excitation energies utilizing the standard coupled cluster hierarchy were presented [10] up to the quadruple excitation level for the open shell  $B_2$  molecule using an excited closed shell state as a reference one.

Optimum geometries and harmonic spectra were obtained theoretically [11] for a number of different states of  $B_3$  cluster.  $B_3$  is found to be an equilateral triangle in its  $2A'_1$  ground state. Estimated dissociation energy is 197.9 kcal / mole. From a statistical thermodynamical analysis,  $B_3$  should be stable against dissociation to  $B_2$  and  $B$  up to very high temperatures. Ab initio electronic structure calculations on several low-lying valence states of  $B_3$  were also carried out using correlation-consistent polarized valence basis sets and SCF (self-consistent-field) treatments [12]. Stable triangular structures, linear structures, and Jahn–Teller unstable structures were also observed. The ground state of  $B_3$  was predicted to have an equilateral triangular structure and to be of  $^2A'_1$  symmetry in the  $D_{3h}$  point group. By carrying out a systematic basis set and electron correlation investigation, it was determined accurately the isotropic and anisotropic parts of the hyperfine coupling tensor of the  $B_3$  molecule using the multi-CI SCF restricted–unrestricted method [13]. The spin polarization of the  $1s$ -orbital on each B atom was found to be very small. This implies that in  $B_3$  the isotropic hyperfine coupling is dominated by valence-orbital contributions rather than by  $1s$ -orbital contributions.

The PES (potential energy surface) of  $B_4$  cluster was ab initio studied using extended basis sets and coupled cluster methods [14]. The ground state  $^1A_{1g}$  is the singlet square that undergoes pseudo Jahn–Teller distortion to a rhombic structure  $^1A_g$ , but the energy gain is too small. Total atomization energies of  $B_2$ ,  $B_3$ , and  $B_4$  clusters were computed as 62.2, 189.1 – 192.6, and 312.2 kcal / mole, respectively. The two small boron clusters  $B_3$  and  $B_4$  in their neutral and anionic forms were studied by photoelectron spectroscopy and ab initio calculations [15]. Vibrationally resolved photoelectron spectra were observed for  $B_3^-$  at 355, 266, and 193 nm, and the EA (electron affinity) of  $B_3$  was measured to be 2.82 eV. An unusually intense peak due to two-electron transitions was observed in the 193 nm-spectrum of  $B_3^-$  at 4.55 eV. It was confirmed that both  $B_3^-$  and  $B_3$  are of  $D_{3h}$  symmetry. The photoelectron spectra of  $B_4^-$  were also obtained at the three photon energies, but much broader spectra were observed. The  $B_3^-$  anion was found to have the lowest electron detachment energy, 1.6 eV, among all boron clusters with more than three atoms, consistent with its extremely weak mass-signals. The neutral  $B_4$  cluster was found to have a  $D_{2h}$  rhombus structure, which is only slightly distorted from a perfect square. For  $B_4^-$ , it was identified computationally two low-lying isomers  $^2B_{1u}$  and  $^2A_g$ , both of  $D_{2h}$  symmetry, with the slightly more stable  $^2B_{1u}$  state.

The electronic structure and chemical bonding of boron clusters  $B_5$  and  $B_5^-$  were investigated [16] using anion photoelectron spectroscopy and ab initio calculations. Extensive searches were carried out for global minimum of  $B_5^-$ , which was found to have a planar structure with a closed-shell ground-state. Excellent agreement was observed between ab initio

detachment energies and the experimental spectra. A bonding orbital was found to be completely delocalized over all 5 atoms in the  $B_5^-$ . Such bonding makes  $B_5^-$  more rigid towards butterfly out-of-plane distortions. The structure and stability of  $B_5$ ,  $B_5^+$  and  $B_5^-$  clusters were investigated theoretically also in [17]. Eight  $B_5$ , seven  $B_5^+$ , and seven  $B_5^-$  isomers were identified. The planar 5-membered ring structures,  $B_5$  and  $B_5^+$ , were found to be the most stable on the neutral and cationic PES, respectively. The most stable  $B_5^-$  isomer has an arrangement of atoms similar to the neutral. Natural bond orbital analysis suggests that there are 3-centered bonds in both the neutral and anionic structures, as well as the multi-centered centripetal bond in the cationic structure.

The electronic structure and chemical bonding of  $B_6$  and  $B_6^-$  clusters were investigated using anion photoelectron spectroscopy and ab initio calculation [18]. The global minimum of  $B_6^-$  has a doublet ground state. The corresponding ground-state structure of  $B_6^-$  is planar. The chemical bonding in  $B_6^-$  can be interpreted in terms of linear combinations of MOs of two  $B_3^-$  fragments. The antiaromatic nature of chemical bonding was established for both  $B_6^-$  and  $B_6^{2-}$ . Electronic structure, isomerism, and chemical bonding in  $B_7^-$  and  $B_7$  clusters were studied in [19]. The structures of  $B_7$ ,  $B_{10}$  and  $B_{13}$  boron clusters were studied [20] using the FP (full-potential) LMTO (linear-muffin-tin-orbitals) MD (molecular dynamics) method. Seven stable structures for  $B_7$  and fifteen for  $B_{10}$  were obtained.  $C_{2h}$ - $B_{10}$  is the most stable among the 15 structures, but  $C_{2v}$ - $B_{10}$  is not stable. For  $B_{13}$ , three degenerate ground-state structures were found. The potential surface near  $C_{2v}$ - $B_7$  (ground state) and  $D_{6h}$ - $B_7$  is very flat. As a fundamental unit in constructing bigger clusters,  $C_{2v}$ - $B_7$  will change its form easily. The most stable structures for  $B_7$ ,  $B_{10}$  and  $B_{13}$  clusters are two-dimensional (quasi)planar clusters, rather than the three-dimensional ones.

Probes of bonding in small boron clusters  $B_{2-8^+}$  performed by the measurements of threshold energies and fragmentation patterns for collision-induced dissociation showed [21] that primary fragmentation channel is loss of  $B^+$  in all cases and  $B_5^+$  is a particularly abundant cluster in the distribution produced. The stabilities of  $B_n$  clusters with  $4 \leq n \leq 8$  based on the vibrational analysis were investigated by ab initio MO-calculations in [22]. It was found that there exist two types of stable clusters: a low-symmetry, structurally "soft", species with lower frequencies and lower geometrical change barriers and a high-symmetry, structurally "hard", species with higher frequencies. By means of ab initio techniques, the equilibrium geometries, total, binding and fragmentation energies of clusters  $B_n$ , with  $n = 2-8$  were calculated both in the neutral and cationic states in [23]. The experimental and theoretical evidence that 8- and 9-atom boron clusters are perfectly planar molecular wheels, with a hepta- or octa-coordinated central boron atom, respectively, were reported in [24]. DFT (density functional theory) calculations using a PW (plane wave) basis set and a PP (pseudopotential) were employed [25] to investigate the structure, vibrational characteristics, and energetics of small (up to 10 atoms) boron clusters. Comparison with other studies revealed a great deal of consensus about the most stable structures for  $B_2$ ,  $B_3$ ,  $B_4$ ,  $B_7$ , and  $B_8$ , and maybe  $B_5$  as well. Additionally, all studies agree about the existence of two stable  $B_6$  isomers.

Geometries, electronic structures and energies of the neutral and cationic clusters  $B_{2-12}$  and  $B_{2-12}^+$  were investigated by the ab initio MO method [26]. The geometries of boron-cluster cations  $B_{3-12}^+$  are essentially the same as those of the neutral clusters – the (pseudo)planar cyclic structures. Clusters of 8–11 atoms characteristically have the most stable structure of a cyclic form with 1 atom in the middle. The capped pentagonal  $B_6$ ,  $B_7$  and  $B_7^+$  and the trigonal



bipyramidal  $B_{12}$  and  $B_{12}^+$  seem to be the exceptions. The electronic and geometric structures, total and binding energies, harmonic frequencies, point symmetries, and HOMO–LUMO (highest occupied MO–lowest unoccupied MO) gaps of small neutral boron  $B_n$  clusters ( $n = 2–12$ ) were investigated in [27] using DFT. Linear, (quasi)planar, open- and 3D-cage structures were found. None of the lowest energy structures and their isomers has an inner atom. Within the size range, the (quasi)planar, i.e. convex, structures have the lowest energies.

It is expedient to consider boron icosahedron  $B_{12}$  separately from other boron clusters. At the first time, the electron structure of a regular icosahedron of boron atoms was investigated [28] theoretically by the method of MOs. It was found that 30 bonding orbitals are available for holding the icosahedron together, besides the 12 outward-pointed equivalent orbitals of the separated atoms. In [29], the energy spectrum of a real boron icosahedron – unit cell of the  $\alpha$ -rhombohedral boron crystal – was studied using MO–LCAO (linear-combinations-of-atomic-orbitals) method. It is an electron-deficient structure. Besides, in distorted in crystalline field icosahedron the bond lengths are different and now there is no 5-fold symmetry axis. It was found that molecular levels placed at  $-9.35$  eV should be half-filled, while all lower energy levels should be filled. Using a PW expansion, it was performed [30] ab initio calculations of the energy bands, equilibrium structural parameters, atomic positions, and cohesive energy of boron icosahedron  $B_{12}$ . As for the calculated charge-density contour plots, they revealed strong intra-icosahedral bonding. Based on the group properties of a regular icosahedron, its normal vibrational modes were pictured [31]. There are 8 distinct frequencies for the 30 normal modes with 1-, 3-, 4-, and 5-fold degeneracies. Icosahedral oscillations can be pictured in terms of three equilibrium descriptions: the first involves 2 parallel regular pentagons and 2 polar atoms; the second has 2 polar triangles and 1 equatorial puckered hexagon; while the third consists of 6 pairs of atoms on opposite faces of a cube. It was shown [32] that by the interaction between electron and pair of phonons, which are the slightly modified 2 breathing modes of the isolated icosahedron  $B_{12}$ , an electron trapping level generates in icosahedral boron-rich solids. The polar vibrations for the  $B_{12}$  icosahedron were demonstrated [33] within the harmonic approximation by using the shell model. The tensor nature of dynamical effective charges was emphasized. It was shown that the effective charge of the regular  $B_{12}$  is very small ( $\approx 0.01e$ ), while that of  $\alpha$ -rhombohedral boron unit cell is enhanced by the deformation. The covalent-to-metallic bonding conversion in boron icosahedral cluster solids was discussed [34] in relation to the occupation by an atom the center of this cluster. The corresponding change in the electron localization was quantitatively estimated by using ELI (electron localization indicator). Namely, the distributions of the ELI were compared for the pair of clusters  $B_{12}^+$  and  $B_{13}^-$ . This comparison revealed that the bonding conversion from covalent to metallic one involves a decrease in both the electron-density and ELI between boron atoms.

Bonding of small boron cluster cations from  $B_2^+$  to  $B_{13}^+$  was examined [35, 36] by measurements of appearance potentials and fragmentations patterns for collision-induced dissociation. Cluster stabilities were generally found to increase with increasing size. The lowest energy fragmentation channel for all size cluster ions is loss of a single B atom. Clusters, smaller than 6 atoms, preferentially lose  $B^+$  ion, while for larger clusters the charge remains on the  $B_{n-1}^+$  fragment. Electronic and geometric isomers of  $B_{13}$  clusters were calculated within the LDA (local density approximation) [37]. The filled icosahedral structure was found unstable. While heating and slow cooling lead to a considerably more stable (by 0.68 eV) structure with high

symmetry ( $C_{3v}$ ) and coordination. The remarkable stability of this isomer may explain the measured high survival of  $B_{13}^+$  clusters on collision and its relatively low reactivity. Analogous problem was considered [38] for the neutral and cationic clusters  $B_{12}$  and  $B_{13}$ . Several planar and non-planar stationary structures were optimized for neutrals and cations of each cluster size. A characteristic cyclic form with 1 atom in the middle was found to be stable for each cluster, while the icosahedral  $B_{12}^+$  was found to be the most stable. The triplet icosahedral state was found to be stable, but energetically unfavorable than the cyclic  $B_{12}$ . The structures and energies of  $B_{13}^+$ , observed experimentally to be an unusually abundant species among cationic boron clusters, were studied systematically with DFT in [39]. The most thermodynamically stable  $B_{12}^+$  and  $B_{13}^+$  clusters are confirmed to have (quasi)planar rather than globular structures. However, the computed dissociation energies of the 3D  $B_{13}^+$  clusters are much closer to the experimental values than those of the (quasi)planar structures. Hence, planar and 3D  $B_{13}^+$  may both exist. The curiously stable cationic  $B_{13}^+$  cluster and its neutral and anionic counterparts were examined in [40] though the use of DFT. While no minima that corresponded to the filled icosahedron could be found for the cluster, an intriguing atom-in-cage structure was found that is a local minimum on the cationic, neutral, and anionic surfaces. In the structure found for the  $B_{13}^-$  anionic cluster, the 12 external boron atoms are arranged as 3 of 6-membered rings back-to-back. The (quasi)planar structures are seen to be more stable than 3D isomers, but their ordering by stability changes depending on the charge state. It was found that planar structures benefit from  $\pi$ -delocalization and in the case of the global minimum of the  $B_{13}^+$  cationic cluster this delocalization is reminiscent of aromaticity. As it was postulated, the lowest-energy  $B_{13}^+$  isomer proved to be highly aromatic. The topological resonance energy of this cationic boron cluster is positive in sign and very large in magnitude. This constitutes the definitive reason why  $B_{13}^+$  is kinetically stable and (quasi)planar in geometry [41]. The electron-deficient and multivalent character of boron is responsible for the high aromaticity of this cluster. In addition, its minimum bond resonance energy is not too small. Some of thermo-chemical parameters of a set of small-sized neutral  $B_n$  and anionic  $B_n^-$  boron clusters, with  $n = 5-13$ , were determined using coupled-cluster theory calculations [42]. Enthalpies of formation, adiabatic electron EAs were evaluated in good agreement with experiments (values are given in eV):  $B_5$  (2.29 – 2.48 and 2.33),  $B_6$  (2.59 – 3.23 and 3.01),  $B_7$  (2.62 – 2.67 and 2.55),  $B_8$  (3.02 – 3.11 and 3.02),  $B_9$  (3.03 and 3.39),  $B_{10}$  (2.85 and 2.88),  $B_{11}$  (3.48 and 3.43),  $B_{12}$  (2.33 and 2.21), and  $B_{13}$  (3.62 and 3.78). The calculated adiabatic detachment energies to the excited states of  $B_6$ , which have geometries similar to the state of  $B_6^-$ , are 2.93 and 3.06 eV, in excellent agreement with experiment. Based on the ab initio QC (quantum chemical) methods, fragmentation channels, IPs, and the Coulomb explosion of multi-charged boron clusters  $B_n$  ( $n = 2-13$ ), were determined [43]. The electron-deficient boron clusters sustain more stability and hardly fragment when they are negatively charged. Stability of boron clusters decreases with increasing ionization. Only by the first ionization the odd-size clusters are more stable than the even-size clusters. Further ionizations cause the repulsive Coulomb force between the constituent atoms to get stronger, and lead first to metastable states, then to the Coulomb explosion of clusters. None of the cationic boron clusters studied remains stable after 6 times ionization. The critical charge for metastability was estimated as  $Q_m \leq n/2$  for even-size clusters, and  $Q_m \leq (n-1)/2$  for odd-size clusters. In addition, the critical charge for the Coulomb explosion is found to be  $Q_c \leq n/2+1$  and  $Q_c \leq (n+1)/2$ , respectively. Several dissociation channels of  $B_n^+$  and  $B_{13}^Q$  isomers with the

lowest fragmentation energies were presented. All of the vibrational frequencies were found positive indicating that no transition state is possible for the clusters studied.

The structures of  $B_{14}$  and  $B_{14}^{2-}$  in octahedral symmetry were investigated by ab initio calculations [44]. The geometrical structures and properties of small cationic boron clusters  $B_n^+$  ( $n = 2–14$ ) were determined [45] using the LSD formalism. Most of the final structures of the cationic boron clusters prefer (quasi)planar arrangements and can be considered as fragments of a planar surface or as segments of a sphere. The calculated adiabatic IPs of  $B_n$  exhibit features similar to those of measured IPs. Most of the calculated normal modes of the cationic clusters have frequencies around  $1000\text{ cm}^{-1}$  and strong IR (infrared) intensities. A linear search for minima on PESs based on analytical gradient methods and the determination of binding energies of small boron clusters  $B_n$  ( $n = 2–14$ ) were conducted using the ab initio HF (Hartree–Fock), and SCF CI and QC methods, as well as by means of DFT at the levels of LSD and non-local corrections to the exchange–correlation functional [46, 47]. The final optimized HF-topologies of the neutral boron clusters are identical with those derived with the LSD approximation. The most stable boron clusters have convex or (quasi)planar structures and the convex clusters seem to be segments of the surface of a sphere. The geometries of  $B_n^+$  clusters for  $n \leq 14$  were optimized in [48] applying DFT. The calculation suggested that the experimental results for the  $B_n^+ \rightarrow B^+ + B_{n-1}$  fragmentation energies are too small, while experimental  $B_n^+ \rightarrow B + B_{n-1}^+$  fragmentation energies for  $B_4^+$ ,  $B_5^+$ , and  $B_{13}^+$  are too large. Then, the fragmentation energies were calibrated based on coupling cluster theory. Overall corrected fragmentation energies are found to be in reasonable agreement with experiment. The most stable structure for each cluster was found to be (quasi)planar. The larger clusters are derived from fusing 6- and / or 7-membered atomic rings, which share 4 atoms for the 6 – 6 and 6 – 7 rings and 5 atoms for the 7 – 7 rings. Based on ab initio DFT and QC methods, accurate calculations on small boron clusters  $B_n$  ( $n = 2–14$ ) were carried out in [49 – 51] to determine their electronic and geometric structures. Most of these final structures with  $n > 9$  are composed of two fundamental units: either of hexagonal or pentagonal pyramids different from the classical forms of crystalline boron. Using “Aufbau principle”, one can easily construct various very stable boron species. The resulting (quasi)planar and convex structures can be considered as fragments of planar surfaces and segments of nanotubes or hollow spheres, respectively.

Above a certain size, boron clusters prefer a cylindrical arrangement over a planar one. Experimental determination of the collision cross section combined with DFT calculations showed [52] that the transition to cylindrical structures takes place at  $B_{16}^+$ . The structure and chemical bonding of  $B_{16}^-$  were studied [53] using ab initio calculations and photoelectron spectroscopy. Its global minimum is found to be a (quasi)planar and elongated  $C_{2h}$ -structure. Addition of an electron to  $B_{16}^-$  resulted in a perfectly planar and closed shell  $B_{16}^{2-}$  ( $D_{2h}$ ).

Photoelectron spectroscopy reveals a relatively simple spectrum for  $B_{19}^-$ , with a high electron-binding energy [54]. Theoretical calculations show that the global minimum of  $B_{19}^-$  is a nearly circular planar structure with a central  $B_6$  pentagonal unit bonded to an outer  $B_{13}$  ring.

Experimental studies and computational simulations revealed [55] that boron clusters, which favor 2D structures up to 18 atoms, prefer 3D structures beginning at 20 atoms. Using global optimization methods, it was found that the  $B_{20}$  neutral cluster has a double-ring tubular structure with diameter of  $\sim 5.2\text{ \AA}$ . For the  $B_{20}^-$  anion, the tubular structure is shown to be isoenergetic to 2D structures, which were observed and confirmed by photoelectron



spectroscopy. The 2D-to-3D structural transition observed at  $B_{20}$  suggests that it may be considered as the embryo of the thinnest single-walled boron nanotubes.  $B_n^-$  cluster anions were produced by laser vaporization of a target made of enriched  $^{10}\text{B}$  isotope in the presence of the He carrier gas and analyzed with TOF (time-of-flight) mass-spectrometer. High-level ab initio MO methods were employed [56] to determine the relative stability among four neutral and anionic  $B_{20}$  isomers, particularly, the double-ring tubular isomer versus three low-lying planar isomers. They also suggest that the planar-to-tubular structural transition starts at  $B_{20}$  for neutral clusters but should occur beyond the size of  $B_{20}^-$  for the anion clusters. In order to elaborate a direct experimental method available for structural determination of boron clusters, photoelectron spectroscopy of size-selected cluster anions was combined with quantum calculations to probe the atomic and electronic structures and chemical bonding of small boron clusters up to 20 atoms [57]. Based on this method the experimental and theoretical evidences were presented showing that small boron clusters prefer planar structures and exhibit aromaticity and antiaromaticity according to the Huckel rules. Aromatic boron clusters possess more circular shapes whereas antiaromatic ones are elongated. It was found that for neutral boron clusters the planar-to-3D structural transition occurs at  $B_{20}$ , which possesses a double-ring structure, even though the  $B_{20}^-$  anion remains planar.

Based on a series of ab initio studies [58] had pointed out the remarkable structural stability quasi-planar boron clusters, and postulated the existence of novel layered boron solids built from elemental subunits. The equilibrium geometries and the systematics of bonding in various isomers of a 24-atom boron cluster was investigated [59] using Born–Oppenheimer MD within the framework of DFT. The  $B_{24}$  isomers studied were the rings, convex and (quasi)planar structures, the tubes, and closed structures. A staggered double ring is found to be the most stable structure among these isomers. Using ab initio QC methods, different structures of  $B_{32}$  clusters was investigated in [60]. The most stable isomers have (quasi)planar or tubular structures often containing dove-tailed hexagonal pyramids. In contrast, hollow spheres are less stable. Their stability can be understood as a competition between a curvature strain (favoring (quasi)planar clusters) and elimination of dangling bonds (favoring tubular and cage structures).

The boron clusters  $B_n$ ,  $n = 2-52$ , formed by laser ablation of hexagonal boron nitride were discovered with a TOF mass-spectrometer [61]. Using ab initio QC and DFT methods, it was investigated the structural transition from planar 2D boron clusters into 3D double-ring system and then into triple-ring system [62]. The first structural transition occurs at  $B_{19}$  and  $B_{20}$  clusters, while the second transition occurs between  $B_{52}$  and  $B_{54}$  clusters. The effect of the repulsive Coulomb forces in boron clusters when they are multi-ionized also was studied. A mass spectrometric study of boron cluster anions  $B_n^-$ ,  $n = 7-55$ , produced by laser vaporization from two different types of boron-containing sample rods: boron-rich boride and pure boron, was reported in [63]. In mass spectra recorded from the boride sample, a repeating intensity pattern of boron cluster anions having local maxima at  $(B_{13}^-)(B_{12})_{0,2,3}$  as well as at  $B_{26}^-$  was observed. Similar phenomena were not observed with a pure boron sample. These facts were attributed to the structural differences between the two materials, in particular,  $(B_{12})(B_{12})_{12}$  super-icosahedral structure characteristic of the crystalline boron-rich borides.

And finally, let refer to some studies considering the issue of boron clusters. Some symmetrical clusters of boron, and carbon as well, were discussed [64] by introducing the concept of conjugate polyhedra. It was concluded that if a polyhedron of carbon is given, its conjugate polyhedron of boron can be obtained and the conjugate polyhedron should be of

same symmetry. Based on ab initio QC and HF approximations, and DFT and LMTO methods within the ASA (atomic-sphere-approximation) in [65] the geometric and electronic structures of some atomic-scaled boron clusters were determined. In [66], there were reported experimental and theoretical evidences that small boron clusters prefer planar structures and exhibit aromaticity and antiaromaticity according to the Huckel rules. The planarity of the species was further elucidated on the basis of multiple aromaticity and antiaromaticity, and conflicting aromaticity. The major aims of the current research in field of boron clusters, which are developing, simulating, modeling, and predicting new boron structures to build pre-selected, uniform nanostructural materials with specific properties, e.g. superhardness, superconductivity, superlightness, and propellance, were formulated in the review [67]. According to these and other results obtained by Boustani and co-workers, one can conclude that most structures of boron clusters can be classified into four groups: (quasi)planar, tubular, convex, and spherical clusters. The transition of the (quasi)planar surfaces into tubules may be pictured by rolling the surfaces and forming cylinders. The closure of boron (quasi)planar surfaces into tubules goes through an energy barrier path. Small boron clusters as individual species in the gas phase were reviewed in [68]. Free boron clusters were characterized using photoelectron spectroscopy and ab initio calculations, which have established the (quasi)planar shapes of small boron clusters for the first time.

Recently, it was experimentally detected [69] the highly stable quasi-planar boron cluster  $B_{36}$  of hexagonal shape with the central hexagonal hole.

### **Boron vapor – Experimental part**

There are evidences [70 – 72] that liquid boron consists not of icosahedra, but mainly (quasi)planar clusters. Ab initio MD simulations of the liquid boron structure yields that at short length scales icosahedra  $B_{12}$ , a main structural motif of boron crystals and boron-rich compounds, are destroyed upon melting although atoms form an open packing with still 6-coordination, i.e., the structure of liquid boron is similar to the boron non-icosahedral forms. According to measurements of the structure factor and the pair distribution function, process of melting is associated with relatively small changes in short-range order of the system. Results of a comprehensive study of liquid boron atomic structure with X-ray measurements coupled with ab initio MD simulations also show that there is no evidence of survival of the icosahedral arrangements into the liquid, but many atoms appear to adopt a geometry corresponding to the quasi-planar pyramids.

We can conclude that, during melting of boron it takes place the boron clusters emission and thus boron vapor formed have to consist of mainly from boron clusters.

We developed [73] a method of generating substantially pure boron cluster-ions by a heating within a suitable temperature range the boron-rich material electrode, which induces its controlled thermal decomposition in a stoichiometrically favorable manner – providing boron vapor and all other species not in the vapor state. Magnetic confinement of the released electrons causes collisions resulting in ionization of the vapor to the plasma state. This plasma may then be extracted and accelerated at the suitable energy, e.g. toward a work-piece for use as a plasma-process feed gas.

Such a method of coating by boron has a variety of applications, including surface chemical and wear protection, neutron absorption, prevention of impurity emission from

heated filaments and ion beams, elimination of metal dust from vacuum systems, boridizing, reactive chemistry, etc.

Using the method of plasma spray, boron can be deposited onto most metals and a wide variety of ceramics and insulators including boron nitride BN and quartz. Adhesion of boron coatings to these materials is particularly strong. In this work, a high electric current (of 75 A) has been drawn between two graphite electrodes connected by an electrically conductive boron-rich boride powder (the thickness of powder separating the electrodes has been up to 2.5 cm) while in vacuum. The powder was observed to melt and begin emitting boron vapor, which was used to coat a glass slide test sample. A high coating rate of over 0.003 in. / min at a distance of 2 in. from the evaporation source was observed.

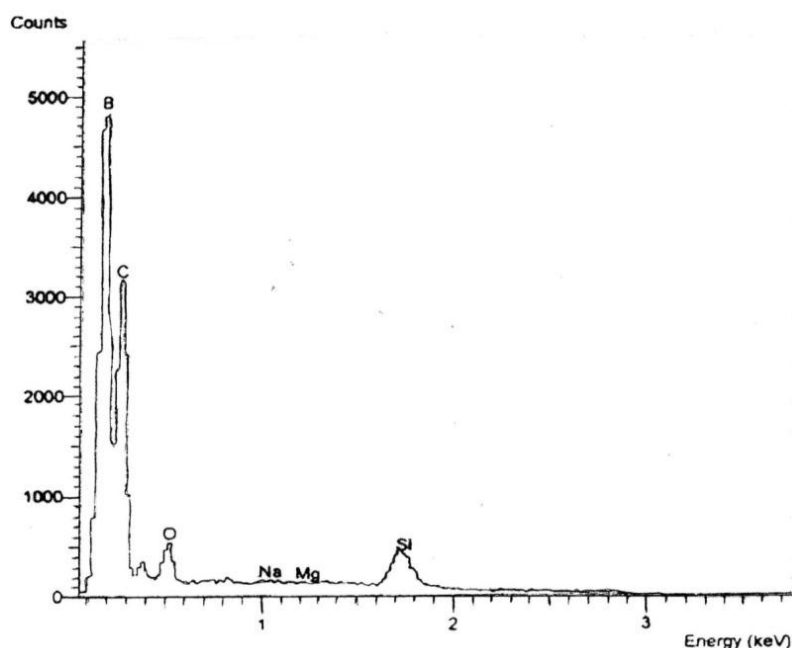


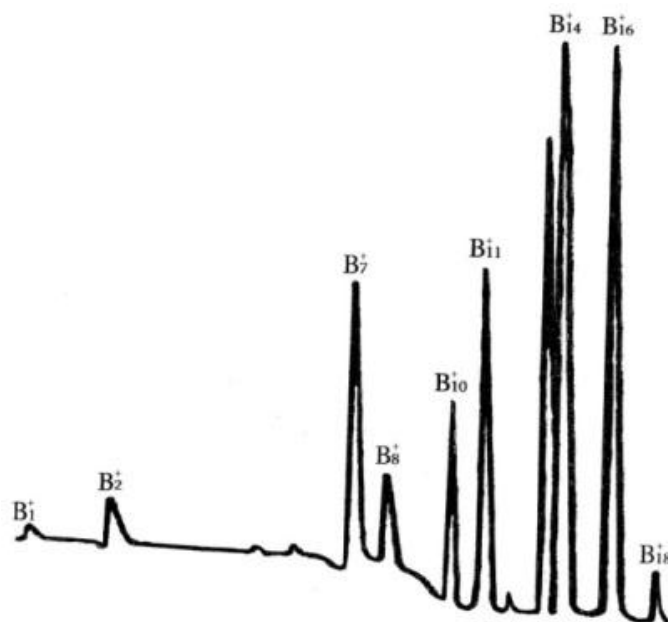
Figure 1. EDAX Measurement of coating produced onto a glass slide.

Figure 1 shows an EDAX analysis (energy dispersive analysis by X-ray) of the resultant coating material. The peak at the far left is due to boron coating. The other peaks are from the glass substrate. As is known, EDAX is low-sensitive to light elements, such as boron. It is a reason why the boron peak observed in the mass spectrum appears unnaturally small compared to the background elements from the glass slide substrate.

In the process of melting and evaporation of a boron-rich material with the nitrogen source in form of high-purity pressed boron nitride rods, the shell structures of chemical composition  $BN_x$  with boron excess ( $x \ll 1$ ) contaminated with carbon has been synthesized [74]. The obtained material is conductive despite the fact that all the boron nitrides of stoichiometric chemical composition BN are insulators. “Metallic” boron nitride is modeled as a mixture of structural modifications of semiconducting boron and boron carbide heavily doped with nitrogen [75].

Previously, we reported (see [63]) a mass spectrometric study of boron cluster anions  $B_n^-$ ,  $n = 7 - 55$ , including the heavier species containing  $B_{12}$ -icosahedra, which were produced by laser vaporization both from pure boron (i.e. homogeneous) and boride (i.e. heterogeneous) target rods. While at lower masses these spectra were similar, at higher masses the boride spectrum exhibited a completely different pattern: in addition to the local maximum at  $B_{13}^-$ ,

characteristic of the pure boron spectrum as well, a repeating intensity pattern having two additional local maxima were observed. These observations can be attributed to the structural differences between the two target materials. Further, we had demonstrated [76] that created boron clusters can be self-assembled into nanostructures.



**Figure 2.** Mass spectra of boron cluster cations generated by the thermal vaporization of: a boron-rich material.

From the mass spectra of small boron cluster anions generated by the laser vaporization, one can see that main maximum is placed within the range B<sub>11</sub> – B<sub>13</sub> (see [63]). The mass spectrum of small boron cluster cations generated by the thermal vaporization in present work is shown in **Figure 2**. The spectrum shape is similar, unless main maximum is shifted in the range B<sub>14</sub> – B<sub>16</sub>.

### **Binding energy taking into account atomic charges and dipole moment – Teorizing**

From the review given into Introduction, we can assume that, at the sufficiently low number of atoms  $n$  formation of the 3D clusters are not preferable kinetically, even that is preferable energetically, i.e. because of higher binding energy per atom. The 2D – (quasi)planar – structures built up from boron atoms, seem to be preferable because they are open for further adding of atoms to realize B atoms' ability to bound up to 6 other boron atoms in the cluster's plane.

However, small boron clusters would be quasi-planar, not ideally planar. Due to clusters' finite sizes: atoms at the periphery have fewer neighboring atoms, i.e. possess lower coordination numbers, than their counterparts placed at the central part. It leads to the formation of bonds with unequal lengths and then distortion of a structure consisting of only regular triangles with B atoms at the vertices. This is a reason why small boron clusters are not ideally planar, but buckled and / or puckered.

When number of atoms  $n$  becomes sufficiently high, the saturation of all the 6 potentially possible bonds of a boron atom can be achieved by the alternative way – by

wrapping of the plane into a cylinder (i.e. boron nanotube) or sphere (i.e. boron fullerene). But, these processes result in formation of 3D structures. The cluster  $B_{21}$  serves for the embryo of small boron nanotubes. Thus, here we consider boron (quasi)planar clusters with number of constituting atoms up to  $\sim 15$ . The clusters with high  $n$  possess several isomers. We will analyze only one of them – most stable, usually, with highest number of B–B bonds and symmetric.

On the basis of quasi-classical theory of substance [77], the B–B interatomic pair potential was constructed [78, 79] within the initial quasi-classical approximation. This potential was successfully exploited in calculations of binding energies of all-boron nanostructures [80 – 83], as well as some boron-isotopic effects in boron-rich solids [84 – 88]. According to the quasi-classical B–B pair potential, the binding energy of  $\varepsilon_b \approx 2.80$  eV corresponds the equilibrium interatomic distance (B–B pair bond length) of  $l_b \approx 1.78$  Å. Below these values are used for estimating binding energy of small boron clusters.

For further consideration we also need to introduce atomic units (a.u.) of energy, length and electric dipole moment respectively,  $E_{\text{a.u.}} \approx 27.212$  eV,  $l_{\text{a.u.}} \approx 0.52918$  Å and  $p_{\text{a.u.}} \approx 2.5417$  Dy. And finally, let's  $N = 1, \dots, n$  numbers atoms constituting the (quasi)planar boron cluster  $B_n$ ,  $C_N$  is the coordination number of the corresponding boron atom in this structure, and  $\nu$  is the atoms' valence – number of the valence electrons. As is known, for boron atom  $\nu = 3$ . In the **Table 1** shown below, boron atoms constituting small cluster are denoted as  $N[C_N]$ .

### *Effective atomic charges and dipole moment*

In average, an atom utilizes  $\nu/C_N$  electrons per bond for bounding with nearest neighbors (because boron clusters like other all-boron structures are electron-deficient, effective numbers of bounding electrons mostly could be fractions, lesser than 1). The  $N$ -atom in average a half of these electrons,  $\nu/2C_N$ , transfers to each of neighboring atoms. It is clear that, for any atom in average the total number of transferred electrons is same,  $\nu/2$ . From their side, neighboring atoms transfer a part of their valence electrons to the  $N$ -atom. Net number of transferred and received electrons determines the effective charge number for each atom constituting a cluster.

Atoms of the central part are highly-coordinated. Thus, they receive more electron charge than transfer, and could be charged negatively. On contrary, atoms at the periphery receive lesser electrons than transfer, and could be charged positively.
















When a cluster shapes itself asymmetrically, it possesses a non-zero dipole moment, value of which can be calculated from the standard relation

$$p = e \left| \sum_{N=1}^{N=n} Z_N \vec{r}_N \right|, \quad (1)$$

where  $\vec{r}_N$  denote radius-vectors of atomic sites in the cluster, and  $Z_N$  is the effective charge number of the  $N$ -atom. When calculating  $\vec{r}_N$ , we can neglect by the changes in bond length assuming it being same as in non-distorted ideally planar structure. As mentioned, within the quasi-classical approximation  $l_b \approx 1.78$  Å and, consequently,  $el_b \approx 8.55$  Dy.

Planar images of the clusters considered and their calculated dipole moment are shown below in the **Table 1**.

Table 1. Structure, dipole moment and binding energy of small boron clusters.

$B_n$	Structure	Binding energy $E_b$ , eV / atom		Dipole moment $p$ , Dy	
		Formula	Value	Formula	Value
B <sub>1</sub>		0	0	0	0
B <sub>2</sub>		$\frac{\varepsilon_b}{2}$	1.40	0	0
B <sub>3</sub>		$\varepsilon_b$	2.80	0	0
B <sub>4</sub>		$\frac{5\varepsilon_b}{4} + \frac{3\varepsilon_e}{16}$	5.02	0	0
B <sub>5</sub>		$\frac{7\varepsilon_b}{5} + \frac{73\varepsilon_e}{320}$	5.77	$\frac{\sqrt{3}el_b}{8}$	1.85
B <sub>6</sub>		$\frac{3\varepsilon_b}{2} + \frac{9\varepsilon_e}{32}$	6.48	0	0
B <sub>7</sub>		$\frac{12\varepsilon_b}{7} + \frac{15\varepsilon_e}{56}$	6.97	0	0
B <sub>8</sub>		$\frac{13\varepsilon_b}{8} + \frac{729\varepsilon_e}{3200}$	6.39	0	0
B <sub>9</sub>		$\frac{16\varepsilon_b}{9} + \frac{35\varepsilon_e}{288}$	5.96	0	0
B <sub>10</sub>		$\frac{19\varepsilon_b}{10} + \frac{7\varepsilon_e}{80}$	6.03	0	0
B <sub>11</sub>		$\frac{20\varepsilon_b}{11} + \frac{1197\varepsilon_e}{8800}$	6.19	0	0
B <sub>12</sub>		$\frac{23\varepsilon_b}{12} + \frac{7\varepsilon_e}{96}$	5.96	$\frac{\sqrt{3}el_b}{8}$	1.85
B <sub>13</sub>		$2\varepsilon_b + \frac{37\varepsilon_e}{416}$	6.32	0	0
B <sub>14</sub>		$2\varepsilon_b + \frac{13\varepsilon_e}{896}$	5.72	$\frac{\sqrt{3}el_b}{8}$	1.85
B <sub>15</sub>		$2\varepsilon_b + \frac{\varepsilon_e}{24}$	5.94	0	0



### Relative stability

To estimate relative probabilities of formation of (quasi) planar boron clusters  $B_n$ ,  $n=1,2,3,\dots$ , we need to start from the estimation of their relative stabilities, i.e. binding energies per atom.

Initially, binding energy per atom can be estimated in a “tight-binding” approximation, i.e. taking into account only interactions between nearest neighboring atoms:

$$E_{b0} = \frac{\varepsilon_b}{2n} \sum_{N=1}^{N=n} C_N, \quad (2)$$

where  $\varepsilon_b/2$  is the binding energy per a B atom bounded with another B-atom. As mentioned, in the quasi-classical approximation, the numerical value of the parameter  $\varepsilon_b$  is about 2.80 eV.

The  $N$ -atom’s binding energy correction related to the its electrostatic (Coulomb) interaction with neighboring  $N'$ -atom with effective charge number of  $Z_{N'}$  in eV equals to  $-Z_N Z_{N'} \varepsilon_e / 2$ , where  $\varepsilon_e = E_{\text{a.u.}} l_{\text{a.u.}} / l_b$  is the energy parameter inversely proportional to the bond length. Here, we again can neglect by the changes in bond length assuming  $l_b$  to be of 1.78 Å within the initial quasi-classical approximation. It means that  $\varepsilon_e \approx 8.09$  eV. By the introducing the factor 2 in the numerator, we take into account that same correction should be attributed to the counterpart  $N'$ -atom as well. Thus, correction to the binding energy per atom related to the effective atomic charges is

$$E_e = -\frac{\varepsilon_e}{2n} \sum_{N=1}^{N=n} Z_N \sum_{N'=1}^{N'=C_N} Z_{N'}. \quad (3)$$

When  $Z_N Z_{N'} < 0$ , the pair of atoms are attracted each by other and binding energy increases. But, when  $Z_N Z_{N'} > 0$ , they are repulsed and binding energy decreased.

Now we can find final expression of the corrected binding energy per atom:

$$E_b = E_{b0} + E_e = \frac{1}{2n} \sum_{N=1}^{N=n} \left( \varepsilon_b C_N - \varepsilon_e Z_N \sum_{N'=1}^{N'=C_N} Z_{N'} \right). \quad (4)$$

Calculated binding energies for ground-state isomers are presented in the **Table 1**.

Theoretically obtained  $E_e - n$  dependence, in general, correlates with experimental cluster-ion intensity dependences from its mass. However main maximum is slightly shifted toward smaller clusters. Such discrepancies may be related to clusters charge – we have calculated binding energy per atom for neutral species, not positive ions as in experiment presented in **Figure 2**.

### Conclusions

Studying the boron vapor has shown that, it mainly consists of small (quasi)planar clusters. Boron atoms in nonequivalent sites possess different effective charges. It leads to the nonzero dipole moment for asymmetric species. Binding energy per atom for small boron (quasi)planar clusters are calculated based on quasi-classical B–B interatomic pair potential and taking into account the corrections related to electrostatic interactions between effective atomic charges. This value is found to be correlated with clusters formation probabilities.

## Acknowledgement

One of the Authors, Levan Chkhartishvili, is thankful to the Shota Rustaveli National Science Foundation (Georgia) for supporting his participation in ICANM 2015 to present this paper.

## References

1. R. Becker, L. Chkhartishvili, P. Martin, Boron, the New Graphene? *Vac. Technol. & Coat.*, 2015, 16, 4, 38-44.
2. Ch. Feldman, K. Moorjani, N. Blum. Mass-spectrometry and optical absorption of boron amorphous films. In: *Boron. Obtaining, Structure, and Properties*. 1974, Moscow, Nauka, 130-138.
3. W. R. M. Graham, W. Weltner. B atoms, B<sub>2</sub> and H<sub>2</sub>BO molecules: ESR and optical spectra at 4 °K. *J. Chem. Phys.*, 1976, 65, 4, 1516-1521.
4. M. Dupuis, B. Liu. The ground electronic state of B<sub>2</sub>. *J. Chem. Phys.*, 1978, 68, 6, 2902-2910.
5. I. Carmichael. Ab initio calculation of the hyperfine coupling constants in B<sub>2</sub>. *J. Chem. Phys.*, 1989, 91, 2, 1072-1178.
6. Bruna, P.J., Wright, J.S. (1989) Strongly Bound Multiply Excited States of B<sub>2</sub><sup>+</sup> and B<sub>2</sub>. *J. Chem. Phys.* 91(2):1126-1136.
7. P. J. Bruna, J. S. Wright. Theoretical study of the ionization potentials of boron dimer. *J. Phys. Chem.*, 1990, 94, 5, 1774-1781.
8. P. W. Deutsch, L. A. Curtiss, J. A Pople. Boron dimer: Dissociation energy and ionization potentials. *Chem. Phys. Lett.*, 1990, 174, 1, 33-36.
9. S. R. Langhoff, Ch. W. Bauschlicher. Theoretical study of the spectroscopy of B<sub>2</sub>. *J. Chem. Phys.* , 1991, 95, 8, 5882-5888.
10. K. Hald, P. Jorgensen, J. Olsen, M. Jaszunski. An analysis and implementation of a general coupled cluster approach to excitation energies with application to the B<sub>2</sub> molecule. *J. Chem. Phys.*, 2001, 115, 2, 671-679.
11. J. M. L. Martin, J. P. Francois, R. Gijbels. Ab Initio Study of Boron, Nitrogen, and Boron–Nitrogen Clusters. I. Isomers and thermochemistry of B<sub>3</sub>, B<sub>2</sub>N, BN<sub>2</sub>, and N<sub>3</sub>. *J. Chem. Phys.*, 1989, 90, 11, 6469-6485.
12. R. Hernandez, J. Simons. Electronic energies, geometries, and vibrational frequencies of the ground and low-lying excited states of the boron trimer. *J. Chem. Phys.*, 1991, 94, 4, 2961-2967.
13. B. Fernandez, P. Jorgensen, J. Simons. Interpretation of the hyperfine coupling constants of the boron trimer in rare-gas matrices. *J. Chem. Phys.*, 1993, 98, 4, 3060-3065.
14. J. M. L. Martin, J. P. Francois, R. Gijbels. Potential energy surface of B<sub>4</sub> and total atomization energies of B<sub>2</sub>, B<sub>3</sub>, and B<sub>4</sub>. *Chem. Phys. Lett.*, 1992, 189, 6, 529-536.

15. H.-J. Zhai, L.-Sh. Wang, A. N. Alexandrova, A. I. Boldyrev, V. G. Zakrzewski. Photoelectron spectroscopy and ab initio study of  $B_3^-$  and  $B_4^-$  anions and their neutrals. *J. Phys. Chem. A*, 2003, 107, 44, 9319-9328.
16. H.-J. Zhai, L.-Sh. Wang, A. N. Alexandrova, A. I. Boldyrev. Electronic structure and chemical bonding of  $B_5^-$  and  $B_5$  by photoelectron spectroscopy and ab initio calculations. *J. Chem. Phys.* 2002, 117, 17, 7917-7924.
17. Q. Sh. Li, H. W. Jin. Structure and stability of  $B_5$ ,  $B_5^+$ , and  $B_5^-$  clusters. *J. Phys. Chem. A*, 2002, 106, 30, 7042-7047.
18. A. N. Alexandrova, A. I. Boldyrev, H.-J. Zhai, L.-Sh. Wang, E. Steiner, P. W. Fowler. Structure and bonding in  $B_6^-$  and  $B_6$ : Planarity and antiaromaticity. *J. Phys. Chem. A*, 2003, 107, 9, 1359-1369.
19. A. N. Alexandrova, A. I. Boldyrev, H.-J. Zhai, L.-Sh. Wang. Electronic structure, isomerism, and chemical bonding in  $B_7^-$  and  $B_7$ . *J. Phys. Chem. A*, 2004, 108, 16, 3509-3517.
20. P.-L. Cao, W. Zhao, B.-X. Li, B. Song, X.-Y. Zhou. A full-potential linear-Muffin-Tin-Orbital molecular-dynamics study of  $B_7$ ,  $B_{10}$  and  $B_{13}$  clusters. *J. Phys. Cond. Matter*, (2001) 13, 22, 5065-5076.
21. L. Hanley, S. L. Anderson. Production and collision-induced dissociation of small boron cluster ions. *J. Phys. Chem.*, 1987, 91, 20, 5161-5163.
22. H. Kato, E. Tanaka. Stabilities of small  $Be_n$  and  $B_n$  clusters ( $4 \leq n \leq 8$ ) by vibrational analysis. *J. Comput. Chem.*, 1991, 12, 9, 1097-1109.
23. A. K. Ray, I. A. Howard, K. M. Kanal. Structure and binding in small neutral and cationic boron clusters. *Phys. Rev. B*, 1992, 45, 24, 14247-14255.
24. H.-J. Zhai, A. N. Alexandrova, K. A. Birch, A. I. Boldyrev, L. Sh. Wang. Hepta- and octa-coordinate boron in molecular wheels of eight- and nine-atom boron clusters: Observation and confirmation. *Angew. Chem. Int. Ed.*, 2003, 42, 48, 6004-6008.
25. M. L. Drummond, V. Meunier, B. G. Sumpter. Structure and stability of small boron and boron oxide clusters. *J. Phys. Chem. A*, 2007, 111, 28, 6539-6551.
26. H. Kato, K. Yamashita, K. Morokuma. Ab initio MO study of neutral and cationic boron clusters. *Chem. Phys. Lett.*, 1992, 190, 3-4, 361-366.
27. M. Atis, C. Ozdogan, Z. B. Guvenc. Structure and energetic of  $B_n$  ( $n = 2-12$ ) clusters: Electronic structure calculations. *Int. J. Quan. Chem.*, 2007, 107, 3, 729-744.
28. H. C. Longuet-Higgins, M. V. de Roberts. The electronic structure of an icosahedron of boron atoms. *Proc. Roy. Soc. A*, 1955, 230, 1180, 110-119.
29. N. E., Solov'ev, E. M. Averbakh, Ya. A. Ugaj. Icosahedron electron energy levels in  $\alpha$ -rhombohedral boron. *Phys. Solid State*, 1984, 26, 1, 195-199.
30. S. Lee, D. M. Bylander, L. Kleinman. Bands and bonds of  $B_{12}$ . *Phys. Rev. B*, 1990, 42, 2, 1316-1320.
31. Ch. L. Beckel, J. P. Vaughan. Vibrations of regular boron icosahedra. *AIP Conf. Proc.*, 1986, 140, 305-311.
32. H. Werheit, U. Kuhlmann. Electron-phonon interaction in  $B_{12}$  icosahedra. *Solid State Commun.*, 1993, 88, 6, 421-425.

33. K. Shirai, S. Conda. Polar Vibrations and the effective charges of the icosahedral boron solid. *J. Phys. & Chem. Solids*, 1996, 57, 1, 109-123.
34. M. Yamaguchi, Y. Ohishi, S. Hosoi, K. Soga, K. Kimura. Metallic-covalent bonding conversion in boron icosahedral cluster solids studied using electron localizability indicator. *J. Phys. Conf. Ser.*, 2009, 176, 012027, 1-10.
35. L. Hanley, J. L. Whitten, S. L. Anderson. Collision-induced dissociation and ab initio studies of boron cluster ions: Determination of structures and stabilities. *J. Phys. Chem.*, 1988, 92, 20, 5803-5812.
36. L. Hanley, J. L. Whitten, S. L. Anderson. Collision-induced dissociation and ab initio studies of boron cluster ions: Determination of structures and stabilities [Erratum to document cited in CA109(18):156723t]. *J. Phys. Chem.*, 1990, 94, 5, 2218-2218.
37. R. Kawai, J. H. Weare. Anomalous stability of  $B_{13}^+$  clusters. *Chem. Phys. Lett.*, 1992, 191, 3-4, 311-314.
38. H. Kato, K. Yamashita, K. Morokuma. Ab initio study of neutral and cationic  $B_{12}$  and  $B_{13}$  clusters. *Bull. Chem. Soc. Jpn.*, 1993, 66, 11, 3358-3361.
39. F. L. Gu, X. Yang, A.-Ch. Tang, H. Jiao, P. von R. Schleyer. Structure and stability of  $B_{13}^+$  clusters. *J. Comput. Chem.*, 1998, 19, 2, 203-214.
40. J. E. Fowler, J. M. Ugalde. The curiously stable  $B_{13}^+$  cluster and its neutral and anionic counterparts: the advantages of planarity. *J. Phys. Chem. A*, 2000, 104, 2, 397-403.
41. J.-I. Aihara.  $B_{13}^+$  is highly aromatic. *J. Phys. Chem. A*, 2001, 105, 22, 5486-5489.
42. T. B. Tai, D. J. Grant, M. T. Nguyen, D. A. Dixon. Thermochemistry and electronic structure of small boron clusters ( $B_n$ ,  $n = 5-13$ ) and their anions. *J. Phys. Chem. A*, 2010, 114, 2, 994-1007.
43. N. Akman, M. Tas, C. Ozdogan, I. Boustani. Ionization energies, coulomb explosion, fragmentation, geometric, and electronic structures of multicharged boron clusters  $B_n$  ( $n = 2-13$ ). *Phys. Rev. B*, 2011, 84, 075463, 1-10.
44. Q. Sh. Li, F. L. Gu, A. C. Tang. Quantum chemistry study on  $B_{14}$ ,  $B_{14}^{2-}$ , and  $B_{14}H_{14}^{2-}$ . *Int. J. Quan. Chem.*, 1994, 50, 3, 173-179.
45. I. Boustani. Systematic LSD investigation on cationic boron clusters:  $B_n^+$  ( $n = 2-14$ ). *Int. J. Quan. Chem.*, 1994, 52, 4, 1081-1111.
46. I. Boustani. A comparative study of ab initio SCF-CI and DFT. example of small boron Clusters. *Chem. Phys. Lett.*, 1995, 233, 3, 273-278.
47. I. Boustani. Structure and stability of small boron clusters. A density functional theoretical study. *Chem. Phys. Lett.*, 1995, 240, 1-3, 135-140.
48. A. Ricca, Ch. W. Bauschlicher Jr. The structure and stability of  $B_n^+$  clusters. *Chem. Phys.*, 1996, 208, 2, 233-242.
49. I. Boustani. New convex and spherical structures of bare boron clusters. *J. Solid State Chem.*, 1997, 133, 1, 182-189.
50. I. Boustani. New quasi-planar surfaces of bare boron. *Surf. Sci.*, 1997, 370, 2-3, 355-363.
51. I. Boustani. Systematic ab initio investigation of bare boron clusters: determination of the geometry and electronic structures of  $B_n$  ( $n = 2-14$ ). *Phys. Rev. B*, 1997, 55, 24, 16426-16438.

52. E. Oger, N. Crawford, R. Kelting, P. Weis, M. Kappes, R. Ahlrichs. Boron cluster cations: transition from planar to cylindrical structures. *Angew. Chem. Int. E.*, 2007, 46, 44, 8503-8506.
53. A. P. Sergeeva, D. Yu. Zubarev, H.-J. Zhai, A. I. Boldyrev, L.-Sh. Wang. A photoelectron spectroscopic and theoretical study of  $B_{16}^-$  and  $B_{16}^{2-}$ : An all-boron naphthalene. *J. Am. Chem. Soc.*, 2008, 130, 23, 7244-7246.
54. W. Huang, A. P. Sergeeva, H.-J. Zhai, B. B. Averkiev, L.-Sh. Wang, A. I. Boldyrev. A Concentric planar doubly  $\pi$ -aromatic  $B_{19}^-$  cluster. *Nat. Chem.*, 2010, 2, 3, 202-206.
55. B. Kiran, S. Bulusu, H.-J. Zhai, S. Yoo, X. Ch. Zeng, L.-Sh. Wang. Planar-to-tubular structural transition in boron clusters:  $B_{20}$  as the embryo of single-walled boron nanotubes. *Proc. Natl. Acad. Sci. USA*, 2005, 102, 4, 961-964.
56. W. An, S. Bulusu, Y. Gao, X. C. Zeng. Relative stability of planar versus double-ring tubular isomers of neutral and anionic boron clusters  $B_{20}$  and  $B_{20}^-$ . *J. Chem. Phys.*, 2006, 124, 154310, 1-6.
57. L.-Sh. Wang. Probing the electronic structure and chemical bonding of boron clusters using photoelectron spectroscopy of size-selected cluster anions. In: 16th Int. Symp. Boron, Borides & Rel. Mater., 2008, Matsue, KM, 61-61.
58. I. Boustani, A. Quandt, E. Hernandez, A. Rubio. New boron based nanostructured materials. *J. Chem. Phys.*, 1999, 110, 6, 3178-3185.
59. S. Chacko, D. G. Kanhere, I. Boustani. Ab initio density functional investigation of  $B_{24}$  clusters: rings, tubes, planes, and cages. *Phys. Rev. B*, 2003, 68, 035414, 1-11.
60. I. Boustani, A. Rubio, J. A. Alonso. Ab initio study of  $B_{32}$  clusters: Competition between spherical, quasiplanar and tubular isomers. *Chem. Phys. Lett.*, 1999, 311, 1, 21-28.
61. S. J. la Placa, P. A. Roland, J. J. Wynne. Boron clusters ( $B_n$ ,  $n = 2 - 52$ ) produced by laser ablation of hexagonal boron nitride. *Chem. Phys. Lett.*, 1992, 190, 3-4, 163-168.
62. I. Boustani. Structural transitions and properties of boron nanoclusters. In: 17th Int. Symp. Boron, Borides & Rel. Mater., 2011, Ankara, BKM, 49-49.
63. S.-J. Xu, J. M. Nilles, D. Radisic, W.-J. Zheng, S. Stokes, K. H. Bowen, R. C. Becker, I. Boustani. Boron cluster anions containing multiple  $B_{12}$  icosahedra. *Chem. Phys. Lett.*, 2003, 379, 3-4, 282-286.
64. A.-Ch. Tang, Q.-Sh. Li, Ch.-W. Liu, J. Li. Symmetrical clusters of carbon and boron. *Chem. Phys. Lett.*, 1993, 201, 5-6, 465-469.
65. I. Boustani, A. Quandt. Boron in ab initio calculations. *Comput. Mater. Sci.*, 1998, 11, 1, 132-137.
66. H.-J. Zhai, B. Kiran, J. Li, L.-Sh. Wang. Hydrocarbon analogues of boron clusters – Planarity, aromaticity and antiaromaticity. *Nat. Mater.*, 2003, 2, 12, 827-833.
67. I. Boustani. Theoretical prediction and experimental observation of boron quasiplanar clusters and single-wall nanotubes. In: 15th Int. Symp. Boron, Borides & Rel. Mater., 2005, Hamburg, UH, 41-41.
68. A. N. Alexandrova, A. I. Boldyrev, H.-J. Zhai, L.-Sh. Wang. All-boron aromatic clusters as potential new inorganic ligands and building blocks in chemistry. *Coord. Chem. Rev.*, 2006, 250, 21-22, 2811-2866.

69. Z. A. Piazza, H.-Sh. Hu, W.-L. Li, Y.-F. Zhao, J. Li, L.-Sh. Wang. Planar hexagonal B<sub>36</sub> as a potential basis for extended single-atom layer boron sheets. *Nat. Commun.*, 2014, 5, 3113, 1-15.
70. N. Vast, S. Bernard, G. Zerah. Structural and electronic properties of liquid boron from a molecular-dynamics simulation. *Phys. Rev. B*, 1995, 52, 6, 4123-4130.
71. Sh. Krishnan, S. Ansell, J. J. Felten, K. J. Volin, D. L. Price. Structure of liquid boron. *Phys. Rev. Lett.*, 1998, 81, 3, 586-589.
72. D. L. Price, A. Alatas, L. Hennet, N. Jakse, Sh. Krishnan, A. Pasturel, I. Pozdnyakova, M.-L. Saboungi, A. Said, R. Scheunemann, W. Schirmacher, H. Sinn. Liquid boron: X-ray measurements and ab initio molecular dynamics simulations. *Phys. Rev. B*, 2009, 79, 134201, 1-5.
73. R. C. Becker. Method for generating a boron vapor. U.S. Patent: #5,861,630, 1999.
74. R. Becker, L. Chkhartishvili, R. Avci, I. Murusidze, O. Tsagareishvili, N. Maisuradze, "Metallic" boron nitride. *Eur. Chem. Bull.*, 2015, 4, 1-3, 8-23.
75. R. Becker, L. Chkhartishvili. On possible nature of metallic conductance of boron-nitrogen compounds. In: *Abs. 3rd Int. Conf. "Nanotechnologies"*. 2014, Tbilisi, Publ. House Tech. Univ., 13-14.
76. I. Boustani, R. Becker. Boron clusters, single- and multi-walled nanotubes: Theoretical prediction and experimental observation. In: *Proc. 9th Ann. Nanotechnol. Conf. & Trade Show. 2006*, Boston, NSTI, MO 60.802.
77. L. Chkhartishvili. *Quasi-Classical Theory of Substance Ground State*. 2004, Tbilisi, Tech. Univ. Press.
78. L. Chkhartishvili, D. Lezhava, O. Tsagareishvili, D. Gulua. Ground-state parameters of diatomic molecules B<sub>2</sub>, BC, BN and BO. *Trans, Acad. MIA Georg.*, 1999, 1, 295-300.
79. L. Chkhartishvili, D. Lezhava, O. Tsagareishvili. Quasi-classical determination of electronic energies and vibration frequencies in boron compounds. *J. Solid State Chem.*, 2000, 154, 1, 148-152.
80. L. Chkhartishvili. Molar binding energy of the boron nanosystems. In: *Proc. 4th Int. Boron Symp. 2009*, Eskisehir, Osmangazi Univ. Press, 153-160.
81. L. Chkhartishvili. On quasi-classical estimations of boron nanotubes ground-state parameters. *J. Phys. Conf. Ser.*, 2009, 176, 012013, 1-9.
82. L. Chkhartishvili. Geometrical models for bare boron nanotubes. In: *Physics, Chemistry and Applications of Nanostructures*. 2011, Singapore: World Scientific, 118-121.
83. L. Chkhartishvili. Nanotubular boron: Ground-state estimates. In: *New Developments in Materials Science*. 2011, New York, Nova Sci. Publ., Ch.8, 67-80.
84. L. S. Chkhartishvili, D. L. Gabunia, O. A. Tsagareishvili. Estimation of the isotopic effect on the melting parameters of boron. *Inorg. Mater.*, 2007, 43, 6, 594-596.
85. L. S. Chkhartishvili, D. L. Gabunia, O. A. Tsagareishvili. Effect of the isotopic composition on the lattice parameter of boron. *Powder Metall. & Met. Ceram.*, 2008, 47(9-10):616-621.
86. L. Chkhartishvili. Isotopic effects of boron (Review). *Trends Inorg. Chem.*, 2009, 11, 105-167.



87. D. Gabunia, O. Tsagareishvili, L. Chkhartishvili, L. Gabunia. Isotopic composition dependences of lattice constant and thermal expansion of  $\beta$ -rhombohedral boron. J. Phys. Conf. Ser., 2009, 176, 012022, 1-10.
88. L. Chkhartishvili, O. Tsagareishvili, D. Gabunia. Isotopic expansion of boron. J. Metall. Eng., 2014, 3, 3, 97-103.

## POLY(GLYCEROL-SUCCINATE) OLIGOESTERS AS BIO-BASED SURFACTANTS FOR STABILITY OF O / W EMULSION FORMULATED WITH RICE BRAN OIL

V. Aomchad, J. Singkhonrat

Thammasat University  
 Faculty of Science and Technology  
 Department of Chemistry,  
 Pathumthani, Thailand  
 jirada@tu.ac.th

Accepted October 19, 2015

**Abstract**

Poly(glycerol-succinate) oligoesters, PGS oligoester, were synthesized and characterized by nuclear magnetic resonance and liquid chromatography mass spectrometer. The objectives of this work are to observe the detailed characterization of PGS's structure and to optimize the conditions. The influence of PGS and chitosan concentration on the physical stability of emulsion was studied in 0.25 – 5 wt. % range by visual inspection and microstructural techniques.

**1. Introduction**

PGSs resulting from the one pot synthesis of glycerol and succinic acid were expected to be branched [1]. Dendrimers, hyperbranched, highly branched and branched polymers have attracted a considerable attention in recent years because of their singular characteristics in the field of macromolecules and were defined the chemical structure as depicted in the **Figure 1**. They have the hydrophilic structure and could be further grafted with fatty alkyl chains leading to amphiphilic structures [2]. In our work, we using rice bran oil (RBO) grafted onto PGS to promote fully synthesized bio-sourced surfactant. The synthesized surfactants were applied into the applications of microencapsulation to develop a drug delivery system and test of stability in the mixing of water and oil.

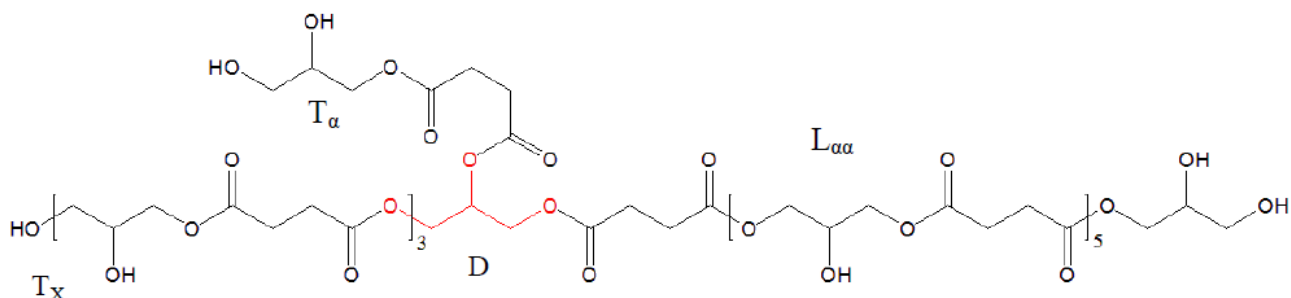


**Figure 1.** Chemical structure of PGSs, with terminal units ( $T_x$ ,  $T_\alpha$ ,  $T_\beta$ ), linear units ( $L_{\alpha\alpha}$ ,  $L_{\alpha\beta}$ ) and the dendritic unit (D).  $R = \text{CH}_2\text{-COOH}$  when  $T_x$  is a succinyl,  $R = \text{H}$  when  $T_x$  is non-grafted and  $R = (\text{CH}_2)_n\text{-CH}_3$  when  $T_x$  is a acyl group of fatty acid.

## 2. Methods

### 2.1. One-pot synthesis of non-grafted and grafted poly(glycerol-succinate) oligoester (PGSs)

PG<sub>1.5</sub>S: 0.3 mmol of succinic acid and 0.45 mmol of glycerol were mixed and equipped with a Dean-Stark apparatus. Staring time of reaction was taken when temperature reached 120 °C for 24 h to obtain a brown gel. Grafted PGS oligoester was synthesized following the same procedure as above mentioned with the formulations are described in **Table 1**.

**Table 1.** Composition of the various molar ratios of functional groups used to synthesis.

PGSs	Alkyl chains	Molar ratios of functional groups			Abbreviations
		G / S	Fr / S	Sor / S	
Non-grafted	–	1.5	–	–	PG <sub>1.5</sub> S
Grafted	Rice bran oil ester	1.5	0.05	–	PG <sub>1.5</sub> SFr <sub>0.05</sub>
	Rice bran oil ester and sorbitol	1.5	0.01	0.05	PG <sub>1.5</sub> SSorFr <sub>0.01</sub>

### 2.2. Characterization of non-grafted and grafted poly(glycerol-succinate) oligoester (PGSs)

Three types of PGS were obtained as one-phase brown gel. The following NMR results indicated whether the  $\alpha$ - and  $\beta$ -carbons (primary and secondary alcohol) of glyceride characteristics have been esterified (esterification indicated by D as dendrimer, L as linear and T as terminal) or not and the type of the structural unit (shown in **Table 2**) have been calculated.

**Table 2.** The succinate and glycerol region <sup>13</sup>C NMR spectra of the indicated copolymerized with glycerol.

Functional Group	Chemical shift	PGSs		
		PG <sub>1.5</sub> S	PG <sub>1.5</sub> SFr <sub>0.05</sub>	PG <sub>1.5</sub> SSorFr <sub>0.01</sub>
Succinate groups	–CH <sub>2</sub> –COOH	28.70	28.81	28.77
	–CH <sub>2</sub> –COOR	29.48	29.33	29.32
	–CH <sub>2</sub> –COOR	171.83	172.03	172.04
	–CH <sub>2</sub> –COOH	–	172.99	–
	–CH <sub>2</sub> –COO– (sorbitan)	–	–	211.15
Glyceryl groups	L <sub><math>\alpha\beta</math></sub> , HO–CH <sub>2</sub> –CHOR–CH <sub>2</sub> –OR	60.35	60.37	60.31
	T <sub><math>\beta</math></sub> , HO–CH <sub>2</sub> –CHOR–CH <sub>2</sub> –OH	60.77	60.71	60.68
	T <sub><math>\alpha</math></sub> , HO–CH <sub>2</sub> –CHOH–CH <sub>2</sub> –OR	62.19	62.22	62.22
	D, RO–CH <sub>2</sub> –CHOR–CH <sub>2</sub> –OR	62.55	62.58	62.54
	L <sub><math>\alpha\beta</math></sub> , HO–CH <sub>2</sub> –CHOR–CH <sub>2</sub> –OR	63.10	63.08	63.08
	T <sub><math>\alpha</math></sub> , HO–CH <sub>2</sub> –CHOH–CH <sub>2</sub> –OR	63.67	63.65	63.56
	L <sub><math>\alpha\alpha</math></sub> , RO–CH <sub>2</sub> –CHOH–CH <sub>2</sub> –OR	65.27 & 65.71	65.29 & 65.70	65.27 & 65.59
	T <sub><math>\alpha</math></sub> , HO–CH <sub>2</sub> –CHOH–CH <sub>2</sub> –OR	67.18	67.14	67.12
	D, RO–CH <sub>2</sub> –CHOR–CH <sub>2</sub> –OR	69.44	69.47	69.42
	L <sub><math>\alpha\alpha</math></sub> , RO–CH <sub>2</sub> –CHOH–CH <sub>2</sub> –OR	69.91	69.93	69.89
	L <sub><math>\alpha\beta</math></sub> , HO–CH <sub>2</sub> –CHOR–CH <sub>2</sub> –OR	72.61	72.64	72.58
T <sub><math>\beta</math></sub> , HO–CH <sub>2</sub> –CHOR–CH <sub>2</sub> –OH	75.96	75.93	75.90	

## 2.3. Applications of PGSs

### 2.3.1. Formulation of o / w emulsions

The emulsion was prepared by mixing in a ratio 1 : 1 of aqueous phase and oil phase in the presence of PG<sub>1.5</sub>SF<sub>R0.05</sub>. Aqueous phase were consisted of chitosan (2.5 or 5 wt. %) and gum Arabic (2.5 wt. %) distilled water, added to a final weight of 100 g. The emulsion was mixed at 70 °C and held at 30 °C for 30 min, then immediately homogenised using a homogenizer (Ross High Shear Mixers LSK-I Model, Germany). After homogenisation, the mixture was cooled to 4 °C and aged at this temperature for 4 h. Then, then samples were tested for visual inspection of their stability in 3 conditions: centrifuge 3000 rpm for 5 min, kept at room temperature and at below 5 °C for 7 weeks.

### 2.3.2. Microencapsulation of curcumin by complex coacervation

For the simple emulsion, active compound (ascorbic acid or curcumin) solution was added to RBO in the presence of PG<sub>1.5</sub>SF<sub>R0.05</sub>, then slowly added to aqueous chitosan solution to form the double emulsion and followed by adding the above solution to gum arabic solution. pH was adjusted to 4.0 using acetic acid then slow cooling and freeze-dried to obtain the coacervate material for further morphological and FT-IR characterization.

## 3. Results and discussion

### 3.1. Synthesis and characterization of PGSs

<sup>13</sup>C-NMR is a technique for the study of the topology of branched and hyperbranched polymers and oligomers. The degree of branching (DB) has been defined by Fréchet and Frey commonly determined by the relative proportions among the NMR resonance peak areas. All mathematic models were used here to extract these data by quantitative <sup>13</sup>C-NMR as shown in **Table 3**. FTIR spectra exhibited a positive peak at 3680 – 3300 cm<sup>-1</sup> for the –OH stretch, 2932 and 2884.9 cm<sup>-1</sup> for –CH<sub>2</sub>– stretch in core structure, and 1731.6 cm<sup>-1</sup> for C=O stretch peak of the ester.

**Table 3.** Conversion and polymerization characteristics of the PGSs.

PGSs	Conversion	DB <sub>Frey</sub> (%)
PG <sub>1.5</sub> S	94.9	22.61
PG <sub>1.5</sub> SF <sub>R0.05</sub>	94.4	24.23
PG <sub>1.5</sub> SSorF <sub>R0.01</sub>	95.7	16.21

### 3.2. Application

#### 3.2.1. Formulation of o / w emulsions

Simple emulsion showed a thermodynamically unstable system due to flocculation, creaming, coalescence, phase inversion and Ostwald riping [3]. A new synthesised surfactant, PG<sub>1.5</sub>SF<sub>R0.05</sub>, is introduced as an emulsifier which can stabilise the emulsion by absorption at the

interface, caused lowering the interfacial tension. PG<sub>1.5</sub>SF<sub>R0.05</sub> can perform to improve the emulsion stability when used 5 wt. % and combined with 5wt% gum Arabic. The emulsion observed to be stable for 2 weeks at room temperature and colorised after 6 weeks as shown in Figure 2B.



**Figure 2.** A) Water: RBO (with PG<sub>1.5</sub>SF<sub>R0.05</sub> 2.5 wt. %) in a ratio of 50 : 50; B) Water (with gum Arabic 5 wt. %): RBO (with PG<sub>1.5</sub>SF<sub>R0.05</sub> 5 wt. %) in a ratio of 50 : 50.

### 3.2.2. Microencapsulation of curcumin by complex coacervation

To achieve the coacervation of a core material viable, a water-in-oil emulsion was first prepared using rice bran oil, a 1 % solution of active compound (curcumin or ascorbic acid) and PG<sub>1.5</sub>SF<sub>R0.05</sub>, as the surfactant. Optimized microcapsule formulations (w / o / w) were prepared containing chitosan, gum arabic and active compound at ratios of 1 : 1 : 0.2, with 0.004 g / mL of the PG<sub>1.5</sub>SF<sub>R0.05</sub>.

#### 3.2.2.1. Loading efficiency

The quantitative of active compound (ascorbic acid or curcumin) loading efficiency in the complex coacervated was measured following the equation

$$\eta = \frac{C_f}{C_i} \cdot 100 \%,$$

where  $C_f$  and  $C_i$  were the final and initial loading contents of curcumin. We have received the standard curve from UV-Vis spectroscopy, which has revealed equation as followed  $y = 0.1555x - 0.0027$ ,  $R^2 = 0.9998$  for curcumin and  $y = 0.0359x - 0.0956$ ,  $R^2 = 0.9945$  for ascorbic acid. The result of loading efficiency for curcumin was higher than 97.96 % (average of  $98.040 \pm 0.112$  %) but loading efficiency for ascorbic acid was lower than 44 %. It is suggested that the formation of these complex coacervation is in agreement with typical microencapsulation of hydrophobic agents using complex coacervation reported to produce high encapsulation efficiency. In addition, the microencapsulation of hydrophilic active agents by complex coacervation often reported to produce low EE [4].

### 3.2.2.2. Morphological characterization of the microcapsules by optical microscopy

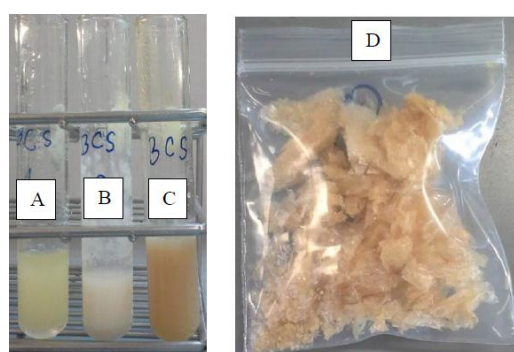


**Figure 3.** Blank appearance of (A) simple emulsion (w / o); (B) double emulsion by 5 wt. % chitosan solution (w / o / w); (C) complex coacervation and (D) freeze-dry.

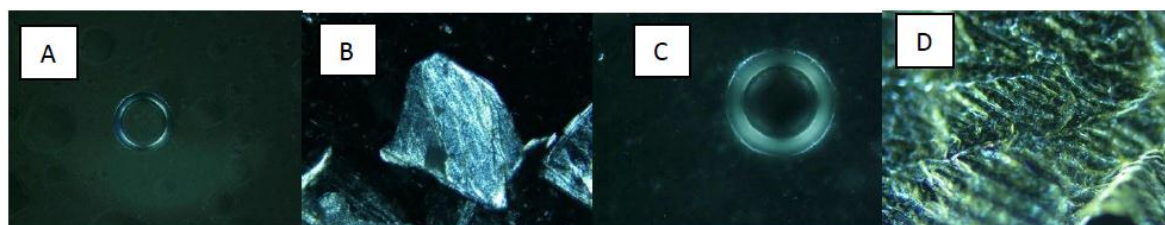


**Figure 4.** Blank micrograph of A) the simple emulsion (20 ×). B) the double emulsion by 5 wt. % chitosan solution (40 ×). C) the coacervated microcapsule (prior to freeze-drying) (40 ×). D) freeze-dried coacervated microcapsules (10 ×).

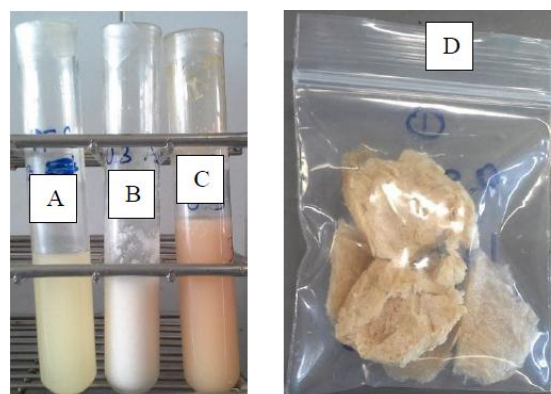


**Figure 5.** Ascorbic acid in (A) simple emulsion (w / o); (B) double emulsion by 5 wt. % chitosan solution (w / o / w); (C) complex coacervation and (D) freeze-dry.



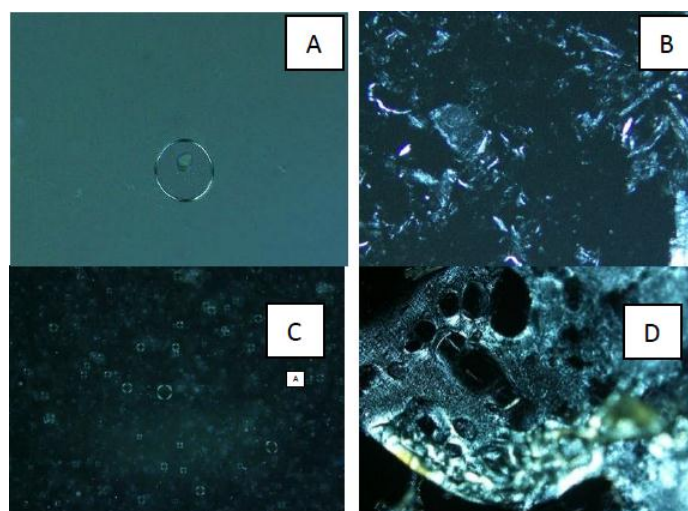


**Figure 6.** Micrograph of ascorbic acid in A) the simple emulsion (20 ×). B) the double emulsion by 5 wt. % chitosan solution (20 ×). C) the coacervated microcapsule (prior to freeze-drying) (10 ×). D) freeze-dried coacervated microcapsules (10 ×).

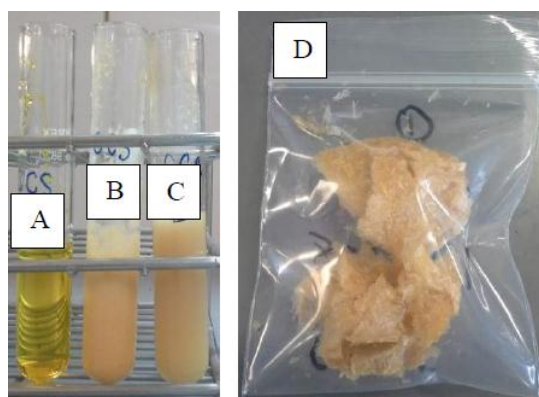


**Figure 7.** Appearance of Curcumin in (A) simple emulsion (w / o); (B) double emulsion by 5 wt. % chitosan solution (w / o / w); (C) complex coacervation and (D) freeze-dry.

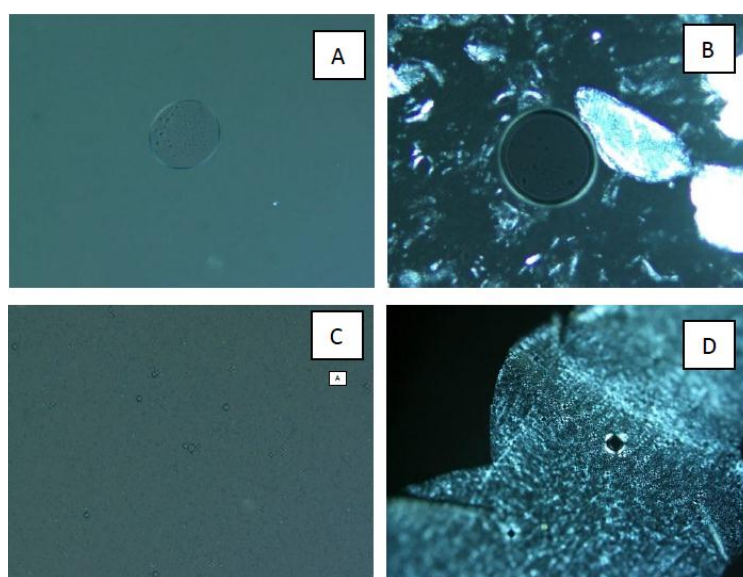


**Figure 8.** Micrograph of Curcumin in A) the simple emulsion (20 ×). B) the double emulsion by 5 wt. % chitosan solution (20 ×). C) the coacervated microcapsule (prior to freeze-drying) (10 ×). D) freeze-dried coacervated microcapsules (10 ×).

The formation of an oil drop in water was occurred and revealed simple emulsion with low stability supported by the picture (Figure 3A) and microscope image (Figure 4A). Loadings of ascorbic acid and curcumin were investigated with homogenous appearance (Figures 5A and 7A) and showed the uptake images in Figures 6A and 8A, respectively. Figures 4B and 6B showed no optical microscope images of the double emulsion after adding chitosan solution as wall material. The presence of droplets on the microscope slide of figure 8B indicated the successful formation of the double emulsion when loading the o / w emulsion with curcumin. All pictures of complex coacervation revealed pink creamy emulsions according to gum Arabic used in the coacervation process and showed in Figures 3C, 5C and 7C. Figure 4C revealed thicker wall image of microcapsule successfully formed. The freeze-dried microcapsules were observed and showed the agglomerated microcapsules formed connections with each other through solid bridges in their microscope images (Figures 6D and 8D).

### 3.2.2.3. Fourier transform infrared spectroscopy (FT-IR)

The spectrum of microcapsule was obtained in the range from 4000 to 400  $\text{cm}^{-1}$  (Figure 9). During complex coacervation, the carboxyl groups of polysaccharides interact with the amino groups of proteins in gum Arabic to form a complex containing an amide bond. The spectrum of chitosan and  $\text{PG}_{1.5}\text{SF}_{\text{R}0.05}$  showed intense vibrations between 3663 and 3166  $\text{cm}^{-1}$ . The peak that appears the intensity at approximately 1749  $\text{cm}^{-1}$  for the gum Arabic is characteristic of carboxylic groups that are negatively charged. The binding of positive and negative charges (i.e., amino and carboxyl groups) is expected to promote the process of coacervation and the formation of amides. Major peaks can be observed at approximately 1661 and 1457  $\text{cm}^{-1}$ , which could indicate the presence of an amide, confirming the formation of this complex. The peak appearing at approximately 1108  $\text{cm}^{-1}$  for the gum Arabic was characteristic of the amine groups, which can be positively charged.

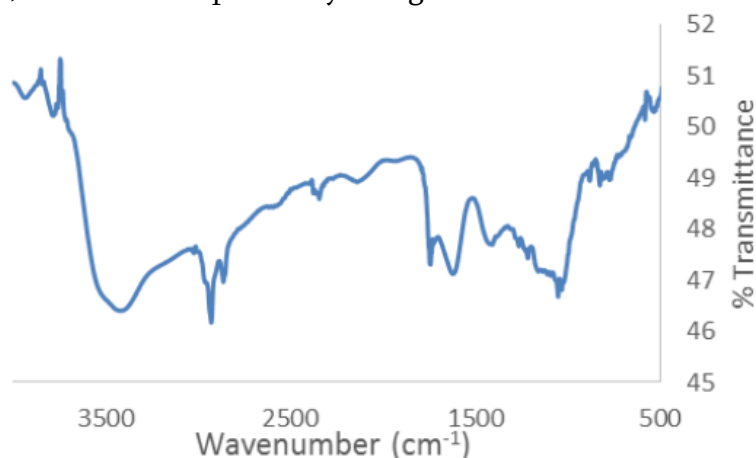


**Figure 9.** FT-IR spectra of the freeze-dried coacervated microcapsules loading of curcumin.

## 4. Conclusions

The one pot PGSs synthesis in various molar ratios of functional groups showed that grafted  $\text{PG}_{1.5}\text{SF}_{\text{R}0.05}$  was successfully synthesized and had a good in physico-chemical behavior of the surfactant.  $\text{PG}_{1.5}\text{SF}_{\text{R}0.05}$  has been successfully applied in emulsion formulation to improve the

textural characteristics and stability of emulsion, while gum arabic is usually added to increase the viscosity and gelling properties. The application in formulation of the microencapsulation was confirmed by FT-IR, which could indicate the presence of amide (to promote the process of coacervation). In a drug delivery system, PG<sub>1.5</sub>SFR<sub>0.05</sub> can be applied for complex coacervation formed by chitosan solution (see [5]) with highly loading efficiency of curcumin.

### **References**

1. M. Agach, S. Delbaere, S. Marinkovic, B. Estrine, V. Nardello-Rataj. Synthesis, characterization, biodegradability and surfactant properties of bio-sourced lauroyl poly(glycerol-succinate) oligoesters. *Colloids & Surfaces A*, 2013, 419, 263-273.
2. C. Khongphow, S. Puttamat, J. Theerakul, J. Singkhonrat. Characterisation of poly(glycerol-succinate) oligomers as bio-based non-ionic surfactants by nuclear magnetic resonance and mass spectrometry. *Colloids & Surfaces A*, 2015, 468, 301-308.
3. Q. Zhao, M. Zhao, B. Yang, C. Cui. Effect of xanthan gum on the physical properties and textural characteristics of whipped cream. *Food Chem.*, 2009, 116, 624-628.
4. M. G. Santos, F. T. Bozza, M. Thomazini, C. S. Favaro-Trindade. Microencapsulation of xylitol by double emulsion followed by complex coacervation, *Food Chem.*, 2015, 171, 32-39.
5. N. Calero, J. Munoz, P. W. Cox, A. Heuer, A. Guerrero. Influence of chitosan concentration on the stability, microstructure and rheological properties of O/W emulsions formulated with high-oleic sunflower oil and potato protein. *Food Hydrocolloids*, 2013, 30, 152-162.

FACILE PREPARATION OF P3HT–ZnO HETEROSTRUCTURE:  
STRUCTURAL AND SPECTROSCOPIC PROPERTIES

G. L. Kabongo<sup>1,2,3</sup>, G. H. Mhlongo<sup>2</sup>, B. M. Mothudi<sup>1</sup>, M. S. Dhlamini<sup>1</sup>

<sup>1</sup>University of South Africa

Department of Physics

PO Box 392, 0003, South Africa

geekale@gmail.com

<sup>2</sup>Council of Scientific & Industrial Research

National Centre for Nano-Structured Materials

Pretoria, South Africa

<sup>3</sup>Université Pédagogique Nationale

Département de Physique

Kinshasa, République Démocratique du Congo

Accepted October 19, 2015

### Abstract

In the current research work we demonstrate the ability to enhance the absorption properties of poly(3-hexylthiophene) (P3HT) via ZnO nanocrystals doping. Structural properties, optical absorption and vibrational modes of the samples were probed by means of X-ray diffraction (XRD), Ultraviolet–Visible (UV–Vis) spectroscopy, Raman spectroscopy and Fourier Transform InfraRed (FTIR) Spectroscopy. The effective enhancement of the absorption characteristics reveals that P3HT–ZnO heterostructure is an outstanding candidate for efficient hybrid photovoltaic (HPV) applications.

### 1. Introduction

Over the past decade conjugated polymer such as P3HT have stimulated much attention in the scientific community owing to its attractive structural, optical and electrical properties which are of considerable interest in the development of efficient low-cost optoelectronic devices such as solar cells, gas sensors, photodetectors, organic field-effect transistors (OFETs), etc [1 – 4].

Recently the inorganic-organic structures have gained momentum in the development of efficient low-cost bulk heterojunction (BHJ) hybrid photovoltaic devices. Several heterostructures of interest are possible among which those based on Fe<sub>2</sub>O<sub>3</sub>, CdSe, PbS, TiO<sub>2</sub>, CdS and ZnO semiconductors, just to cite few [5 – 10]. Due to the fact that some of the commonly used semiconductors are disadvantageous at some extent, ZnO appear to be the most promising alternative owing to its outstanding characteristics such as low-cost, non-toxic, low crystallization temperature, etc [11].

The current study focuses on the synthesis of a promising hybrid semiconductor material which has not been extensively investigated so far. Since the inception of the concept of organic-inorganic hybrid solar cells, only few works to the best of our knowledge have been reported on the enhancement of optical absorption properties of ZnO nanocrystals doped P3HT nanocomposite [12, 13]. Overall, in this report we demonstrate a systematic harvesting of light absorption induced by ZnO nanocrystals in P3HT which was prepared via a direct solution mixing procedure.

### 2. Experimental

The ZnO nanocrystals powder used in the current study was synthesized following the procedure described in our previous works [14, 15]. In a typical procedure ZnO nanocrystals powder was dissolved in absolute ethanol via a systematic sonication for 15 min at room temperature to obtain a clear aqueous ZnO solution (S1). On the other hand, P3HT solution was obtained by dissolving poly(3-hexylthiophene-2,5-diyl) in chlorobenzene (solvent) under rigorous stirring for 2 h at 40 °C. The resulting yellowish solution (S2) of P3HT (0.54 mg / ml) was then used to fabricate the reference film (F1) and further mixed to the ZnO solution for the fabrication of the P3HT–ZnO film (F2). To form P3HT–ZnO solution, S1 and S2 were mixed and stirred for 30 min resulting in a bluish-dark solution (S3). At the same time the glass slides were rigorously cleaned in successive acetone and alcoholic solution several times under constant sonication for 30 min. To fabricate the films, S2 and S3 were respectively deposited on pre-heated glass slides by drop casting process and allowed to dry in air for 48 hours in the dark. XRD measurements were carried out on RigakuSmartlab diffractometer using Cu K $\alpha$  radiation ( $\lambda=0.1540593$  nm) using a 45 kV tube voltage and 200 mA tube current (X-ray generator parameters). The experiment was carried out using the out-of-plane and in-plane 1D grazing incidence XRD mode. The room temperature (RT) UV–Vis absorption spectra of the P3HT and P3HT–ZnO films were investigated using a Perkin–ElmerLambda 1050 UV / Vis / NIR spectrophotometer equipped with integrated sphere. Raman scattering were collected using a Horiba Jobin-Yvon HR800 Raman spectrometer equipped with a visible microscope with a 514 nm excitation Ar<sup>+</sup> laser with a spectral resolution of 0.4 cm<sup>-1</sup> at RT. Fourier transform infrared (FTIR) spectra were collected at RT in the transmittance mode using a Perkin–Elmer 100 FTIR spectrometer.

### 3. Results and discussion

**Figure 1** depicts grazing incidence X-ray diffraction (GIXRD) patterns of the as-prepared films. Three intense diffraction peaks at  $2\theta = 5.48, 19$  and  $23^\circ$  of the patterns were assigned to (100), (010)' and (010) crystallographic reflexions of P3HT. The most prominent (010) diffraction peak is associated with the  $\pi$ – $\pi^*$  stacking of the polythiophene backbones [16]. However, the additional reflexions observed at  $2\theta = 31, 34, 36^\circ$  correspond to the hexagonal wurtzite structure of ZnO (see **Figure 1a**). More importantly, the change in scanning orientation from out-of-plane to in-plane revealed a systematic change of the structure crystallinity which may be related to the different lattice orientations exhibited by P3HT and ZnO.

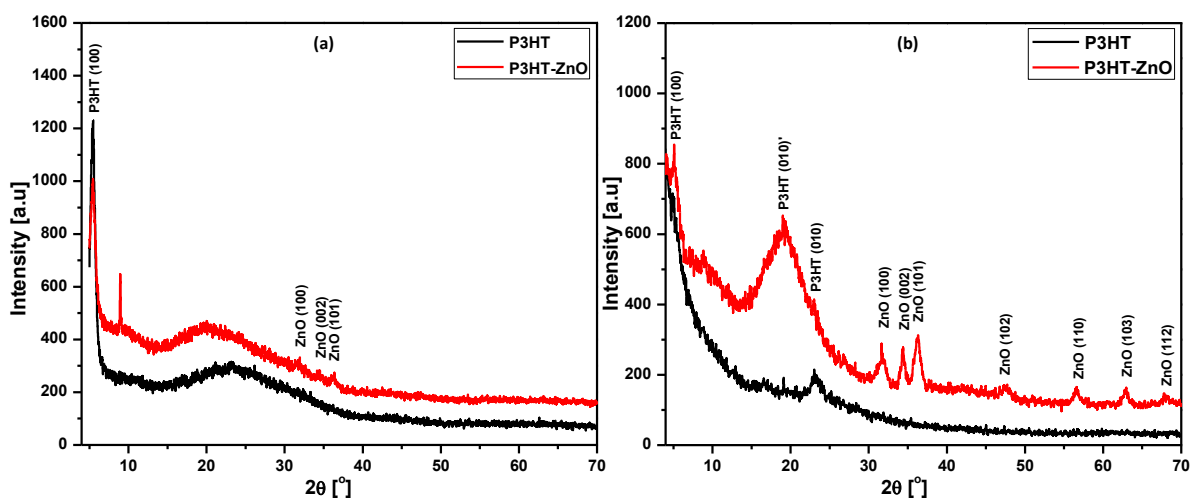


Figure 1. Out-of-plane (a) and in-plane (b) GIXRD patterns of the prepared samples.

Figure 2 shows typical broad absorption spectra ranging from 350 – 750 nm of P3HT due to intermolecular  $\pi$ - $\pi^*$  ordering. There was a distinguished enhancement of the absorption spectra of doped as compared to un-doped P3HT film, implying effective improved photo generated exciton due to ZnO doping. Moreover, the slight red shift observed in the doped  $\pi$ - $\pi^*$  spectrum edge denotes a reduced band gap due to enhanced electron delocalization being assigned to charge transfer [17, 18]. The resulting graded of the band gap which may lead to the broadening of the absorption spectrum of the doped P3HT film suggest a good match with the solar irradiance spectrum as compared to the P3HT film.

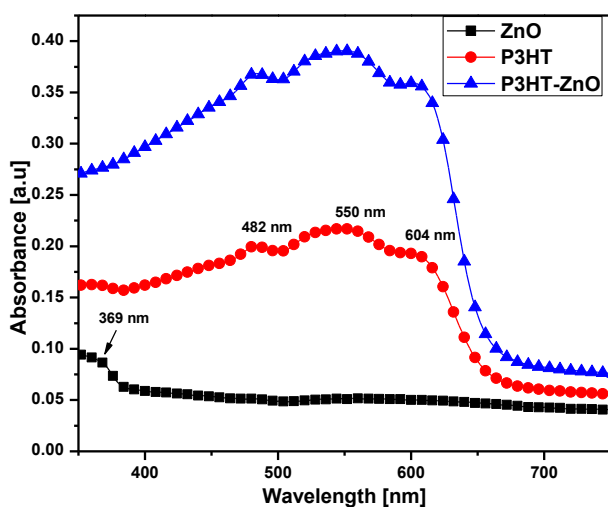


Figure 2. UV-Vis absorption spectra of the samples.

Figure 3 shows Raman scattering spectra recorded for P3HT and P3HT-ZnO films. Various Raman characteristic peaks were observed in the scattering spectrum. The most prominent Raman band was observed at about  $1447.3\text{ cm}^{-1}$  which was associated with a less intense peak at  $1379.4\text{ cm}^{-1}$ , the peaks were assigned to the C=C stretching vibrations of thiophene ring and C-C skeletal stretching vibrations [19, 20]. Moreover, the band at about  $598.8\text{ cm}^{-1}$  was assigned to in-plane thiophene ring deformation. Furthermore, the peaks observed at  $675$  and  $725.4\text{ cm}^{-1}$  were assigned to the symmetric and antisymmetric C-S-C deformation vibrations on the thiophene ring, respectively, while the peak at about  $873\text{ cm}^{-1}$  was due to C-H out-of-plane deformation. Finally, the peaks located at about  $2827$  and  $289\text{ cm}^{-1}$  correspond to the C-H symmetric and antisymmetric stretching, respectively.



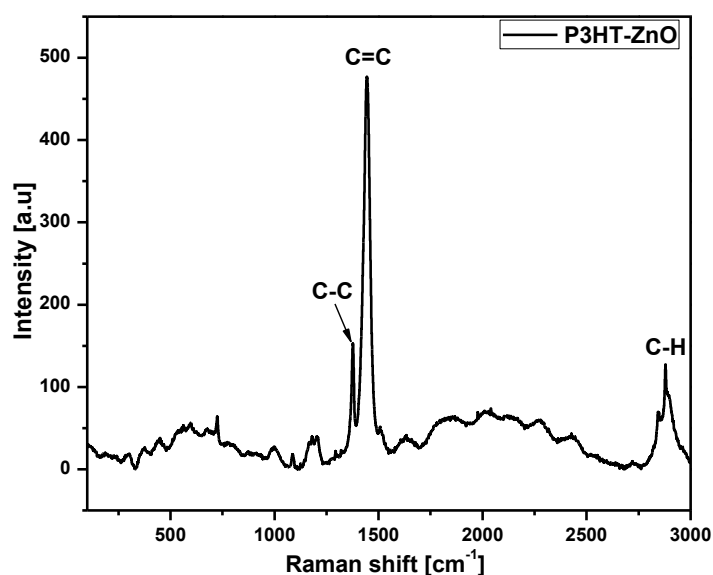


Figure 3. Raman scattering spectra of P3HT–ZnO film.

Figure 4 shows the FTIR spectra of P3HT and P3HT–ZnO films. The spectra look similar with slight differences mostly related to the intensities of the absorption peaks which is most pronounced in the P3HT–ZnO film. However, both spectra exhibited two main bands at about  $3030\text{ cm}^{-1}$  and  $2931 - 2847\text{ cm}^{-1}$  which are respectively due to C=CH and stretching vibrations of C–H bonds on the thiophene ring. Moreover, the broad absorption band in the range of  $3300 - 3500\text{ cm}^{-1}$  was ascribed to  $\equiv\text{C-H}$  bonds [19].

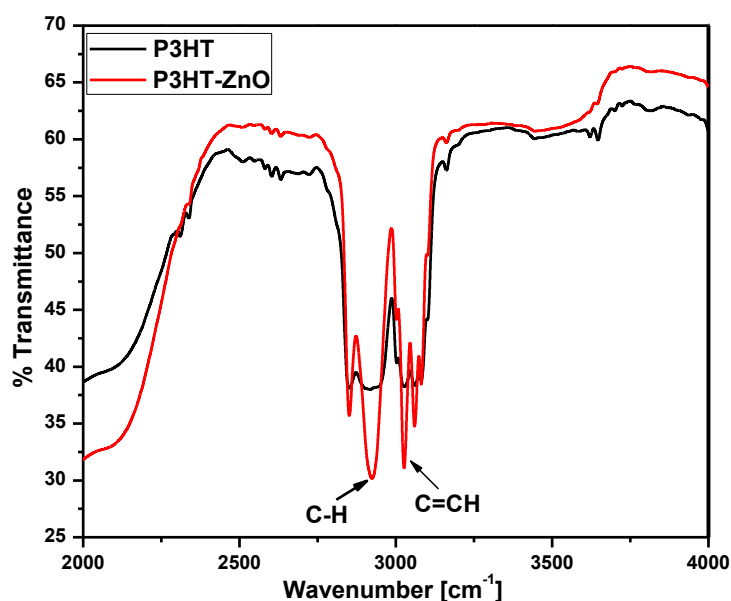


Figure 4. FTIR spectra for P3HT and P3HT–ZnO films.

#### 4. Conclusion

In the current research work we have successfully prepared a hybrid material for solar cell active layers via a direct solution mixing procedure. The obtained enhanced absorption characteristic due to improved photoinduced charge transfer between the organic and inorganic semiconductors is paving the way to potential high efficient and low-cost hybrid optoelectronic devices.

## Acknowledgements

This work has been financially supported by the University of South Africa (UNISA) and National Research Foundation (NRF) (Grant # 88028).

We gratefully acknowledge the support of the Council of Scientific and Industrial Research (CSIR) of South Africa.

## References

1. S. D. Oosterhout, L. J. A. Koster, S. S. van Bavel, J. Loos, O. Stenzel, R. Thiedmann, V. Schmidt, B. Campo, Th. J. Cleij, L. Lutzen, D. Vanderzande, M. M. Wienk, R. A. J. Janssen. Controlling the morphology and efficiency of hybrid ZnO: Polythiophene solar cells via side chain functionalization. *Adv. Energy Mater.*, 2011, 1, 90-96.
2. H. Tai, X. Li, Y. Jiang, G. Xie, X. Du. The enhanced formaldehyde-sensing properties of P3HT-ZnO hybrid thin film OTFT sensor and further insight into its stability. *Sensors*, 2015, 15, 2086-2103.
3. F. Guo, B. Yang, Y. Yuan, Zh. Xiao, Q. Dong, Y. Bi, Ji. Huang. A nanocomposite ultraviolet photodetector based on interfacial trap-controlled charge injection. *Nat. Nanotechnol.*, 2012, 7, 798-802.
4. M. Choe, B. H. Lee, W. Park, J.-W/ Kang, S. Jeong, K. Cho, W.-K. Hong, B. H. Lee, K. Lee, S.-J. Park, T. Lee. Characteristics of light-induced electron transport from P3HT to ZnO-nanowire field-effect transistors. *Appl. Phys. Lett.*, 2013, 103, 223305.
5. S. D. Oosterhout, M. M. Wienk, S. S. van Bavel, R. Thiedmann, L. J. A. Koster, J. Gilot, J. Loos, V. Schmidt, R. A. J. Janssen. The effect of three-dimensional morphology on the efficiency of hybrid polymer solar cells. *Nat. Mater.*, 2009, 8, 818-824.
6. Y. Peng, G. Song, X. Hu, G. He, Zh. Chen, X. Xu, J. Hu. In situ synthesis of P3HT-capped CdSe superstructures and their application in solar cells. *Nanoscale Res. Lett.*, 2013, 8, 106-113.
7. J. Seo, S. J. Kim, W. J. Kim, R. Singh, M. Samoc, A. N. Cartwright, P. N. Prasad. Enhancement of the photovoltaic performance in PbS nanocrystal:P3HT hybrid composite devices by post-treatment-driven ligand exchange. *Nanotechnol.*, 2009, 20, 095202.
8. H. Geng, C. M. Hill, Sh. Pan, L. Huang. Electrogenerated chemiluminescence and interfacial charge transfer dynamics of poly(3-hexylthiophene-2,5-diyl) (P3HT)-TiO<sub>2</sub> nanoparticle thin film. *Phys. Chem. Chem. Phys.*, 2013, 15, 10, 3504-3509.
9. S. A. Dowland, L. X. Reynolds, A. Mac Lachlan, U. B. Cappel, S. A. Haque. Photoinduced electron and hole transfer in CdS:P3HT nanocomposite films: Effect of nanomorphology on charge separation yield and solar cell performance. *J. Mater. Chem. A*, 2013, 1, 13896-13901.
10. W. J. E. Beek, L. H. Slooff, M. M. Wienk, J. M. Kroon, R. A. J. Janssen. Hybrid solar cells using zinc oxide precursor and conjugated polymer. *Adv. Mater.*, 2005, 15, 1703-1707.

11. X. Chen, L. Chen, Y. Chen. Self-assembly of discotic liquid crystal decorated ZnO nanoparticles for efficient hybrid solar cells. *RSC Adv.*, 2014, 4, 3627-3632.
12. F. Gao, Sh. Ren, J. Wang. The renaissance of hybrid solar cells: progresses, challenges, and perspectives. *Energy Environ. Sci.*, 2013, 6, 2020-2040.
13. A. J. Moule, L. Chang, Ch. Thambidurai, R. Vidua, P. Stroevea. Hybrid solar cells: Basic principles and the role of ligands. *J. Mater.*, 2012, 22, 2351-2368.
14. G. L. Kabongo, G. H. Mhlongo, B. M. Mothudi, K. T. Hillie, H. C. Swart, M. S. Dhlamini. Enhanced exciton emission from ZnO nano-phosphor induced by Yb<sup>3+</sup> ions. *Mater. Lett.*, 2014, 119, 71-74.
15. G. L. Kabongo, G. H. Mhlongo, Th. Malwela, B. M. Mothudi, K. T. Hillie, M. S. Dhlamini. Microstructural and photoluminescence properties of sol-gel derived Tb<sup>3+</sup> doped ZnO nanocrystals. *J. Alloys & Comp.*, 2014, 591, 156-163.
16. J. D. Roehling, I. Arslana, A. J. Moulé. Controlling microstructure in poly(3-hexylthiophene) nanofibers. *J. Mater. Chem.*, 2012, 22, 2498-2506.
17. W. Shen, J. Tang, R. Yang, H. Cong, X. Bao, Y. Wang, X. Wang, Zh. Huang, J. Liu, L. Huang, J. Jiao, Q. Xu, W. Chen, L. A. Belfiore. Enhanced efficiency of polymer solar cells by incorporated Ag–SiO<sub>2</sub> core-shell nanoparticles in the active layer. *RSC Adv.*, 2014, 4, 4379-4386.
18. P. Chawla, S. Singh, Sh. N. Sharma. An insight into the mechanism of charge-transfer of hybrid polymer:ternary/quaternary chalcopyrite colloidal nanocrystals. *Beilstein J. Nanotechnol.*, 2014, 5, 1235-1244.
19. S. Abdul Almohsin, J. B. Cui. Graphene-enriched P3HT and porphyrin-modified ZnO nanowire arrays for hybrid solar cell applications. *J. Phys. Chem. C*, 2012, 116, 9433-9438.
20. X. Bai, Ch. Sun, S. Wu, Y. Zhu. Enhancement of photocatalytic performance via a P3HT-g-C<sub>3</sub>N<sub>4</sub> heterojunction. *J. Mater. Chem. A*, 2015, 3, 2741-2747.

IN-PLANE SHEAR DEFORMABILITY OF OUT-OF-AUTOCLAVE  
PREPREGS UNDER DOUBLE-DIAPHRAGM VACUUM COMPACTION

H. A. Alshahrani, M. H. Hojjati

Concordia University  
Concordia Center for Composites  
Montreal, Quebec, Canada  
h\_alshah@encs.concordia.ca

Accepted October 19, 2015

**Abstract**

During the diaphragm forming process for carbon / epoxy prepregs, a vacuum seal is applied between the upper and lower diaphragms to compact and hold the laminate. Therefore, a thorough characterization of the in-plane shear behavior of fabrics under diaphragm forming conditions must take into account the effect of vacuum-sealing and compaction between the two diaphragms during bias extension. The study presented here examined the shear angles of out-of-autoclave 8-harness satin woven carbon / epoxy prepregs under diaphragm compaction. A bias extension test was conducted to study the effect of diaphragm compaction and ply interactions on shear properties. The test was performed at different compaction levels, and changes in shear angle with respect to vacuum levels and diaphragm compaction forces were observed. The contribution of diaphragm material and ply interaction to shear stiffness was evaluated and compared with results from a direct bias extension test. The samples were tested at both room temperature and at elevated temperatures using a radiant heater. The results show that shear angle decreases significantly as vacuum pressure and compaction is applied between the two diaphragms. This finding indicates that vacuum levels and compaction forces have a significant influence on the deformation limit and wrinkling onset during the diaphragm forming process.

**1. Introduction**

Conventional composite manufacturing techniques, such as hand lay-up, are labor intensive, costly and efficient only for small production runs. In order to automate the composite manufacturing techniques and reduce processing costs for the aerospace industry, alternative approaches, such as the resin-transfer molding, stamping, and diaphragm-formation processes, have been developed.

Double-diaphragm forming, which was initially applied to thermoplastic matrix composites, is one of the most important sheet-forming processes for composite materials. A typical double-diaphragm forming process consists of three steps [1, 2]. A flat laminate must first be placed between two deformable sheets known as diaphragms, which are themselves clamped over a forming box. The space between the diaphragms is subjected to a full vacuum seal. Next, the laminate between the diaphragms is heated up to processing temperature. Finally, controlled vacuum pressure applied to the forming-box cavity below the lower diaphragm causes forming to take place. Polymeric diaphragms are commonly used due to their ability to deform without rupturing under high processing temperatures [3, 4].

In-plane shear deformation is the dominant deformation mechanism used during formation of double-curved parts [5]. This deformation mechanism affects woven fabrics, warping the rotation of the yarns at their crossovers and causing a change in fiber orientation. Rotation around weave crossover is mainly limited by the ability of fiber yarns to contact each other (known as “locking angle”; see [6, 7]). A critical locking angle is reached when all yarns come into contact with each other and become compressed, causing a rapid increase in force that results in wrinkling [8]. Simulations conducted in [1, 2] confirm the necessity of scaling up the in-plane shearing stiffness from what was measured in bias extension tests without compaction pressures in order to properly test this phenomenon. The present study implements compaction between two diaphragms during the bias extension test in order to understand the relative magnitude of in-plane shear stiffness under diaphragm forming conditions; these results can then be incorporated into bias extension test simulations.

The purpose of this study is to evaluate the magnitude of in-plane shear stiffness and shear angles under double-diaphragm vacuum compaction using a bias extension test. Changes in shear angle with respect to applied compaction forces are observed. In addition, the contribution of diaphragm compaction to shear stiffness is measured by comparing the results of the compaction test with results from a direct bias extension test.

## 2. Experiment

### 2.1. Materials

The out-of-autoclave prepreg selected for this study was the 8-harness satin woven carbon/epoxy from Cytec Engineered Materials. The resin code is (Cycom 5320) toughened epoxy and the fabric has 3K fibers per tow. The fabric areal weight is 375 g / m<sup>2</sup> and the resin content is 36 % by weight. The measured thickness of uncured one-ply is approximately 0.47 mm. The diaphragm material used in this study was a translucent silicone rubber (EL1040T) manufactured by Torr Technologies Inc. (thickness 1.6 mm).

### 2.2. Bias extension test under diaphragms compaction

A bias extension test was conducted to study in-plane shear deformation under diaphragm forming compaction. Prepreg samples were placed between two diaphragm films; compaction was generated using a sealed vacuum bag due to the difficulty of sealing the two diaphragms together. **Figure 1** illustrates in detail the attachment of the prepreg sample and diaphragm films to the custom grips. The bias extension setup clamped in the tensile machine is shown in its entirety in **Figure 2**. The load needed to extend the prepreg sample under diaphragm compaction can be described by the following formula [9]:

$$F_s = F_t - F_d - F_f. \quad (1)$$

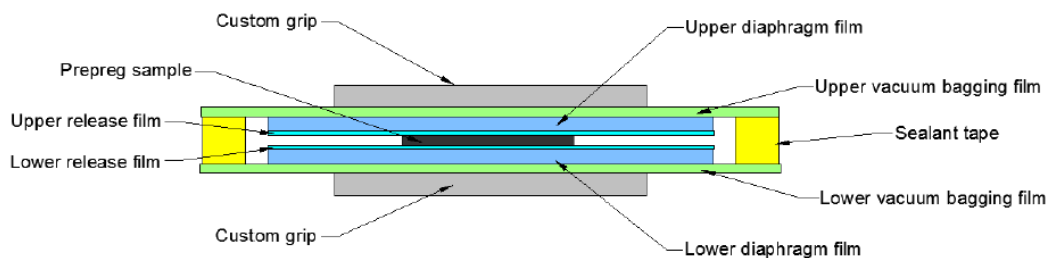


**Figure 1.** Detailed diagram of attachment of prepreg sample and diaphragm films to the customs grips.

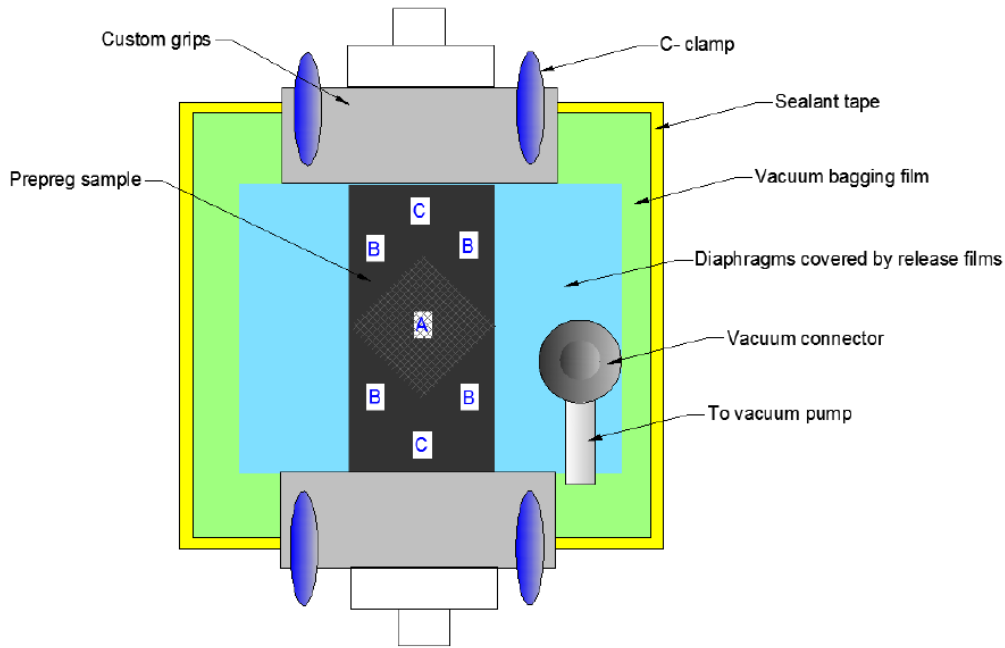


**Figure 2.** Bias extension setup under diaphragm forming compaction.

In this equation,  $F_s$  is the load needed to extend the prepreg sample,  $F_t$  is the total measured load of the bias extension setup with the prepreg sample,  $F_d$  is the load required to extend the bias extension setup without the prepreg sample, and  $F_f$  is the friction force between the sample and diaphragm films. The test conditions of this case are presented in **Table 1**.

**Table 1.** Test conditions of bias extension under compaction.

Temperature, °C	Cross-head rates, mm/min	Number of layers, ±45°	Level of compaction, kPa
RT	20	2	100, 50, 20
50	20	2	100
90	20	2	100

### 3. Results and discussion

Bias extension samples were taken in a 50 °C environment under 100 kPa of compaction in order to study the effect of diaphragm forming compaction on in-plane shear deformation, with the goal of applying these findings to future diaphragm forming simulations. In order to determine the magnitude of each load at each displacement, the bias extension setup was tested twice, once with the prepreg sample and once without it. The orange dashed line in **Figure 3** represents the total measured load of the bias extension setup with the prepreg sample ( $F_t$ ); the onset of sample buckling corresponds to the large deformation point (between 20 to 25 mm). The load required to extend the bias extension setup without the prepreg sample ( $F_d$ ) is shown by the blue dashed line in **Figure 3**. Note that, in this case, no buckling is observed at the large deformation point. The load needed to extend the prepreg sample ( $F_s$ ) was calculated according to equation (1); the results are illustrated by the black diamonds in **Figure 3**. The magnitude of the load response gives a good indication of the actual load needed to elongate the prepreg samples. However, slight differences in the magnitude of the load needed to extend the prepreg sample were found among all test trials. This difference is attributed to a loss of compaction in the prepreg sample during testing.



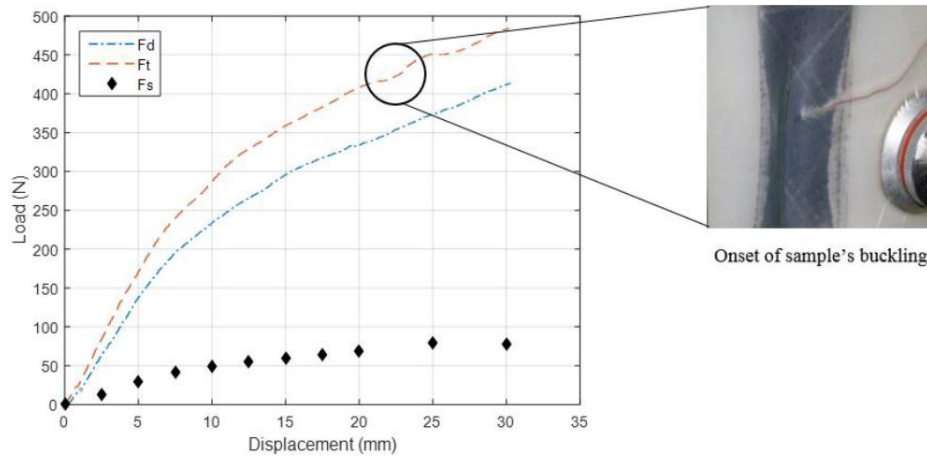


**Figure 3.** Load-displacement response to the bias extension test under 100 kPa compaction at 50 °C.  $F_s$  indicates the load needed to extend the prepreg sample;  $F_t$  is the total measured load of the bias extension setup with the prepreg sample;  $F_d$  is the load required to extend the bias extension setup without the prepreg sample.

### 3.1. Change in shear angle

The change in shear angle can be measured by analyzing the series of test images taken by the digital cameras during the study with AutoCAD. A comparison of the measured angle found during the compaction test and the angle found during the direct bias extension test is shown in **Figures 4** and **5**. The results show that the shear angles decreased significantly in the bias extension test with compaction. Therefore, it appears that the compaction parameter applied during double-diaphragm forming successfully restricted the in-plane shear deformation. Note, however, that the laminate must be in a flat and tense state at the onset of the procedure to avoid any compression that may lead to wrinkling during the forming step. Controlling this factor during the initial forming step is therefore essential in order to avoid a compressive state and to reach a higher degree of deformability. A detailed comparison between the direct bias extension test and the bias extension test under 100 kPa compaction for both temperatures is summarized in **Table 2**. It can be seen that the load needed to extend the prepreg sample in the direct bias test was very low compared with the load needed in the compaction test. On the other hand, the shear angles measured during the compaction test were significantly smaller than those measured during the direct bias test.

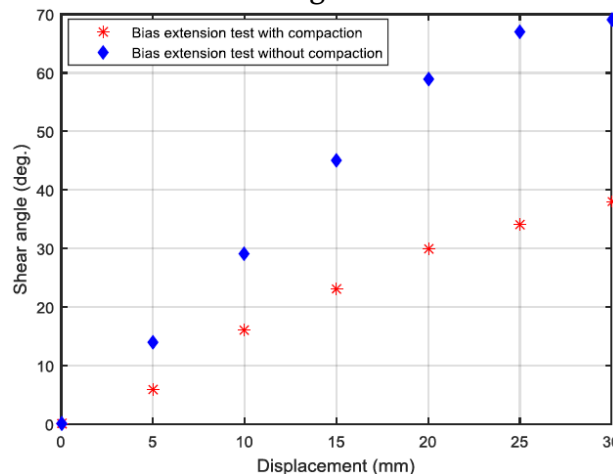


**Figure 4.** Comparison between measured shear angle using direct bias extension test and measured shear angle using bias extension test with 100 kPa compaction, both at 50 °C.

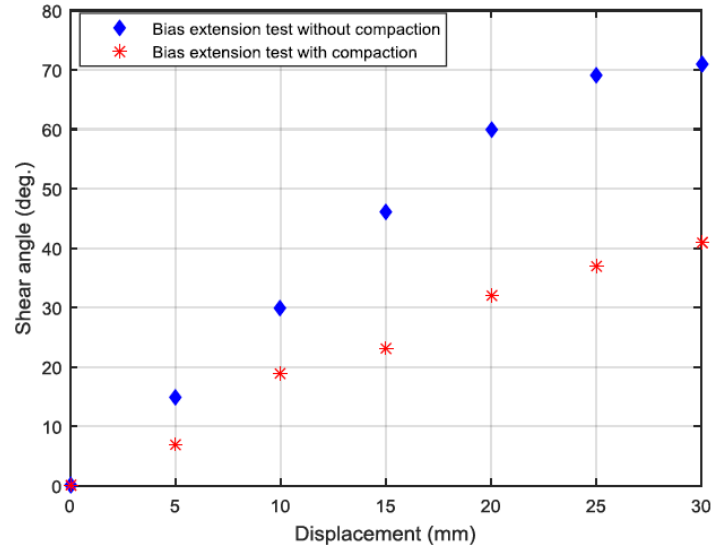


**Figure 5.** Comparison between measured shear angle using direct bias extension test and measured shear angle using bias extension test with 100 kPa compaction, both at 90 °C.

**Table 2.** Comparison between direct bias test and bias under 100 kPa compaction.

Displacement (mm)	50 °C				90 °C			
	Direct bias test		Bias test under 100 kPa		Direct bias test		Bias test under 100 kPa	
	Load (N)	Shear angle (deg.)	Load Fs (N)	Shear angle (deg.)	Load (N)	Shear angle (deg.)	Load Fs (N)	Shear angle (deg.)
5	1.462718	14	29.32702	6	0.389929	14	21.355	7
10	1.716431	29	49.05017	16	0.902454	31	45.5031	19
15	4.068002	45	60.1025	23	1.862866	46	52.9534	23
20	13.42035	59	68.148	30	3.698215	62	59.3367	32
25	35.78173	67	80.2394	34	8.361	69	69.5943	37
30	66.72067	69	78.9854	38	9.36147	70	72.8692	41

### 3.2. Influence of compaction level

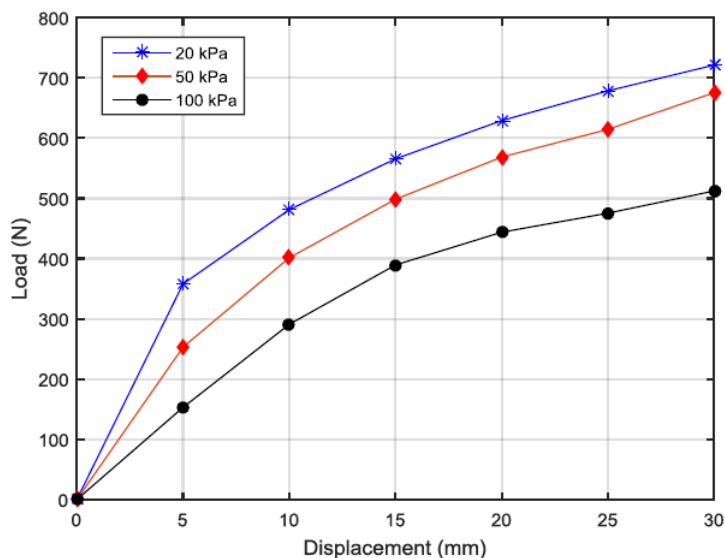


**Figure 6.** The effect of compaction level on the load response.

The goal of the compaction procedure carried out during the bias extension test in this study was to simulate the vacuum applied between double diaphragms during the forming process. The effect of this vacuum parameter was investigated at three compaction levels: 20, 50 and 100 kPa, as shown in **Figure 6**. An unexpected correlation was observed between compaction level and load response: as the level of vacuum compaction increased, the load decreased at each selected displacement. For instance, the load measured at 15 mm displacement and 50 kPa was around 498 N, while a load of 573 N was measured at the same displacement with 20 kPa. However, further investigation is necessary to confirm this phenomenon and arrive at reproducible data.

### 4. Conclusion

A new bias extension test was evaluated under vacuum compaction at different temperatures and compaction levels. The results show that shear angle decreases significantly as vacuum pressure, and therefore compaction, is applied between two diaphragms. This finding indicates that compaction force has a significant influence on the deformation limit and wrinkling onset during the diaphragm forming process; thus, compaction should be taken into appropriate consideration in future simulations. It was found that the load required to extend a prepreg sample during a direct bias test is very low compare to the load required during the bias test under compaction. On the other hand, the shear angles produced during the bias test under compaction were significantly smaller. In addition, load response was found to increase as vacuum compaction level decreased. However, further investigation is necessary to confirm this phenomenon and arrive at reproducible data.

### Acknowledgements

The authors of this paper would like to acknowledge the financial support of NSERC (Natural Sciences and Engineering Research Council of Canada). Thanks to Bombardier Aerospace for supplying the materials. Supporting provided by Najran University is also gratefully acknowledged.

### References

1. X. Yu, L. Zhang, Y.-W. Mai. Modelling and finite element treatment of intra-ply shearing of woven fabric. *J. Mater. Proc. Technol.*, 2006,138, 2003, 47-52.
2. X. Yu, L. Ye, Y.-W. Mai, B. Cartwright, D. Mc Guckin, R. Paton. Finite element simulations of the double-diaphragm forming process. *Revue Européenne des Éléments Finis*, 2005, 14, 6-7, 633-651.
3. P. J. Mallon, C. M. O'Brádaigh, R. B. Pipes. Polymeric diaphragm forming of complex-curvature thermoplastic composite parts. *Composites*, 1989, 20, 1, 48-56.
4. C. O'Brádaigh, P. Mallon. Effect of forming temperature on the properties of polymeric diaphragm formed thermoplastic composites. *Composites Sci. & Technol.*, 1989, 35, 1987, 235-255.
5. A. C. Long. *Composites Forming Technologies*. 2007, CRC Press.
6. N. Hamila, Ph. Boisse. Simulations of textile composite reinforcement draping using a new semi-discrete three node finite element. *Composites B*, 2008, 39, 6, 999-1010.
7. S. V. Lomov, Ph. Boisse, E. Deluycker, F. Morestin, K. Vanclooster, D. Vandepitte I. Verpoest, A. Willems. Full-field strain measurements in textile deformability studies. *Composites A*, 2008, 39, 8, 1232-1244.
8. G. Lebrun, M. N. Bureau, J. Denault. Evaluation of bias-extension and picture-frame test methods for the measurement of intraply shear properties of PP / glass commingled fabrics. *Composite Struct.*, 2003, 61, 4, 341-352.
9. M. Phung. *Deformation Mechanisms of Composite Prepregs During Forming (PhD.Thesis)*. 2004, RMIT University.

## DEVELOPMENT OF THERMOPLASTIC STARCH NANOCOMPOSITES FOR WET CONDITIONS

M. Oishi<sup>1,2</sup>, Ch. Dal Castel<sup>1</sup>, R. Park<sup>1</sup>, B. Wolff<sup>1,3</sup>, L. Simon<sup>1</sup>

<sup>1</sup> University of Waterloo  
Department of Chemical Engineering  
Waterloo, Canada

lsimon@uwaterloo.ca

<sup>2</sup> Nippon Paper Industries  
Tokyo, Japan

masatoshi-oishi@nipponpapergroup.com

<sup>3</sup> Polymer Specialties International  
Newmarket, Canada

bryon.wolff@psi-cda.com

Accepted October 19, 2015

### Abstract

The need for environmentally friendly materials for applications in packaging has never been greater. One of the challenges in packaging applications is to have a material that has the right balance of properties and cost. A new type of thermoplastic starch copolymer has been investigated for its physical properties; this thermoplastic starch copolymer was prepared by reacting starch and polyesters. This paper will discuss the investigation on the use of cassava starch and clay to further improve the formulation of thermoplastic starch copolymer. The objective of adding cassava starch is to reduce cost, whereas the objective of adding clay is to further improve the properties under wet conditions. The materials were processed using a lab-scale twin screw extruder and injection molding. Addition of Na-montmorillonite improved water resistant and mechanical properties.

### 1. Introduction

Starch is a widely available, low cost, and naturally renewable. In addition, starch is generated from carbon dioxide and water by photosynthesis in plant, and it is a biodegradable agro-polymer. For these reasons starch is expected as a promising alternative to petrochemical resources for packaging applications.

Starch based polymers can provide biodegradable and sustainable solutions for the products such as single use disposable packaging, consumer goods and other plastics. The general procedure to process starch based polymers involves the granular disruption by the combination of temperature, shear, and a plasticizer, which is usually water and / or glycerol. The resultant material is known as thermoplastic starch (TPS). In recent years, there are many

research related to starch-based plastics because it is compostable and in order to reduce the amount of petroleum-derived plastics in solid waste streams. However, the use of TPS is limited in industrial applications, owing to its low mechanical property and humidity.

A new type of thermoplastic starch copolymer has been developed by Polymer Specialties International Ltd., Canada. This thermoplastic starch copolymer was prepared by reactive extrusion with the addition starch, polyester (and other chemicals) in order to obtain a thermoplastic starch copolymer (WO 2013/116945 – Process for making starch-resin copolymer, Polymer Specialties International).

Preliminary work in our laboratory with this material showed some promising results with respect with resistance to water. Under wet conditions this new thermoplastics starch copolymer exhibits far better mechanical properties than regular thermoplastic starch.

In this study, we tried to further improve the formulation of thermoplastic starch copolymer (TPSC) using cassava starch and nanoclays. The objective of adding cassava starch is to reduce cost, whereas the objective of adding nanoclays is to further improve the properties such as tensile, flexural and other dynamic mechanical properties under wet conditions.

## 2. Material and method

### 2.1. Materials

Thermoplastic starch copolymer was supplied by Polymer Specialties International Ltd. (Canada), unmodified cassava starch was supplied by Bahiamido (Brazil), and glycerol (98 %) was purchased from Sigma Aldrich (USA). Two types of nanoclays were used in this study, one based on unmodified Na-montmorillonite clay (Na-MMT (Cloisite Na<sup>+</sup>)) and organically modified montmorillonite (Cloisite 30B), both were purchased from Southern Clay (USA).

### 2.2. Preparation of TPSC nanocomposites

The TPSC nanocomposites were prepared in aqueous media. TPSC, cassava starch, and nanoclays were dried in a convection oven at 50 °C for 1 week prior to use. The procedure consisted of two steps. The first step was the preparation of starch nanocomposites and second was the preparation of TPSC nanocomposites.

#### *Preparation of starch nanocomposites*

For the preparation of starch nanocomposites, the 5 wt. % nanoclay and glycerol were dispersed in distilled water by sonication for overnight at room temperature. A separate mixture of 10 wt. % of cassava starch was prepared in distilled water; the suspension was heated to 80 °C with continuous stirring for 20 min to achieve gelatinization of starch. The dispersion with nanoclay and glycerol was added to the starch mixture and heated to 80 °C under continued stirring. The resulting products were left for drying overnight 50 °C in convection oven followed by drying in a vacuum oven at 50 °C for 24 h.

#### *Preparation of TPSC nanocomposites*

The TPSC nanocomposite was prepared by mixing TPSC and starch nanocomposites using a laboratory scale twin-screw extruder. Both materials were dried at 50 °C for 24 h to

minimize moisture in the extrusion process. The components were introduced in the feeding zone and allowed to melt at 150 °C and mixing speed was set at 75 rpm. Mechanical test samples were prepared by injection molding. Barrel temperature was 150 °C and the pressure was 100 psi. Two different specimen geometries (rectangular bar and dumbbell) were prepared. After injection molding, the specimens were kept in an oven 115 °C for 11 min. Then, the bars were conditioned at 23 °C at 50 % relative humidity for flexural, tensile and impact tests.

### 2.3. Characterizations

#### *Mechanical properties*

The mechanical properties for TPSC nanocomposites were determined from the tensile and flexural stress-strain curves following ASTM methods D1708 and D790. The average slope of the elastic region of each tensile and flexural curve was determined as the modulus of the material. The average maximum stress achieved in the tensile and flexural tests was also calculated as the yield strength of the materials. The standard deviation was calculated using the test result of 5 specimen bars. The dynamical mechanical thermal analysis were carried out with a DMTA-V (Rheometric Scientific) using a single cantilever test. The dynamic storage modulus ( $E'$ ) was measured as a function of temperature from 30 to 110 °C, at a constant heating rate of 3 °C / min and displacement amplitude of 0.1 %, at a frequency of 1 Hz. Samples were conditioned at different relative humidity levels (50 and 100 %) at 23 °C for different time (from 0 to 24 h).

#### *Morphology*

The surface morphology of the TPSC nanocomposites was investigated with scanning electron microscopy (SEM) analysis using a LEO1550 (Zeiss). The specimens were sputter-coated with gold prior to the experiment to avoid any charging during scanning (15 mA, 120 s). The size of features in the image (diameter) was measured using the Image J software.

#### *Water absorption studies*

For water absorption characterization studies, the samples were dried in a vacuum oven until constant weight was obtained and then placed in desiccators to cool before water absorption testing by gravimetric methods and this weight was taken as initial weight ( $W_i$ ). The samples were then soaked in deionized water for different periods (0 to 30 days), after which they were blotted-dry with a lint free cloth. The increase in weight was taken as final weight ( $W_f$ ). Water absorption is expressed as the increase in weight percent. The percentage of water absorption was calculated by the equation (1). In addition, the diffusion of water for period between 1 and 24 h was calculated. It is of great significance for composites because it tells how much of a liquid diffuses into a composite, how rapidly and to what extent. From the curves of water absorption as a function of time the water diffusion coefficients were calculated for each specimen. Among several authors, Fick's second law is generally considered the starting point of the mathematical description of diffusion, although it may not be obeyed by polymers or polymer composites. The Boltzmann's form of Fick's general diffusion equation used in this work.

$$\text{Water absorption (\%)} = ((W_f - W_i) / W_i) \times 100. \quad (1)$$



### 3. Results and discussion

#### 3.1. Mechanical properties

The results of flexural and tensile experiments are presented in **Table 1**. The flexural and tensile strength of TPSC decreased after addition of cassava starch without nanoclays. However, these strengths were significantly raised due to the addition of cassava starch with nanoclays. Especially by incorporation of Na-MMT, the flexural and tensile strength was significantly increased. These results suggested that the presence of an unmodified clay affected mechanical properties of TPSC matrix more significantly than the organically modified clay. The increase in properties is related to the reinforcement effect of nanoclays in the polymer matrix and it is supported by morphological analysis results. It is likely that the high interfacial surface area provided by well dispersed nanoparticles enhanced the load transfer between the polymer matrix and nanoparticles, resulting in improvement of compression-mechanical properties of composite samples. Other authors observed similar effect in other polymers.

**Table 1.** Mechanical properties of TPSC and TPSC-nanocomposites.

	Starch composite (wt. %)					Mechanical properties				
	TPSC	Cassava starch	Glycerol	Cloisite 30 B	Na – MMT	Flexural strength (MPa)	Flexural modulus (MPa)	Tensile strength (MPa)	Tensile modulus (MPa)	Elongation at bleak (%)
No.1	100	0	0	0	0	9.0	204.8	6.79	116.5	9.56
No.2	70	24.0	6	0	0	6.8	384.4	5.02	139.1	4.34
No.3	70	22.5	6	1.5	0	7.0	396.8	5.46	163.0	3.50
No.4	70	21.0	6	3.0	0	7.3	380.2	5.91	151.7	4.99
No.5	70	22.5	6	0	1.5	7.9	405.9	5.23	153.8	4.33
No.6	70	21.0	6	0	3.0	8.4	483.6	6.38	161.1	4.82

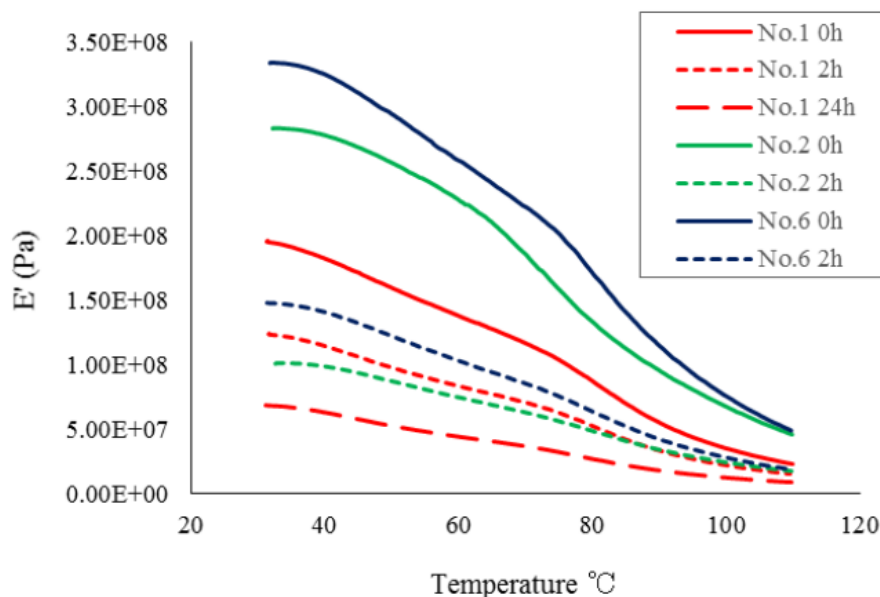


**Figure 1.** DMTA of TPSC and TPSC-nanocomposites.

The DMTA analysis was carried out to follow the temperature dependence of storage modulus ( $E'$ ) of the TPSC nanocomposites. Results are shown in **Figure 1** for samples 1, 2 and 6 for three different situations: without contact to water (labelled as 0h), immersed in water for 2 hours (labelled as 2h) and immersed in water for 24 h (labelled as 24h). It was observed that in the entire range of temperature (30 to 110 °C), the addition of starch composites to the blend system extensively increased the storage modulus. For samples without contact to water (0h), the storage modulus of Na-MMT composite was higher than that of other samples. This is likely due to a better dispersion of the clay and to greater reinforcing effect of the stiffer clay silicate layers in the TPSC nanocomposites. In addition, these samples were treated in water for 2 and 24 h. After 2 h of contact to water, the storage modulus of samples which contained starch decreased. The addition of Na-MMT resulted higher modulus than other samples for the same conditions (2 h water treatment). The modulus of samples with starch was not measured after 24 h of water contact because samples were brittle.

### 3.2. Morphology

The SEM images from the fractured surfaces of the thermoplastic starch copolymer (TPSC) and TPSC nanocomposites with 3 wt. % of Na-MMT are shown in **Figure 2**. The images were taken with a magnification of 2000 times at the microscope to show an overview of the fractured surfaces. From **Figure 2b** it can be seen that the dispersion of starch granules with the size about 10  $\mu\text{m}$ . There were some broken starch granules which have the size less than 10  $\mu\text{m}$  as well. However, the location of the nanoclay was not confirmed in the TPSC nanocomposites by the SEM images.

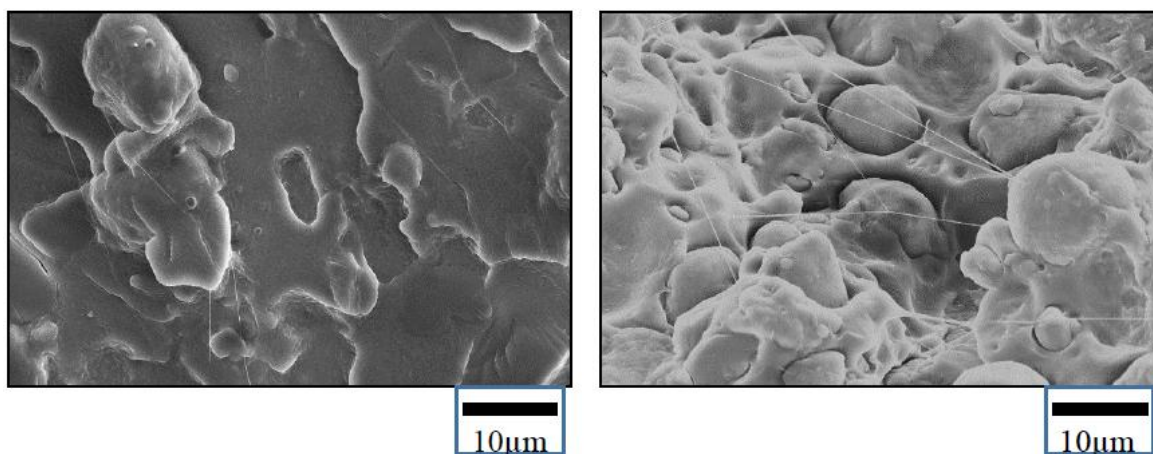


**Figure 2.** SEM images of TPSC (2a, left) and TPSC with 3 wt. % of Na-MMT (2b, right).

### 3.3 Water absorption studies

From **Table 2**, it can be seen that TPSC with starch composites showed a drastic increase in the water absorption with a value of 30.4 % for 24 h and diffusivity was higher than other samples. In addition, these samples were broken and degraded within 24 h. On the other hands, the blends with nanoclay decreased water absorption and diffusivity when compared to starch without nanoclay. Some cracks were observed in the TPSC nanocomposites, although samples were not broken completely.

**Table 2.** Water absorption and diffusivity of TPSC and TPSC-nanocomposites.

	Water absorption (%)									Diffusivity ( $\text{mm}^2 \text{s}^{-1}$ $\times 10^8$ )
	0h	2h	6h	8h	24h	48h	96h	144h	168h	
<b>No.1</b>	0.0	1.7	3.4	4.0	7.3	9.6	11.2	10.4	10.4	0.45
<b>No.2</b>	0.0	6.5	15.0	18.5	30.4	–	–	–	–	6.27
<b>No.6</b>	0.0	4.3	8.6	9.7	18.9	21.4	19.7	19.4	20.1	2.65

#### 4. Conclusions

New TPSC nanocomposites with nanoclay were prepared via a simple method. Mechanical properties and water resistance of the TPSC nanocomposites were measured. Addition of nanoclay improved mechanical properties and decreased water absorption. Because of its renewability, biodegradability and low cost, starch based materials became one of feasible agro-based sources that can replace petroleum based materials in packaging applications. They are in tune with the concept of sustainable development.

#### Acknowledgements

The authors would like to thank the University of Waterloo for technical supports about characterization, and Nippon paper industry for financial support.

## PRODUCTION OF ULTRAFINE-GRAINED TITANIUM BY INDUSTRIAL CALIBER ROLLING

G. Krállics<sup>1</sup>, J. Gubicza<sup>2</sup>, Z. Bezi<sup>3</sup>

<sup>1</sup>Budapest University of Technology & Economics  
Department of Materials Science and Engineering  
Budapest, Hungary  
krallics@eik.bme.hu

<sup>2</sup>Eötvös Loránd University  
Department of Materials Physics  
Budapest, Hungary

<sup>3</sup>Bay Zoltán Nonprofit Ltd. for Applied Research  
Engineering Division  
Budapest, Hungary

Accepted October 19, 2015

### Abstract

The possibility of mass production of ultrafine-grained (UFG) titanium by industrial caliber rolling was examined. As complementary investigations, laboratory caliber rolling tests were also performed. The mechanical and metallurgical characteristics of the rolled materials were studied. The process led to an UFG microstructure with high dislocation density, accompanied by high tensile strength and good ductility. Mathematical modeling indicated that the refinement of the grains was caused by the large shear strains and the non-monotonicity of deformation, i.e. caliber rolling can be regarded as a severe plastic deformation procedure. In addition, the characteristics of the samples processed by industrial caliber rolling were compared to those produced under laboratory conditions. The microstructure and the mechanical properties of the materials processed by the two ways were similar, indicating that industrial caliber rolling is capable of mass production of UFG titanium.

### 1. Introduction

In the past decades, several severe plastic deformation (SPD) procedures were developed for processing bulk metallic materials with ultrafine-grained (UFG) microstructure. Accumulative roll bonding (ARB) [1, 2], equal channel angular pressing (ECAP) [3, 4], high pressure torsion (HPT), [5] and repetitive corrugation and straightening [6] are some examples for these processes. SPD procedures usually produce UFG materials under laboratory conditions, i.e. their productivity is low. Significant breakthrough in the application of UFG materials (i.e. their commercialization) can only be achieved if they were manufactured in an industrial environment.

The common characteristic of the SPD techniques is the large shear strain and the non-monotonic nature of the deformation. The concept of monotonic deformation was introduced

by [7]. As he wrote, a forming process develops monotonically if no component of the rate of strain tensor changes its sign, i.e. the eigenvectors of the rate of strain tensor are parallel to the eigenvectors of the strain tensor during the whole deformation process and the Lode parameter remains constant. Studying the possible ways of deviation from the monotonic deformation contributes to develop processes which assure the production of fine grains. Although, caliber rolling is not an usual SPD method, its industrial application for producing UFG titanium is promising due to its productivity and non-monotonic nature.

According to former experience, titanium is an ideal material for devices to be implanted into the human body. It is chemically inert, does not react with human body fluids, and, if it is necessary, after proper surface treatment the bone is able to adhere to titanium implants. However, if the adherence of the implant to the bone is contraindicated, it can be impeded by tailoring the titanium surface morphology. This dual feature makes this metal well and widely applicable for different medical purposes.

Besides the listed favourable biological properties, titanium makes possible the application of up-to-date diagnostic procedures (e.g. Magnetic Resonance Imaging (MRI) and Computer Tomography (CT)) on persons having titanium implants, because it does not show magnetic properties in strong magnetic fields and does not interfere with X-ray radiation. These statements apply for titanium alloys, as well.

From the physiological viewpoint, pure titanium is better than its alloys since the alloying elements may yield toxic reactions in the human body. At the same time, the strength of pure titanium is much lower than that of its alloyed counterparts. In pure metals the strength can be improved by grain refinement with the application of SPD procedures, resulting in high strength semi-products for the fabrication of implants and prostheses. The usage of pure titanium significantly decreases the risk of irritations caused by the alloying elements, therefore the implant might stay in the body if the risk of removal is too high. While medical application of titanium alloys is widespread universally, examples for the application of commercial purity (CP) titanium are rare. Further, there is no solution yet for the industrial mass production of bulk UFG titanium. The present paper studies the microstructure and the mechanical properties of CP-Ti processed by caliber rolling in both laboratory and industrial environments. The degree of non-monotonicity for these procedures is also investigated. It is found that caliber rolling may be a candidate for mass production of UFG CP-Ti for medical applications.

## 2. Experiments and process modeling

### 2.1. Rolling experiments in laboratory and industry

Grade 2 titanium specimens with 200 mm in length and 30 mm in diameter in an annealed condition (annealing at 650 °C for 2 h then cooling in air) were used for the laboratory rolling tests. The initial mechanical properties were as follows: *yield strength*,  $YS = 332$  MPa, ultimate tensile strength,  $UTS = 439$  MPa, reduction in area,  $Z = 58$  %, elongation to failure,  $A = 22$  %, strain energy density to fracture,  $W_f = 412$  J / cm<sup>3</sup>.

The laboratory caliber rolling was carried out on samples pre-heated to 450 °C. A twin-motor rolling mill with the power of  $2 \times 7.5$  kW was used in the experiments. The diameter of the roll was 180 mm. The roll stand can be used in both symmetrical and asymmetrical modes (see **Figure 1**). The first mode enables both flat and caliber rolling processes. The caliber rolls

used in the present study are shown in **Figure 2**. Four reductions were performed in the first part of the process. The roll speed was 6 rpm. After the first part of the rolling procedure the specimen was reheated to 450 °C. The second part of the rolling process was performed in six passes using the same heating procedure between subsequent passes as applied in the first part of the process. In the first and second parts of the procedure different roll pairs were used, as shown in **Figure 2**. After the last pass in the second part a final diameter of 8 mm was achieved.

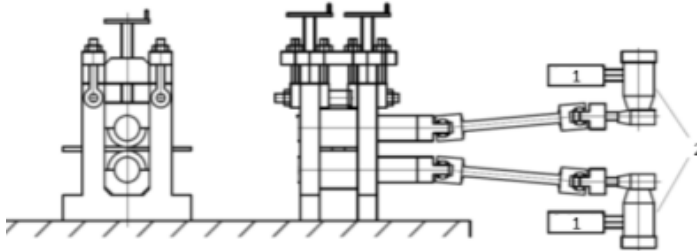


**Figure 1.** The sketch of the experimental roll stand for caliber rolling. 1 – speed control, 2 – twin motor drive.



**Figure 2.** The pairs of rolls.

Industrial warm caliber rolling of titanium was performed using the rolling mill system of OAM Ózd Steelworks Ltd. (Ózd, Hungary). The shape and the size of the roll cavities for the twelve passes are shown in **Figure 3** and **Table 1**. At the beginning of the process the material was heated to the rolling temperature of ~ 300 °C in an induction furnace. This temperature was lower than that applied for laboratory rolling, since the heat production rate during industrial rolling was larger due to the higher rolling speed. During the rolling process the “elongation section” was executed in the first six mill stands. The speed of the first pair of rolls was 8 rpm. The finish rolling was performed in the next six stands. The diameter of the rolls was 415 mm. The oval piece was rotated by 90 ° at each stand in order to arrive in the next mill position. The bars with 1000 mm in length were continuously moved through the six mill stands. The temperature was measured by contact thermometers. The cross section of the bar was reduced from 70 to 34 mm during the elongation section of rolling. The process parameters are listed in **Table 2**. The rolled bars were cut to smaller pieces with 2000 mm in length. They were heated to ~ 300 °C before the finish rolling. In this final step of processing the diameter of the bars was reduced from 34 to 20 mm. The process parameters for finish rolling are listed in **Table 3**. The speed of the first pair of rolls in the finish rolling process was 40 rpm which is larger than in the case of the elongation section of rolling.

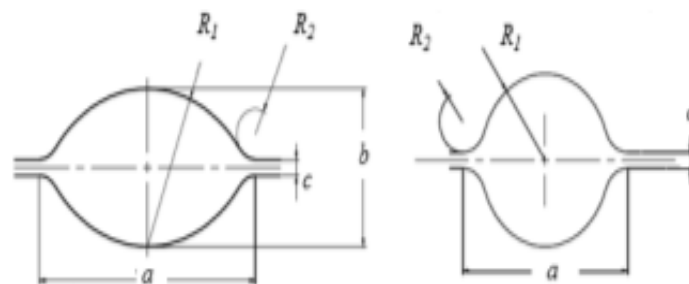


**Figure 3.** The shape and the size of the roll cavities (left side odd, right side even ones).



## Production of ultrafine-grained titanium by industrial caliber rolling.

**Table 1.** The size of the roll cavities for the twelve passes applied in industrial caliber rolling.

Cavity No	<i>a</i> mm	<i>b</i> mm	<i>c</i> mm	<i>R</i> <sub>1</sub> mm	<i>R</i> <sub>2</sub> mm	Cavity No	<i>a</i> mm	<i>c</i> mm	<i>R</i> <sub>1</sub> mm	<i>R</i> <sub>2</sub> mm
1	91.73	50	5	50	8	2	71.77	5	29	10
3	74.13	48	5	40	8	4	57.63	5	22,5	7
5	60.79	32	4	32	8	6	43.48	3	17	6
7	49.18	25	3	27	6	8	37.08	3	14	6
9	40.18	20	3	22	6	10	31.62	3	11,5	6
11	32.98	18	2	16	5	12	31.44	2	10	5

**Table 2.** Parameters of elongation rolling ( $\varnothing 70 \rightarrow \varnothing 34$  mm).

Pass No.	Stretching factor	Maximum roll force [kN]	Maximum roll torque [Nm]	Temperature [°C]
1	1.26	1100	36000	420
2	1.24	920	28000	435
3	1.26	950	27000	446
4	1.23	845	21000	452
5	1.28	810	19000	440
6	1.23	600	14500	460

**Table 3.** Parameters of finish rolling ( $\varnothing 34 \rightarrow \varnothing 20$  mm).

Pass No.	Stretching factor	Maximum roll force [kN]	Maximum roll torque [Nm]	Temperature [°C]
7	1.2	700	15500	485
8	1.26	510	10500	495
9	1.22	550	8500	523
10	1.22	425	6000	460
11	1.14	380	3500	480
12	1.15	260	3200	515

The industrial manufacturing process resulted in four products. The first two ones were obtained by caliber rolling. The third and fourth product was obtained by the combination of caliber and flat rolling processes.

**Table 4.** The rolled industrial products.

Products	Elongation rolling	Finish rolling	Cold rolling
1	$\varnothing 70 \Rightarrow \varnothing 34$ mm / 6 passes	$\varnothing 34 \Rightarrow \varnothing 20$ mm / 6 passes	
2	$\varnothing 70 \Rightarrow \varnothing 34$ mm / 6 passes	$\varnothing 34 \Rightarrow \varnothing 20$ mm // 6 passes	$\varnothing 20 \Rightarrow \varnothing 18$ mm / 2 passes
3	$\varnothing 70 \Rightarrow \varnothing 34$ mm / 6 passes	$\varnothing 34 \Rightarrow \square 14 \times 45$ mm / 2 passes	
4	$\varnothing 70 \Rightarrow \varnothing 34$ mm / 6 passes	$\varnothing 34 \Rightarrow \square 14 \times 45$ mm / 2 passes	$\square 14 \times 45 \Rightarrow \square 7 \times 51$ mm / 1 pass

In order to improve the quality of the surface and the dimensional accuracy in addition to increasing the strength of the rods further cold rolling was performed. In this process the

diameter was reduced by about 2 mm with a scattering of about 1 mm. The flat bars were further reduced to 7 mm thickness. Their width increased to 51 mm. The processing history of the four industrially manufactured samples is listed in **Table 4**.

It should be noted that the shape and size of cavities in the laboratory rolling procedure were designed in order to obtain similar deformation and thermal conditions as in the industrial environment. For instance, the average equivalent strains calculated for the whole volume of the material after the laboratory and the industrial caliber rolling procedures were 2.64 and 2.50, respectively.

### 2.2. Modelling the strain path of the rolling process

Finite element modelling (FEM) was employed to analyse the caliber rolling process theoretically. The details of FEM procedure can be found in [8]. In the present work the objective of the modelling was to demonstrate the cyclic nature of the process, indicating that it is non-monotonic, resulting in fine grains. The permanent deformation of the samples is demonstrated by the strain trajectory approach as initiated by [9], representing the deviatoric strain tensor ( $e$ ) in a five-dimensional vector space as:

$$e_1 = \sqrt{\frac{3}{2}} \ln V'_{11}, \quad e_2 = \sqrt{2} \left( \ln V'_{22} + \frac{1}{2} \ln V'_{11} \right), \quad (1)$$

$$e_3 = \sqrt{2} \ln V'_{12}, \quad e_4 = \sqrt{2} \ln V'_{23}, \quad e_5 = \sqrt{2} \ln V'_{31}$$

where  $\ln \mathbf{V}'$  is the logarithmic deviatoric strain tensor. Some examples for the strain trajectories are shown in **Figure 4**.

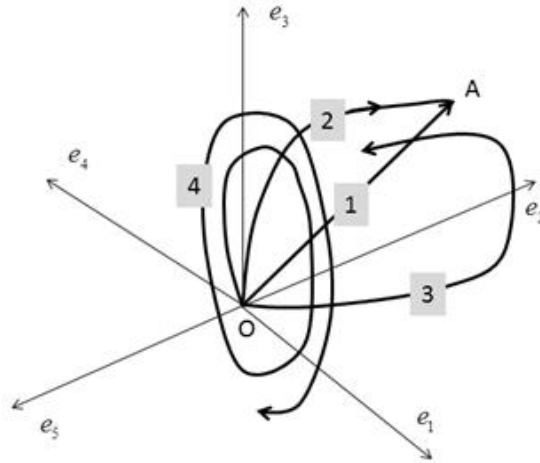


**Figure 4.** Examples for the strain trajectories in the five dimensional vector space.

In **Figure 4** trajectory #1 is monotonic, #2 is nearly monotonic, # 3 is simple non-monotonic and #4 is cyclic non-monotonic. In order to appreciate the measure of the non-monotonicity of deformation, consider the nearly monotonic trajectory #2 [10]. During deformation the end-point of the strain vector travels along the curved OA trajectory. The ideally monotonic deformation corresponds to the straight line OA. Therefore, at the deformation time,  $t$ , the measure of non-monotonicity is given as:

$$NM(t) = \frac{\bar{\varepsilon}(t)}{\bar{\varphi}(t)} \geq 1, \quad (2)$$

where  $\bar{\varepsilon}$  is the total equivalent strain, which is equivalent to the length of the trajectory,  $\bar{\varphi}$  is the equivalent logarithmic strain, which equals the length of the straight trajectory OA. In the

case of non-monotonic deformation the complete trajectory is separated into  $n$  nearly monotonic portions.. For each part the  $(NM)_i$  is determined as the ratio of the length of the local trajectory part and the straight segment connecting its end points. In this case the measure of non-monotonicity of the whole deformation is given as:

$$NM = \sum_{i=1}^n (NM)_i. \quad (3)$$

The larger the value of  $NM$ , the higher the degree of non-monotonicity of deformation. It should be noted that although all  $(NM)_i$  values are larger than one,  $NM$  may decrease with increasing strain as the end points of the segments may vary during the development of the deformation trajectory.

### 2.3. Material testing

The mechanical properties of the rolled materials were investigated by tensile test using an Instron universal mechanical testing machine (type 8809) at room temperature and the cross-head velocity of 6 mm / min. The tests were carried out on cylindrical specimens with the length and diameter of 25 and 5 mm, respectively, machined out of the rolled bars. For both laboratory and industrial rolling 3 – 3 samples were tested under the same conditions.

The grain structure in the initial and the rolled specimens was examined by a Tecnai G2 X-TWIN transmission electron microscope (TEM). The TEM foils were prepared from both the cross- and longitudinal sections of the rods which were thinned by mechanical grinding to a thickness of 20 – 40  $\mu\text{m}$ . The foils were further thinned by Ar-ion milling using a Gatan Model 691 precision ion polishing system. The microstructures of the initial and the rolled samples were also examined by X-ray line profile analysis. Before measurements the surface was mechanically polished to a mirror finish with diamond paste. The surface layer, distorted during polishing, was removed by chemical etching using hydrogen fluoride. The measurements of the X-ray diffraction lines were performed on the longitudinal sections using a special high-resolution diffractometer with  $\text{Co K}\alpha_1$  radiation (wavelength:  $\lambda = 0.1789 \text{ nm}$ ). The scattered intensity was detected by imaging plates. The line profiles were evaluated using the Convolutional Multiple Whole Profile (CMWP) fitting procedure. In this method, the diffraction pattern is fitted by the sum of a background spline and the convolution of the instrumental pattern and the theoretical line profiles related to the crystallite size, dislocations and twin faults. The details of the procedure are available elsewhere [11].

### 3. Results and discussion

The results of the mechanical tests carried out on the industrially rolled materials are shown in **Figure 5**. Similar data for the materials rolled in laboratory have been published in [8]. Caliber rolling performed in laboratory [8] resulted in a slightly higher strength and a similar ductility compared to the process carried out under industrial conditions.

The reason for the slightly better mechanical performance of the material rolled in the laboratory can be attributed to a more rigorous control of the thermo-mechanical conditions (e.g. the temperature of the sample) during the manufacturing process.

Caliber rolling both in laboratory and industrial environments yielded about two times larger strength than that for the initial annealed state. The parameters characterizing the

ductility do not show uniform tendencies. The elongation to failure slightly decreased due to rolling while the reduction of area remained unchanged within experimental error. At the same time, the strain energy density to fracture increased to more than twice the value characteristic of the initial state. This can be attributed to much larger flow stress values for the rolled specimens. The various industrially manufactured samples show slightly different mechanical performances (see **Figure 5**) which can be attributed to the deviations in the processing conditions.

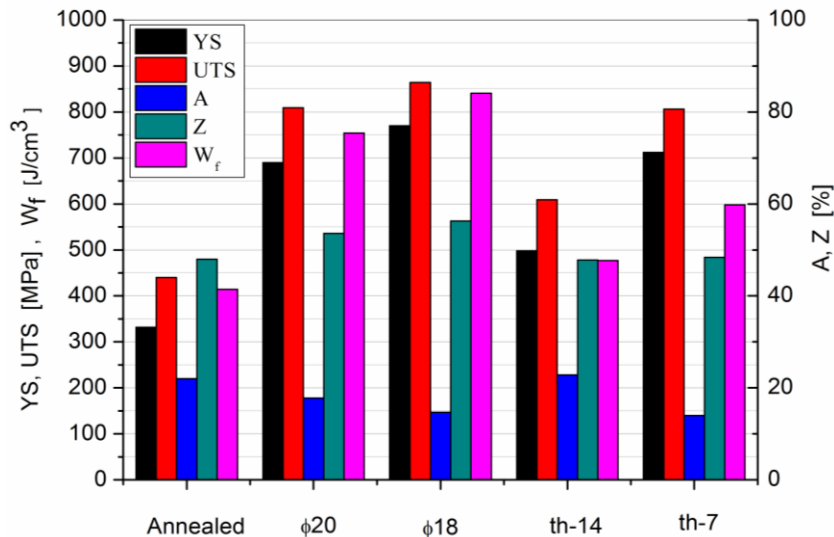


**Figure 5.** Mechanical properties of industrially rolled titanium samples. YS: yield strength, UTS: ultimate tensile strength, A: elongation to failure, Z: reduction in area,  $W_f$ : strain energy density to fracture. The experimental error of the values is about 8 %.  $\phi 20$ : sample from product 1,  $\phi 18$ : sample from product 2, th-14: sample from product 3, th-7: sample from product 4 (see **Table 4**).

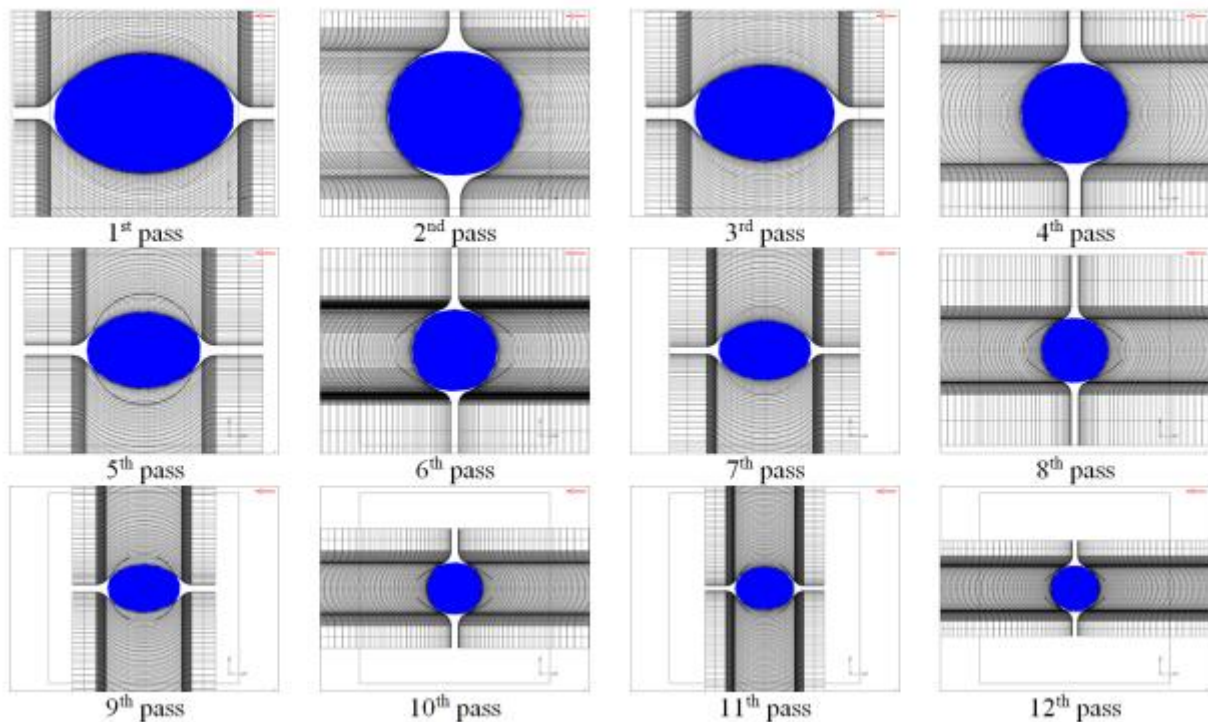


**Figure 6.** Roll cavity filling during industrial caliber rolling as shown by FEM analysis.



The progress of the industrial caliber rolling process obtained by FEM analysis is illustrated in **Figure 6**, where roll cavity filling is shown for different rolling passes. **Figure 7** shows the total plastic strain and the parameter of non-monotonicity at five different points in the sample. The locations of these points on the cross-section of the initial rod are shown at the upper left corner in **Figure 7**. Both the strain and the parameter of non-monotonicity change mainly when the rods travel through the roll cavities. The total strain increases with increasing the duration of caliber rolling in all points and it reaches a value of about 3.5 – 5.1 at the end of deformation. The degree of non-monotonicity first increases up to about 1.5, then it varies between 1.2 and 2 for long rolling times. *NM* has considerably higher values than one which indicates a non-monotonic nature of deformation in industrial caliber rolling.

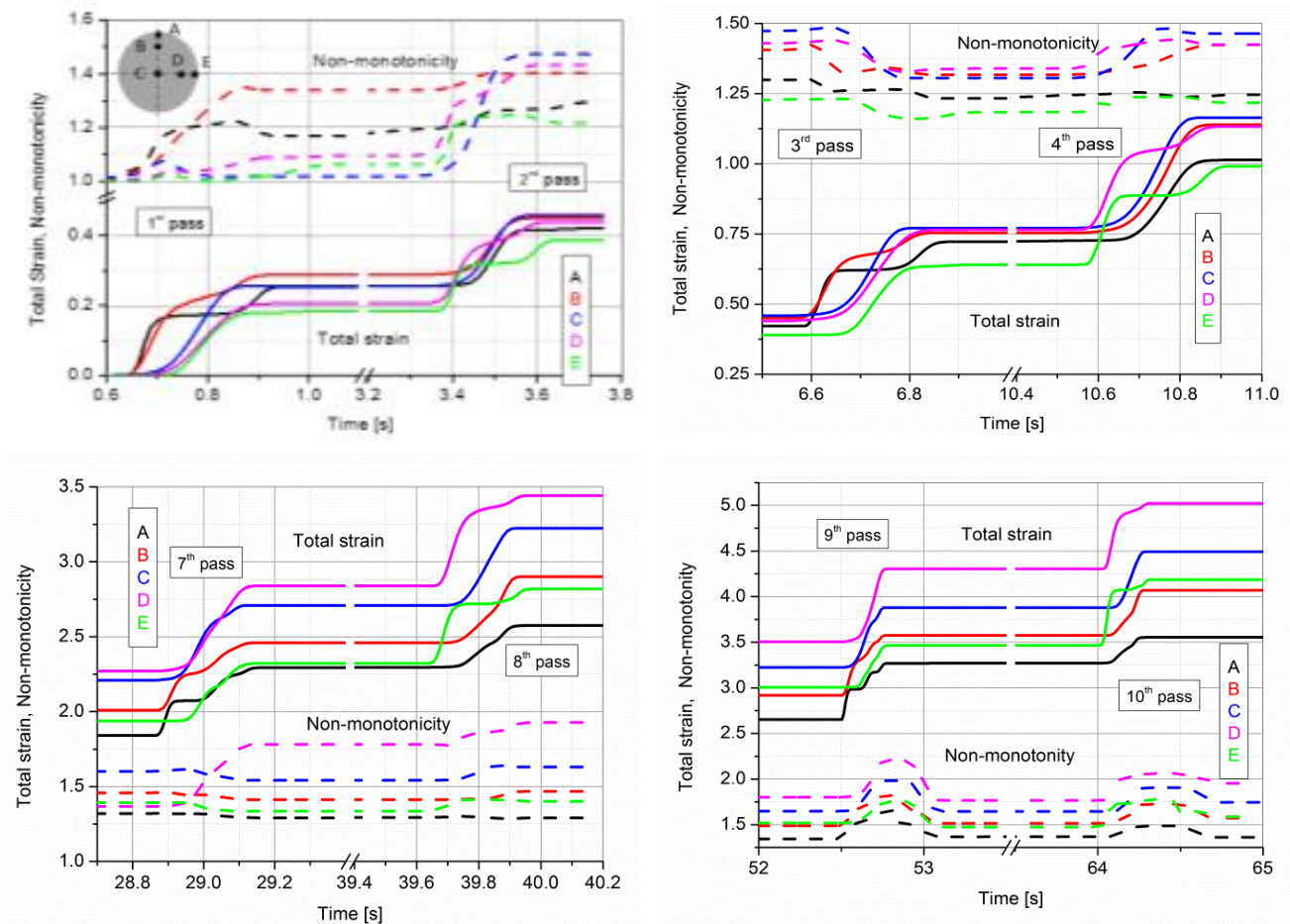
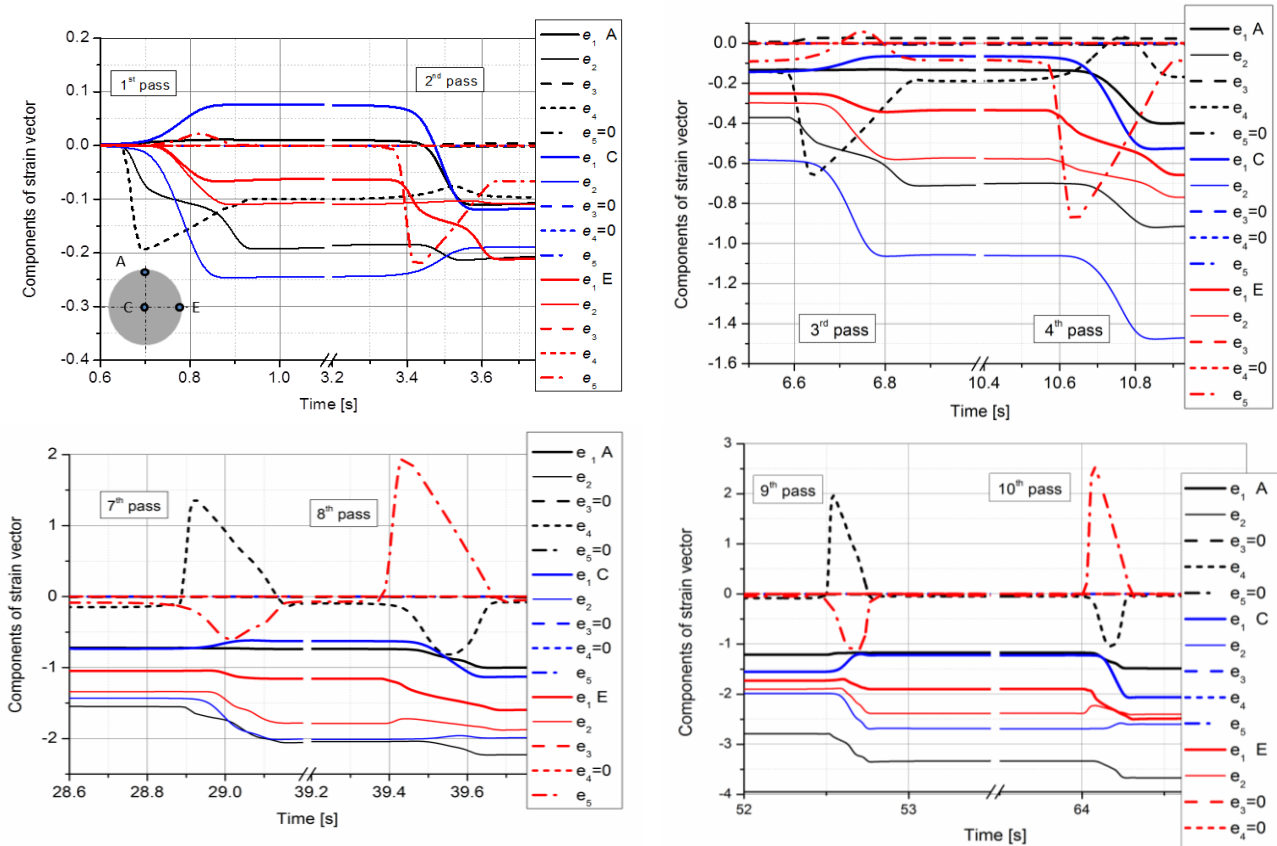


Figure 7. Changing of the total strain and the parameter of non-monotonicity at points A, B, C, D and E during industrial rolling.

In the FEM analysis the components of the logarithmic deviatoric strain tensor were determined which gave the components of the strain vector. The evolution of these components were visualised as rolling proceeds in **Figure 8**. It is revealed that considerable shear strains are developed during caliber rolling which most probably resulted in a grain refinement during deformation.

TEM images (not shown here) revealed that the grain size in the initial Ti material was between 1 and 4  $\mu\text{m}$ . Rolling in laboratory yielded significant grain refinement down to the UFG regime, as illustrated in the TEM images of **Figure 9**, obtained at the end of the

manufacturing process. In the cross-section the average grain size was about 300 nm. In the longitudinal section the grains were elongated with an average width and length of 300 nm and 1  $\mu\text{m}$ , respectively. Electron diffraction patterns for the specimen rolled in laboratory are also presented in the insets of **Figure 9**. The transition from a spotted to a ring-like diffraction pattern due to rolling also confirms the strong grain-refinement.



**Figure 8.** Changing the components of the strain vector at points A, C and E during caliber rolling.

After industrial rolling the grains are also elongated in the longitudinal section, as revealed in **Figures 9** and **10**. The average width and the length of the grains are 500 nm and 1  $\mu\text{m}$ , respectively. In the cross-section, considerable elongation of the grains was not observed. In this section the mean grain size is 500 nm. It can be concluded that both laboratory and industrial rolling procedures resulted in UFG microstructures, but the grain refinement was slightly stronger in the former case, as also indicated by the electron diffraction patterns. The smaller grain size can explain the slightly higher strength of the material rolled in laboratory. It is noted that the grain size obtained on the cross-section of the sample rolled in laboratory (300 nm) is close to the value (265 nm) determined for Ti processed by eight passes of ECAP at 400 – 450 °C and subsequently rolled at room temperature to a total strain (reduction in cross-section area) of 73 % [12].

The crystallite size and the dislocation density were determined on the longitudinal sections by X-ray line profile analysis. The average crystallite sizes determined by X-ray line profile analysis (62 and 127 nm for the laboratory and industrial rolling processes, respectively) are smaller than the grain size values obtained by TEM, which has already been observed for other plastically deformed metals [13].



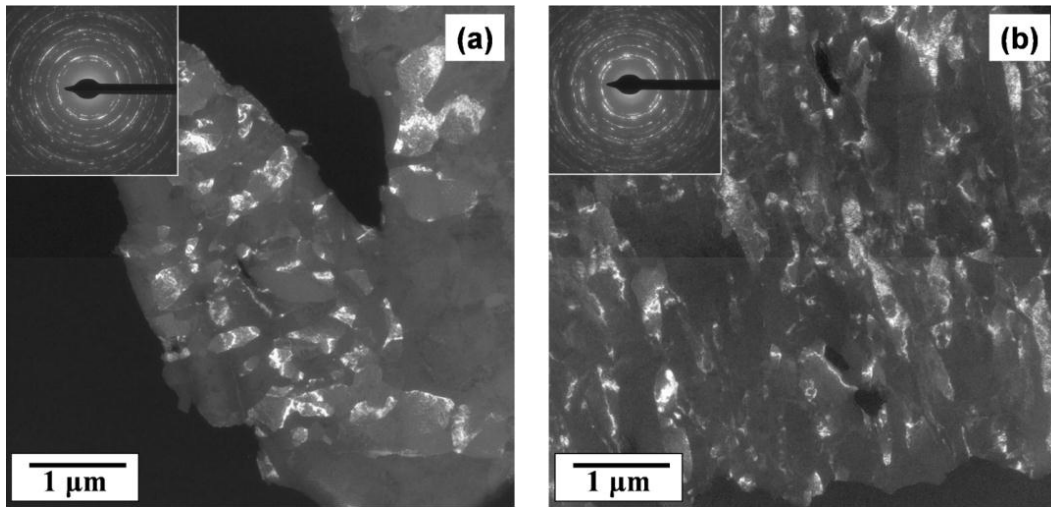


**Figure 9.** Dark field TEM images of the grain structure in laboratory rolled Grade 2 titanium. (a) cross- and (b) longitudinal sections. The rolling direction is vertical in figure (b). The insets show the corresponding diffraction patterns

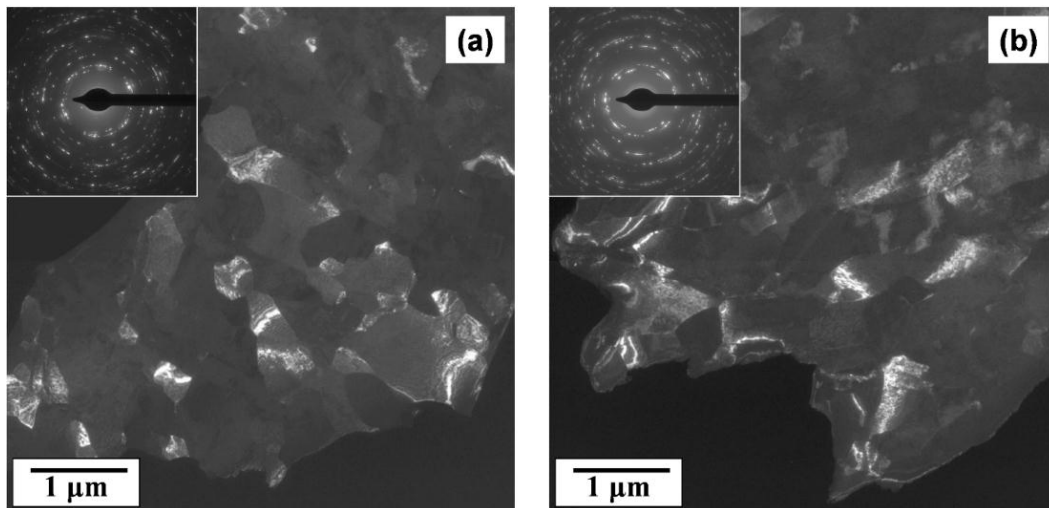


**Figure 10.** Dark field TEM images of the grain structure in industrially rolled Grade 2 titanium. (a) cross- and (b) longitudinal sections. The rolling direction is vertical in figure (b). The insets show the corresponding diffraction patterns.

This phenomenon can be attributed to the fact that the crystallites are equivalent to the domains in the microstructure which scatter X-rays coherently. As the coherency of X-rays breaks even if they are scattered from volumes having quite small misorientations ( $1 - 2^\circ$ ), the crystallite size corresponds rather to the subgrain size in severely deformed microstructures [13]. The dislocation density increased to  $4.7$  and  $3.9 \cdot 10^{14} \text{ m}^{-2}$  during laboratory and industrial rolling processes, respectively. The reduction in the crystallite size and the increment in dislocation density are stronger in the laboratory rolling procedure, but the difference between the dislocation densities obtained by the two types of rolling is not very large.

#### 4. Conclusions

1. It was shown that warm caliber rolling carried out on Grade 2 titanium at about 450 °C in laboratory yielded an UFG microstructure with high strength and good ductility.
2. Finite element modelling confirmed the non-monotonic nature of caliber rolling which is necessary for the production of a fine-grained structure.
3. Caliber rolling carried out in industrial environment yielded similar small grain size and improved mechanical properties as the process performed in laboratory. It was proposed that this technology might be a candidate process for mass-production of UFG titanium with high strength and good ductility. This may open a new gate to commercialization of SPD-processed materials.

#### Acknowledgements

This study was supported by the Hungarian Scientific Research Fund, OTKA, Grant Nos. K 100500 and K 109021.

#### References

1. Y. Saito, H. Utsunomiya, N. Tsuji, T. Sakai. Novel ultra-high straining process for bulk materials – Development of the accumulative roll-bonding. *Acta Materi.*, 1999, 47, 2, 579-583.
2. N. Tsuji, Y. Saito, S.-H. Lee, Y. Minamino. Accumulative roll-bonding and other new techniques to produce bulk ultrafine grained materials. *Adv. Engi. Mater.*, 2003), 5, 5, 338-344.
3. A. Ma, Y. Nishida, K. Suzuki, I. Shigematsu, N. Saito. Characteristics of plastic deformation by rotary-die equal-channel angular pressing. *Scripta Mater.*, 2005, 52, 6, 433-437.
4. R. Z. Valiev, T. G. Langdom. Principles of equal-channel angular pressing as a processing tool for grain refinement. *Prog. Mater. Sci.*, 2006, 51, 881-981.
5. A. P. Zhilyaev, T. G. Langdon. Using high-pressure torsion for metal processing. Fundamentals and applications. *Progr. Mater. Sci.*, 2008, 53, 893-979.
6. J. Huang, Y. T. Zhu, D. J. Alexander, X. Liao, T. C. Lowe, R. J. Asaro. Development of repetitive corrugation and straightening. *Mater. Sci. & Eng.A*, 2004, 371, 35-39.
7. G. A. Smirnov–Aljajev. *Resistance of Materials to Plastic Deformation*. 1978, Leningrad, Mashinostroenie.
8. G. Krállics, J. Gubicza, Z. Bezi, I. Barkai. Manufacturing of ultrafine-grained titanium by caliber rolling in the laboratory and in industry. *J. Mater. Proc. Technol.*, 2014, 214, 1307-1315.
9. A. A. Ilyushin. *Continuum Mechanics*. 1990, Moscow, Moscow Univ. Press.

10. G. Krállics, D. Malgyn. Finite element simulation of equal channel angular pressing. In: Severe Plastic Deformation: Towards Bulk Production of Nanostructured Materials (Ed. A. Burhanettin). 2005, New York: Nova Sci. Publ. Inc., 445-464.
11. G. Ribárik, J. Gubicza, T. Ungár. Correlation between strength and microstructure of ball milled Al–Mg alloys determined by X-ray diffraction. Mater. Sci. & Eng. A, 2004, 387-389, 343-347.
12. Y. T. Zhu, J. Y. Huang, J. Gubicza, T. Ungár, Y. M. Wang, E. Ma, R. Z. Valiev. Nanostructures in Ti processed by severe plastic deformation. J. Mater. Res., 2003, 18, 1908-1917.
13. J. Gubicza, T. Ungár, Characterization of defect structures in nanocrystalline materials by X-ray line profile analysis. Zeitschrift fur Kristallographie, 2007, 222, 567-579.

NANOCRYSTALLINE HARDYSTONITE SYNTHESIZED BY SOLID  
STATE PROCESS AS A NOVEL BIO-CERAMIC FOR MEDICAL  
PURPOSES; PREPARATION AND CHARACTERIZATION

E. Karamian<sup>1</sup>, H. Gheisari<sup>2</sup>

<sup>1</sup> Islamic Azad University – Najafabad Branch  
Advanced Materials Research Center  
Najafabad, Isfahan, Iran  
ebkaramian91@gmail.com  
ekaramian@pmt.iaun.ac.ir

<sup>2</sup> Islamic Azad University– Lenjan Branch  
Department of Mechanical and Industrial  
Isfahan, Iran

Accepted October 19, 2015

### Abstract

In this study, Hardystonite powder ( $\text{Ca}_2\text{ZnSi}_2\text{O}_7$ ) was synthesized by mechanical activation method as a solid state process. Specimens were composed of a blend of pure calcite, silica amorphous and ZnO with 50, 30 and 20 wt. %, respectively. These powders were milled by high energy ball mill using ball-to-powder ratio 10 : 1 and rotation speed (600 rpm) for 5 and 10 h. Then, the mixtures mechanically activated have been heated at 1100 °C for 3 h. XRD, SEM and BET performed on the samples to characterize. According to XRD results, the sample milled for 10 h just indicated the Hardystonite phase, with crystal size about 40 nm, while the sample milled for 5 h illustrate Hardystonite phase along with several phases. Based on energy transfer analysis, the energy amount transferred to the starting materials is 11.2 MJ /g for 10 h, causes the synthesis temperature reduces to 1100 °C.

### 1. Introduction

Previous studies showed that some Ca, Si containing bioactive glass, glass-ceramics and ceramics were biocompatible [1 – 3] and could induce hydroxyapatite (HAp) formation in body fluid environment [4]. Zn was reported to be involved in bone metabolism [5]. Zn could stimulate bone formation and increase bone protein, calcium content, and alkaline phosphatase activity in humans and animals [6]. Hardystonite ( $\text{Ca}_2\text{ZnSi}_2\text{O}_7$ ) is a mineral containing Ca, Zn, and Si, with a melting temperature of 1425 °C and a density of 3.40 g / cm<sup>3</sup>, and so far has no important industrial applications. Considering chemical composition, Hardystonite might be biocompatible and used as biomaterials. To our knowledge, there was no report about preparation of Hardystonite ceramic [7]. Recently, silicate based bioceramics such as wollastonite ( $\text{CaSiO}_3$ ) [8, 9], dicalcium silicate ( $\text{Ca}_2\text{SiO}_4$ ) [10], bredigite ( $\text{Ca}_7\text{MgSi}_4\text{O}_{16}$ ) [11] and Akermanite ( $\text{Ca}_2\text{MgSi}_2\text{O}_7$ ) [12] have showed excellent in vitro bioactivity, mechanical property and biocompatibility. Most attractive is that in vivo studies also proved that silicate bioceramics could promote new bone formation.

Zinc has a stimulatory effect on bone formation and mineralization and moreover, it inhibits osteoclastic bone restoration [13]. Previously, the study of Zn-doped CaSiO<sub>3</sub> [14] demonstrated that the incorporation of Zn could promote human bone osteoblastic-like cells proliferation and ALP activity. Recent studies revealed that some zinc-containing silicate ceramics such as willemite (Zn<sub>2</sub>SiO<sub>4</sub>) [15] and Hardystonite (Ca<sub>2</sub>ZnSi<sub>2</sub>O<sub>7</sub>) [14, 16 – 18] were also able to enhance one marrow stem cell proliferation and differentiation. In this study, Hardystonite powder was synthesized by solid state method. The starting materials were mechanical activated by high energy ball milling and compacted by uniaxial pressing then the powder mixture milled was heated at high temperature, 1100 °C. The aim of the present work was to investigate characterization of nanostructure Hardystonite ceramic as opposed to previous studies. The results of this paper can be used for further researches and it would promote the possibility of usages of nanostructure Hardystonite ceramic in orthopaedic applications.

In this study, energy transferred to the starting materials mixture, causes the materials to be mechanically activated and leads to the synthesis temperature of Hardystonite reduces to low temperature.

## **2. Materials and methods**

Hardystonite was synthesized by pure calcite (Merck, 99%), amorphous pure silica and pure zinc oxide (ZnO, 98 %) with 50, 30 and 20 wt. %, respectively. The powder mixture was milled by high energy ball mill, ball-to-powder ratio 10 : 1 and rotation speed 600 rpm, for 5 and 10 h. Then, the mixture milled has been heated at 1100 °C for 3 h in muffle furnace at air atmosphere. Phase structure analysis was carried out by X-ray diffraction (XRD) (Philips X'Pert-MPD diffractometer with Cu K $\alpha$  radiation ( $\lambda_1 = 0.15418$  nm) over the  $2\theta$  range of 10 – 90 deg.). The obtained experimental patterns were compared to the standards compiled by the Joint Committee on Powder Diffraction and Standards (JCDPS) which involved card # 01-072-1 for hardystonite phase. Hardystonite crystalline size of was determined using XRD patterns and modified Scherrer equation. Scanning electron microscopy (SEM) analyses evaluations were performed using a Philips XL30 to investigate the morphology. SEM micrograph was performed using a LEO 435 VP to investigate the morphology. SEM samples coated with Au by sputter spraying, low vacuum and 100 – 120 V accelerating voltage, for 120 s. The powder prepared coated with Au by spraying, low vacuum and 25 kV accelerating voltage. Mechanical activation has been done by PE2 high energy planetary ball mill machine for 5 and 10 h. The specific surface area of powder mixture milled has been done by BET technique, Kelvin B100.

### **2.1. The modified Scherrer equation**

The purpose of modified Scherrer equation given in this paper is to provide a new approach to the kind of using Scherrer equation, so that a least squares method can be applied to minimize the sources of errors. Modified Scherrer equation plots  $\ln \beta$  against  $\ln (1 / \cos \theta)$  and obtains the intercept of a least squares line regression,  $\ln(K\lambda/L)$ , from which a single value of  $L$  is obtained through all of the available peaks. The modified Scherrer equation can provide the advantage of decreasing the sum of absolute values of errors,  $\sum(\pm\Delta\ln\beta)^2$ , and producing a single line through the points to give a single value of intercept  $\ln(K\lambda/L)$  [19].

## 2.2. Energy transfer

**Figure 1** shows the schematic diagram of the planetary ball mill and the vial: indicating by  $W_p$  and  $W_v$  the absolute angular velocity of the plate of the mill and of one vial and by  $R_p$  and  $R_v$  the vectorial distances from the centre of the mill to the centre of the vial and from the centre of the vial to its periphery (vial radius), it can be shown the absolute velocity of one ball leaving the wall is given by:

$$V_b = [(W_p R_p)^2 + W_v^2 (R_v - d_b / 2)^2 (1 - 2W_v / W_p)]^{1/2}, \quad (1)$$

the velocity of the ball with  $d_b$  diameter, after the hits, equals that of the inner wall and can be expressed as follow:

$$V_s = [(W_p R_p)^2 + W_v^2 (R_v - d_b / 2)^2 + 2W_p W_v R_p (R_v - d_b / 2)]^{1/2}. \quad (2)$$

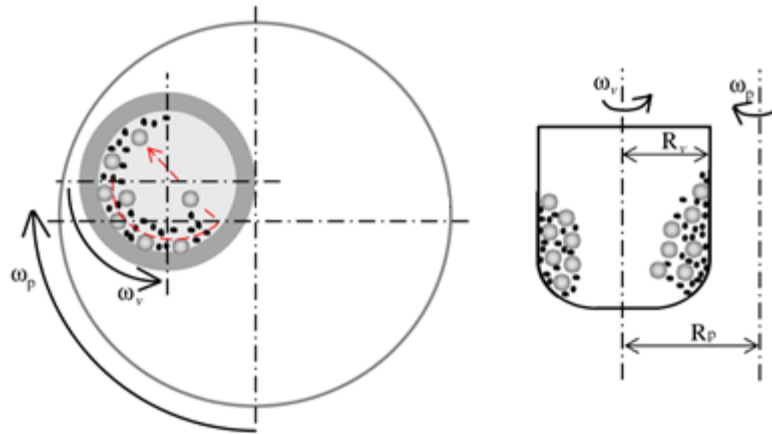


**Figure 1.** The schematic diagram of the planetary ball mill and the vial.

We have to consider now the mechanism of energy transfer. When the ball is thrown, it possesses the kinetic energy:

$$E = 1/2 m_b V_b^2. \quad (3)$$

After a short succession of hits, during which decreasing fractions of kinetic energy are released, the balls residual energy becomes:

$$E = 1/2 m_b V_s^2 \quad (4)$$

and the total energy released by the ball during the series of collision events is given by:

$$\Delta E_b = E_b - E_s = -m_b [W_v^3 (R_v - d_b / 2) / W_p + W_p W_v R_p] (R_v - d_b / 2). \quad (5)$$

with the assumption that the total energy transferred by the planetary mill per gram of reactant mixture and required to synthesis of nano-structure powders is a constant value, the Burgio model defines this amount of energy by the following expression:

$$E_t / g = \frac{(N_b \varphi_b f_b K_a m_b) [W_v^3 (R_v - d_b / 2) / W_p + W_p W_v R_p] (R_v - d_b / 2) t}{m_{ch}} = A (J / g), \quad (6)$$

where  $N_b$  is the number of balls;  $K_a$  is a constant that accounts for the elasticity of collisions, and a value of 1 represents perfectly inelastic collisions;  $m_{ch}$  is the mass of the powder charge; and  $t$  is the synthesis time measured.  $\varphi_b$  is a parameter that accounts for the degree of filling of the vial;  $f_b$  is the frequency with which the balls are launched against the opposite wall of the vial.

$$\varphi_b = 1 - \left( \frac{d_b^3 N_b}{\pi R_v^2 H_v} \right)^\varepsilon, \quad (7)$$



$$f_b = \frac{K(W_p - W_v)}{2\pi}, \quad (8)$$

$$m_b = \frac{\pi\rho_b d_b^3}{6}. \quad (9)$$

where  $H_v, \rho_b$  are respectively the height of the vial and the density of balls?  $K$  is a proportionality constant and is approximately equal to unity and  $\varepsilon$  is a parameter called ball diameter distribution coefficient depending on the balls diameter [20].

### 3. Results

#### 3.1. SEM micrographs

Figures 1 and 2 show the SEM micrographs the materials milled before and after heating.

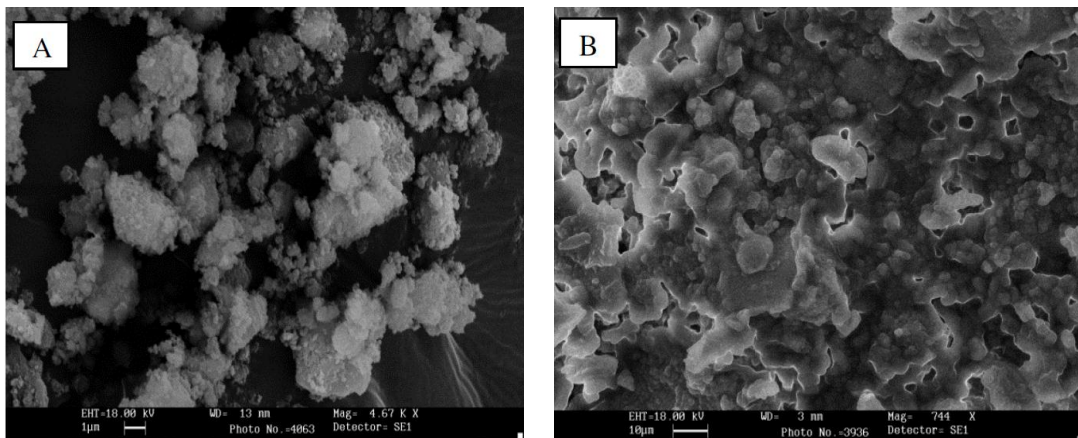


Figure 2. SEM micrographs of the powder mixture milled for 5 h (A) and then heated at 1100 °C for 3 h (B).

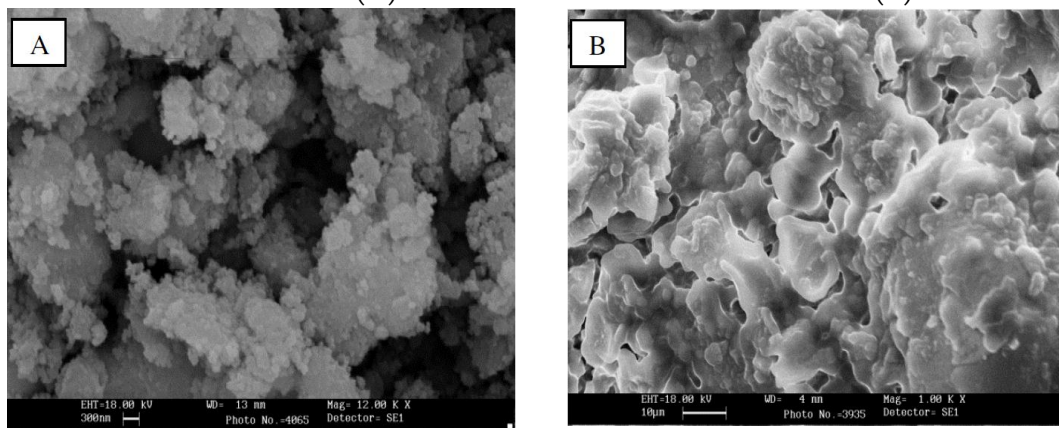
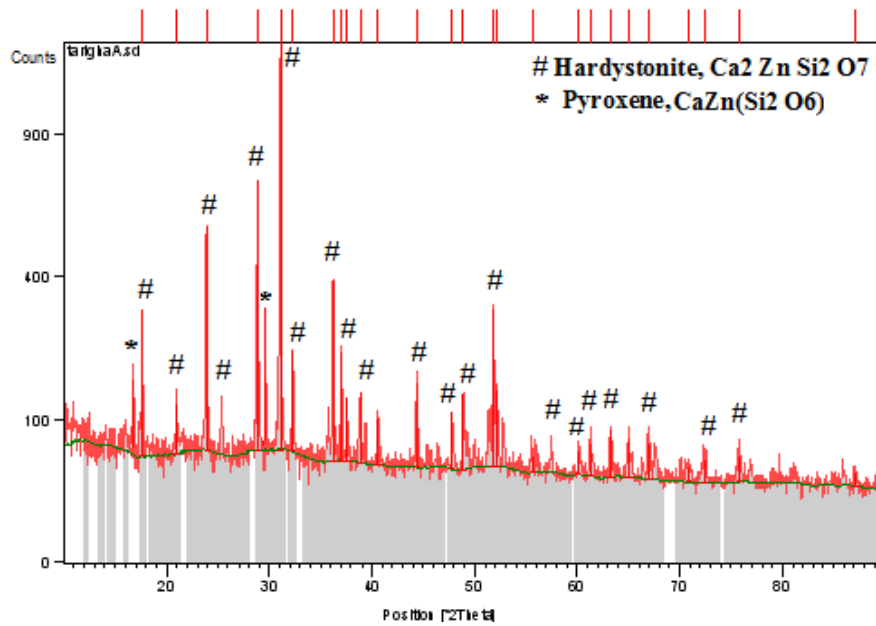


Figure 3. SEM micrographs of the powder mixture milled for 10 h (A) and then heated at 1100 °C for 3 h (B)

Considering SEM micrographs in figure 2 and 3, particles size average of powder mixture materials is micron range.

#### 3.2. XRD results

Figures 4 and 5 show the XRD patterns of the materials mixture milled heated at three temperatures.



**Figure 4.** XRD pattern of the materials mixture milled for 5 h and then heated at 1100 °C for 3 h.

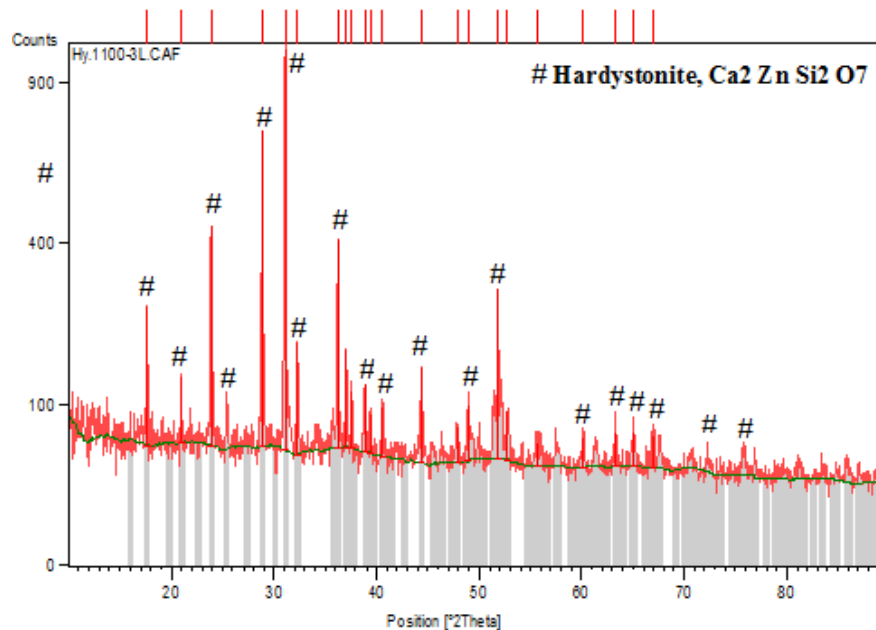


**Figure 5.** XRD patterns of the materials milled for 10 h and then heated at 1100 °C for 3 h

### 3.3. Estimation of crystal size

The modified Scherrer equation can provide the advantage of decreasing the sum of absolute values of errors,  $\sum(\pm \Delta \ln \beta)^2$ , and producing a single line through the points to give a single value of intercept  $\ln(K\lambda/L)$ .

At this sample, **Figure 6**, the linear regression plot is obtained as  $y = -0.7214x - 5.8252$ . This is equivalent to  $\ln \beta = \ln(1/\cos \theta) + \ln(K\lambda/L)$ . As you know,  $K$  (shape factor) and  $\lambda$  (XRD radiation wavelength) are 0.89 and 1.54 Å, respectively. From this line, the intercept is  $-5.8252$  and  $e^{-5.8252} = K\lambda/L$  and  $L = 460 \text{ \AA} = 46 \text{ nm}$  ( $L =$  crystal size average). So, crystal size average of Hardystonite synthesized is almost 46 nm.

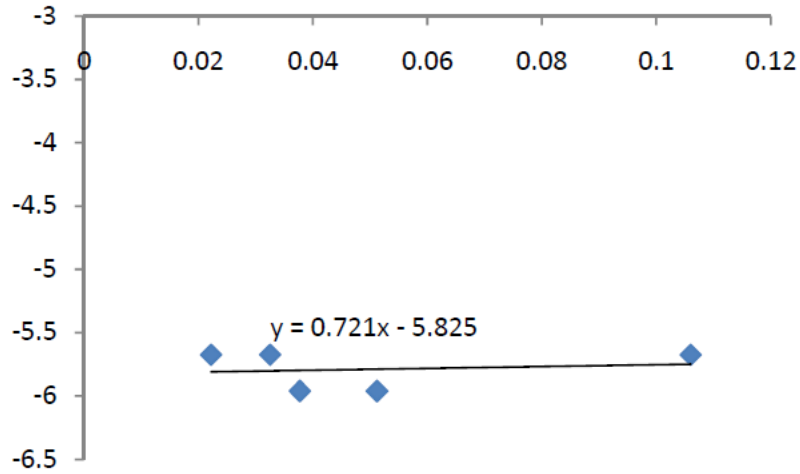


**Figure 6.** Plot of  $\ln \beta$  vs.  $\ln (1 / \cos \theta)$  of sample milled for 10 h and heated at 1100 °C, 3 h.

### 3.4. Energy transfer analysis

Considering the results of optimization, Table 1, is presented for the object of minimum cost function,  $W_v = 1.32W_p$ . It means that the vial spinning rate should be higher than the plate spinning rate (in the opposite direction). On the other hand,  $\varepsilon = 0.398$  which means that the ball size distribution is close to 40 %. The number of ball categories,  $s$ , is thus:

$$N_b = 3 \text{ and } \varepsilon = 0.4 \implies s = \text{Integer}(0.4 \times 3) = 1. \quad (10)$$

According to balls size and above interpretation one can write:

$$d_b = 10, N_b = 3, S = 1 \implies (3 \times 10) = 30. \quad (11)$$

So we can say that the size of balls used in proposed design should be 10 mm for the maximum energy transfer to the raw materials.

According to the ball mill parameters given in the **Table 1** and Eq. (6), it was concluded that the energy transfer by the planetary mill per gram of the materials mixture for 5 and 10 h milling time are:

$$E_{t/g} = 5.6 \text{ MJ / g for 5 h (milling time)}$$

and

$$E_{t/g} = 11.2 \text{ MJ / g for 10 h (milling time).}$$

**Table 1.** The milling parameters optimized values in planetary ball mill.

Symbol	Milling parameters	Optimized values
$N_b$	Number of balls	3
$d_b$	Balls diameter (m)	0.01
$R_v$	Vial radius (m)	0.035
$H_v$	Vial height (m)	0.07
$\varepsilon$	Ball size distribution coefficient	0.398
$W_p$	Velocity of the plate (rad / s)	62.8
$W_v$	Velocity of vial (rad / s)	82.89
$R_p$	Distance between the center of the plate and the center of the vial (m)	20.0

### 3.5. Powder density

Real density or pure density of the Hardystonite powder was calculated by Pycnometer. Considering to this method pure density was  $2.97 \text{ g/cm}^3$ .

### 3.6. BET result

The specific surface area of the prepared powder was calculated from the  $\text{N}_2$  gas adsorption isotherms using the multipoint BET technique. The average particle size of the prepared powder, assuming that the particles synthesized were spheroid, was calculated as shown in Eq. (12):

$$D = 6000 / (S_{\text{BET}} d), \quad (12)$$

where,  $d$  and  $D$  are true density ( $\text{g/cm}^3$ ) and the average particle size (micron) of materials mixture milled, respectively. The specific surface area determined by BET was  $7.1 \text{ m}^2/\text{g}$ , and pure density calculated by Pycnometer method was  $2.97 \text{ g/cm}^3$ . So, according to Eq. (12) the particles size was estimated about 285 nm. In fact, the powder mixture is sub-micron size. In addition, it is confirmed in SEM micrograph (**Figure 3**). So, particle size calculated is similar to particle size observed in SEM micrograph. Therefore, calculated particles size, by assuming that the synthesized particles are spheroid in Eq. (12), is acceptable. In fact, most of the particles are spheroid.

## 4. Discussion

According to the XRD patterns, Hardystonite phase was synthesized in both the samples (**Figures 4** and **5**). But, there is single phase, Hardystonite, just the sample milled for 10 h (**Figure 5**).

In addition, synthesis of Hardystonite phase is affected by using mechanical activation. In fact, mechanical activation intense the syntheses of Hardystonite phase in the sample. In addition, Hardystonite crystal size average is almost 46 nm. Based on energy transfer analysis, the mechanical energy amount transferred to the starting materials mixture is almost  $11.2 \text{ MJ/g}$  for 10 h milling time. This energy causes the synthesis temperature of Hardystonite reduces to  $1100 \text{ }^\circ\text{C}$ .

Most of energy transferred to particles materials save in the materials as crystal defects such as grain boundary, dislocations density and vacancy concentration. These crystal defects lead to high path atom diffusely. These high paths causes increasing and intensity of chemical reaction and improvement of Hardystonite phase synthesis. In fact, it causes the synthesis temperature of Hardystonite reduces to low temperature,  $1100 \text{ }^\circ\text{C}$ .

According to calculation by BET result and SEM micrographs observation, most of the powder particles milled for 10 h are spheroid. In fact, the morphology of powder milled is spheroid and about 285 nm. In fact, the powder mixture is sub-micron size. Moreover, raw materials milled sub-micron particles size, high of specific surface area, lead to increasing of free energy. This high free energy causes driving force to react between raw materials particles. Surface to bulk atoms ratio of particles, SBR, increases by increasing specific surface area of particles size. Regarding to surface diffusion activation energy in comparison bulk diffusion activation energy is too low amount. So, atom diffusion increases between particles and it causes to intensive reaction between raw materials and lead to Hardystonite phase synthesis at low temperature, low thermal energy, after milling for 10 h by high energy ball mill.

## 5. Conclusions

According to above discussion, we can conclude:

1. Hardystonite nano crystallite, about 46 nm, has been synthesized at 1100 °C by starting materials mixture mechanical activated for 10 h. Whereas, based on the previous studies, Hardystonite phase was synthesized above 1100 °C.
2. According to calculation by BET result and SEM micrographs observation, most of the powder particles milled for 10 h are spheroid. In fact, the morphology of powder milled is spheroid.
3. Based on energy transfer analysis, the energy amount transferred to mixture materials is almost 11.2 MJ/g for 10 h milling time. This energy causes the materials to be mechanically activated.
4. In fact, the energy transferred to the materials mixture (11.2 MJ/g), causes the synthesis temperature of Hardystonite reduces to 1100 °C.

## References

1. T. Kokubo, S. Ito, M. Shigematsu, S. Sakka, T. Yamamuro. *J. Mater. Sci.*, 1987, 22, 4067-4070.
2. T. Kokubo. *J. Non-Cryst. Solids*, 1990, 120, 138-151.
3. Y. Abe, T. Kokubo, T. Yamamuro. (1990) *J. Mater. Sci. Mater. Med.* 1, 233-238.
4. P. Li, Ohtsuki C., Kokubo T., K. Nakanishi, N. Soga, T. Nakamura, T. Yamamuro. *J. Appl. Biomater.*, 1993, 4, 229-230.
5. WHO Expert Committee on Trace Element in Human Nutrition. Trace elements in human nutrition. WHO Tech. Rep. Ser., 1973, 532, 9-15.
6. Yamaguchi M., Oishi H., Suketa Y., (1998) *Biochem. Pharmacol*, 37, 4075-4080.
7. Ch. Wu, Ch. J., W. Z. *Ceramics Int.*, 2005, 31, 27-31.
8. P. N. Deaza, F. Guitian, S. Deaza. *Scr. Metall. Mater.*, 1994, 31, 1001-1005.
9. K. L. Lin, W. Y. Zhai., S. Y. Ni, J. Chang, Y. Zeng, W. J. Qian. *Ceram. Int.*, 2005, 31, 323-326.
10. Z. R. Gou, J. Chang, W. Y. Zhai. *J. Eur. Ceram. Soc.*, 2005, 25, 1507-1514.
11. C. T. Wu, J. Chang, J. Y. Wang, S. Y. Ni, W. Y. Zhai. *Biomaterials*, 2005, 26, 2925-2931.
12. C. T. Wu, J. Chang. *J. Biomater. Appl.*, 2006, 21, 119-129.
13. M. Yamaguchi. *Trace Elem. Exp. Med.*, 1998, 11, 119-135.
14. C. T. Wu, Y. Ramaswamy, J. Chang, J. Woods, H. Zreiqat. *J. Biomed. B*, 2008, 87, 346-353.
15. M. L. Zhang, W. Y. Zhai, J. Chang. *J. Mater. Sci. Mater. Med.*, 2010, 21, 1169-1173.
16. C. T. Wu, J. Chang, W. Y. Zhai. *Ceram. Int.*, 2005, 31, 27-31.
17. Y. Ramaswamy, C. T. Wu, H. Zhou, H. Zreiqat. *Acta Biomater.*, 2008, 4, 1487-1497.
18. H. X. Lu, N. Kawazoe, G. P. Chen, X. G. Jin, J. Chang. *J. Biomaterials. Appl.*, 2010, 25, 39-56.
19. A. Minshi, M. R. Foroughi, M. R. Monshi. Modified Scherrer equation to estimate more accurately nano-crystallite size using XRD. *World J. Nano Sci. & Eng.*, 2012, 2, 3, 154-160.
20. M. Abdellahi, M. Bahmanpour. A novel technology minimizing the synthesis time of nano structured powders in planetary mills. *Mater. Res.*, 2014, 17, 3, 7-22.

## NANO / MICRO FIBROUS GELATIN–PLA YARNS FABRICATION AND CHARACTERIZATION FOR BIOMEDICAL APPLICATIONS

N. Movagatian<sup>1</sup>, A. Hadjizadeh<sup>1</sup>, M. Latifi<sup>2</sup>

<sup>1</sup> Amirkabir University of Technology  
Faculty of Biomedical Engineering  
Tehran, Iran  
afra.hadjizadeh@aut.ac.ir

<sup>2</sup> Amirkabir University of Technology  
Textile Excellence & Research Centers  
Textile Engineering Department  
Tehran, Iran

Accepted October 19, 2015

### Abstract

Nano / micro fibrous structures made of biodegradable polymers offer many advantages for biomedical applications, including tissue engineering scaffolds and drug delivery systems. In this study, a blend of gelatin (a biodegradable polypeptide) and polylactic acid (a biodegradable polymer) were electrospun to produce nanofibers. These nano / micro fibers were spontaneously collected in the form of yarn using a typical collector system. The produced yarns having 100 – 200  $\mu\text{m}$  diameter and consisting nanofibers (500 – 100 nm) were observed by light and electron microscopy. The fibers then were fixed by glutaraldehyde for gelatin cross linking and the tensile properties of the yarns were tested. Appropriate growth factors will be incorporated in to the yarns by physical adsorption to the gelatin molecules for the sustained release purposes in tissue engineering constructs.

### 1. Introduction

Nano fiber porous polymeric structures with high porosity and interconnected pores structures made of biodegradable polymers, offer a lot of advantages to biomedical applications, such as drug delivery [1, 2], tissue engineering scaffolds [3, 4], etc. [5], due to their highly porous microstructure with interconnected pores and large surface area. Among various techniques developed for producing porous structures, electrospinning as a simple and low-cost method for manufacturing nanoscale polymer fibers is the most suitable technique for the aforementioned applications. This technique has the capability of producing nano / micro fibrous structures [6] using various natural macromolecule, synthetic polymers [7] and their mixture to mimic the structure and the function of native extracellular matrix (ECM).

Electrospinning relies on the induction of electrical charges within a spinnable polymer fluid by applying a high voltage to the fluid. When the fluid gains enough charges, called critical charge amount, a fluid jet will start to erupt from the droplet formed at the tip of the conductive needle, leading to the formation of a cone shape called Taylor cone. The jet will fly



towards a grounded collector, being the region of negative potential. The parameters that affect electrospinning and as a result the fibers properties can be classified into polymer solution parameters, process parameters and ambient parameters such as temperature and moisture. The second class include the applied voltage, flow rate, tip to collector distance, collector geometry. With the understanding and changing these parameters, it is possible to produce fibrous structures of various morphological, physical and mechanical properties [9].

Yarns are key building blocks to construct complicated fibrous structures for many applications in diverse areas [10] including biomedical, such as sutures or scaffolds to direct cells in tissue engineering applications. In this paper, we report a novel mechanism for the direct twisting of electrospun nanofibers into yarns. In this study, a combination of gelatin (a biodegradable polypeptide) and poly-lactic acid (a degradable polymer) have been electrospun to produce nano fibers, By using a special collector, for gathering nano fibers to form a yarn.

## 2. Methods

### 2.1. Materials

In this study, a solution of PLA and gelatin type A (from Sigma Aldrich Company) blend with the concentration of 14 % and the ratio of 1 : 1 in Triethoxyethanol (TFE) solvent was prepared and stirred on a high speed magnetic stirrer for 24 h.

### 2.2. Electrospinning

**Figure 1** schematically illustrates the basic setup for electrospinning of nanofiber yarns. It consists of two needle nozzles, a rotating collector, and yarn taking up system, a neutral plane and a high-voltage DC power supply. During electrospinning, two needle nozzles were connected separately with the positive and negative polarities of the DC power supply. Nanofibers were electrospun from the oppositely charged nozzles deposited onto the neutral plane and then taken up by the rotating collector.

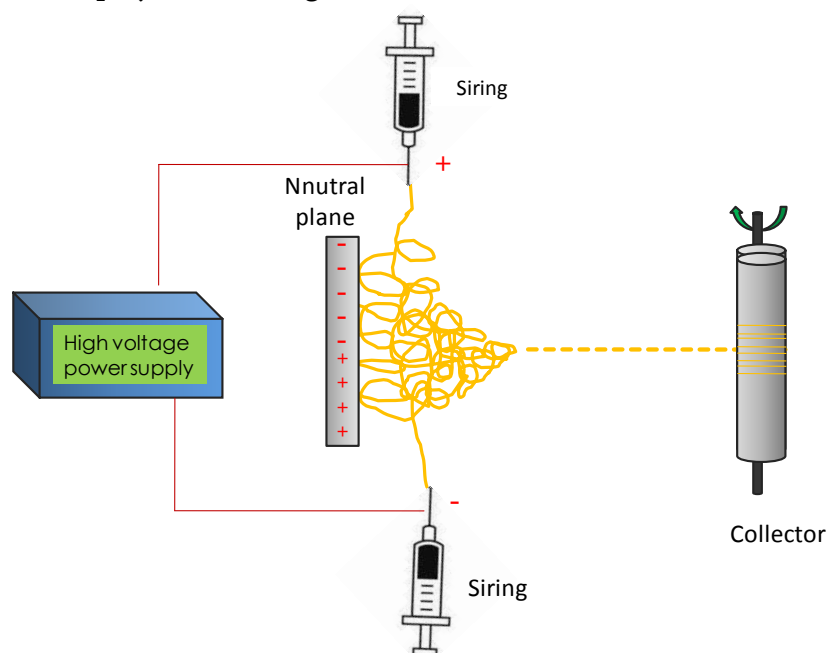


**Figure 1.** Schematic illustration of the electrospinning set-up used to produce electrospun yarn.

In this process, the polymer solution was injected by two nozzles with opposite charges, located in front of each other. Because of this difference in charge, coming out fibers attract to each other in the distance between the nozzles and discharge at the end. By locating a neutral plane in the field, due to the repulsive force of the negative and attraction from positive pole of the screen surface electrons are displaced as a result and charge density varies in different parts of the plane. In this case, half of the plane next to the positive pole has a negative charge density. Nanofibers that electrospinn from positive nozzle has positive charge adsorb slowly into this half of the plane. A similar event happens for the fiber coming out from the nozzle with a negative charge and adsorb into the second half. And the whole screen has neutral charge density. By putting a link in the direction of yarn nanofibers that is electrospun from two nozzles moving towards the neutral plane, nano-fibers are involved with end of the link yarn and thus the spinning triangle is formed as shown in **Figure 1**. Yarn spinning around its axis and taking up the link at the same time can produce extended continues yarn with relative orientation.

### 2.3. Gelatin fixation

In order to cross-link the gelatin molecules and thus improve the resistance and durance of the gelatin in the yarns, the yarn was treated with glutaraldehyde by keeping the yarn in a container in the presence of 5 % glutaraldehyde vapor for 24 h according to the procedure described in [11].

### 2.4. Measurement of tensile properties

Tensile properties of the yarns were measured by gauge strength equipment. This system is based on constant rate elongation (CRE). The distance between two jaws was 25 mm and the jaw speed movement was selected 5 mm / min. Tensile properties, including specific stress, elongation to rupture and the elastic modulus of the samples was measured.

### 2.5. Dying with methyl orange

Methyl orange in reaction with gelatin molecules causes a color change from white to orange. After putting gelatin + poly lactic acid yarn in a mixture of buffer with pH = 4 and methyl Orange, the color of the gelatin-PLA yarn was changed. While, after an hour the color of pure poly lactic acid fiber sheet that is free of gelatin, did not change.

## 3. Results

### 3.1. Gelatin-poly lactic acid yarn fabrication

Equipment shown in **Figure 1** was used for yarn production. In this technique, 2 nozzles with 0.6 mm outer diameter and 3 cm length placed at a certain distance from each other. After examining different concentrations, the results showed that there is a possibility of electrospinning at 14 wt. %. Optical microscope observations showed grainy fibers at much lower concentrations in spinning triangle, also in higher concentrations, polymer solution drying at the tip of the needle causing the problem in yarn fabrication process. Production of uniform nanofibers without beads and yarn without tear was possible in a voltage of 12 kV, the distance between the nozzles 22 cm, the feed rate 0.5 ml / h, collecting speed 0.4 rpm. Ambient temperature and humidity was in the range of 23 – 25 °C and 30 – 35 %, respectively.

### 3.2. Morphology of fibers and yarn

SEM images showed the morphology of yarn as well as nano/ micro fibers involved. According to the images, there is a well formed nanofibers in the yarn produced by pure PLA (**Figure 2**) and gelatin–PLA blend (**Figure 3**) with a solution concentration of 14 %. The produced yarns having 100 – 200  $\mu\text{m}$  diameter consisted nanofibers of 500 – 100 nm in diameters as observed by electron microscopy (**Figures 2** and **3**). It was also possible to produce micro fibrous yarn by using higher solution concentration of gelatin–PLA blend (*Figure 4*).

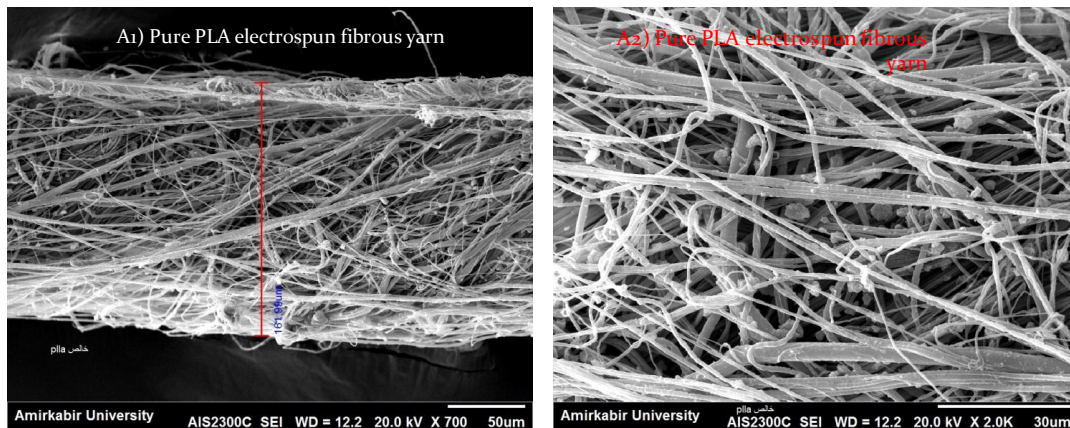


**Figure 2.** SEM images of nano fibrous pure PLA yarn with different magnifications: A1) yarn morphology ( $\times 700$ ), B1) fiber morphology ( $\times 2000$ ).

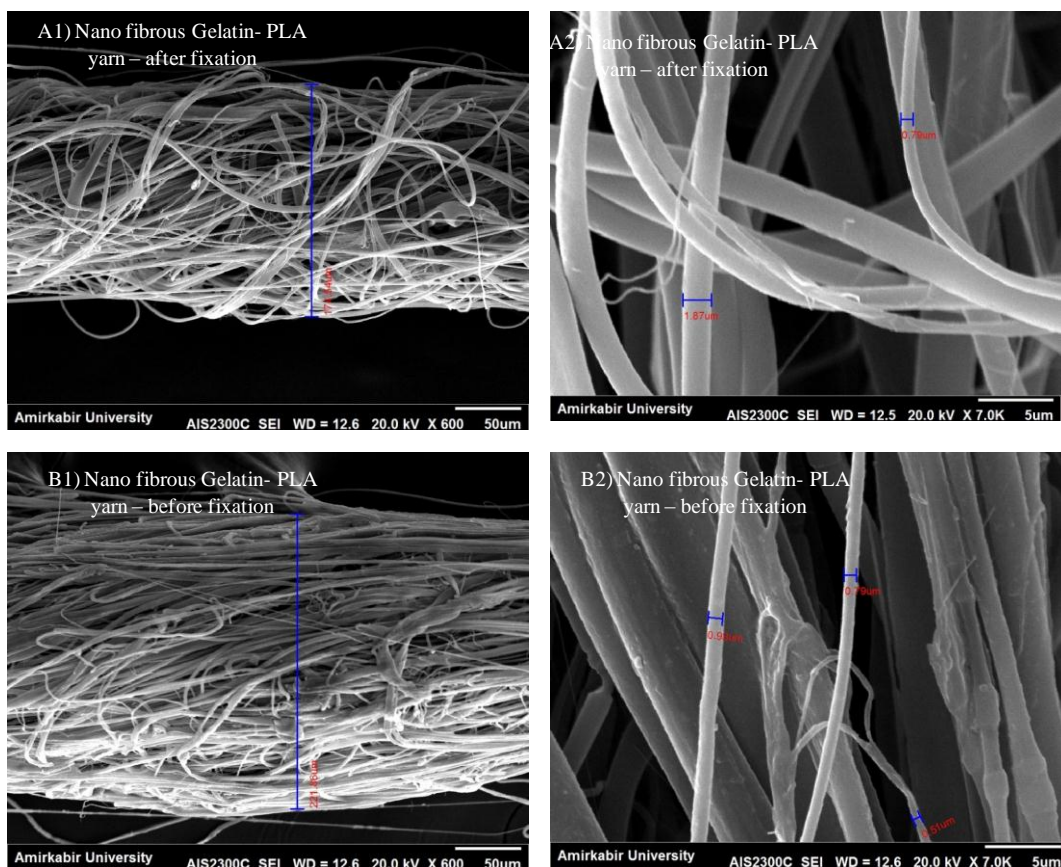


**Figure 3.** SEM images of nano fibrous gelatin–PLA yarn: A1 – A2 after gelatin fixation with glutaraldehyde, B1 – B2 before gelatin fixation with glutaraldehyde; A1 – B1 ( $\times 600$ ) show yarn morphology and A2 – B2 ( $\times 7000$ ) show fiber morphology.



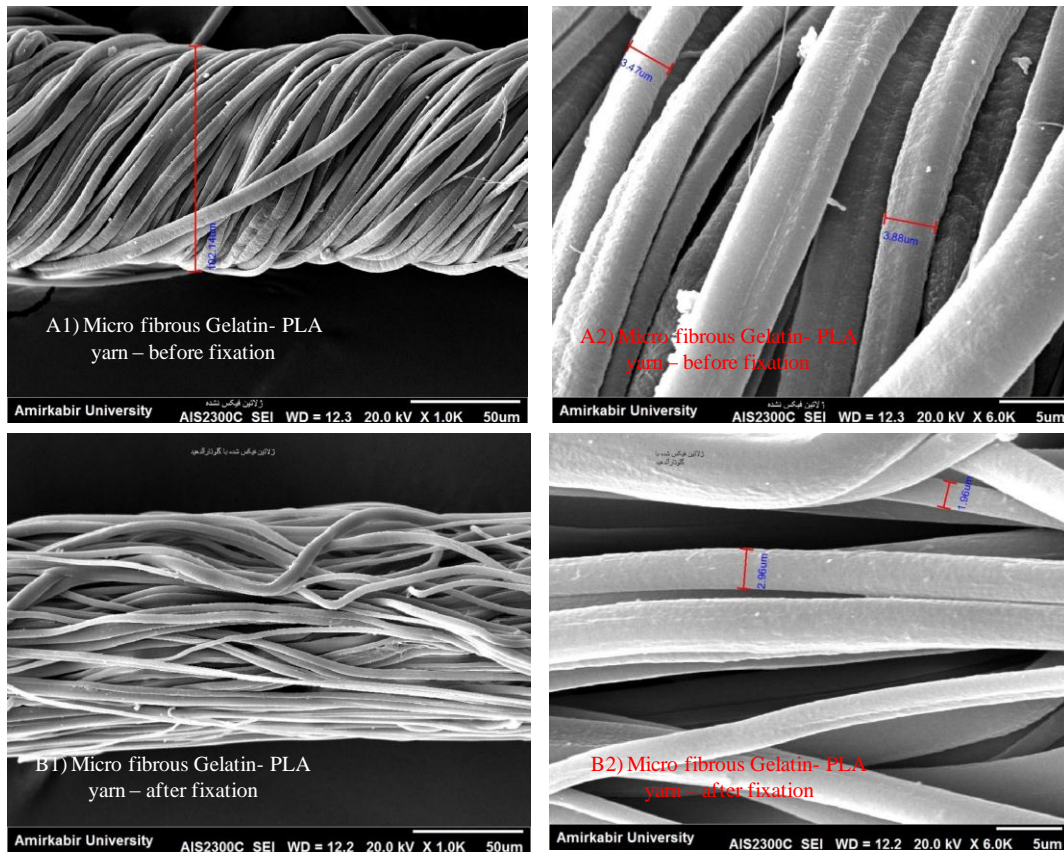


**Figure 4.** SEM images of micro fibrous gelatin–PLA yarn: A1 – A2 after gelatin fixation with glutaraldehyde, B1 – B2 before gelatin fixation with glutaraldehyde; A1 – B1 ( $\times 1000$ ) show yarn morphology and A2 – B2 ( $\times 6000$ ) show fiber morphology.

### 3.3. Dying with methyl orange

Methyl orange (Orange III) is a colored compound used in dyeing and printing textiles materials. Methyl orange is also used as an indicator in the titration of weak bases with strong acids by chemists. It changes the color from red (pH=3.1) to orange-yellow (pH=4.4) (**Figure 5**).

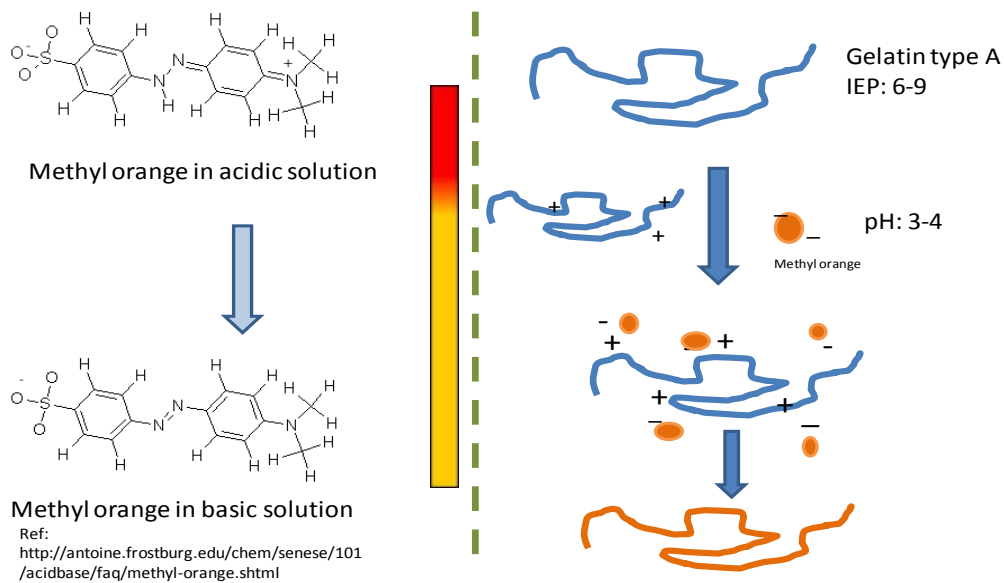


**Figure 5.** A) Methyl orange (Orange III) changes the color from red (pH=3.1) to orange-yellow (pH=4.4), B) schematic showing the mechanism of dying of gelatin by methyl orange.

Gelatin is produced by the denaturing of collagen. As a polypeptide, gelatin is an amphoteric compound due to the presence of amino-acids functional groups and of terminal amino and carboxyl groups. In acidic media (i.e. in the presence of high concentrations of  $H^+$  ions) gelatin is positively net charged. In an alkaline media (i.e. in the presence of  $OH^-$  ions), gelatin is negatively net charged. At the IEP (Isoelectric point), positive charges from  $NH_3^+$  groups are equal negative charges from  $COO^-$  groups. IEP is a characteristic of gelatin determined by raw materials pre-treatment and the type of process type: Type A (acid) gelatins exhibit an IEP in the range 6.0 – 9.5. Type B (alkaline) gelatins have an IEP in the range 4.5 – 5.6. IEP is of interest to explain the possible interactions of gelatin with other compounds, in particular anionic molecules.



Figure 6. Gelatin + PLA yarn and PLA sheet after dyeing with methyl orange.

Methyl orange in reaction with gelatin molecules causes a color change from white to orange. After putting gelatin + poly lactic acid yarn in a mixture of buffer with  $pH=4$  and methyl Orange, the color of the gelatin–PLA yarn was changed. While, after an hour the color of pure poly lactic acid fiber sheet that is free of gelatin, did not change (Figure 6).

### 3.4. Measurement of tensile properties

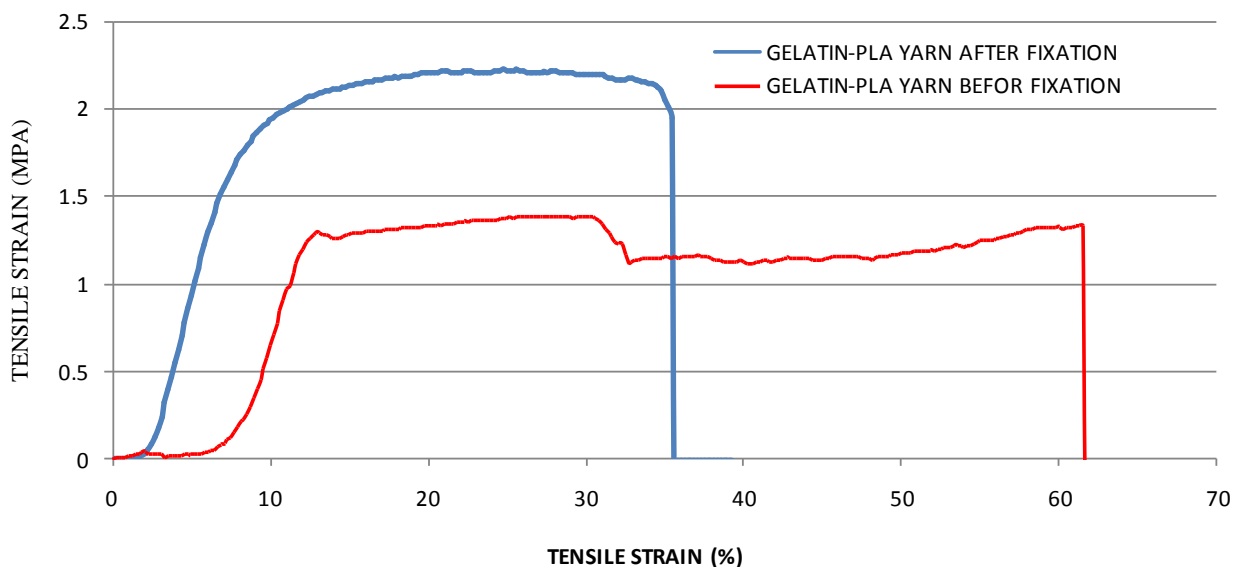


Figure 7. Stress–strain curve of micro fibrous gelatin–PLA yarn.

The tensile properties of both fixed and not fixed samples were measured and compared. According to the results obtained, an increased tensile property in fixed samples was noticeable (Figure 7).

#### 4. Conclusion

There are several methods for producing yarn of nanofibers. A good option for the production of continuous yarn is electrospinning method with two nozzles with opposite charge. In this research by using this method a continuous yarn was produced from poly-lactic acid (a biodegradable polymer) and gelatin (biodegradable polypeptide).

Investigation the morphology of nanofibers and yarn showed that the nano fibers with diameters range 100 – 500 nm cause a twisted yarn with diameter in the range of 100 –500  $\mu\text{m}$ . by fixation the yarn in glutaraldehyde, its tensile properties such as strength, elongation and elastic modulus were increased.

#### Acknowledgments

The authors would like to acknowledge the financial support of Iran National Science Foundation (INSF) for conducting this study.

#### References

1. D. J. Yang, C. D. Xiong, T. Govender, Y. Z. Wang. Preparation and drug-delivery potential of metronidazole-loaded PELA tri-block co-polymeric electrospun membranes. *J. Biomater. Sci. Polym. Ed.*, 2009, 20, 9, 1321-1334.
2. E. Llorens, S. Calderon, L. J. del Valle, J. Puiggali. Polybiguanide (PHMB) loaded in PLA scaffolds displaying high hydrophobic, biocompatibility and antibacterial properties. *Mater. Sci. Eng. C*, 2015, 50, 74-84.
3. A. Hadjizadeh, A. Ajji, M. Jolicoeur, B. Liberelle, G. De Crescenzo. Effects of electrospun nanostructure versus microstructure on human aortic endothelial cell behavior. *J. Biomed. Nanotechnol.*, 2013, 9, 7, 1195-1209.
4. S. Morelli, S. Salerno, J. Holopainen, M. Ritala, L. D. Bartolo. Osteogenic and osteoclastogenic differentiation of co-cultured cells in polylactic acid-nanohydroxyapatite fiber scaffolds. *J. Biotechnol.*, 2015, 204, 53-62.
5. Z. Wang, C. Zhao, Z. Pan. Porous bead-on-string poly(lactic acid) fibrous membranes for air filtration. *J. Colloid Interface Sci.*, 2015, 441, 121-129.
6. A. Hadjizadeh, A. Ajji, M. N. Bureau. Nano/micro electro-spun polyethylene terephthalate fibrous mat preparation and characterization. *J. Mech. Behav. Biomed. Mater.*, 2011, 4, 3, 340-351.
7. H. Savoji, A. Hadjizadeh, M. Maire, A. Ajji, M. R. Wertheimer, S. Lerouge. Electrospun nanofiber scaffolds and plasma polymerization: a promising combination towards complete, stable endothelial lining for vascular grafts. *Macromol. Biosci.*, 2014, 14, 8, 1084-1095.



8. S. J. Lee, J. J. Yoo, G. J. Lim, A. Atala, J. Stitzel. In vitro evaluation of electrospun nanofiber scaffolds for vascular graft application. *J. Biomed. Mater. Res. A*, 2007, 83, 4, 999-1008.
9. S. Ramakrishna. *An Introduction to Electrospinning and Nanofibers*. 2005, World Sci. Publ. Co Inc.
10. K. Z. X. Wang, M. Zhu, H. Yu, Zh. Zhou, Y. Chen, B. S. Hsiao. Continuous polymer nanofiber yarns prepared by self-bundling electrospinning method. *Polymer*, 2008. 49, 11, 2755-2761.
11. R. B. Montero, X. Vial, D. T. Nguyen, S. Farhand, M. Reardon, S. M. Pham, G. Tsechpenakis, F. M. Andreopoulos. BFGF-containing electrospun gelatin scaffolds with controlled nano-architectural features for directed angiogenesis. *Acta Biomate*, 2012, 8, 5, 1778-1791.

INVESTIGATION OF THE OPTICAL ABSORPTION  
SPECTRA OF THIN EPITAXIAL LEAD SELENIDE  
LAYERS APPROACHING THE NANOSCALE THICKNESS

A. M. Pashaev<sup>1</sup>, O. I. Davarashvili<sup>2</sup>, M. I. Erukashvili<sup>2</sup>,  
Z. G. Akhvlediani<sup>2,3</sup>, L. P. Bychkova<sup>2</sup>, V. P. Zlomanov<sup>4</sup>

<sup>1</sup>National Aviation Academy  
Baku, Azerbaijan

<sup>2</sup>I. Javakhishvili Tbilisi State University  
Tbilisi, Georgia  
omardavar@yahoo.com

<sup>2</sup>I. Javakhishvili Tbilisi State University  
E. Andronikashvili Institute of Physics  
Tbilisi, Georgia

<sup>4</sup>M. Lomonosov Moscow State University  
Moscow, Russia

Accepted March 16, 2015

## Abstract

By sophisticated treatment of the optical absorption spectra of thin epitaxial layers of lead selenide of different thickness approaching the nanorange, the presence of similar additional absorption for all layers was revealed. Such absorption was detected between the absorption edge and the absorption on free current carriers increasing with the wavelength. When constructing the absorption spectra by the experimentally investigated transmission spectra, the criteria of their treatment were strengthened by considerations for the absorption relation between the layers with low and high concentrations of current carriers, and from which level of absorption the transitions related to the absorption edge were to be considered. This resulted in the fact that, upon straightening the squared absorption coefficients, the obtained values of the forbidden gap width were in good correlation with the results obtained with the corresponding deformation of thin layers, and the contribution of the additional absorption to their determination was negligible.

## 1. Introduction

To suggest the use of strained epitaxial layers of IV–VI semiconductors for designing of high-sensitive and high-temperature IR photodetectors [1], it is essential to determine precisely the forbidden gap width of these layers. The additional absorption was detected in thin layers, especially in the ones  $\geq 1 \mu\text{m}$  in thickness, in previous works [2, 3]. In recent works [4, 5], it was shown that the additional absorption between the absorption edge and the absorption on free carriers increasing with the wavelength has no effect on the determination of the forbidden gap width [6]. It is of interest to study such additional absorption in strained layers  $< 200 \text{ nm}$  in thickness, which are promising for application. Besides, it is desirable to supplement the criteria of treatment of the optical absorption spectra for correct determination of the forbidden gap width of thin layers by addition of new verified considerations.

## 2. Objects and methods of investigation

The epitaxial PbSe layers were grown on KCl, NaCl and BaF<sub>2</sub> substrates by molecular epitaxy with a “hot wall”. The temperature of the source of epitaxy representing polycrystalline PbSe was over the range of 450 – 510 °C, while the temperature of the substrate was over the range of 240 – 320 °C. At the distance between the open tip of a quartz ampoule with the source of epitaxy and the substrate equal to 10 – 12 mm, the layers ~ 1 μm thick grew for 1 – 2 h, and the ones < 200 nm thick – for tens seconds [7].

The deformation of epitaxial layers  $\varepsilon = (a_1 - a_s)/a_s$  was determined by the results of X-ray measurements of lattice constants by a symmetric scheme. Radiation of CoK $\alpha$  ( $\lambda = 1.7889 \text{ \AA}$ ) was used.

The thickness of layers was determined by comparing the intensity of reflection from the layer-coated substrate and that of the uncoated one. The structure of the layers was also studied by the X-ray method.

The layers thicker than 20 nm grew uniform and monocrystalline. The optical transmission spectra were detected at  $T = 300 \text{ K}$  by using the prism-diffraction spectrophotometer SPECORD-75IR. Precision measurements of the transmission of layers were carried out by using the masks in measurement and reference modes.

## 3. Results and discussion

The PbSe layers grown on the NaCl and KCl substrates oriented in the (100) direction were chosen for the investigation. The layers differed in thickness by about an order of magnitude, 1.4 μm and 180 nm for layers SL-592 and SL-578, respectively. **Table 1** gives the data on absorption coefficients  $\alpha$  and  $\alpha_{\text{fr.car.}}$ , their squared remainder and their squared product by coefficient  $1/\gamma$  considering for the degeneracy the concentration of current carriers in the layers of about  $10^{19} \text{ cm}^{-3}$ . The lattice constants of layers SL-592 and SL-578 made up  $a = 6.122$  and  $6.149 \text{ \AA}$ , respectively. This means that layer SL-592 is somewhat contracted (lattice constants:  $a_{\text{PbSe}} = 6.126 \text{ \AA}$  and  $a_{\text{NaCl}} = 5.640 \text{ \AA}$ ), while layer SL-578 is stretched ( $a_{\text{KCl}} = 6.290 \text{ \AA}$ ) with “negative” deformation  $\varepsilon = 0.0037$ .

**Table 1.** Data on absorption coefficients, their squared values and squared products by  $1/\gamma$  for layer SL-592.

$h\nu$ , eV	$\alpha$ , cm <sup>-1</sup>	$\alpha_{\text{fr.car.}}$ , cm <sup>-1</sup>	$\alpha_{\text{fr.car.}}^2$ , cm <sup>-2</sup>	$\alpha^* = \alpha - \alpha_{\text{fr.car.}}$ , cm <sup>-1</sup>	$\alpha^{*2} = (\alpha - \alpha_{\text{fr.car.}})^2$ , cm <sup>-2</sup>	$1/\gamma$	$\alpha'^2 = (\alpha^*/\gamma)^2$ , cm <sup>-2</sup>
0.167	7419	7419	5.50E+07	0	5.5E+07	20.88	3.44E-02
0.222	5342	2798	7.83E+06	2544	6.5E+06	9.56	5.92E+08
0.279	5976	1484	2.20E+06	4493	2.0E+07	4.55	4.17E+08
0.334	6955	931	8.66E+05	6024	4.6E+07	2.53	2.32E+08
0.360	7669	768	5.89E+05	6901	4.8E+07	2.02	1.92E+08
0.384	10137	646	4.18E+05	9491	9.0E+07	1.70	2.61E+08
0.417	11531	542	2.94E+05	10989	1.2E+08	1.42	2.42E+08

The data on the absorption coefficients were obtained by solving the equation linking transmission, reflection coefficients and propagation constants with the absorption coefficient according to the model of the Fabry–Perot interferometer [8]. The corresponding initial data were taken from work [3] where the analysis had been performed by interference maxima in the transmission spectrum.

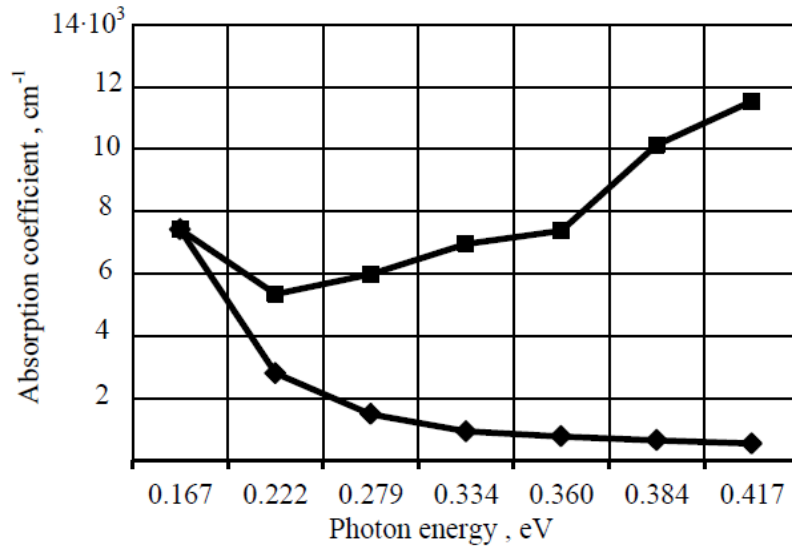


**Figure 1.** Spectra dependence of the total absorption coefficient  $\alpha$  (■) and the absorption coefficient on free carriers  $\alpha_{fr.car.}$  (◆) for layer SL-592.

**Figure 1** shows the spectral dependences of the total absorption coefficient  $\alpha$  obtained by the equation and the absorption coefficient on free carriers  $\alpha_{fr.car.}$ . The latter was obtained from the condition of equality of absorption  $\alpha$  and absorption  $\alpha_{fr.car.}$  ( $\alpha_{fr.car.} \sim \lambda^2$ ) at the wavelength corresponding to the long-wavelength maximum (five maxima were considered).

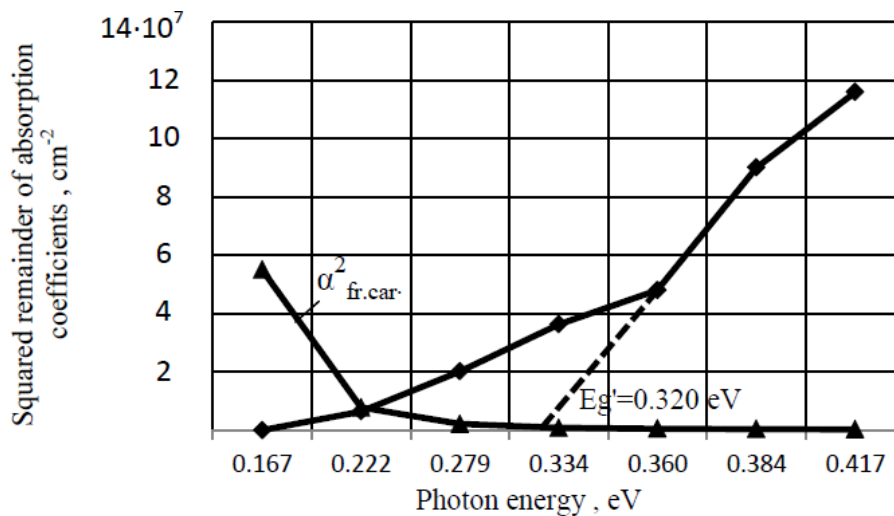


**Figure 2.** Dependence of the squared remainder of absorption coefficients  $\alpha^* = \alpha - \alpha_{fr.car.}$  on the photon energy  $h\nu$  for layer SL-592.

In **Figure 2**, the relations  $(\alpha - \alpha_{\text{fr.car.}})^2 = f(h\nu)$  and  $\alpha_{\text{fr.car.}}^2 = f(h\nu)$  are shown. By extrapolating the  $(\alpha - \alpha_{\text{fr.car.}})^2 = f(h\nu)$  to zero energy of the photon beginning from the squared absorption coefficients  $\geq 5 \cdot 10^7 \text{ cm}^{-2}$ , the absorption edge making up 0.320 eV was determined. At close values of the effective mass of electrons and holes, the above mentioned value of the absorption edge corresponds to the sum  $2E_F + E_g$  (where  $E_F$  is the Fermi level at the concentration of current carriers  $1 \cdot 10^{19} \text{ cm}^{-3}$  at  $T = 300 \text{ K}$ ).

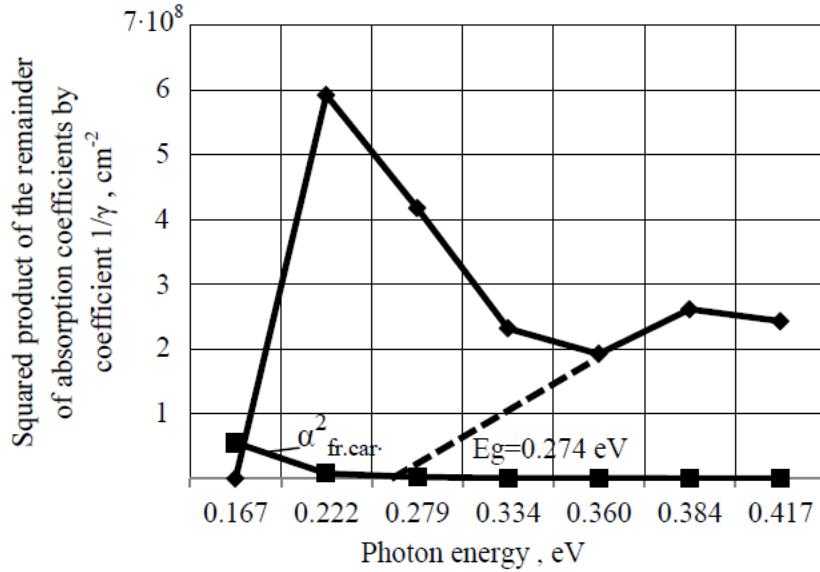


**Figure 3.** Dependence of the squared product of the remainder of absorption coefficients  $\alpha^* = \alpha - \alpha_{\text{fr.car.}}$  by coefficient  $1/\gamma$  (♦) on the photon energy  $h\nu$  for layer SL-592.

The forbidden gap width  $E_g$  was determined by extrapolating the relation  $((\alpha - \alpha_{\text{fr.car.}})/\gamma)^2 = f(h\nu)$  to the zero energy of the photon. The coefficient  $\gamma$  considering for degeneration was calculated at the Fermi level  $E_F = 0.03 \text{ eV}$ . **Figure 3** shows the extrapolation of this function, and the  $E_g$  value makes up 0.274 eV.

Unlike work [3], where, upon growing of the PbSe layers on the KCl substrate, the forbidden gap width made up 0.286 eV in the layers  $\sim 1 \mu\text{m}$  thick. In our case its smaller value is related to somewhat contraction of the layer.

From **Figure 3** it is also obvious that multiplication by the coefficient  $1/\gamma$  at the energy less than  $E_g$  yields an improbable result – transitions of current carriers to the energy levels with a maximum at  $\sim 0.22 \text{ eV}$ . Hence, the squared remainder  $\alpha^{*2} = (\alpha - \alpha_{\text{fr.car.}})^2$  at the energy lower than  $E_g$  shows the presence of additional absorption. From **Table 1** and **Figure 1**, it is seen that the additional absorption above the absorption by free carriers exceeds the latter by  $(2.5 - 3.0) \cdot 10^3 \text{ cm}^{-1}$ .

Like **Table 1**, **Table 2** gives the data on the total absorption coefficient and their remainder  $\alpha^* = \alpha - \alpha_{fr.car.}$ , and also the corresponding squared values the spectrum under study and their multiplication by the coefficient  $1/\gamma$  for layer SL-578. There is as well given the transmission which was used in the solution of the equation by the model of the Fabry-Perot interferometer for determining the coefficient  $\alpha$ .

**Table 2.** Data on absorption coefficients, their squared values and square products by  $1/\gamma$  for layer SL-578.

$h\nu$ , eV	$\alpha$ , $cm^{-1}$	$\alpha_{fr.car.}$ , $cm^{-1}$	$\alpha_{fr.car.}^2$ , $cm^{-2}$	$\alpha^* = \alpha - \alpha_{fr.car.}$ , $cm^{-1}$	$\alpha^{*2} = (\alpha - \alpha_{fr.car.})^2$ , $cm^{-2}$	$1/\gamma$	$\alpha'^2 = (\alpha^*/\gamma)^2$ , $cm^{-2}$	$T_{max}$
0.248	42322	42322	1.80E+09	0	1.01E-01	6.727	4.55E+00	0.205
0.261	39104	36756	1.35E+09	2347	5.51E+06	5.681	1.78E+08	0.197
0.276	33304	31791	1.01E+09	1513	2.29E+06	4.742	5.15E+07	0.195
0.292	28571	27363	7.49E+08	1208	1.46E+06	3.913	2.23E+07	0.189
0.310	25469	23418	5.48E+08	2051	4.21E+06	3.198	4.30E+07	0.179
0.335	22426	19430	3.78E+08	2996	8.98E+06	2.491	5.57E+07	0.172
0.347	21828	17846	3.18E+08	3982	1.59E+07	2.237	7.93E+07	0.169
0.353	22472	17096	2.92E+08	5376	2.89E+07	2.125	1.30E+08	0.166
0.360	23357	16377	2.68E+08	6979	4.87E+07	2.021	1.99E+08	0.163
0.366	23585	15738	2.48E+08	7847	6.16E+07	1.929	2.29E+08	0.162
0.378	24148	14568	2.12E+08	9579	9.18E+07	1.767	2.87E+08	0.161
0.381	24830	14294	2.04E+08	10536	1.11E+08	1.731	3.33E+08	0.160
0.397	27359	13068	1.71E+08	14291	2.04E+08	1.575	5.07E+08	0.158

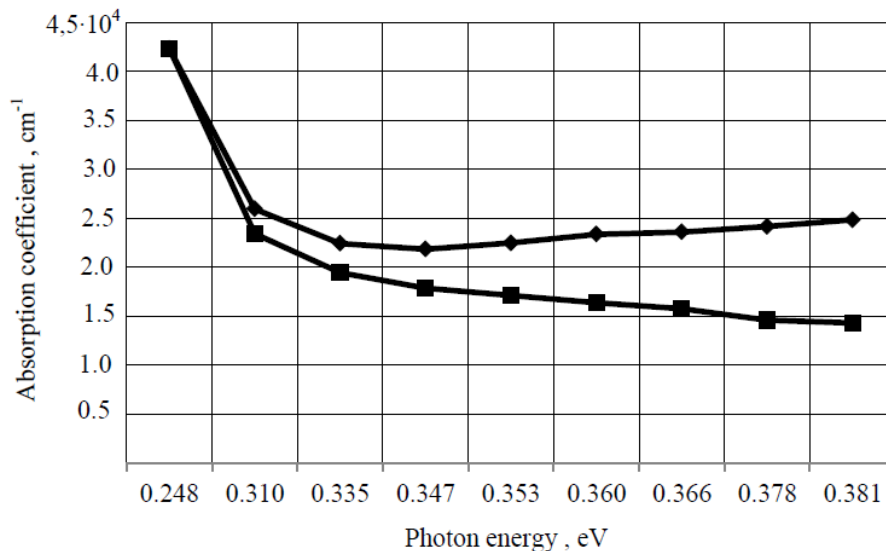


**Figure 4.** Spectra dependence of the total absorption coefficient  $\alpha$  ( $\blacklozenge$ ) and the absorption coefficient on free carriers  $\alpha_{fr.car.}$  ( $\blacksquare$ ) for layer SL-578.

In **Figure 4**, there are shown the spectral dependences of the total absorption coefficient  $\alpha$  and coefficient of the absorption on free carriers  $\alpha_{fr.car.}$ . As in **Figure 1**, here is observed the



minimum  $\alpha$ , which is caused by an increase in the band absorption with increasing energy and the reverse course of absorption on free carriers.

**Figure 5** shows the relation  $(\alpha - \alpha_{fr.car.})^2 = f(h\nu)$  for layer SL-578. The extrapolation to the zero energy of the photon results in the value 0.356 eV. In this case, in the straightening, the points with the values of squared remainders of absorption coefficients are considered for layer SL-578.

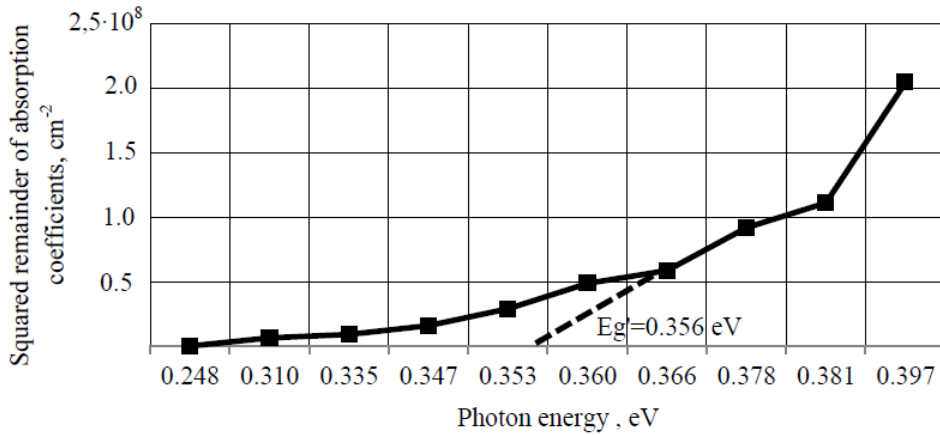


**Figure 5.** Dependence of the squared remainder of absorption coefficients  $\alpha^* = \alpha - \alpha_{fr.car.}$  on the photon energy  $h\nu$  for layer SL-578.

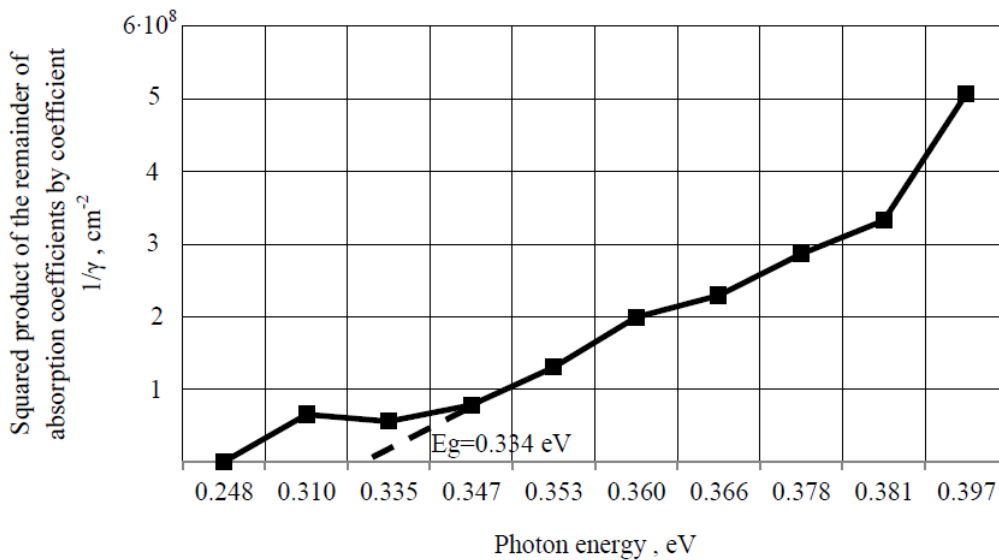


**Figure 6.** Dependence of the squared product of the remainder of absorption coefficients  $\alpha^* = \alpha - \alpha_{fr.car.}$  by coefficient  $1/\gamma$  on the photon energy  $h\nu$  for layer SL-578.

**Figure 6** shows the relation  $((\alpha - \alpha_{fr.car.})/\gamma)^2 = f(h\nu)$ . In the calculation of the coefficient  $\gamma$  [2], the Fermi level was equal to  $E_F = 0.03$  eV, identical to that for layer SL-592.

The extrapolation of this relation to the zero energy of the photon results in the value  $E_g = 0.334$  eV. From these extrapolations, it can be inferred that the value of  $2E_F$  makes up 0.022 eV, hence  $E_F = 0.011$  eV. Therefore, hereinafter there is good reason to take a smaller

value of  $E_F$  for calculation of the coefficient  $\gamma$  for such width of the forbidden gap and deformation  $\varepsilon = 0.0037$ . From **Table 2** and **Figure 4**, it is evident that the additional absorption over the spectral region from 0.310 to 0.334 eV also exceeds the absorption on free carriers by  $(2.5 - 3.0) \cdot 10^3 \text{ cm}^{-1}$ . Hence, the additional absorption in the epitaxial layers of different thickness has close values and is likely to be associated with virtual transitions between different branches of allowed bands. This fact received mention in work [9] as well.

It should be noted that, according to work [10], with the energy exceeding the forbidden gap width by  $2.1E_F$ , the absorption coefficient in the pure IV–VI semiconductor with a low concentration of current carriers increases almost twice as much as compared to the degenerate semiconductor. From **Tables 1** and **2**, it is seen that, at  $1/\gamma \approx 2.1$ , the energy with which this condition is fulfilled for layers SL–592 and SL–578 makes up 0.320 and 0.356 eV, respectively. This means that, with the energy exceeding  $E_g$  by  $2E_F$ , not only the absorption edge can be determined, but also the character of its growth in the pure semiconductor can be assessed.

#### 4. Conclusion

By using the data of our previous works and by the optical transmission spectra by the model of the Fabry–Perot interferometer, we determined the total absorption coefficient  $\alpha$  over the spectral region of 3 – 5  $\mu\text{m}$  for the epitaxial PbSe layers grown on the NaCl and KCl substrates, the thickness of layers making up 1.4  $\mu\text{m}$  and 180 nm, respectively. We sequentially determined the absorption coefficients on free carriers  $\alpha_{\text{fr.car.}}$ , their remainder  $\alpha^* = \alpha - \alpha_{\text{fr.car.}}$  and also the value of  $\alpha' = \alpha^*/\gamma$  for considering of the degeneration in the layers. By extrapolating the relation  $((\alpha - \alpha_{\text{fr.car.}})/\gamma)^2 = f(h\nu)$  to the zero energy of the photon, the forbidden gap width was determined. It made up 0.274 and 0.334 eV, respectively, which was in good correlation with the deformation in the layers. The additional absorption was revealed between the absorption edge and the absorption on free carriers increasing with the wavelength. This absorption had equal values for the layers of different thickness.

It was found that additional absorption has little or no effect on the determination of the value of the of forbidden gap width. The 2-fold increase relation of the absorption with the energy twice as high as the Fermi level  $E_F$  in lead selenide could be an appropriate checking factor of correct determination of the forbidden gap width in the degenerate layer [11, 12].

#### References

1. A. M. Pashaev, O. I. Davarashvili, M. I. Erukashvili, Z. G. Akhvlediani, L. P. Bychkova, V. P. Zlomanov. Modeling of the dielectric state in PbSnSe and PbSnTe nanolayers with high concentration of nonstoichiometric defects. In: Abs.17th Int. Conf. Radiat. Eff. Insulators. 2013, Helsinki, PB–16.
2. A. Pashaev, O. Davarashvili, M. Erukashvili, Z. Akhvlediani, R. Gulyaev, V. Zlomanov. Unrelaxed state in epitaxial heterostructures based on lead selenide. J. Mod. Phys., 2012, 3, 6, 502-510.

3. A. M. Pashaev, O. I. Davarashvili, M. I. Erukashvili, Z. G. Akhvlediani, L. P. Bychkova, M. A. Dzagania. Study on the forbidden gap width of strained epitaxial lead selenide layers. *J. Mater. Sci. & Eng.*, 2012, 2, 2, 142-150.
4. A. M. Pashaev, O. I. Davarashvili, M. I. Erukashvili, Z. G. Akhvlediani, M. A. Dzagania, V. P. Zlomanov. Specific features of the absorption spectra of epitaxial lead selenide layers. *Bull. Natl. Acad. Sci. Georgia*, 2014, 40, 4, 278-284.
5. A. M. Pashaev, O. I. Davarashvili, M. I. Erukashvili, Z. G. Akhvlediani, L. P. Bychkova, M. A. Dzagania, V. P. Zlomanov. Additional absorption in the optical spectra of epitaxial lead selenide layers. *Bull. Natl. Acad. Sci. Georgia*, 2014, 40, 4, 285-292.
6. A. M. Pashaev, O. I. Davarashvili, M. I. Erukashvili, Z. G. Akhvlediani, L. P. Bychkova, M. A. Dzagania. Interpretation of the optical transmission spectra of lead selenide nanolayers with the aim of determination of the width of their forbidden gap. *Trans. Natl. Acad. Sci. Azerbaijan*, 2013, 15, 3, 3-12.
7. A. M. Pashaev, O. I. Davarashvili, M. I. Erukashvili, Z. G. Akhvlediani, R. G. Gulyaev, L. P. Bychkova. Epitaxial lead selenide layers over a wide range of their thickness on dielectric substrates. *J. Mater. Sci. & Eng. B*, 2013, 3, 2, 97-103.
8. A. M. Pashaev, O. I. Davarashvili, M. I. Erukashvili, Z. G. Akhvlediani, L. P. Bychkova, V. P. Zlomanov. Analysis of the optical transmission spectra of epitaxial lead selenide layers. *Trans. Natl. Acad. Sci. Azerbaijan*, 2011, 13, 3, 3-12.
9. Y. I. Ukhanov. *Optical Properties of Semiconductors*. 1972, Nauka: Moscow.
10. E. D. Palik, D. L. Mitchell, I. N. Zemel. Magneto-optical studies on the band structure of PbS. *Phys. Rev. A*, 1964, 135, 3, 763-778.
11. A. Pashaev, O. Davarashvili, M. Erukashvili, Z. Akhvlediani, R. Gulyaev, V. Zlomanov. New opportunities in lead selenide nanolayers. *Adv. Mater. Res.*, 2013, 815, 473-477.
12. A. Pashaev, O. Davarashvili, M. Erukashvili, Z. Akhvlediani, R. Gulyaev, V. Zlomanov. Stretching strain-effective "negative" pressure in lead selenide nanolayers. *Int. J. Eng. & Innov. Technol.*, 2014, 3, 11, 318-323.

VOLUME OF INTERSECTION OF SIX SPHERES:  
A SPECIAL CASE OF PRACTICAL INTEREST

L. Chkhartishvili<sup>1</sup>, S. G. Narasimhan<sup>2</sup>

<sup>1</sup>Georgian Technical University  
Department of Engineering Physics  
Tbilisi, Georgia  
chkharti2003@yahoo.com

<sup>2</sup>Shanmugha Arts, Science, Technology & Research Academy  
(SASTRA University)  
School of Mechanical Engineering  
Thanjavur, India  
gnaras15@gmail.com

Accepted April 30, 2015

**Abstract**

A number of scientific and technical problems need the calculation of the intersection volume of spheres with different radii and distances between centers. Present work aims to summarize previous attempts made in this direction and solve the six-sphere problem for a special case of practical interest.

**1. Problem of intersection volume of spheres**

**1.1. A single sphere**

The problem of intersection volume of spheres is reduced to a trivial problem of classical geometry [1]: determination of the volume  $V$  of the sphere with given radius  $R_1$ , which as a whole is contained inside the intersection of all other spheres:

$$V(R_1) = \frac{4\pi R_1^3}{3}. \quad (1)$$

**1.2. Two spheres**

In the engineering practice, e.g., for determining the moments of inertia of machine parts [2], the volume of intersection of two spheres with given radii  $R_1$  and  $R_2$ , and distance  $D_{12}$  between their centers are calculated numerically. As for the general solution of this geometrical problem, it was done by us analytically [3] in relation to the physical problem of calculation of crystalline band structures within an approximation of quasi-classical type. The matrix elements of the secular equation determining the band structure were expressed by the volume of intersection of two spheres and then the corresponding formula was obtained:

$$\begin{aligned}
 V(R_1, R_2, D_{i12}) &= & (2) \\
 &= \frac{4\pi R_1^3}{3}, & D_{i12} < R_2 - R_1 \\
 &= \frac{4\pi R_2^3}{3}, & D_{i12} < R_1 - R_2 \\
 &= \frac{\pi(R_1 + R_2 - D_{i12})^2((R_1 + R_2 + D_{i12})^2 - 4(R_1^2 - R_1R_2 + R_2^2))}{12D_{i12}} & |R_1 - R_2| \leq D_{i12} \leq R_1 + R_2 \\
 &= 0 & D_{i12} > R_1 + R_2.
 \end{aligned}$$

One can see that,  $V(R_1, R_2, D_{i12})$  is a piecewise algebraic function. It and its partial derivative  $\partial V(R_1, R_2, D_{i12})/\partial D_{i12}$  in the argument  $D_{i12}$  are continuous at both of boundaries of analyticity  $D_{i12} = |R_1 - R_2|$  and  $D_{i12} = R_1 + R_2$ . As for the partial derivatives of higher-orders, they are discontinuous functions.

### 1.3. Three spheres

It seems that, before 1997 there were made no attempts to determine the volume of the intersection of three spheres in general – as an explicit function of their radii  $R_1, R_2, R_3$  and distances  $D_{12}, D_{13}, D_{23}$  between centers. Although, it was considered a several cases, when spheres' parameters are related to each other in a special way [2, 4, 5]; and Gibson & Scheraga [6, 7] summarizing the previous efforts performed in this direction had generalized Powell's formula [4] for the spheres of equal radii. The expressions were derived not only for the case of spheres of unequal size that insect in pair of points (**Figure 1**), but also for other types of triple intersection. However, we should note that these expressions being analytical at the same time are only implicit representations of the function  $V(R_1, R_2, R_3, D_{i12}, D_{i13}, D_{i23})$ .

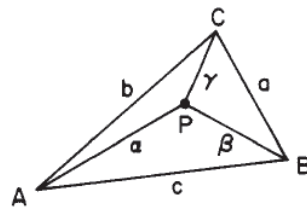


**Figure 1.** Representation of tetrahedron formed by centers of spheres at points  $A, B, C$  and point  $P$ , which is one of two points common to surfaces of all three spheres [6]. Here:  $R_1 \equiv \alpha, R_2 \equiv \beta, R_3 \equiv \gamma, D_{12} \equiv c, D_{13} \equiv b, D_{23} \equiv a$ .

In 1997, developing the method of analysis of crystalline electronic energy spectrum based on the quasi-classically calculated characteristics of atomic orbitals, Chkhartishvili had demonstrated [8] that the energy and configuration characteristics of quasi-classical electronic states of crystals can be expressed by the analytical combinations of elliptic integrals. In particular, the volume of intersection of three spheres was expressed by the linear combination of elliptic integrals. In 2001, Chkhartishvili had found out [9] that (**Figures 2 and 3**), the integrand part standing under the square root is a perfect square. This finding allowed to conduct the integration in elementary functions and express the required volume as a piecewise analytic combination of algebraic and inverse trigonometric functions.

MATHEMATICAL NOTES, VOL. 69, NO. 3, 2001, PP. 421-428.  
 Translated from *Matematicheskie Zametki*, vol. 69, no. 3, 2001, pp. 466-476.  
 Original Russian Text Copyright ©2001 by Chkhartishvili

### Volume of the Intersection of Three Spheres

L. S. Chkhartishvili

Received November 15, 1999

**Abstract**—The volume of the intersection of three spheres is represented as a continuous piecewise analytic combination of algebraic and inverse trigonometric functions of the radii and the distances between the centers of the spheres.

**KEY WORDS:** volume of the intersection of spheres, total energy potential, atomic potential, quasiclassical analysis of electron-energy spectra, hydrogen-like ions, secular equation.

The geometrical problem about the volume of the intersection of three spheres arose in consideration of the physical problem of calculating the electronic structure of a substance by the quasiclassical method.

After the fundamental work [1] of Bohr, the semiclassical analysis of electron-energy spectra of light atoms became very popular (see, e.g., [2]). The heavy atoms can be calculated within the framework of approximation of local electron densities with the use of the quasiclassical decompositions for the total energy functional [3]. But, because of a singularity at the point where the nucleus is located and of the electron shell effect, the atomic potentials do not generally satisfy the standard quasiclassical condition of spatial smoothness. Why are such approaches successful?

The quasiclassical expression for bound state energies obtained by Maslov [4] shows [5] that the exact and quasiclassical spectra of a physical system are close to each other independently of the smoothness properties of the potential if  $\hbar^2/2me\Phi R^2 \ll 1$ , where  $\Phi$  and  $R$  are the characteristic values of the potential and the radius of its action, respectively. Let  $Z$  be the charge number of the nucleus; then  $\Phi \sim eZ/\hbar r_0 R$ , and the criterion takes the form  $R_Z/2R \ll 1$ . Here  $R_Z = 4\pi\epsilon_0\hbar^2/me^2Z$  is the Bohr radius of a hydrogen-like ion. Even for light atoms, the radii of electron clouds are several times larger than  $R_Z$ ; thus, approximately, atoms are quasiclassical electron systems in the sense specified.

The classically available domain for an electron bound in an atom is bounded by two spherical surfaces centered at the point where the nucleus is located. In the lowest quasiclassical approximation, the partial electron densities of atomic orbitals averaged over directions vanish outside these domains and are nonzero constants inside them. As the result, the total electron density in an atom is expressed by a radial step-function, which implies that the atomic potential has a similar form. Molecular and crystal potentials can be approximated by a superposition of atomic potentials and are step-functions defined in three-dimensional space. Therefore, if the basis for expansion of the wave function is formed by linear combinations of piecewise constant quasiclassical atomic orbitals, then the electronic structure of the molecule or crystal is determined by a secular equation whose matrix elements are linear combinations of the finitely many volumes of the overlapping domains of the triples of classically available domains for the electron states located at certain atom nodes. It is easy to see that such volumes are algebraic sums of the volumes of the intersections of the triples of the spheres bounding these domains.

Thus the physical problem of calculating the electron structure of a substance in the lowest quasiclassical approximation can be considered solved if we solve the purely geometric problem of evaluating the function  $V = V(R_1, R_2, R_3, D_{12}, D_{13}, D_{23})$ , which expresses the dependence

0001-4346/2001/6934-0421\$25.00 ©2001 Plenum Publishing Corporation 421



Figure 2. “Three apples”. Cover of 1995 August 21 issue of magazine ‘Chemical & Engineering News’.

Figure 3. First page of paper (Math. Notes, 2001, 69, 3, 421-428) bearing explicit analytical solution of problem of intersection volume of three spheres.

In particular, when intersection region is bounded by parts of all three spheres or they intersect in pair of points (Figure 4):

$$V(R_i, R_j, R_k; D_{ij}, D_{ik}, D_{jk}) = V_i + V_j + V_k \tag{3}$$

$$i, j, k, = 1, 2, 3,$$

where

$$V_i = \frac{H(2d_{ij}d_{ik} - (d_{ij}^2 + d_{ik}^2)\cos t_i)}{3\sin t_i} - \frac{d_{ij}(3R_i^2 - d_{ij}^2)}{3} \arccos \frac{d_{ik} - d_{ij}\cos t_i}{r_{ij}\sin t_i} - \frac{d_{ik}(3R_i^2 - d_{ik}^2)}{3} \arccos \frac{d_{ij} - d_{ik}\cos t_i}{r_{ik}\sin t_i} + \frac{2R_i^3}{3} \arccos \frac{d_{ij}d_{ik} - R_i^2\cos t_i}{r_{ij}r_{ik}}. \tag{4}$$

Here  $H$  is the half-length of common chord connecting the pair of points, where all three spheres intersect:

$$H^2 = \frac{(R_i^2R_j^2 + R_k^2D_{ij}^2)(D_{ik}^2 + D_{jk}^2 - D_{ij}^2)}{2(D_{ij}^2D_{ik}^2 + D_{ij}^2D_{jk}^2 + D_{ik}^2D_{jk}^2) - (D_{ij}^4 + D_{ik}^4 + D_{jk}^4)} + \tag{5}$$



$$\begin{aligned}
 & + \frac{(R_i^2 R_k^2 + R_j^2 D_{ik}^2)(D_{ij}^2 + D_{jk}^2 - D_{ik}^2)}{2(D_{ij}^2 D_{ik}^2 + D_{ij}^2 D_{jk}^2 + D_{ik}^2 D_{jk}^2) - (D_{ij}^4 + D_{ik}^4 + D_{jk}^4)} + \\
 & + \frac{(R_j^2 R_k^2 + R_i^2 D_{jk}^2)(D_{ij}^2 + D_{ik}^2 - D_{jk}^2)}{2(D_{ij}^2 D_{ik}^2 + D_{ij}^2 D_{jk}^2 + D_{ik}^2 D_{jk}^2) - (D_{ij}^4 + D_{ik}^4 + D_{jk}^4)} - \\
 & - \frac{R_i^2 D_{jk}^4 + R_j^2 D_{ik}^4 + R_k^2 D_{ij}^4 + D_{ij}^2 D_{ik}^2 D_{jk}^2}{2(D_{ij}^2 D_{ik}^2 + D_{ij}^2 D_{jk}^2 + D_{ik}^2 D_{jk}^2) - (D_{ij}^4 + D_{ik}^4 + D_{jk}^4)},
 \end{aligned}$$

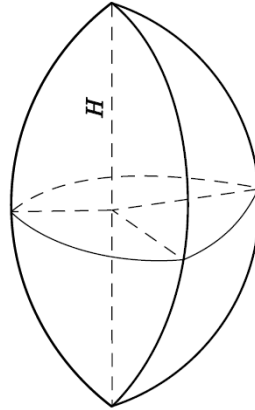


**Figure 4.** Intersection region, when it is bounded by parts of all three spheres or they intersect in pair of points.

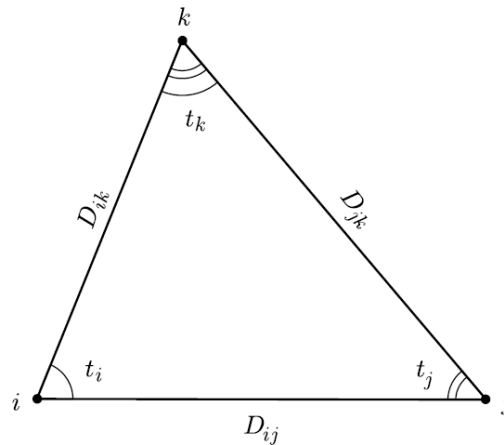


**Figure 5.** Line segments linking centers of spheres and angles between them.

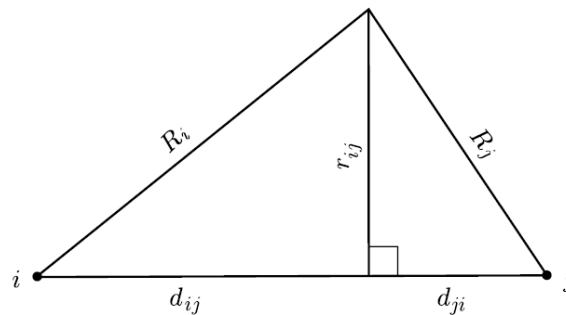


**Figure 6.** Radius of intersection circle between two spheres and distances between that circle and centers of spheres.

$t_i$  is the angle between line segments linking center of  $i$ -sphere with  $j$ - and  $k$ -spheres (Figure 5),

$$\cos t_i = \frac{D_{ij}^2 + D_{ik}^2 - D_{jk}^2}{2D_{ij}D_{ik}}, \quad (6)$$

$r_{ij} = r_{ji}$  are the radius of the intersection circle between  $i$  - and  $j$  -spheres (**Figure 6**),

$$r_{ij} = r_{ji} = \frac{\sqrt{2(R_i^2 R_j^2 + R_i^2 D_{ij}^2 + R_j^2 D_{ij}^2) - (R_i^4 + R_j^4 + D_{ij}^4)}}{2D_{ij}}, \quad (7)$$

and  $d_{ij}$  and  $d_{ji}$  are the distances between that circle and centers of  $i$  - and  $j$  -spheres, respectively (**Figure 6**),

$$d_{ij} = \frac{R_i^2 - R_j^2 + D_{ij}^2}{2D_{ij}} \quad (8)$$

and

$$d_{ji} = \frac{R_j^2 - R_i^2 + D_{ij}^2}{2D_{ij}}. \quad (9)$$

We can see that, the  $V(R_1, R_2, R_3, D_{12}, D_{13}, D_{23})$  is a piecewise combination of algebraic and inverse trigonometric functions. It and its partial derivatives  $\partial V(R_1, R_2, D_{12})/\partial D_{12}$ ,  $\partial V(R_1, R_2, D_{12})/\partial D_{13}$ ,  $\partial V(R_1, R_2, D_{12})/\partial D_{23}$ , respectively, in arguments  $D_{12}$ ,  $D_{13}$ ,  $D_{23}$  are continuous at corresponding boundaries of analyticity. As for the partial derivatives of higher-orders, they are discontinuous functions.

In some cases, the intersection volume between three spheres is reduced to that of a pair of spheres or even a sphere from these three. The general constructing principles of an algorithm of numerical calculations, according to the obtained formulas, have been formulated in the Annex of our Monograph [10].

Above solution of the geometrical problem was provoked by the development of a quasi-classical theory of substance [11]. Within this approach, matrix elements of the secular equation, determining electronic structure of a substance, are analytically expressed by linear combinations of three-center volume integrals, each of which is reduced to a intersection volume of threes spheres. The distances between centers of spheres are the distances between atomic sites of the substance structure; and the radii of spheres are the inner or outer radii of radial layers of quasi-homogeneity of overlapping electron densities of pairs of constituent atoms and electric field potential formed by a third atom. Quasi-classical method, including obtained analytical expression of  $V(R_1, R_2, R_3, D_{12}, D_{13}, D_{23})$ , was successfully tested, e.g., for boron nitride (BN) structural modifications [12].

The application of this expression seems to be useful in the old intersecting spheres model of molecules developed by Antoci [13 – 16]. Relatively recently, same formula was utilized [17] to calculate the total energy of protein structures used in biotechnology.

#### 1.4. More than three spheres and applications

Cases of more than spheres are too difficult to be solved in general. Only attempt of such kind for four, six and twelve spheres belongs to Lustig [5]. All other available reports describe the numerical algorithms.

A fast computer algorithm was presented [18] for complete analytical calculation of van der Waals volumes. This algorithm computes overlaps of any order, not only second- and third-

order atomic spheres overlaps like previously suggested analytical algorithms giving insufficient numerical approximations of the exact van der Waals volumes. It was noted that, practical situations frequently involve six-order overlaps. Computed volumes of 63 chemicals were compared with Monte Carlo measured values.

Frequently, packings of spheres serve as useful models of the geometry of many physical systems and the description of the void region (not occupied by the spheres), in general, composed of disconnected cavities is crucial. An algorithm for decomposing void space into cavities and determining the exact volumes of such cavities in 3D packings of monodisperse and polydisperse spheres was presented in [19].

In [20], it was presented a simple algorithm for the calculation of the volume of a union of spheres of different radii based on the ideas of [18]. Analytical formulas for atomic volumes were derived. This could be achieved without explicit calculation of multiple intersections of the overlapping atoms. Such ideas were implemented for the calculation of the occupied volume inside the polyhedra defined by power Voronoi diagram. This allows calculating the required values for spheres with different radii. Algorithm was applied to the calculation of the solvation shell volume for complex solute molecules in molecular dynamics models of solutions.

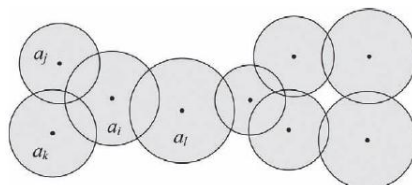


**Figure 7.** Beta-decomposition idea for 2D molecule [21].



**Figure 8.** All of 3D space volume primitives together (including 3D atomic shells) [21].

The mass properties such as the volume of the union of the atoms – given in 3D space set of spherical balls called atoms – are important for many disciplines, particularly for computational and structural chemistry and biology. In [21], algorithms that compute the mass properties of both the union of atoms and their offsets both correctly and efficiently have been proposed. They employ the beta-decomposition approach (**Figure 7**) to decompose the target mass property – volume into a set of primitives (**Figure 8**) – using the simplexes of the beta-complex. Then, the volume is computed by appropriately summing up the volume corresponding to each simplex.

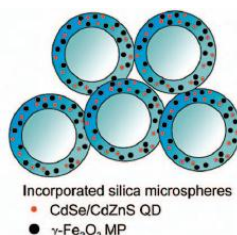


**Figure 9.** Magnetic and fluorescent silica microspheres fabricated by incorporating maghemite ( $\gamma\text{-Fe}_2\text{O}_3$ ) nanoparticles and CdSe / CdZnS core / shell quantum dots into silica shell around preformed silica microspheres of sizes  $\sim 500$  nm [24].

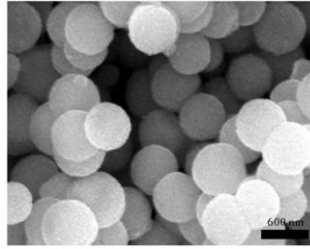


**Figure 10.** Scanning electron microscopy image of monodisperse hollow single crystalline magnetite microspheres synthesized at temperature 180 °C by one-step process through a template-free hydrothermal method [25].

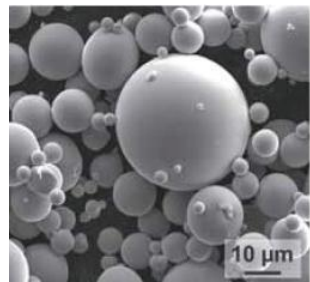


**Figure 11.** Scanning electron microscopy image of gas-atomized Fe-based powder with nominal composition  $\text{Fe}_{74}\text{Mo}_4\text{P}_{10}\text{C}_{7.5}\text{B}_{2.5}\text{Si}_2$ . The powder particle size extends from few up to 50 μm and particle surfaces are very smooth [26].

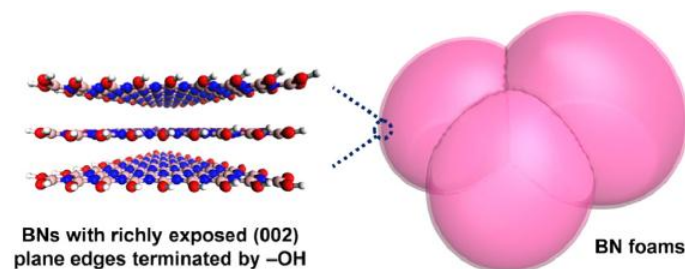


**Figure 12.** Schematic illustration of the preparation of BN foams with richly exposed plane edges that terminated with hydroxyl groups [27].

In general, determination of intersection volume of an union of spheres is important for morphological studies of porous / powdered materials (**Figures 9 – 12**) – see, e.g., [22 – 27].

## 2. Determination of constant orientation workspaces of 6-DOF parallel manipulator “Stewart platform”

Determining the volume of workspace of a Stewart platform is an important technical problem in the field of robotics because currently the 6-DOF parallel manipulator “Stewart platform” (**Figure 13**) is widely industrialized (one of its principal applications is flight simulator). The results of geometrical optimization of different workspaces of this robot [28] have to be used in various applications and also helpful in a better analysis of the Stewart platform itself. So far determination of workspaces of a 6-DOF parallel manipulator has been done only through analytical and numerical methods.



**Figure 13.** Stewart platform.

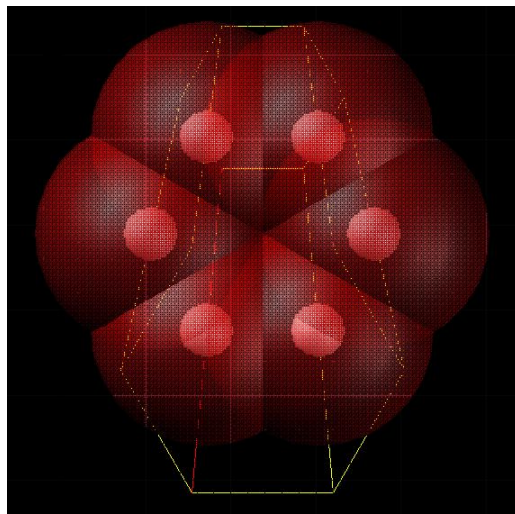


**Figure 14.** Stewart platform with workspace (big) spheres and void (small) spheres inside them.

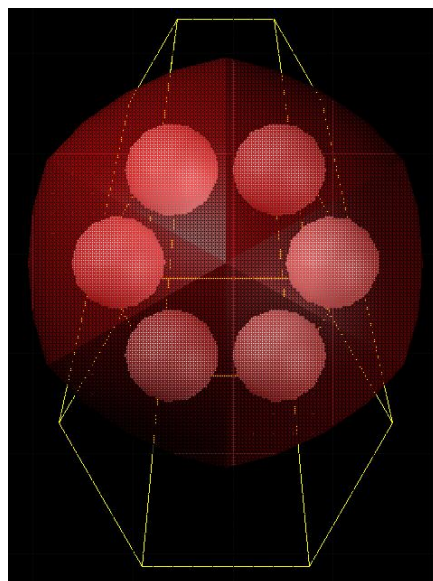


**Figure 15.** Final volume of intersection of six spheres, whose value needs to be find out.

In the geometrical approach, one has to try to find the workspace of the mobile platform (regular hexagon), resting on all the six legs. For each leg, its workspace is a part of a sphere whose size depends upon the dimensions of the leg or a void sphere presented inside each of these spheres (**Figure 14**). The net volume of workspace of a platform is the sum of these parts. We have found out the various combinations in which these spheres will intersect. In **Figure 15**, it is shown a specific case in combinations of spheres of the legs to achieve the theoretical workspace of the platform.

So, in general we need to calculate the volume of intersection of six spheres to determine the workspace volume. On the system under the consideration, the constraints are: (1) equal radii for all six spheres, and (2) equal distances between centers of nearest pairs of spheres, so that all centers of the spheres are in the same plane and are the vertices of a regular hexagon.



**Figure 16.** Intersection of six spheres and void spheres of different radii.

Apart from the intersection of six spheres, which is the theoretical workspace, due to the combination of two legs, to which the mobile platform is attached, another (void) sphere crops up, which intersects with this six sphere intersection. Then, the real workspace, through which the platform moves, is the six sphere intersection minus the void sphere intersection. Thus, there are many specific cases, where to compute the final volume we have to find out the volume of intersection of the intersection of six spheres of equal radii with another sphere of a different radius. In the **Figure 16**, the volume of intersection of six spheres and the spheres of different radii, whose intersection with the former should be calculated, are shown together.

### 3. Volume of intersection of six spheres in special case

#### 3.1. Volume of intersection of six spheres of equal radii centered at vertices of regular hexagon

Thus, we consider six spheres with equal radii of  $R$  centered at the vertices of a regular hexagon with sides of  $D$ . Denote their intersection volume by the function of these two variables:  $V = V(R, D)$ . From the **Figure 18**, we can see that at  $R \leq D$  a pair of spheres centered at the ends of a hexagon's large diagonal do not intersect and then the required volume identically equals to zero:  $V(R, D) \equiv 0$ .

The volume  $V(R, D) > 0$  only at  $R > D$ . Let's analyze this case. Assume that centers of all the spheres are placed in the  $xOy$  plane, i.e., the  $Oz$  axis is perpendicular to the hexagon



plane. When its center coincides with the origin  $O$ , at the altitude of  $z$  the intersection of a sphere with the plane parallel to the  $xOy$  plane is a circle of radius

$$R(z) = \sqrt{R^2 - z^2} \tag{10}$$

(Figure 17). At  $z \neq 0$ , spheres are intersected if  $R(z) > D$ , which is a condition analogous to the condition at  $z = 0$ .

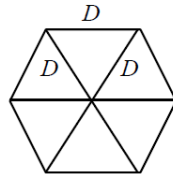


Figure 17. Regular hexagon with sides of  $D$ .

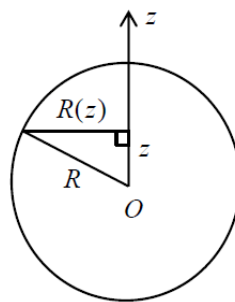


Figure 18. Radius  $R(z)$  of circle of intersection of sphere with plane parallel to hexagon plane at altitude of  $z$ .

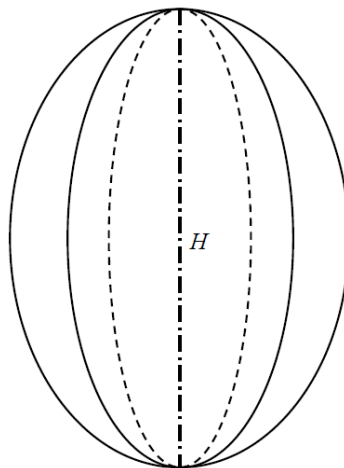


Figure 19. Intersection of six identical spheres.

The intersection of six identical spheres is a convex figure bounded by six identical fragments of all the spheres (Figure 19), for which  $Oz$  is the axis of symmetry of order of 6 and  $xOy$  is the plane of mirror reflection. The coordinates of the vertices of the figure are the solutions of the equation  $R(z) = D$ :

$$z_{\pm} = \pm\sqrt{R^2 - D^2} \tag{11}$$

and, therefore, the height of the intersection figure is

$$H = z_+ - z_- = 2\sqrt{R^2 - D^2} . \tag{12}$$

Let  $S(z)$  denotes the cross section area of the figure at the altitude of  $z$ . It is evident that the volume can be calculated as the following integral:

$$V(R, D) = \int_{z_-}^{z_+} dz S(z) = 2 \int_0^{\sqrt{R^2 - D^2}} dz S(z). \quad (13)$$

In this section, there are six line-segments that connect the spheres' endpoints with the central point placed at the  $Oz$  axis, which divide this cross section into six identical parts. If we denote their areas by  $s(z)$  we will have

$$V(R, D) = 12 \int_0^{\sqrt{R^2 - D^2}} dz s(z). \quad (14)$$

Each of these plane figures are bounded by an arc of a circle of radius  $R(z)$  and the two sides of an equilateral triangle, the third side of which is a chord subtending the said arc (**Figure 20**). Consequently, the area  $s(z)$  is equal to the sum of areas of the circle-segment  $s_{Segment}(z)$  of radius  $R(z)$  and the equilateral triangle  $s'_{Triangle}(z)$ , one side of which coincides with the chord bounding the segment. Denote the side of the triangle, i.e., chord length, by  $X(z)$ . The area of the circle-segment can be calculated as the difference between the areas of the corresponding sector  $s_{Sector}(z)$  and isosceles triangle  $s''_{Triangle}(z)$  with slopes of  $R(z)$  and base of  $X(z)$ . Thus we can write down:

$$\begin{aligned} s(z) &= s_{Segment}(z) + s'_{Triangle}(z) = \\ &= (s_{Sector}(z) - s''_{Triangle}(z)) + s'_{Triangle}(z) = \\ &= s_{Sector}(z) - (s''_{Triangle}(z) - s'_{Triangle}(z)). \end{aligned} \quad (15)$$

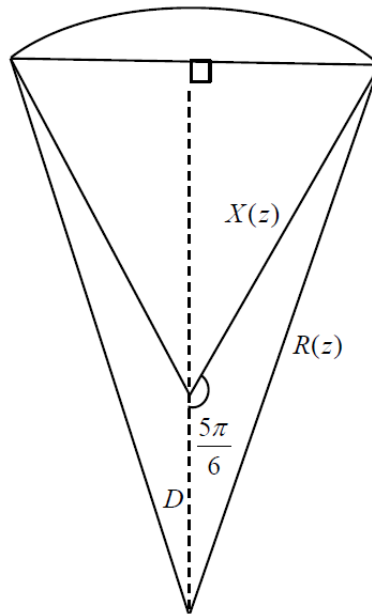


**Figure 20.** One of six identical parts of cross section of intersection of six identical spheres at altitude of  $z$  (I).

According to the law of cosines,

$$R^2(z) = D^2 + X^2(z) - 2DX(z) \cos \frac{5\pi}{6} \quad (16)$$

and then

$$X(z) = \sqrt{R^2 - \frac{1}{4}D^2 - z^2} - \frac{\sqrt{3}}{2}D. \quad (17)$$

Since the base of the isosceles triangle equals to a side of the equilateral triangle  $X(z)$ , and the difference in heights of these triangles at any altitude is  $D$ , the difference of their areas is easily calculated:

$$s''_{Triangle}(z) - s'_{Triangle}(z) = \frac{1}{2}DX(z) = \frac{1}{2}D \left( \sqrt{R^2 - \frac{1}{4}D^2 - z^2} - \frac{\sqrt{3}}{2}D \right). \quad (18)$$

It is convenient to calculate separately its contribution in the required integral:

$$\begin{aligned} V_{Triangles} &= 6D \int_0^{\sqrt{R^2-D^2}} dz \left( \sqrt{R^2 - \frac{1}{4}D^2 - z^2} - \frac{\sqrt{3}}{2}D \right) = \\ &= \frac{3}{4}D(4R^2 - D^2) \arcsin 2\sqrt{\frac{R^2 - D^2}{4R^2 - D^2}} - \frac{3}{2}D^2\sqrt{3(R^2 - D^2)}. \end{aligned} \quad (19)$$

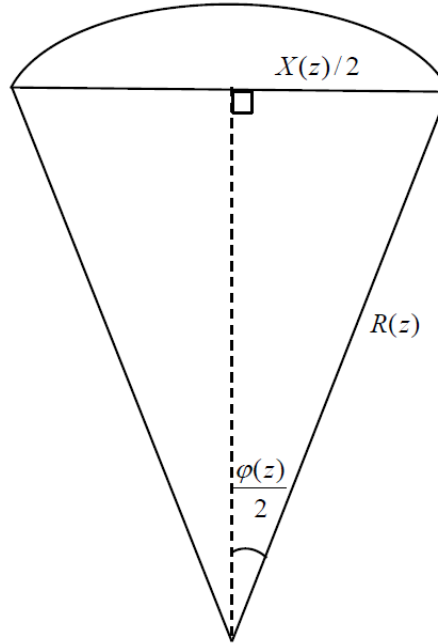


**Figure 21.** One of six identical parts of cross section of intersection of six identical spheres at altitude of  $z$  (II).

From **Figure 21**, we find the sector angle  $\varphi(z)$ :

$$\varphi(z) = 2 \arcsin \frac{1}{2} \frac{\sqrt{R^2 - \frac{1}{4}D^2 - z^2} - \frac{\sqrt{3}}{2}D}{\sqrt{R^2 - z^2}}. \quad (20)$$

Thus, area of the sector is

$$s_{Sector}(z) = \frac{1}{2}\varphi(z)R^2(z) = (R^2 - z^2) \arcsin \frac{1}{2} \frac{\sqrt{R^2 - \frac{1}{4}D^2 - z^2} - \frac{\sqrt{3}}{2}D}{\sqrt{R^2 - z^2}}. \quad (21)$$

As for the corresponding contribution in the required integral, it equals to

$$\begin{aligned}
 V_{Sector} &= 12 \int_0^{\sqrt{R^2-z^2}} dz (R^2 - z^2) \arcsin \frac{1}{2} \frac{\sqrt{R^2 - \frac{1}{4}D^2 - z^2} - \frac{\sqrt{3}}{2}D}{\sqrt{R^2 - z^2}} = \\
 &= 8R^3 \arcsin \sqrt{\frac{R^2 - D^2}{4R^2 - D^2}} - \frac{1}{4}D(12R^2 + D^2) \arcsin 2\sqrt{\frac{R^2 - D^2}{4R^2 - D^2}} - \frac{1}{2}D^2 \sqrt{3(R^2 - D^2)}
 \end{aligned} \tag{22}$$

and we get

$$\begin{aligned}
 V(R, D) &= V_{Sector} - V_{Triangles} = \\
 &= 8R^3 \arcsin \sqrt{\frac{R^2 - D^2}{4R^2 - D^2}} - \frac{(12R^2 - D^2)D}{2} \arcsin 2\sqrt{\frac{R^2 - D^2}{4R^2 - D^2}} + D^2 \sqrt{3(R^2 - D^2)}.
 \end{aligned} \tag{23}$$

As expected the resulting formula gives 0 when  $R = D$ ,

$$V(R, D)|_{R=D} = 0, \tag{24}$$

while at  $R \gg D$  asymptotically tends to the volume of sphere:

$$V(R, D)|_{R \gg D} \approx \frac{4\pi R^3}{3}. \tag{25}$$

Finally, the problem's solution is the following expression:

$$\begin{aligned}
 V(R, D) &= \\
 &= 0 \qquad R \leq D \\
 &= 8R^3 \arcsin \sqrt{\frac{R^2 - D^2}{4R^2 - D^2}} - \left(6R^2 - \frac{D^2}{2}\right)D \arcsin 2\sqrt{\frac{R^2 - D^2}{4R^2 - D^2}} + D^2 \sqrt{3(R^2 - D^2)} \quad R \geq D.
 \end{aligned} \tag{26}$$

### 3.2. Volume of intersection of six spheres of equal radii with spheres of different radii

Is the intersection of the intersection of six spheres of equal radii, centered at vertices of a regular hexagon, with the sphere of a different radius, centered in the hexagon plane, same as the intersection of two spheres of unequal radii? In general, it is not. But, for some constrains for geometric parameters, the standard formula of the volume of intersection of two spheres will work.

As above  $R$  is the radius of a sphere, one of six spheres with equal radii centered at the vertices of a regular hexagon,  $D$  is the side of that regular hexagon, and  $R > D$  is the condition of existence of the intersection between these six spheres. For given  $R$  and  $D$ , the shortest distance  $X$  from the center of the regular hexagon to the surface of a sphere with radius  $R$  can be calculated as:

$$X = \sqrt{R^2 - \frac{D^2}{4} - \frac{\sqrt{3}}{2}D}. \tag{27}$$

Let's introduce two additional geometric parameters:  $r$  – the radius of the sphere that intersects with one of six spheres with radius of  $R$  and  $d$  – the distance between centers of spheres with radii  $R$  and  $r$ . Note that, here we consider the symmetric case, when centers  $S$  and  $s$  of two spheres with radii  $R$  and  $r$ , respectively, and center  $O$  of regular hexagon are located at same line (**Figure 22**).

Asymmetric cases also can be considered analytically, but relations will be significantly complicated.

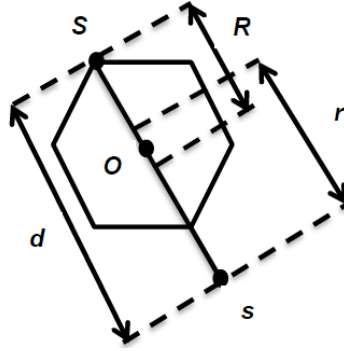


Figure 22. Radii and distances between centers of two intersected spheres.

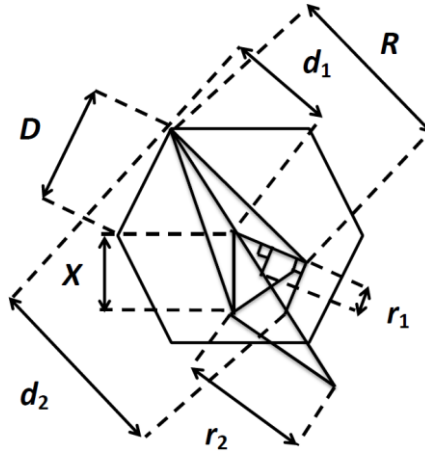


Figure 23. Critical radii and critical distances between centers of two intersected spheres.

From the **Figure 23**, one can see that there are two critical distances,  $d_1$  and  $d_2$ , between centers of spheres with radii  $R$  and  $r$ :

$$d_1 = D \tag{28}$$

and

$$d_2 = D + \frac{2X}{\sqrt{3}}, \tag{29}$$

and correspondingly two critical values  $r_1$  and  $r_2$  of the sphere with radius  $r$ :

$$r_1 = \frac{d - D}{2} \tag{30}$$

and

$$r_2 = \sqrt{(d - D)^2 - \sqrt{3}(d - D)X + X^2}. \tag{31}$$

There are three different cases:

- when  $0 \leq d < d_1$  general formula for intersection of two spheres does not work;
- when  $d_1 \leq d < d_2$  general formula for intersection of two spheres works if  $0 < r \leq r_1$ ; and
- when  $d_2 \leq d < \infty$  general formula for intersection of two spheres works if  $r_1 < r \leq r_2$ .

When the formula works, the volume  $V(R, r, d)$  of intersection of two spheres is continuous piecewise algebraic function of variables  $R$ ,  $r$  and  $d$ :

$$V(R, r, d) = \tag{32}$$

$$= \frac{4\pi r^3}{3} \quad 0 \leq d < R - r$$

$$= \frac{\pi(R+r-d)^2((R+r+d)^2 - 4(R^2 - Rr + r^2))}{12d} \quad |R-r| \leq d < R+r$$

$$= 0 \quad R+r \leq d < \infty.$$

Note that, the condition  $0 \leq d < r - R$ , when the volume of intersection of two spheres coincides with the volume  $4\pi R^3/3$  of a sphere of radius  $R$  is excluded in the system under the consideration because the intersection of six spheres is only a part of a sphere with radius  $R$ .

#### 4. Conclusions

Above described general procedure on how to determine the volume of intersection of six spheres with all the constraints was successfully applied to volume computation in a number of specific cases in the field of parallel manipulators.

Regarding the numerical application of the formula for intersection volume of two spheres in the Stewart platform problem, it has proven that in  $\sim 30\%$  of tested cases it was found to be applicable. In the rest  $\sim 70\%$  of cases, if  $d$  is between  $d_1$  and  $d_2$ ,  $r$  was found to be greater than  $r_1$  (which is violation of a condition) and if  $d$  is itself greater than  $d_2$ , then  $r$  was greater than  $r_2$  (violation of other condition), what makes these cases indeterminable.

#### References

1. A. D. Alexandrov, N. Yu. Netsvetaev. *Geometry*. 1990, Moscow: Nauka.
2. M. V. Favorin. *Moments of Inertia of Bodies*. Reference Book. 1977, Moscow: Mashinostroenie.
3. L. Chkhartishvili. Quasi-classical calculation of the crystalline band structure. *Trans. Georg. Tech. Univ.*, 1996, 3 (411), 45-52.
4. M. J. D. Powell. The volume internal to three intersecting hard spheres. *Mol. Phys.*, 1964, 7, 6, 591-592.
5. R. Lustig. Surface and volume of three, four, six and twelve hard fused spheres. *Mol. Phys.*, 1985, 55, 2, 305-317.
6. K. D. Gibson, H. A. Scheraga. Volume of the intersection of three spheres of unequal size. A simplified formula. *J. Phys. Chem.*, 1987, 91, 15, 4121-4122.
7. K. D. Gibson, H. A. Scheraga. Erratum: Volume of the intersection of three spheres of unequal size. A simplified formula (*Journal of Physical Chemistry* (1987) 91, (4121)). *J. Phys. Chem.*, 1987, 91, 24, 6326-6326.
8. L. Chkhartishvili. Method of the analysis of crystalline electronic energy spectrum based on the quasi-classically calculated characteristics of atomic orbitals. *Trans. Georg. Tech. Univ.*, 1997, 3 (414) – GTU 75 Anniv. Ed., 205-213.
9. L. S. Chkhartishvili. Volume of the intersection of three spheres. *Math. Notes*, 2001, 69, 3, 421-428.
10. L. Chkhartishvili. *Iterative and Transcendental Solutions of Algebraic Equations (Monograph)*. 2012, Saarbrücken: Palmarium Acad. Publ.
11. L. Chkhartishvili. *Quasi-Classical Theory of Substance*. 2004, Tbilisi: Tech. Univ. Press.
12. L. Chkhartishvili. *Quasi-Classical Method of Calculation of Substance Structural Parameters and Electron Energy Spectrum*. 2006, Tbilisi: Tbilisi Univ. Press.



13. S. Antoci. The use of discontinuous trial functions in the computation of the electronic structure of molecules: Calculation of the ESCA spectrum of tetrathiofulvalene (TTF). *J. Chem. Phys.*, 1975, 63, 2, 697-701.
14. S. Antoci, L. Mihich. Removal of the discontinuities of the trial function in the computation of the electronic structure of molecules by the intersecting spheres model: Evaluation of the equilibrium geometry of N<sub>2</sub> and H<sub>2</sub>O. *J. Chem. Phys.*, 1976, 64, 4, 1442-1445.
15. S. Antoci. An asymptotically exact form of the intersecting spheres model of molecules: Formulation. *J. Chem. Phys.*, 1976, 65, 1, 253-256.
16. S. Antoci, L. Barino. An asymptotically exact form of the intersecting spheres model of molecules: Computation of the total energy and the ESCA spectra of H<sub>2</sub><sup>+</sup>, Li<sub>2</sub>, N<sub>2</sub>, F<sub>2</sub> and H<sub>2</sub>O. *J. Chem. Phys.*, 1976, 65, 1, 257-260.
17. A. Shirvani, 2009 – *Private Communication*.
18. M. Petitjean. On the analytical calculation of van der Waals surfaces and volumes: Some numerical aspects. *J. Comput. Chem.*, 1994, 15, 5, 507-523.
19. S. Sastry, D. S. Corti, P. G. Debenedetti, F. H. Stillinger. Statistical geometry of particle packings. I. Algorithm for exact determination of connectivity, volume, and surface areas of void space in monodisperse and polydisperse sphere packings. *Phys. Rev. E*, 1997, 56, 5, 5524-5532.
20. V. P. Voloshin, A. V. Anikeenko, N. N. Medvedev, A. Geiger. An algorithm for the calculation of volume and surface of unions of spheres. Application for salvation shells. In: *Proc. 8th Int. Symp. Voronoi Diag. Sci. & Eng.*, 2011, 5988932, 170-176.
21. D.-S. Kim, J. Ryu, H. Shin, Y. Cho. Beta-decomposition for the volume and area of the union of three-dimensional balls and their offsets. *J. Comput. Chem.*, 2012, 33, 1252-1273.
22. B. T. Holland, Ch. F. Blanford, A. Stein. Synthesis of macroporous minerals with highly ordered three-dimensional arrays of spheroidal voids. *Science*, 1998, 281, 5376, 538-540.
23. A. Fernandez-Nieves, D. R. Link, D. Rudhart, D. A. Weitz. Electro-optics on bipolar nematic liquid crystal droplets. *Phys. Rev. Lett.*, 2004, 92, 105503, 1-4.
24. N. Insin, J. B. Tracy, H. Lee, J. P. Zimmer, R. M. Westervelt, M. G. Bawendi. Incorporation of iron oxide nanoparticles and quantum dots into silica microspheres. *ACS Nano*, 2008, 2, 2, 197-202.
25. F. Marquez, T. Campo, M. Cotto, R. Polanco, R. Roque, P. Fierro, J. M. Sanz, E. Elizalde, C. Morant. Synthesis and characterization of monodisperse magnetite hollow microspheres. *Soft Nano Sci. Lett.*, 2011, 1, 1, 25-32.
26. S. Pauly, L. Lober, R. Petters, M. Stoica, S. Scudino, U. Kuhn, J. Eckert. Processing metallic glasses by selective laser melting. *Mater. Today*, 2013, 16, 1-2, 37-41.
27. Q. Weng, Y. Ide, X. Wang, X. Wang, Ch. Zhanga, X. Jiang, Y. Xue, P. Dai, K. Komaguchi, Y. Bando, D. Golberg. Design of BN porous sheets with richly exposed (002) plane edges and their application as TiO<sub>2</sub> visible light sensitizer. *Nano Energy*, 2015, 2015, 16, 19-27.
28. S. G. Narasimhan, S. Raghuraman, K. Venkatasubramanian, A. K. Dash. Determination of constant orientation workspace of a Stewart platform by geometrical method. *Appl. Mech. & Mater.*, 2015, 813-814, 997-1001.

## MORPHOLOGICAL STUDIES OF BISMUTH NANOSTRUCTURES PREPARED BY HYDROTHERMAL MICROWAVE HEATING

O. V. Kharissova, M. Osorio, B. I. Kharisov

Universidad Autonoma de Nuevo Leon  
Monterrey, Mexico  
bkhariss@hotmail.com

Accepted April 30, 2015

### Abstract

Elemental bismuth nanoparticles and nanotubes were obtained *via* microwave hydrothermal synthesis starting from bismuth oxide ( $\text{Bi}_2\text{O}_3$ ) in the range of temperatures 200 – 220 °C for 10 – 45 min. The formed nanostructures were studied by scanning electron microscopy (SEM) and transmission electron microscopy (TEM). The relationship between reaction parameters and shape of the formed nanostructures is discussed. Molecular mechanics (MM+), semiempiric (PM6) and density functional theory (DFT) B3LYP methods are applied for additional characterization of bismuth nanotubes.

### Introduction

Metallic bismuth is an important element, having a lot of distinct industrial applications as a component of low-melting alloys, catalysts, for production of polonium in nuclear reactors and tetrafluorhydrazine, among others [1, 2]. High-purity metal is used, in particular, for measuring super-strong magnetic fields. Bismuth in nanostructured forms has been mentioned in some recent monographs [3 – 7], reviews [8 – 10], patents [11, 12], and a lot of experimental articles. Bismuth nanoparticles [13], nanopowders, nanowires, nanofilms and other nanostructured forms including nanotubes [14 – 22] have been produced by a host of methods; some representative examples are shown in **Table 1**. Examined techniques for obtaining its nanoforms include chemical reduction of bismuth salts, electrochemical deposition, laser ablation, ultrasonic and microwave treatment, electron- and ion-beam methods, among other methods. As a result of reactions from the same precursors, bismuth can be obtained in various forms depending on reaction conditions, which may influence considerably on the form and / or particle size in the resulting phase. Metallic bulk bismuth, its salts or complexes usually serve as precursors in these reactions.

Among the methods above and a series of other techniques [23], applied for preparation of bismuth nanoforms, *microwave heating* (MW) has been also used to obtain bismuth nanostructures. Thus, microwave treatment (**Table 1**) of bulk bismuth in air in a domestic MW-oven (power 800 W and frequency 2.45 GHz) led to formation of bismuth nanoparticles (60 – 70 nm) with  $\text{Bi}_2\text{O}_3$  impurities, in a difference of a similar treatment in vacuum, when Bi nanotubes formed for 5 – 15 min. The optimal MW-heating process time was 60 min; the process was found to be highly reproducible and easy.

**Table 1.** Examples of production of distinct bismuth nanostructures.

Precursor	Conditions / Techniques	Products	References
Bismuth granules	Stirring in paraffin oil above 280 °C for 10 h	Spherical-shape of the nanoparticles (average diameter of 50 nm), Bi <sub>2</sub> O <sub>3</sub> admixture	[24]
Molten bismuth	In the anodic aluminium oxide template using a hydraulic pressure method	The Bi nanowires, whose majority were single crystalline	[25, 26]
Sodium bismuthate	<i>In situ</i> electron-beam irradiation in a TEM	Nanoparticles (6 nm) with a rhombohedral structure	[27]
	Reduction of sodium bismuthate with ethylene glycol in the presence of poly(vinylpyrrolidone) or acetone	Single-crystalline bismuth nanowires, nanospheres, and nanobelts, as well as and Bi / Bi <sub>2</sub> O <sub>3</sub> nanocables	[28]
BiCl <sub>3</sub>	Reduction of BiCl <sub>3</sub> with <i>t</i> -BuONa and sodium hydride at 65 °C.	Large quantities of colloidal Bi(0) nanoparticles with a diameter in the range 1.8 – 3.0 nm	[29, 30]
	Reduction of BiCl <sub>3</sub> with KBH <sub>4</sub> at room temperature	Nanoparticles with average diameter of about 30 – 80 nm	[31]
	Reduction with Fe powder, 150 °C, 12 h	Dandelion-shape microspheres of ordered bismuth nanowires	[32]
	Metallic zinc powder	Bi nanotubes with diameter of 3 – 5 nm and length up to several micrometers.	[33]
BiI	<i>n</i> -Butyllithium	Bi nanotubes with inner diameter of 4.5 nm and an outer diameter of 6 nm	[34]
[Bi(NO <sub>3</sub> ) <sub>3</sub> ·5H <sub>2</sub> O] Ethylene diamine	Solvothermal method	Single-crystalline metallic bismuth nanowires (average diameter about 20–30 nm and lengths range from 0.2 to 2.5 μm)	[35]
[Bi(NO <sub>3</sub> ) <sub>3</sub> ·5H <sub>2</sub> O] Hydrazine		Bi nanotubes with diameters of 5 nm and lengths 0.5 – 5 μm	[36]
Bi <sub>2</sub> O <sub>3</sub> Ethylene glycol		Bismuth nanotubes (diameter about 3 – 6 nm and length up to 500 nm).	[37]
Bismuth perchlorate	Radiolytic reduction of aqueous solution of the Bi salt with or without polymers	The polymers are used for stabilization of formed nanoparticles	[38]
[Ni(COD) <sub>2</sub> ] and [Bi <sub>2</sub> Ph <sub>4</sub> ]	The simultaneous decomposition of <i>bis</i> (cyclooctadiene)nickel(0) [Ni(COD) <sub>2</sub> ] and tetraphenyldibismuthine [Bi <sub>2</sub> Ph <sub>4</sub> ] in tetrahydrofuran (THF) at reflux temperature	Nickel–bismuth alloy nanoparticles with an average size of 8 – 10 nm, NiBi nanowires, pure Bi nanorods with diameters of about 50 nm and superconducting NiBi particles, depending on the synthesis conditions	[39, 40]
Layered Bi(SC <sub>12</sub> H <sub>25</sub> ) <sub>3</sub> with 31.49 Å spacing	Structure-controlling solventless thermolysis	Bismuth nanofilms (average thickness of 0.6 nm) and monodisperse layered Bi nanorhombuses with an average edge length of 21.5 nm and thickness of 0.9 nm	[41]
Bulk bismuth	In air in a domestic MW-oven (power 800 W and frequency 2.45 GHz)	Bi nanoparticles with or without Bi <sub>2</sub> O <sub>3</sub> impurities (depending on synthesis conditions)	[42 – 44]

In this report, we present nanostructures of bismuth, observed as a result of synthesis in the conditions of microwave hydrothermal procedure, and calculation results for their different forms.

## Computational methods applied

16 structures were optimized using the following computational methods: molecular mechanics (MM+), semiempiric (PM6) and Density Functional Theory DFT (B3LYP), implemented in the programs Hyperchem 8.0.4 and Gaussian 09. All structures were characterized calculating their vibration modes. The results were visualized in the program Chemcraft v1.6. In this work, the geometries for bismuth nanotubes with both open and closed extremes were optimized. In both cases, the Hamada index  $m$  was used; it corresponds to armchair ( $m=n$ ) and zigzag ( $m=0$ ) configurations of Bi nanotubes, varying the  $n$  value in the range of 3 – 6. The tubular structures with open extremes were initially constructed on the basis of carbon atoms using the program VMD 1.8.7 (University of Illinois). Then the program Chemcraft was applied to change them to bismuth atoms. The geometry was optimized using the molecular mechanics method MM+ using the program HyperChem v8.0. To generate closed tubes (knowing that bismuth atoms prefer to form tri-coordinated structures [45]), bismuth atoms were manually added step-by-step, optimizing every time by molecular mechanics method (MM+), in order to form the pentagons in the extremes (the presence of pentagons generate curvature defects in the nanostructures) up to closing the structure.

A major precision optimization was carried out using the semiempiric method PM6, implemented in the program Gaussian 09. Also, the molecular dynamic calculations were made with 2,000 steps with 1 ps each one at ambient temperature (298.15 °K) in the same method. For the optimized structures, where imaginary vibrational modes were not found, the calculations were refined at a higher level using the method B3LYP in combination with a series of bases def2-SVP.

## Experimental

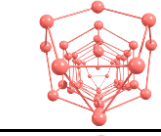
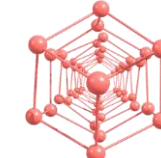
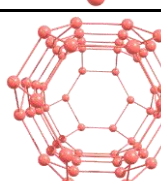
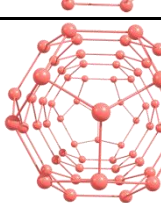
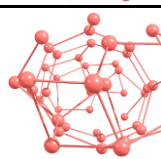
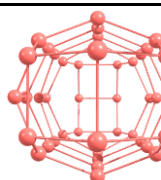
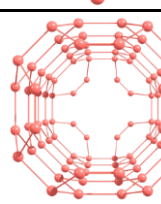
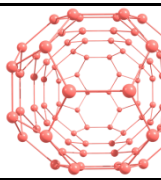
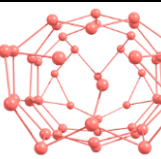
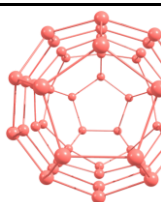
The reactions were carried out in a teflon autoclave (equipment MARS-5), using dibismuth trioxide as a precursor and ethyleneglycol (EG) as a reductant. Due to the necessity to exceed boiling point of EG (187 °C) and security limits of the equipment, the syntheses were made in the range 200 – 220 °C, reaching pressure close to 300 psi. The reaction times were 10, 15, 30 and 45 min. The formed nanostructures were studied by scanning electron microscopy (SEM, equipment Hitachi S-5500) and transmission electron microscopy (TEM, equipment JEOL 2010-F), both at University of Texas at San Antonio, as well as in a high-resolution HRTEM Hitachi H-9500 (high voltage 300 kV), with image recording using CCD camera ( $4k \times 2.6k$ ) (University of Texas at Arlington). The samples were prepared by ultrasonic dispersing of formed products and further application of suspension onto a lacey grid (Lacey formvar / carbon, 300 mesh, Copper approx. grid hole size:  $63\mu\text{m}$ ), purchased in *Ted Pella, Inc.* Reproducibility of experiments was good and yields of bulk products corresponded to the range 85 – 93 %. The obtained images were analyzed with use of the *Gatan* program [46].

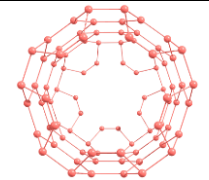
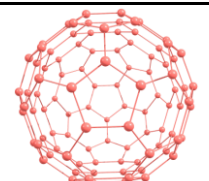
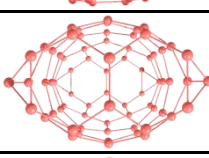
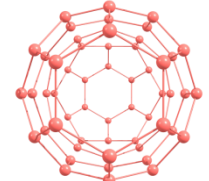
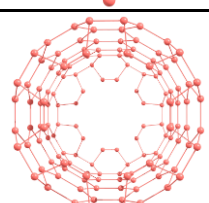
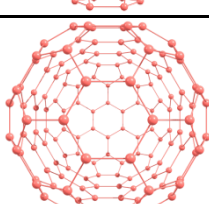
## Results and discussion

### *Theoretic calculations*

The size of bismuth nanotubes was selected as major of 144 atoms. zigzag- and armchair-type nanotubes with closed or open tube extremes were discussed (**Table 2**). A structure with major symmetry was tried to be constructed in each case.

Table 2. Bismuth nanotubes, optimized with use of PM6 method.

$n$	$m$	Structural type	Symmetry	No. atoms	Image	Diameter ( $\text{\AA}$ )
3	0	open	$C_2$	60		5.34
3	0	closed	$C_2$	62		6.70
3	3	open	$C_{3v}$	60		9.92
3	3	closed	$C_{3v}$	62		9.93
4	0	open	$D_{4h}$	48		8.50
4	0	closed	$C_{2v}$	42		8.39
4	4	open	$C_{4v}$	96		13.32
4	4	closed	$C_{2v}$	92		12.98
5	0	open	$C_{5v}$	60		9.15
5	0	closed	$C_{5v}$	50		10.35

5	5	open	$C_{5v}$	90		16.72
5	5	closed	$C_i$	100		16.61
6	0	open	$C_{6v}$	72		12.42
6	0	closed	$C_{3v}$	60		12.16
6	6	open	$C_{6v}$	144		20.14
6	6	closed	$C_{6v}$	144		19.92

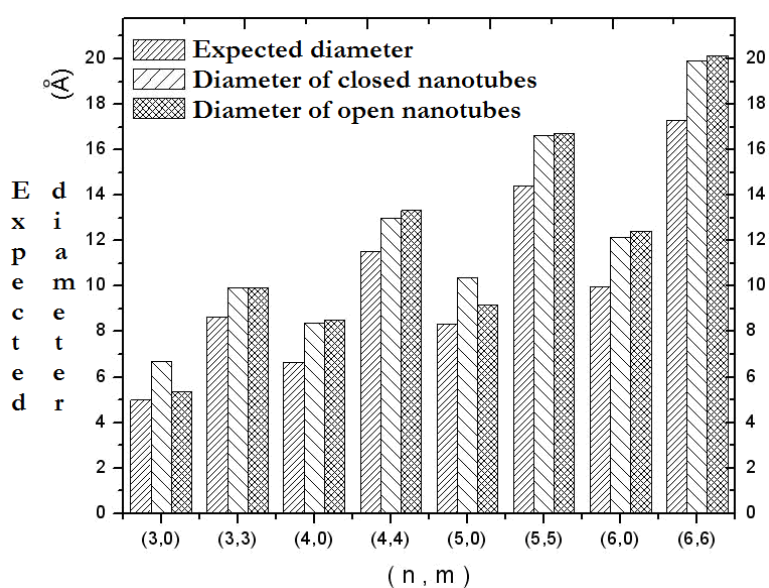


**Figure 1.** A comparison of expected diameters according to the equation (1) and the obtained by PM6 method.

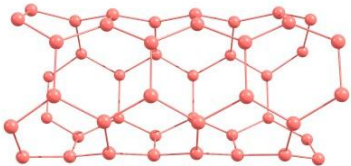
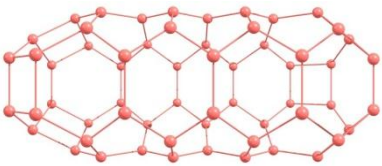
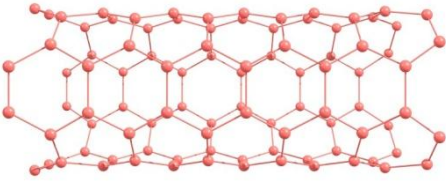
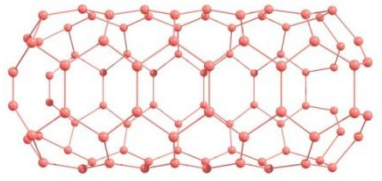
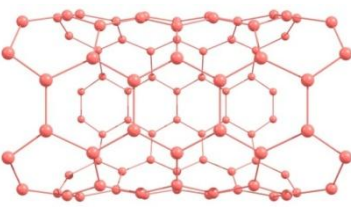
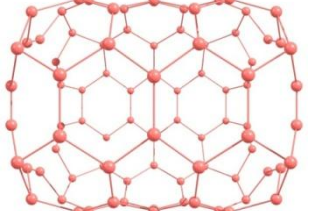
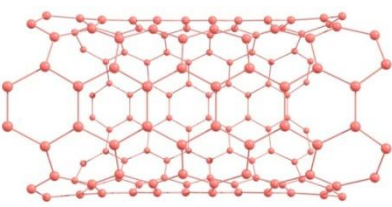
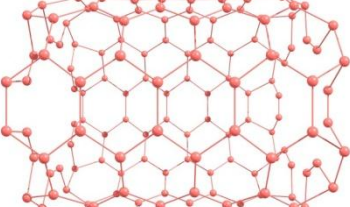


We propose that the diameter of bismuth nanotube in function of Hamada indexes is given by the equation (1),

$$d = \frac{a\sqrt{n^2 + m^2 + nm}}{\pi}, \quad (1)$$

in which the value of unitary vector for a sheet of bismuth hexagons is  $a = 5.23 \text{ \AA}$ . This equation considers that the nanotubes are formed by regular hexagons. However, after relaxing this structure, the change of bond angles and lengths generates slightly major diameters. A comparison of expected diameters according to the equation (1) is shown in **Figure 1**. It is seen that, for the armchair-type nanotubes, this difference increases conformably with increase of the Hamada index. In case of zigzag-type nanotubes, the difference is expressed more clearly for diameters of open nanotubes.

**Table 3.** Comparison of nanotube extremes before and after optimization of nanostructures.

$(n, m)$	Before optimization	After optimization with PM6
(3,3)		
(4,4)		
(5,5)		
(6,6)		

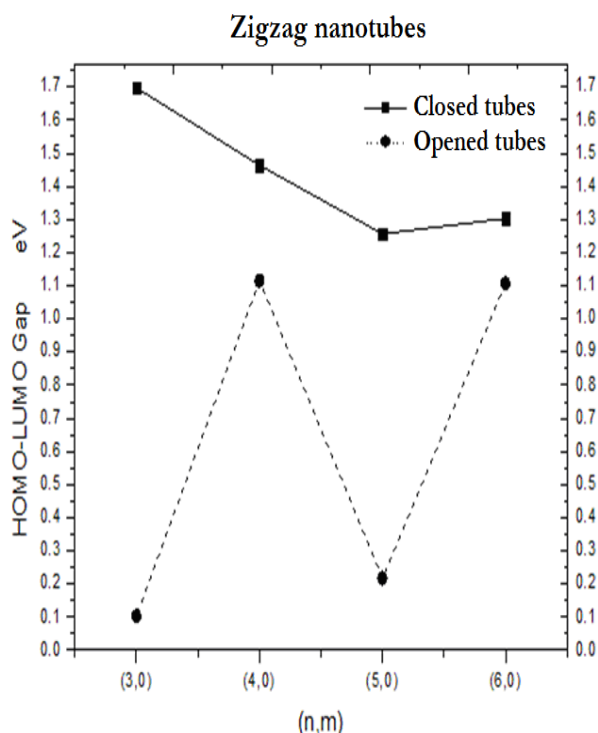
As it was mentioned above, Bi atoms were added to form pentagons in the tube extremes and the molecular mechanics were used to be able to close manually the nanotubes. However, optimizing the geometry of the open nanotubes with PM6 program, the tendency to close the extremes in these structures is observed in all cases. For nanotubes with diameters less than 10 nm, this is reached forming squares in the extremes (**Table 3**), but for higher-diameter structures, structure relaxation is insufficient for closure the extremes. So, it is expected that these structures are less stable in comparison with those closed manually. Even, relaxing the open (5, 0) and open (4, 0) structures, the atoms in the tube wall displace to the interior zone and to the extremes, losing tubular form (**Table 2**).

It is known in computational chemistry, that the stability of a molecule is only relative in comparison with another molecule with equal type and number of atoms and this is associated with potential energy surfaces in the structures. So, in order to compare nanotube energies, the nanotubes with equal number of atoms were constructed for the cases of the open (6, 6) and closed (6, 6) tubes. Both model tubes are formed of 144 atoms. Their energy difference of 132.924 kcal / mol was obtained, taking in account the closed structure (6, 6) (0 kcal / mol). These energies were calculated for the same stationary point (potential energy surface), using the DFT method (B3LYP / SBKJC VDZ ECP) resulting more precise results. A similar analysis was carried out for the open tubes, formed of 60 atoms ((3, 0) and (3, 3), zigzag and armchair, respectively). For this comparison, the less-energy structures are of a zigzag type, which are taken as a reference to obtain  $\Delta E$  (see Table 4).

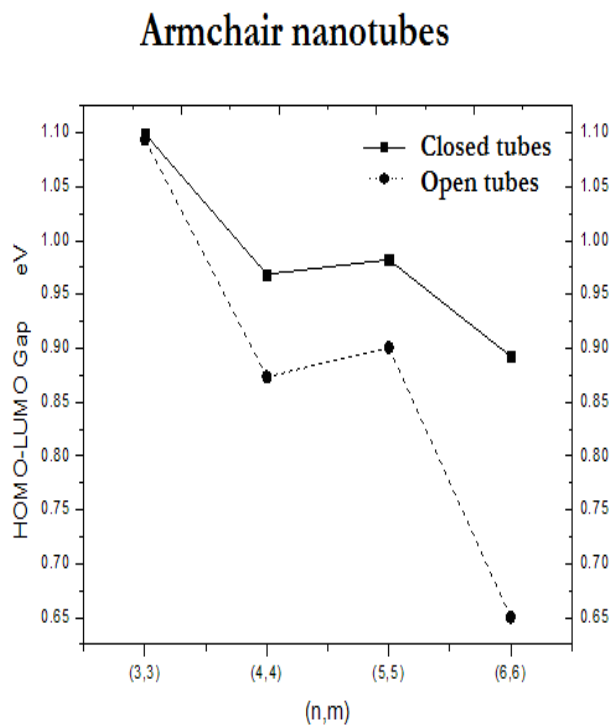
**Table 4.** Comparison of nanotube energies for zigzag and armchair types.

Structure type	Index	Form	Relative energy
Open nanotubes	(3,0)	zigzag	$\Delta E = 22.88$ kcal / mol
	(3,3)	armchair	
Closed nanotubes	(3,0)	zigzag	$\Delta E = 33.04$ kcal / mol
	(3,3)	armchair	

Using these calculations, the gap between HOMO and LUMO molecular orbitals was analyzed. **Figures 2** and **3** show the structures of the type zigzag ( $m=0$ ) and armchair, respectively. It is observed in both graphics, that a better conductivity corresponds to open nanotubes. For the armchair-type nanotubes, the tendency to improve the conductivity is seen conformably increase of diameter.

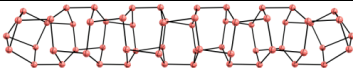
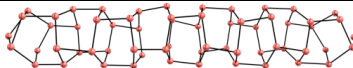
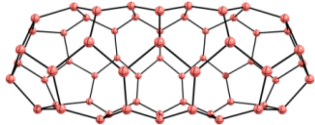
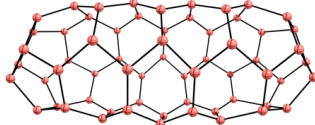
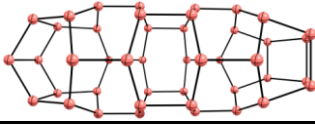
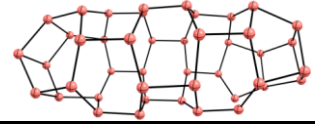
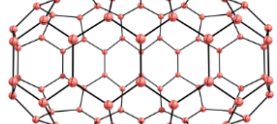
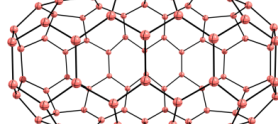
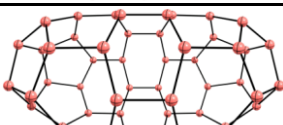
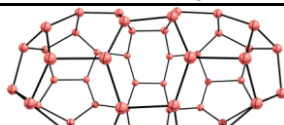
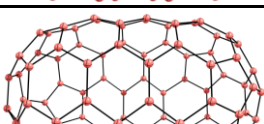
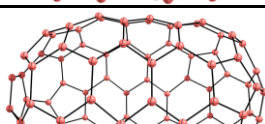
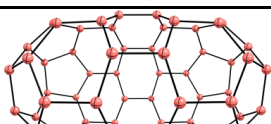
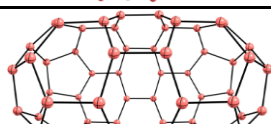
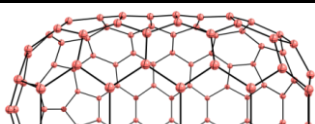
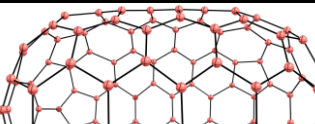


**Figure 2.** Gap between the HOMO–LUMO for zigzag tubes.



**Figure 3.** Gap between the HOMO–LUMO for armchair tubes.

**Table 5.** Molecular dynamics calculations for closed nanotubes.

$(n, m)$	Structure before DM	Structure after DM
(3,0)		
(3,3)		
(4,0)		
(4,4)		
(5,0)		
(5,5)		
(6,0)		
(6,6)		

Calculations of vibration modes suggest difficulties to be stable structures for those with more than one vibration imaginary frequency. For bismuth nanotubes, using these calculations, two negative frequencies for the open (4, 4) nanotube, four negative frequencies for the open (5, 5) nanotube, and four frequencies for the (6, 6) open nanotube were obtained.

Another analysis by calculations of molecular dynamics was carried out, allowing evaluate the stability of bismuth nanotubes. On the basis of obtained results, it was considered to realize calculations for closed nanotubes, since no any of these nanostructures has been collapsed during the optimization of its geometry and no any this structure possesses imaginary frequencies. These calculations were carried out also by the PM6 method, paying attention to the interaction between atoms per a determined period of time (2000 ps) at 298.15 °K. **Table 5** shows images of bismuth nanotubes before and after the molecular dynamics simulation for closed nanotubes. It can be observed that these structures are not collapsed; their changes are minimal. The structures (3, 0) and (5, 5) seem open in their extremes; however, the interatomic distance is considerably shorter the van der Waals radii.

*Discussion of the experimental results*

At < 10 min reaction time and heating at 200°C, it was observed that the bismuth oxide was precipitated in the autoclave having yellow color, so necessary reduction conditions were not reached. For other samples at higher heating times, the color change from yellow to metallic was detected. The samples, heated for 15 min at 200 °C, were analyzed by high-resolution TEM, where 5 nm nanoparticles are seen (**Figure 4a**). **Figure 4b** shows a nanostructure having 5 nm diameter and length of 58 nm, constituted of various aligned more thin structures. It can be affirmed that these nanoparticles grow accordingly to the bottom-up type: the nucleation process takes place, in which, meanwhile the reduction of bismuth oxide occurs, the bismuth atoms are being added to the particle constructing different nanoforms. **Figure 5** shows other aligned structures (nanowires and nanotubes). For the observed nanotubes, their diameter (0.7 – 1.0 nm) was determined applying a *Gatan* analysis.

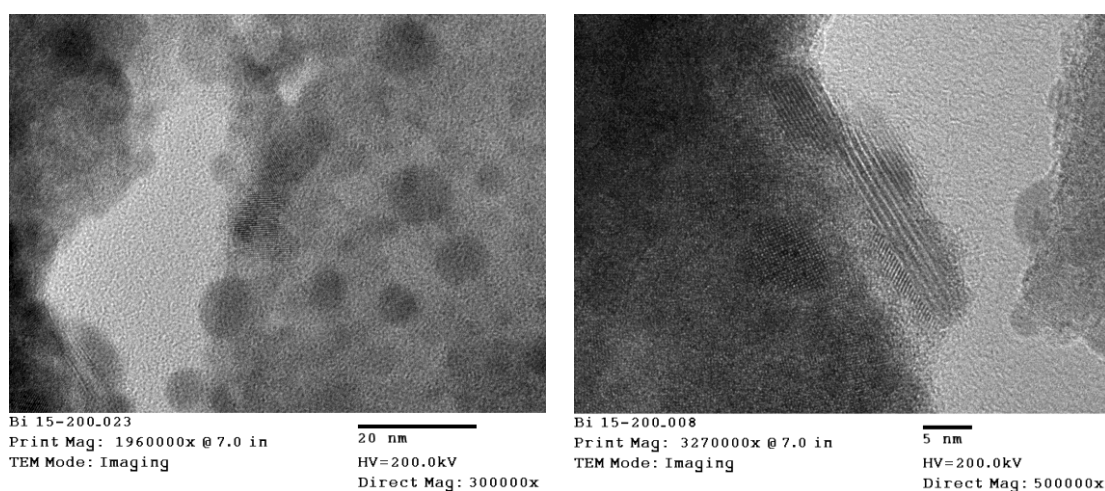


**Figure 4.** TEM images of the formed nanostructures (15 min heating at 200 °C). The image a) shows nanoparticles with < 10 nm size; the image b) shows the growth of nanotube agglomerates.

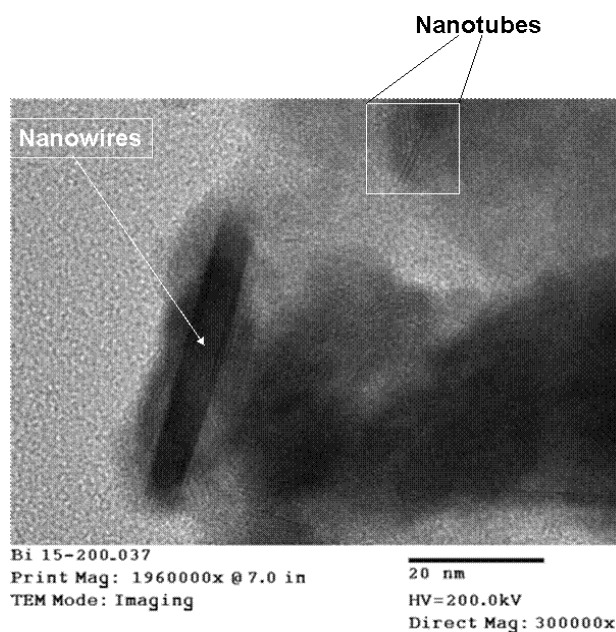


**Figure 5.** TEM image of the sample, heated for 15 min at 200 °C, showing an agglomeration of bismuth nanotubes and nanowires.



Nanoparticles produced by heating for 10 min at 220 °C are shown in **Figures 6a** and **b**. High-resolution TEM images in both figures revealed the nanoparticles with 15 – 20 nm diameters, one of which is shown in a larger scale in **Figure 7**. The nanoparticles are of a faceted form. No nanotubes were observed for 10 min heating.

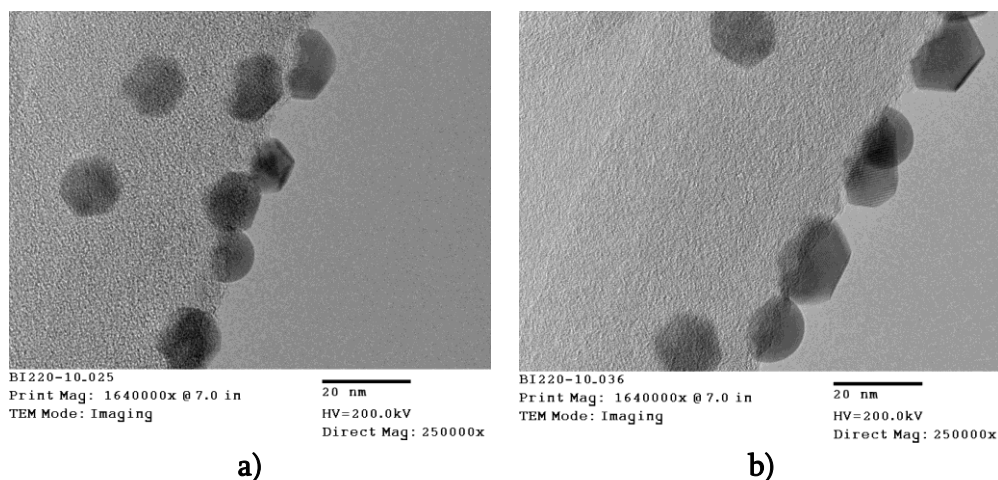


**Figure 6.** a) and b) TEM images of samples, heated for 10 min at 220 °C.

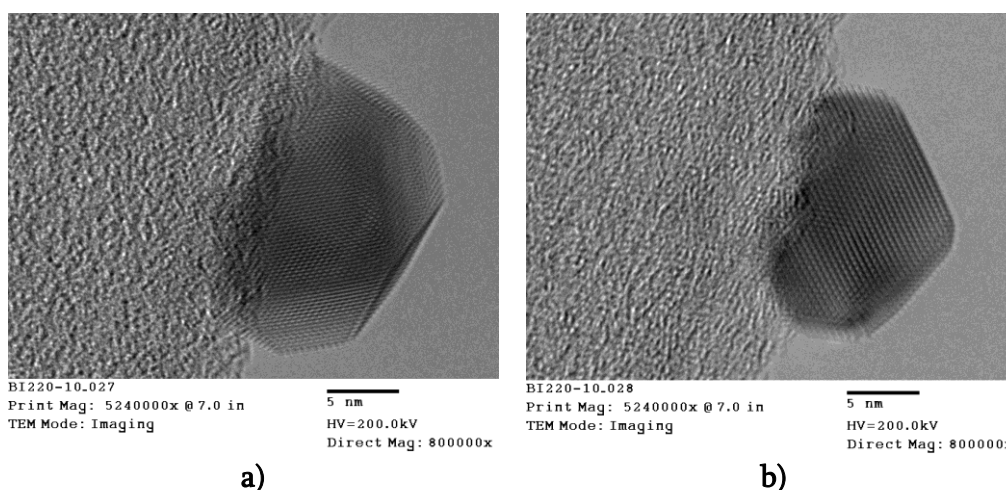


**Figure 7.** High-resolution TEM images of the samples, heated for 10 min at 220 °C: a) nanoparticle with a visible diameter of 18.8 nm; b) nanoparticle with sizes of 13.52 nm × 17.94 nm and interatomic distance of 3.5 Å.

The most interesting results, in our point of view, were observed in case of 15 min heating at 220 °C: the formation of blocks, consisting of 12 nanotubes with 0.78 – 1.08 nm diameter each one (**Figures 8a – d**). These blocks have the length starting from 10 – 15 nm up to 200 nm in several samples and are generally covered by spherical nanoparticles. The nanotubes are perfectly straight (**Figures 8a** and **b**) and may be confused with nanolines, typical for bismuth [47]. However, we strongly attribute them to individual single-wall nanotubes, connected each other by van der Waals forces, paying attention to visible connections between neighboring “lines” (a thin clearer space is seen between and along tube walls (**Figure 8a**), especially at the end of them, where structural defects appear). Similar results were observed at increase of heating time to 30 min both at 200 °C (**Figure 9**) and 220 °C (**Figure 10**). In the last case, the formation of almost Y-junction nanotube conglomerates with diameter of 1.1 – 1.5 nm each one is seen. The length of such conglomerates can reach 45 – 50 nm, for instance as it is shown in **Figure 11**.

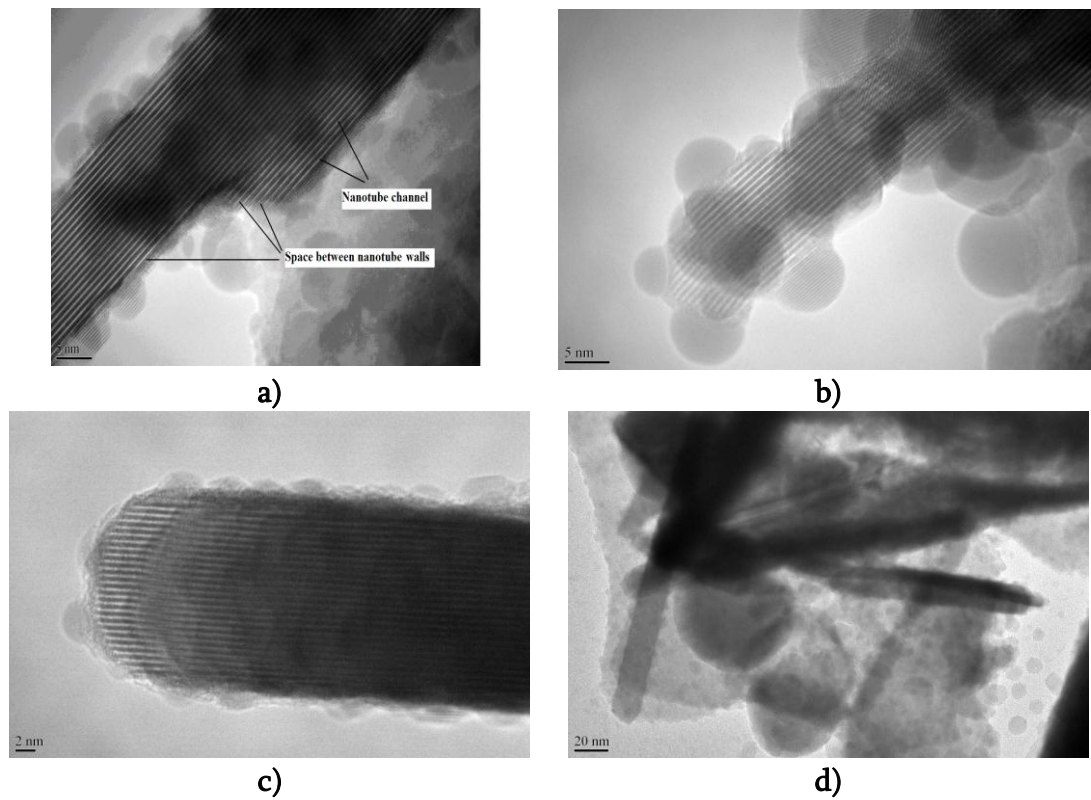


Figure 8. a) – d) HRTEM images of the samples, heated for 15 min at 220 °C.

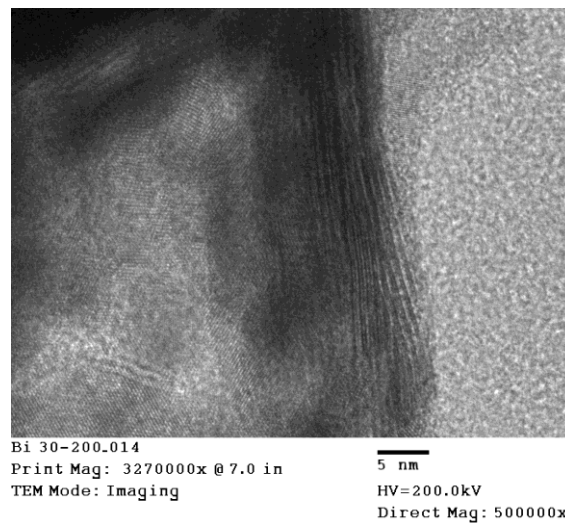


Figure 9. TEM image for the sample, heated for 30 min at 200 °C.

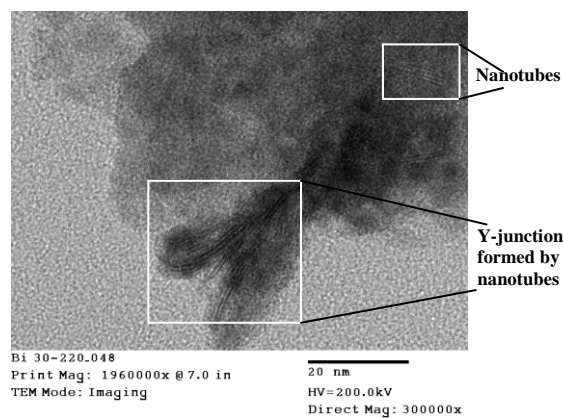
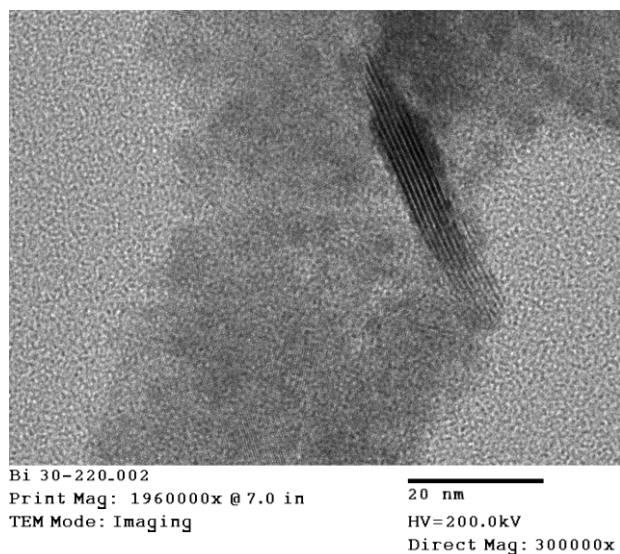
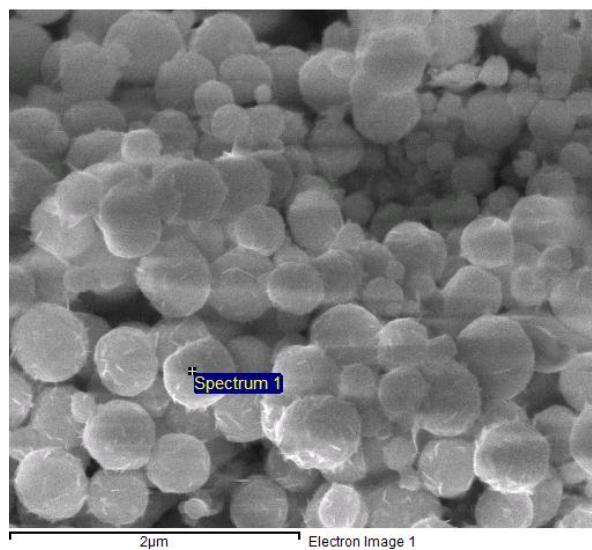


Figure 10. TEM image of the sample, heated for 30 min at 220 °C.





**Figure 11.** TEM image of the conglomerate of six nanotubes with length 45 nm (the sample heated for 30 min at 220 °C).



**Figure 12.** SEM image of spherical nanoparticles (the sample, heated for 45 min at 220 °C).

Further increase of heating time to 45 min leads to formation of two types of nanostructures, depending on temperature: spherical nanoparticles are observed in the samples heated at 200 °C and 220 °C (**Figure 12**), as well as multi-wall nanotubes (**Figure 13**), observed heating at 220 °C only. The maximum observed diameter of spherical nanoparticles reaches 500 nm. For all studied samples with heating time from 10 to 45 min, bismuth atoms were only observed, without oxygen impurity; so, a complete reduction of bismuth oxide to elemental metal nanostructure takes place (**Figure 14**). The results of the present study are summarized in the **Table 6**.

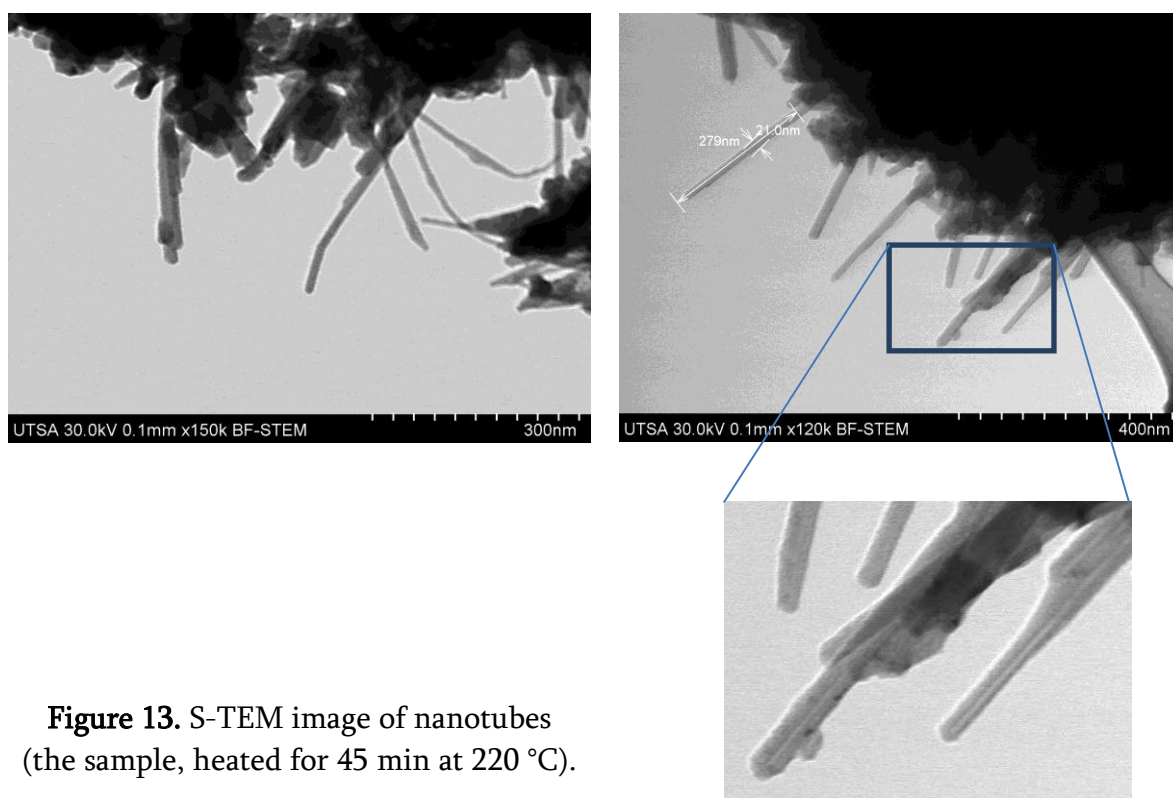


**Figure 13.** S-TEM image of nanotubes (the sample, heated for 45 min at 220 °C).

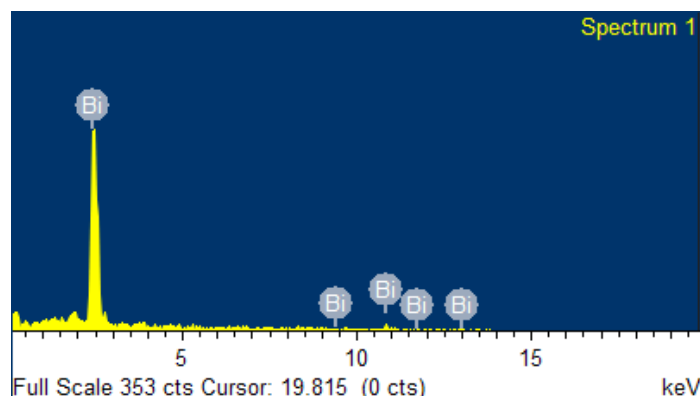


**Figure 14.** Elemental analysis of the sample, heated for 10 min at 220 °C.

**Table 6.** Summary of the obtained experimental results.

Conditions (reaction time and temperature, °C)	Formed metallic bismuth nanostructures
15 min, 200 °C	Nanoparticles with diameter 5 nm and nanotube / nanowire agglomerates with length of 50 – 60 nm
10 min, 220 °C	Faceted nanoparticles with 15 – 20 nm diameters. No nanotubes were observed
15 min, 220 °C	Blocks, consisting of 12 nanotubes with 0.6 – 0.7 nm diameter each one and length starting from 10 – 15 nm
30 min, 200 °C	Blocks of nanotubes with larger length in comparison with 15 min heating.
30 min, 220 °C	Y-junctions of nanotubes with lengths 45 – 50 nm
45 min, 200 °C	Spherical nanoparticles (diameter up to 500 nm)
45 min, 220°C	Spherical nanoparticles (diameter up to 500 nm) and multi-wall nanotubes

Comparing the obtained results with recently reported related investigations, we note that this metal exhibits unusual capacity to form a wide range of nanostructures, in particular nanotubes with different sizes, which are morphologically identical analogues of carbon nanotubes [14, 33]. In particular, it was concluded in the report [14], dedicated to the stability and electronic properties of Bi nanotubes, that hexagonal prismatic nanotubes of zigzag chirality with radius of 11 – 30 Å were found to be the most stable nanostructures. In our present investigation, the microwave-formed Bi nanotubes show lesser radius. In any case, in future investigations it would be very useful to establish a dependence of diameter and length of bismuth nanotubes on synthesis method, as well as to try to obtain nanotubes of other elements, which appear in layered allotropes (P, As, and Sb – see [14] and cited references therein): At last, we can affirm that the microwave hydrothermal method is an adequate technique for fabrication of bismuth nanostructures.

### Conclusions

Elemental bismuth was obtained in the form of nanoparticles and nanotubes in the conditions of microwave hydrothermal heating. Complete reduction of bismuth oxide to metallic bismuth was observed starting from 10 min of treatment. Agglomerates and blocks of metallic nanotubes were observed at intermediate heating times (15 – 30 min), meanwhile short (10 min) and large (45 min) treatment durations led to spherical and truncated spherical nanoparticles. Additionally, nanotubes were observed at large heating times and higher temperature. Applying the calculations of computational chemistry, existence of bismuth nanotubes is confirmed, having the following characteristics:

- The structures correspond to local energy minimums, which imply their stability.
- Up to the (6,6) arrangement, the nanotubes possess semiconductive properties; the conductivity is better for open nanotubes.

### References

1. Ed. N. C. Norman. Chemistry of Arsenic, Antimony and Bismuth. 1997, Springer, 496 pp.
2. F. A. Cotton, G. Wilkinson, C. A. Murillo, M. Bochmann. Advanced Inorganic Chemistry. 1999, Wiley – Interscience, 1376 pp.
3. G. B. Sergeev. Nanochemistry. 2006, Elsevier Science, 262 pp.
4. C. Koch, I. Ovid'ko, S. Seal, S. Veprek. Structural Nanocrystalline Materials: Fundamentals and Applications. 2007, Cambridge University Press, 364 pp.
5. G. E. Fryxell, G. Cao. Environmental Applications of Nanomaterials: Synthesis, Sorbents and Sensors. 2007, Imperial College Press, 520 pp.
6. R. Asthana, A. Kumar, N. B. Dahotre. Materials Processing and Manufacturing Science. 2005, Butterworth – Heinemann, 656 pp.
7. S. Sakka, Handbook of Sol–Gel Science and Technology: Processing Characterization and Applications. 2004, Springer, 1980 pp.
8. B. C. G. Soderberg. Transition metals in organic synthesis: Highlights for the year 2000. Coord. Chem. Rev., 2003, 241, 1, 147-247.
9. G. Cao, D. Liu. Template-based synthesis of nanorod, nanowire, and nanotube arrays. Adv. Colloid & Interface Sci., 2008, 136, 1, 45-64.
10. M. S. Dresselhaus, Y. M. Lin, O. Rabin, A. Jorio, A. G. Souza Filho, M. A. Pimenta, R. Saito, G. Samsonidze, G. Dresselhaus. Nanowires and nanotubes. Mater. Sci. & Eng. C, 2003, 23, 1-2, 129-140.
11. R. M. Penner, M. P. Zach, F. Favier. Methods for fabricating metal nanowires. US Patent # 7220346, 2007. <http://www.freepatentsonline.com/7220346.html>
12. T. Guo. Nanoparticle radiosensitizers. Patent # WO2006037081. 2006.
13. S. F. Li, L. Gao, X. G. Gong, Z. X. Guo. No cage, no tube: Relative stabilities of nanostructures. J. Phys. Chem. C, 2008, 112, 34, 13200-13203.
14. B. Rasche, G. Seifert, A. Enyashin. Stability and electronic properties of bismuth nanotubes. J. Phys. Chem. C, 2010, 114, 50, 22092-22097.

15. G. Zhou, L. Li, G. H. Li. Enhancement of thermoelectric figure of merit in bismuth nanotubes. *Appl. Phys. Lett.*, 2010, 97, 023112, 3 pp.
16. D. Ma, J. Zhao, Y. Li, X. Su, S. Hou, Y. Zhao, X.-L. Hao, L. Li. Organic molecule directed synthesis of bismuth nanostructures with varied shapes in aqueous solution and their optical characterization. *Colloids & Sur. A*, 2010, 368, 1-3, 105-111.
17. S. Derrouiche, L. C. Zoican, C. Wang, L. Pfefferle. Energy-induced morphology changes in bismuth nanotubes. *J. Phys. Chem. C*, 2010, 114, 10, 4336-4339.
18. X. Tao, J. Qu, L. Sun, Y. Zhao. Rapid synthesis and characterization of bismuth nanotubes. *Huahue Yanjiu*, 2009, 20, 3, 74-76.
19. D. Yang, G. Meng, Q. Xu, F. Han, M. Kong, L. Zhang. Electronic transport behavior of bismuth nanotubes with a predesigned wall thickness. *J. Phys. Chem. C*, 2008, 112, 23, 8614-8616.
20. C.-R. Su, J.-M. Li. First principles study on electronic property of bismuth nanotubes. *Yuanzihe Wuli Pinglun*, 2002, 19, 2, 224-226.
21. S. Derouiche, C. Z. Loebbrick, L. Pfefferle. Optimization of routes for the synthesis of bismuth nanotubes: implications for nanostructure form and selectivity. *J. Phys. Chem. C*, 2010, 114, 8, 3431-3440.
22. C. Su, H.-T. Liu, J.-M. Li. Bismuth nanotubes: Potential semiconducting materials. *Nanotechnol.*, 2002, 13, 6, 746-749.
23. Y. Zhao, Z. Zhang, H. Dang. A simple way to prepare bismuth nanoparticles. *Mater. Lett.*, 2004, 58, 5, 790-793.
24. Y. Bisrat, Z. P. Luo, D. Davis, D. Lagoudas. Highly ordered uniform single-crystal Bi nanowires: fabrication and characterization. *Nanotechnol.*, 2007, 18, 39, 395601, 5 pp.
25. Z. Zhang, D. Gekhtman, M. S. Dresselhaus, J. Y. Ying. Processing and characterization of single-crystalline ultrafine bismuth nanowires. *Chem. Mater.*, 1999, 11, 7, 1659-1665.
26. S. Sepulveda-Guzman, N. Elizondo-Villarreal, D. Ferrer, A. Torres-Castro, X. Gao, J. P. Zhou, M. Jose-Yacamán. In situ formation of bismuth nanoparticles through electron-beam irradiation in a transmission electron microscope. *Nanotechnol.*, 2007, 18, 335604, 5 pp.
27. J. Wang, X. Wang, Q. Peng, Y. Li. Synthesis and characterization of bismuth single-crystalline nanowires and nanospheres. *Inorg. Chem.*, 2004, 43, 23, 7552-7556.
28. L. Balan, R. Schneider, D. Billaud, Y. Fort, J. Ghanbaja. A new synthesis of ultrafine nanometre-sized bismuth particles. *Nanotechnol.*, 2004, 15, 8, 940-944.
29. L. Balan, D. Burget. Synthesis of metal / polymer nanocomposite by UV-radiation curing. *Eur. Polymer J.*, 2006, 42, 12, 3180-3189.
30. G. Q. Zhong, H. L. Zhou, J. R. Zhang, Y. Q. Jia. A simple method for preparation of Bi and Sb metal nanocrystalline particles. *Mater. Lett.*, 2005, 59, 18, 2252-2256.
31. Q. Wang, C. Jiang, D. Cao, Q. Chen. Growth of dendritic bismuth microspheres by solution-phase process. *Mater. Lett.*, 2007, 61, 14, 3037-3040.
32. B. Yang, C. Li, H. Hu, X. Yang, Q. Li, Y. Qian. A room-temperature route to bismuth nanotube arrays. *Eur. J. Inorg. Chem.*, 2003, 2003, 20, 3699-3702.
33. R. Boldt, M. Kaiser, D. Kohler, F. Krumeich, M. Ruck. High-yield synthesis and structure of double-walled bismuth nanotubes. *Nano Lett.*, 2010, 10, 1, 208-210.

34. Y. Gao, H. Niu, C. Zeng, Q. Chen. Preparation and characterization of single-crystalline bismuth nanowires by a low-temperature solvothermal process. *Chem. Phys. Lett.*, 2003, 367, 1, 141-144.
35. Y. Li, J. Wang, Z. Deng, Y. Wu, X. Sun, D. Yu, P. Yang. Bismuth nanotubes. A rational low-temperature synthetic route. *J. Am. Chem. Soc.*, 2001, 123, 40, 9904-9905.
36. X.-Y. Liu, J.-H. Zeng, S.-Y. Zhang, R.-B. Zheng, X.-M. Liu, Y.-T. Qian. Novel bismuth nanotube arrays synthesized by solvothermal method. *Chem. Phys. Lett.*, 2003, 374, 3, 348-352.
37. R. Benoit, Nanoparticules de bismuth: Synthèse, caractérisation et nouvelles propriétés. Ph.D. Thesis. Université D'Orléans. 2005. [http://crmd.cnrs-orleans.fr/theses/Rapports-pdf/th%28se\\_Roland\\_Benoit.pdf](http://crmd.cnrs-orleans.fr/theses/Rapports-pdf/th%28se_Roland_Benoit.pdf)
38. T. Ould-Ely, J. H. Thurston, A. Kumar, M. Respaud, W. Guo, C. Weidenthaler, K. H. Whitmire. Wet-chemistry synthesis of nickel-bismuth bimetallic nanoparticles and nanowires. *Chem. Mater.*, 2005, 17, 18, 4750-4754.
39. S. Park, K. Kang, W. Han, T. Vogt. Synthesis and characterization of Bi nanorods and superconducting NiBi particles. *J. Alloys & Comp.*, 2005, 400, 1, 88-91.
40. J. Chen, L.-M. Wu, L. Chen. Syntheses and characterizations of bismuth nanofilms and nanorhombuses by the structure-controlling solventless method. *Inorg. Chem.*, 2007, 46, 2, 586-591.
41. O. V. Kharissova, J. Rangel Cardenas. The microwave heating technique for obtaining bismuth nanoparticles. In: *Physics, Chemistry and Application of Nanostructures*, World Scientific, 2007, 443-446.
42. O. V. Kharissova, M. Osorio, M. Garza. Synthesis of bismuth by microwave irradiation. In: *Abs. MRS Fall Meeting. Boston, 2007*, II5.42, 773-773.
43. O. V. Kharissova, M. Osorio, B. I. Kharisov, M. Jose Yacaman, U. Ortiz Mendez. A comparison of bismuth nanoforms obtained in vacuum and air by microwave heating of bismuth powder. *Mater. Chem. & Phys.*, 2010, 121, 3, 489-496.
44. O. V. Kharissova, B. I. Kharisov. Nanostructured forms of bismuth. *Synth. React. Inorg. Met.-Org. Nano-Met. Chem.*, 2008, 38, 6, 491-502.
45. L. Gao, P. Li, H. Lu, S. F. Li, Z. X. Guo. Size- and charge-dependent geometric and electronic structures of  $Bi_n$  ( $Bi_n^-$ ) clusters ( $n = 2 - 13$ ) by first-principles simulations. *J. Chem. Phys.*, 2008, 128, 194304, 9 pp.
46. <http://www.gatan.com/analysis>
47. J. H. G. Owen, K. Miki, D. R. Bowler. Self-assembled nanowires on semiconductor surfaces. *J. Mater. Sci.*, 2006, 41, 14, 4568-4603.



წყალმცენარე *Spirulina platensis* მიერ ზოგიერთი ქიმიური  
ელემენტის აბსორბირების საკითხის განხილვა ხანმოკლე  
ექსპერიმენტების შედეგების მიხედვით

ნ. კუჭავა

ი. ჯავახიშვილის სახ. თბილისის სახელმწიფო უნივერსიტეტი  
ე. ანდრონიკაშვილის ფიზიკის ინსტიტუტი  
თბილისი, საქართველო  
e.kuchava@mail.ru

მიღებულია 2015 წლის 30 აპრილს

ანოტაცია

განხილულია ბიოტექნოლოგიის ერთ-ერთი საინტერესო ლურჯ-მწვანე წყალმცენარის *Spirulina platensis* უჯრედების მიერ ქიმიური ელემენტების: Cu, Zn, Ni, Ag, Cd და Hg აბსორბირების საკითხი ხანმოკლე (120 წთ და უფრო მცირე დროს) ექსპერიმენტების შედეგების მიხედვით.

ნანონაწილაკების სინთეზი მეცნიერებისა და ტექნიკისათვის შედარებით ახალ სფეროს წარმოადგენს. ამ თვალსაზრისით საინტერესოა მიკროორგანიზმები, რომელთაც ახასიათებს გარემოში არსებულ არაორგანულ იონებზე ზემოქმედების უნარი. დღეისათვის ნანონაწილაკების წარმოქმნელი მიკროორგანიზმების მცირე რაოდენობაა ცნობილი. მხოლოდ რამოდენიმე მათგანს შეუძლია მოგვცეს ქიმიური ელემენტების: ვერცხლის, ოქროს, კადმიუმის, ტიტანის და სხვ. ნანონაწილაკები. აღმოჩნდა, რომ ციანობაქტერია ლურჯ-მწვანე წყალმცენარე *Spirulina platensis* (ქვემოთ: *S. platensis*) წარმოადგენს ნანონაწილაკების მისაღებად საინტერესო ობიექტს [1].

შრომაში [2] დასმულია და ნაწილობრივ გამოკვლეულია კიდევ საკითხი ვერცხლისა და ოქროს ნანონაწილაკების მისაღებად წყალმცენარე *S. platensis* გამოყენების შესახებ. განხილულია ის თავისებურებანი, რომელიც ახასიათებს ნანონაწილაკების მიკრობულ სინთეზს, აგრეთვე, შეფასებულია ვერცხლის კონცენტრაცია *S. platensis* ბიომასაში. ექსპერიმენტებში გამოყენებული იქნა ვერცხლის ნიტრატი  $AgNO_3$ .

შრომაში [3] შესწავლილ იქნა *S. platensis* ბიომასით სარგებლობის შესაძლებლობა. ოქროს ნანონაწილაკების მისაღებად. გამოყენებულ იქნა ოქროს ნაერთი ქლოროაურატი  $HAuCl_4$ . შერჩეულ იქნა ოქროს სხვადასხვა დოზა. ექსპერიმენტები ჩატარდა დროის სხვადასხვა ინტერვალის დაცვით. შესრულებული სამუშაოს შედეგად დადგენილია, რომ საწყისი 1, 5 – 12 დღის შემდეგ წარმოიქმნება ოქროს სფერული ფორმის ნანონაწილაკები, ზომით 8 – 40 ნმ (საშუალოდ 20 – 30 ნმ). გაკეთებულია დასკვნა, რომ ოქროს ნანონაწილაკებით გაჯერებული *S. platensis* ბიომასა შეიძლება გამოყენებულ იქნეს სამედიცინო, ფარმაცევტული და სხვა ტექნოლოგიური მიზნებისათვის. ამავე დროს აღნიშნულია, რომ *S. platensis* მიერ აკუმულირებული ოქროს ნანონაწილაკების კონცენტრაცია რამოდენიმე დღის განმავლობაში სწრაფად



გაიზარდა. *S. platensis* ბიომასის ნიმუშების ანალიზისათვის გამოყენებულ იქნა როგორც ინსტრუმენტალური ნეიტრონული აქტივაციური ანალიზის (ინაა), ასევე ატომურ-აბსორბციული სპექტრომეტრიის (აას) მეთოდები.

ციანობაქტერია *S. platensis*, ზოგიერთ სხვა ბაქტერიასთან ერთად, გამოყენებულია ოქროსა და ვერცხლის ნანონაწილაკების მიკრობული სინთეზის ბიოტექნოლოგიის სრულყოფისათვის [4]. შესწავლილია, აგრეთვე, ბაქტერიებისა და მიკროწყალმცენარეების საშუალებით მიღებული ოქროსა და ვერცხლის ნანონაწილაკების მიკრობული სინთეზის მედიცინაში გამოყენების საკითხები [5]. ზემოთაღნიშნულის გარდა, ბოლო ათეული წლების განმავლობაში საყოველთაოდ გახდა ცნობილი, რომ წყალმცენარე *S. platensis* წარმოადგენს მნიშვნელოვან ობიექტს საკვები ბიოდანამატის სახით სარგებლობისათვის ადამიანის, ცხოველთა და მცენარეთათვის, რადგან ის მდიდარია ვიტამინებით, ცილებით და ცხიმებით. შრომებში [6, 7] ნაჩვენებია, რომ აღნიშნულ წყალმცენარეში მიკროელემენტების: Se, Zn, Mn, Fe, Cr და სხვ. გადანაწილება დაკავშირებულია ცილებთან, რის გამოც ბიოტექნოლოგიისათვის *S. platensis* წარმოადგენს პერსპექტულ მატრიცას. შრომაში [8] დასაბუთებულია *S. Platensis* გამოყენების შესაძლებლობა იმ ფარმაცევტული პრეპარატების მომზადებისათვის, რომელიც შეიცავს ქიმიურ ელემენტებს: Se, I და Cr. აღნიშნულ შრომაში შესწავლილია, აგრეთვე, Cr სხვადასხვა ფორმის: Cr<sup>3</sup> და Cr<sup>6</sup> ქცევის თავისებურებები *S. platensis* ბიომასის უჯრედებთან ურთიერთქმედებისას. კერძოდ, დადგენილ იქნა, რომ აღნიშნული წყალმცენარის ბიომასის უჯრედების მიერ მკვებავი გარემოდან სიცოცხლისათვის აუცილებელი Cr<sup>3</sup> აკუმულირება ხდება უფრო მეტად, ვიდრე ტოქსიკური Cr<sup>6</sup>.

ყოველივე ზემოთაღნიშნულის გამო საჭიროდ მიგვაჩნია *S. platensis* მრავალმხრივი შესწავლის საქმეში შევიტანოთ გარკვეული წვლილი.

ი. ჯავახიშვილის სახ. თბილისის სახელმწიფო უნივერსიტეტის ე. ანდრონიკაშვილის ფიზიკის ინსტიტუტში ციანობაქტერიის *S. platensis* გამოკვლევები ჩატარდა და ტარდება IPPAS B-265 ტიპის *S. platensis* ბიომასის საშუალებით, რომელიც მიღებულ იქნა რუსეთის მეცნიერებათა აკადემიის ვ. ტიმირიაზოვის სახ. მცენარეთა ფიზიოლოგიის ინსტიტუტიდან. აღნიშნული წყალმცენარის კულტივირება წარმოებს Zarrouk მკვებავ გარემოში (pH > 8), მუდმივი განათებისას, 30 – 34 °C ტემპერატურის პირობებში ხდება უწყვეტი ბარბატირება და pH სისტემატური კონტროლი.

ცნობილია, რომ Zarrouk გარემო შეიცავს შემდეგ ქიმიურ ელემენტებს: Na, Cl, N, Fe, K, S, Mg, C, P, Mn, Zn, Cu, Mo, Cr, Ni, W, Ti, Co, Ca, V, H და B. *S. Platensis* უჯრედული ზრდის დინამიკაში საკვლევი წყალმცენარე მკვებავი გარემოდან საჭირო ქიმიურ ელემენტებს გარკვეული რაოდენობით ითვისებს. ამიტომ ერთ-ერთი მნიშვნელოვანი როლი ენიჭება აღნიშნული წყალმცენარის ელემენტური შემადგენლობის შესწავლას.

შრომაში [9] შესწავლილ იქნა *S. Platensis* ზოგიერთი თვისება, კერძოდ, წყალმცენარის ხანგრძლივი უჯრედული ზრდის პროცესში (5 – 7 დღე), მკვებავი გარემოდან ბიოგენური და ტოქსიკური ქიმიური ელემენტების აკუმულირების უნარი, რისთვისაც ჩატარებულ იქნა ორი სახის ექსპერიმენტი. ორივე შემთხვევაში შერჩეულ იქნა მკვებავ გარემოში ერთდროულად ჩასატვირთავ ქიმიურ ელემენტთა განსაზღვრული რაოდენობა, რომლითაც უზრუნველყოფილ იქნა მათი აკუმულაცია *S. platensis* ბიომასის ზრდით და მისი ხარისხის შენარჩუნებით. წარმოებდა ბიოგენური ქიმიური ელემენტების: Co, Cu, Zn, Ni, Mn და Fe, აგრეთვე, ტოქსიკურ ქიმიურ ელემენტთა: Ag, Cd, Cr და Pb შემცველობის შესწავლა *S. Platensis* ლიოფილურად

გამომშრალ ბიომასაში მისი ზრდის დინამიკაში. შესწავლილ იქნა, აგრეთვე, *S. platensis* ბიომასაში Cu, Mn, Zn და Mg შემცველობა ინაა-მეთოდის გამოყენებით.

შრომაში [10] ასევე რამოდენიმე დღის განმავლობაში მიმდინარე ექსპერიმენტების საშუალებით შესწავლილ იქნა *S. Platensis* უჯრედული ზრდის დინამიკაში მკვებავ Zarrouk გარემოში ქიმიური ელემენტების: Cu, Zn და Ni ქცევის თავისებურებები მათი ცალკე-ცალკე ჩატვირთვის დროს, როცა შერჩეულ იყო თითოეული მათგანის გარკვეული რაოდენობა. საჭიროდ იქნა ჩათვლილი მსგავსი საკითხის შესწავლა ისეთი ქიმიური ელემენტებისათვისაც, როგორცაა: Ag, Cd და Hg [11]. ყველა საკვლევი ქიმიური ელემენტის შემთხვევაში შესწავლილ იქნა წყალმცენარის ლიოფილურად გამომშრალი ბიომასის ცვლილება.

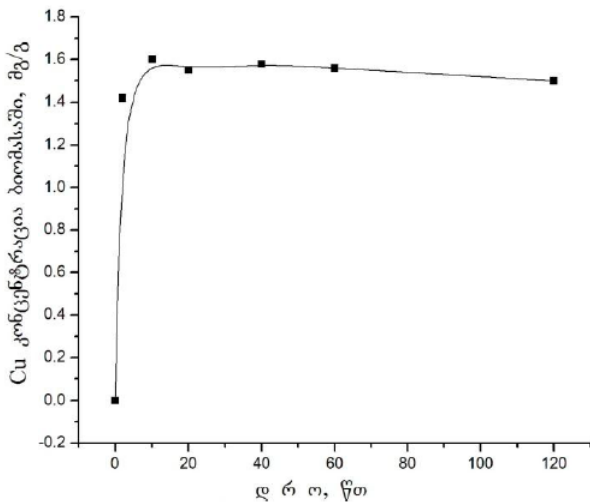
წინამდებარე სამუშაოს მიზანს წარმოადგენს განხილულ იქნეს ქიმიური ელემენტების: Cu, Zn, Ni, Cd, Ag და Hg ქცევის თავისებურებები მათი წინასწარ განსაზღვრული რაოდენობით ცალკე-ცალკე ჩატვირთვისას Zarrouk მკვებავ გარემოში *S. platensis* უჯრედული ზრდის დინამიკაში არა ხანგრძლივი დროით, როგორც ეს არის წარმოდგენილი შრომებში [9 – 11], არამედ ხანმოკლე პერიოდში, კერძოდ, რამდენიმე წუთიდან 60 – 120 წთ განმავლობაში.

ცოცხალ ორგანიზმებში მიმდინარე ფიზიოლოგიურ პროცესებში ქიმიური ელემენტების როლის შესახებ ახალი მონაცემები არ მოგვეპოვება, ამიტომ, გახსენებისათვის, გავიმეორებთ შრომებში [9 – 11] უკვე მოყვანილ მოსაზრებებს.

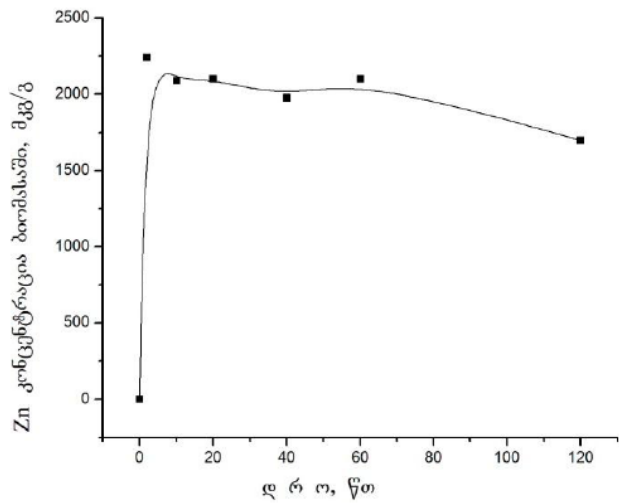
ქიმიური ელემენტის სპილენძის Cu როლი და მნიშვნელობა ცოცხალი ორგანიზმების განვითარებისათვის, სხვა ელემენტებთან შედარებით, უკეთ არის შესწავლილი. მისი თითქმის ყველა ნაერთი არის ტოქსიკური და შეიძლება მათ ჰქონდეთ კარცეროგენული თვისებები [12]. ჩვენს მიერ ჩატარებული ხანმოკლე ექსპერიმენტებისათვის შერჩეულ იქნა სპილენძის ქლორიდი  $CuCl_2$ . Cu კონცენტრაცია მკვებავ გარემოში იყო 100 მგ / ლ, ხოლო სუსპენზიის სიმკვრივე – 7.5 გ / ლ.

ექსპერიმენტები ჩატარდა 22 – 24 °C ტემპერატურაზე. Cu რაოდენობრივი განსაზღვრისათვის წყალმცენარის ბიომასის ნიმუშები შეგროვდა სპეციალურ ფილტრებში, რამდენჯერმე გაირეცხა დისტილირებული წყლით და ჩატარდა ნიმუშების დაბალტემპერატურული გამოშრობა. **ნახაზზე 1** წარმოდგენილია *S. Platensis* მშრალ ბიომასაში Cu იონების აბსორბირების დინამიკა საწყისი 120 წთ განმავლობაში. როგორც **ნახაზიდან 1** ჩანს, წყალმცენარის უჯრედების მიერ აღნიშნული ელემენტის მაქსიმალურად აბსორბირება მოხდა საწყისი 15 – 20 წთ განმავლობაში, ხოლო შემდეგ აღნიშნული რაოდენობა ნაკლებად შეიცვალა.

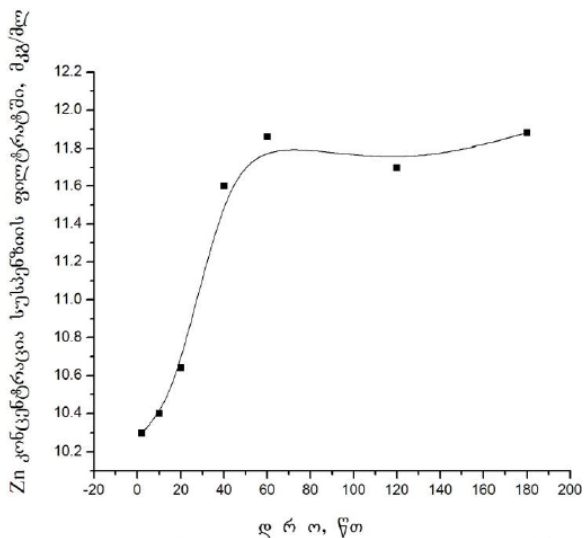
ქიმიური ელემენტი თუთია Zn შედის ცხოველთა ორგანოებისა და მცენარეთა ყველა ნაწილის შემადგენლობაში. ვარაუდობენ, რომ მისი უკმარისობა იწვევს მცენარეთა ზრდის შეჩერებას [12]. ჩვენი ექსპერიმენტებისათვის შერჩეულ იქნა თუთიის სულფატი  $ZnSO_4$ . **ნახაზზე 2** წარმოდგენილია *S. platensis* მშრალ ბიომასაში Zn აბსორბირების დინამიკა 120 წთ განმავლობაში. როგორც **ნახაზიდან 2** ჩანს, Zn იონების მაქსიმალური აბსორბირება დამახასიათებელია კულტივაციის საწყისი წუთებისათვის. **ნახაზი 3** გვიჩვენებს *S. Platensis* სუსპენზიის ფილტრატში Zn შემცველობას (მკგ / მლ) 180 წთ განმავლობაში. როგორც **ნახაზიდან 3** ჩანს, *S. platensis* უჯრედების ზრდის (50 – 60 წთ) განმავლობაში უჯრედების მიერ აბსორბირებულ იქნა მკვებავ გარემოში არსებული Zn მაქსიმალური რაოდენობა (11.9 მკგ / მლ), ხოლო ექსპერიმენტის შემდგომი დროის განმავლობაში წყალმცენარის უჯრედების მიერ აბსორბირებული Zn რაოდენობა მნიშვნელოვნად არ შეცვლილა.



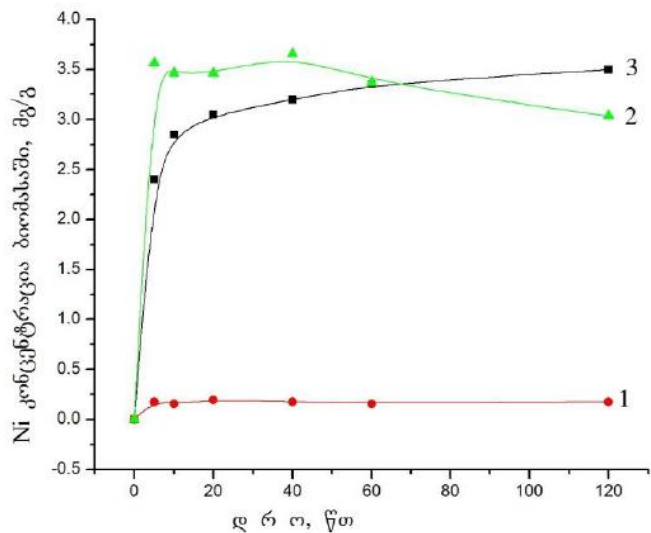
**ნახაზი 1.** Cu (მგ / გ) აბსორბირების დინამიკა *S. platensis* მშრალ ბიომასაში საწყისი 120 წთ განმავლობაში.



**ნახაზი 2.** Zn (მგ / გ) აბსორბირების დინამიკა *S. platensis* მშრალ ბიომასაში საწყისი 120 წთ განმავლობაში.



**ნახაზი 3.** Zn (მგ / მლ) აბსორბირების დინამიკა *S. platensis* მშრალ ბიომასაში საწყისი 180 წთ განმავლობაში.



**ნახაზი 4.** Ni (მგ / გ) აბსორბირების დინამიკა *S. platensis* მშრალ ბიომასაში საწყისი 120 წთ განმავლობაში. Ni გლიცინატი 1 – მკვებავ, 2 – წყლის და სულფატი 3 – წყლის გარემოში

ქიმიური ელემენტის ნიკელის Ni შესახებ ფიქრობენ, რომ ის მონაწილეობს ცოცხალ ორგანიზმებში მიმდინარე ფიზიოლოგიურ პროცესებში. ვარაუდობენ, რომ ნიკელი ახდენს ცილების აქტივაციას, აგრეთვე, მონაწილეობას ღებულობს გლუკოზის მეტაბოლიზმში [12]. *S. platensis* უჯრედების მიერ Ni იონების აბსორბირება ხანგრძლივი დროის (რამდენიმე დღის) განმავლობაში განხილულია შრომაში [10]. წინამდებარე შრომაში კი, როგორც ზემოთ იყო აღნიშნული, იგივე საკითხი განიხილება ხანმოკლე ექსპერიმენტების საშუალებით, კერძოდ, 2, 5, 10, 20, 40, 60 და 120 წთ განმავლობაში მიმდინარე პროცესების საფუძველზე. ამ მიზნით Ni, კონცენტრაციით 100 მგ / ლ, ჩატვირთულ იქნა *S. platensis* უჯრედების სუსპენზიაში (სიმკვრივე 2 გ / ლ) ნიკელის სულფატისა და ნიკელის გლიცინატის სახით. მოხდა ნიმუშების ფილტრაცია.

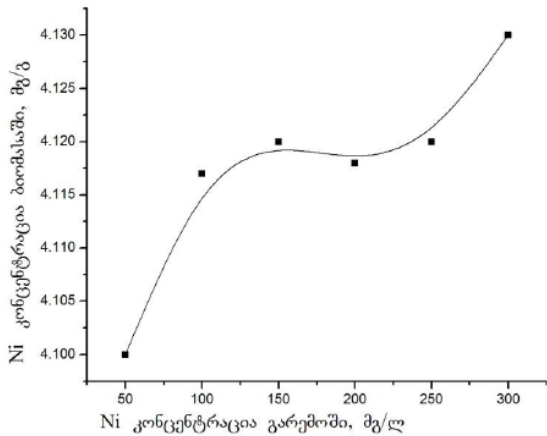
Ni კონცენტრაცია განისაზღვრა როგორც ფილტრატში, ასევე დისტილატით რამდენიმეჯერ გარეცხილ წყალმცენარის ბიომასაში, რომელიც, როგორც სხვა შემთხვევებში, გამომშრალ იქნა დაბალტემპერატურულ პირობებში. ექსპერიმენტები ჩატარდა სამ სერიად. პირველი და მეორე სერიის ექსპერიმენტებში სუსპენზიაში ჩატვირთულ იქნა ნიკელის გლიცინატი (სუსპენზიის pH = 6.5 ), ხოლო მესამე სერიის შემთხვევაში – ნიკელის სულფატი. განხილული ექსპერიმენტების შედეგები წარმოდგენილია **ნახაზზე 4**. აღნიშვნები ასეთია: მრუდი 1 – Ni გლიცინატი Zarrouk გარემოში; მრუდი 2 – Ni გლიცინატი წყლის გარემოში; მრუდი 3 – Ni სულფატი წყლის გარემოში. როგორც **ნახაზიდან 4** ჩანს, *S. platensis* უჯრედების მიერ Ni მაქსიმალურად აბსორბირდა მრუდის 2 შესაბამის შემთხვევაში, გაცილებით უკეთესად, ვიდრე Ni გლიცინატის შემთხვევაში Zarrouk გარემოდან (მრუდი 1). გლიცინატის შემთხვევაში აბსორბირების მაქსიმალური მაჩვენებელი დაფიქსირდა საწყის 5 წთ, სულფატის შემთხვევაში კი – საწყის 120 წთ (მრუდი 3).

საინტერესოა მკვებავ გარემოში Ni სხვადასხვა რაოდენობის ჩატვირთვის ეფექტი *S. platensis* ზრდის დინამიკაზე ხანმოკლე დროის (ჩვენს შემთხვევაში 30 წთ) განმავლობაში. მიღებული შედეგები წარმოდგენილია **ნახაზზე 5**. მკვებავ გარემოში ჩატვირთვისათვის Ni რაოდენობა შერჩეულ იქნა 50 – 300 მგ / ლ ინტერვალში. Ni კონცენტრაცია განსაზღვრულ იქნა მშრალი ბიომასის ნიმუშებში. Zarrouk გარემოში ჩატვირთვისათვის გამოყენებულ იქნა ნიკელის სულფატი 50, 100, 150, 200, 250 და 300 მგ / ლ რაოდენობით. როგორც **ნახაზიდან 5** ჩანს, *S. platensis* მშრალ ბიომასაში Ni კონცენტრაციის მცირეოდენი მომატება შემჩნეულ იქნა მკვებავ გარემოში 150 მგ / ლ და 300 მგ / ლ რაოდენობის Ni ჩატვირთვისას. **ნახაზებიდან 4 და 5** გამომდინარეობს, რომ Ni აბსორბირების მაქსიმალურმა რაოდენობამ *S. platensis* მშრალ ბიომასაში შეადგინა 3.5 – 4.1 მგ / გ.

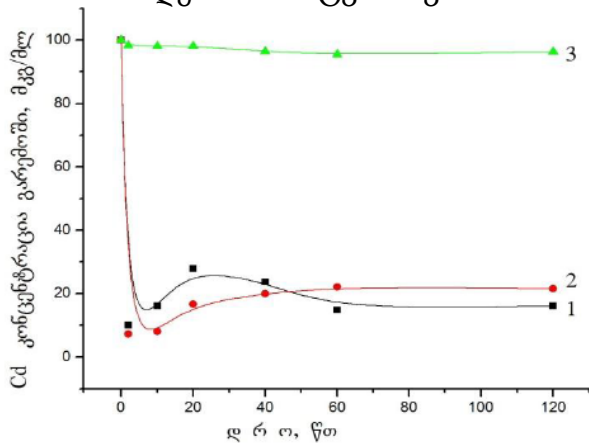
ქიმიური ელემენტი ვერცხლი Ag აღმოჩენილია სხვადასხვა ბიოორგანიზმის შემადგენლობაში, მაგრამ მისი ფიზიოლოგიური როლი ჯერჯერობით უცნობია. ვარაუდობენ, რომ ის ახდენს გავლენას ფერმენტულ სისტემებზე. ვერცხლი პრაქტიკაში გამოიყენება, როგორც ანტისეპტიკური საშუალება. წყალმცენარე *S. platensis* უჯრედების მიერ Ag აბსორბირების საკითხის განხილვისათვის ხანმოკლე ექსპოზიციის დროს, მისი მრავალი ნაერთიდან შერჩეულ იქნა ვერცხლის ნიტრატი AgNO<sub>3</sub>. მიღებული შედეგები წარმოდგენილია **ნახაზზე 6**. როგორც **ნახაზიდან 6** ვხედავთ, საწყისი 60 წთ შემდეგ ვერცხლის კონცენტრაცია მცირედ იცვლება. ამ დროს აბსორბირება არის მყარი და ბიომასის Na<sub>2</sub>EDTA გარეცხვის დროს (მრუდი 2) ჩამოირეცხება Ag მხოლოდ მცირე რაოდენობა. კონტროლის პირობებში წყალმცენარის ბიომასის გარეცხვა ხორციელდებოდა მხოლოდ დისტილირებული წყლით (მრუდი 1). სხვა ქიმიური ელემენტებისაგან განსხვავებით Ag ექსპერიმენტებში დავინახეთ მისი სპეციფიკური ქცევის თავისებურებანი *S. Platensis* უჯრედებთან აბსორბირების თვალსაზრისით.

ჩვენს მიერ განხილული შემდეგი ქიმიური ელემენტი არის Cd, რომლის რაოდენობისა და ცოცხალ ორგანიზმებში როლის შესახებ მასალები თითქმის არ მოიპოვება. ცნობილია მხოლოდ, რომ მის ნაერთებს ახასიათებს ტოქსიკურობა და კარცეროგენული მოქმედება. წყალმცენარე *S. platensis* უჯრედების მიერ Cd აბსორბირების საკითხის განხილვისათვის ჩატარებულ იქნა რამდენიმე ექსპერიმენტი. პირველი მათგანის დროს მკვებავ გარემოში ჩატვირთულ იქნა Cd სამი ნაერთი: Cd-გლიცინატი, CdCl<sub>2</sub> და Cd-EDTA. შედეგები წარმოდგენილია **ნახაზზე 7**.

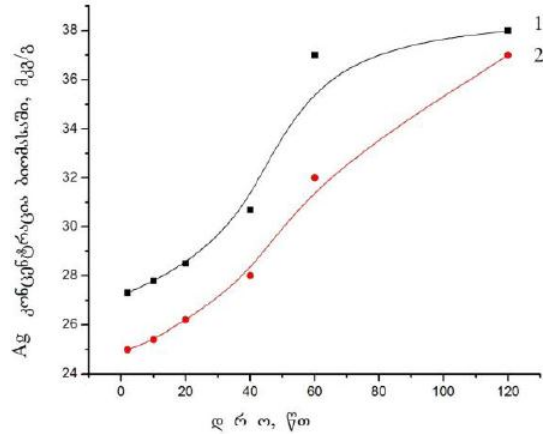




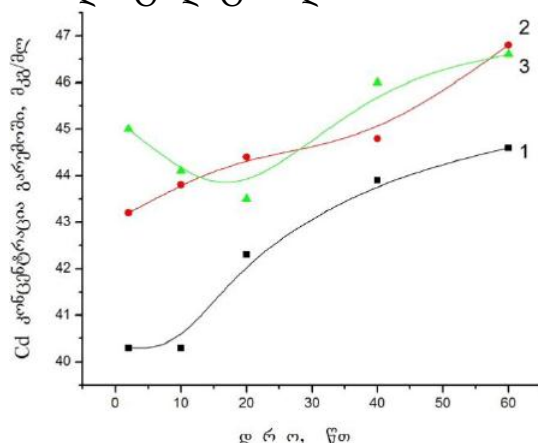
**ნახაზი 5.** Ni (მგ / გ) აბსორბირების დინამიკა *S. platensis* მშრალ ბიომასაში საწყისი 30 წთ განმავლობაში მკვებავ გარემოში Ni სხვადასხვა რაოდენობის ჩატვირთვისას.



**ნახაზი 7.** Cd (მკგ / მლ) აბსორბირების დინამიკა მკვებავ გარემოში Cd 1 – გლიცინატის , 2 – ქლორიდის და 3 – EDTA ჩატვირთვისას საწყისი 120 წთ განმავლობაში.



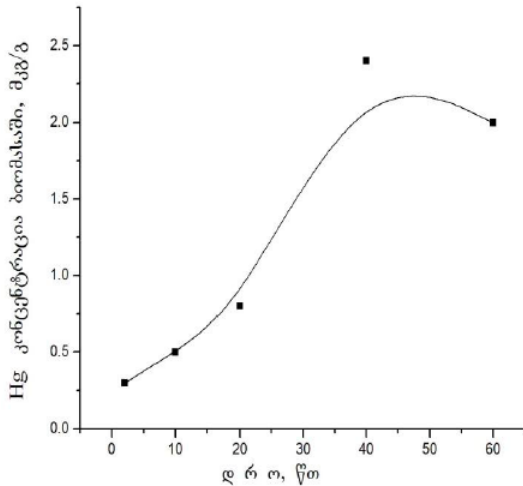
**ნახაზი 6.** Ag (მკგ / გ) აბსორბირების დინამიკა საწყისი 120 წთ განმავლობაში *S. platensis* მშრალ ბიომასაში, რომელიც გარეცხილ იქნა: 1 – დისტილატი და 2 – Na<sub>2</sub>EDTA.



**ნახაზი 8.** Cd (მკგ / გ) აბსორბირების დინამიკა მკვებავ გარემოში 1 – 0 °C, 2 – 35 °C და 3 – 40 °C ტემპერატურების პირობებში საწყისი 60 წთ განმავლობაში.

როგორც **ნახაზიდან 7** ჩანს, წყალმცენარის უჯრედების მიერ Cd ყველაზე მეტად იქნა აბსორბირებული შემთხვევაში 3, შემთხვევაში 1 კი მაქსიმალური შედეგი მიღწეულ იქნა საწყისი 20 წთ, ხოლო შემთხვევაში 2 – 40 – 60 წთ განმავლობაში. შემდეგი ექსპერიმენტის დროს წყალმცენარის კულტივირება მკვებავ გარემოში მოხდა შერჩეული ტემპერატურების: 5, 35 და 40 °C პირობებში. მკვებავ გარემოში არსებული Cd რაოდენობა იყო 50 მგ / ლ. აღნიშნული ექსპერიმენტის შედეგები წარმოდგენილია ნახაზზე 8. როგორც **ნახაზიდან 8** ჩანს, 5 °C ტემპერატურის დროს საწყისი 5 – 20 წთ განმავლობაში *S. platensis* უჯრედების მიერ მკვებავ გარემოში არსებული კადმიუმის აბსორბირებული რაოდენობაა 42.3 მკგ / მლ; საწყისი 5 – 40 წთ განმავლობაში – 43.9 მკგ / მლ, ხოლო 60 წთ განმავლობაში – 44.6 მკგ / მლ. 35 °C და 40 °C ტემპერატურებზე *S. platensis* უჯრედებში მეტაბოლური პროცესები უფრო ინტენსიურად მიმდინარეობს. 35 °C ტემპერატურაზე (მრუდი 2) საწყისი 5 – 20 წთ განმავლობაში მოხდა Cd მთლიანი რაოდენობიდან 44.4 მკგ / მლ აბსორბირება, საწყისი

5 – 40 წთ განმავლობაში – 44.8 მკგ / მლ, ხოლო საწყისი 60 წთ განმავლობაში – 46.8 მკგ / მლ. რაც შეეხება 40 °C ტემპერატურას (მრუდი 3), აქ ასეთ შემთხვევებთან გვაქვს საქმე: საწყის 2 წთ აბსორბირდა მკვებავ გარემოში ჩატვირთული Cd მთლიანი რაოდენობიდან 45 მკგ / მლ, ხოლო საწყის 5 – 20 წთ ინტერვალს შეესაბამება Cd რაოდენობის 43.5 მკგ / მლ აბსორბირება. საწყისი 5 – 40 წთ განმავლობაში Cd მთლიანი რაოდენობიდან აბსორბირდა 46 მკგ / მლ, საწყისი 60 წთ განმავლობაში კი – 46.6 მკგ / მლ.



**ნახაზი 9.** Hg (მკგ / გ) აბსორბირების დინამიკა *S. platensis* მშრალ ბიომასაში საწყისი 60 წთ განმავლობაში

ცნობილია, რომ ქიმიური ელემენტი ვერცხლისწყალი Hg და მისი ნაერთები გარემოში იწვევენ უაღრესად საშიშ დაჭუჭყიანებას. ის გროვდება ადამიანის თირკმელში, ღვიძლში, ელენთაში, ახდენს ცილების მოლეკულების ბიოქიმიური აქტივობის ბლოკირებას. როგორც ზოგ სამეცნიერო ლიტერატურაშია ნათქვამი, ვერცხლისწყალი იწვევს ადამიანის მოძრაობის აპარატის დარღვევას. მიუხედავად იმისა, რომ ვერცხლისწყალი ნაპოვნია ცოცხალი ორგანიზმების შემადგენლობაში, მისი ფიზიოლოგიური როლი უცნობია. ზემოთაღნიშნულის გამო, ცხადია, უაღრესად მნიშვნელოვანია ცოცხალ ორგანიზმებთან ვერცხლისწყლის მოქმედების შესწავლა. ამ დროს ისე, როგორც სხვა ქიმიური ელემენტის შემთხვევაში, ცოცხალ ორგანიზმად განვიხილავთ წყალმცენარე *S. platensis*. ხანმოკლე პერიოდის განმავლობაში (60 წთ) აღნიშნული წყალმცენარის უჯრედების მიერ Hg აბსორბირების შესწავლისათვის მკვებავ გარემოში ჩატვირთული იყო 500 მკგ / გ ვერცხლისწყალი. წყალმცენარის სუსპენზიის სიმკვრივე შეადგენდა 1 გ / ლ. ნიმუშები აღებულ იქნა კულტივაციის დასაწყისიდან 2, 10, 20, 40 და 60 წთ შემდეგ. ყველა აღებული ნიმუშიდან წყალმცენარის ბიომასა გამოყოფილ იქნა ფილტრაციის საშუალებით, გარეცხილ იქნა დისტილატით (pH = 6.5) რამდენჯერმე და ნიმუშებს ჩაუტარდა ლიოფილური გამოშრობა. Hg რაოდენობა შეფასებულ იქნა აას- და ინაა-მეთოდების გამოყენებით. *S. platensis* უჯრედების მიერ Hg აბსორბირების შედეგები საწყისი 60 წთ განმავლობაში წარმოდგენილია **ნახაზზე 9**. როგორც **ნახაზიდან 9** ჩანს, Hg აბსორბირების მაქსიმალური შედეგი მიღებულ იქნა კულტივაციის დასაწყისიდან დაახლოებით მეორმოცე წუთზე.

ამრიგად, წარმოდგენილი გამოკვლევის საფუძველზე შეიძლება ვთქვათ, რომ შესწავლილ იქნა ბიოტექნოლოგიისათვის ერთ-ერთი საინტერესო ლურჯ-მწვანე წყალმცენარის *S. platensis* უჯრედების მიერ ქიმიური ელემენტების: Cu, Zn, Ni, Ag, Cd და Hg მკვებავი გარემოდან აბსორბირების საკითხი.

საჭიროა აღვნიშნოთ, რომ წარმოდგენილ გამოკვლევას აქვს ჩატარებული ხანმოკლე ექსპერიმენტებით მიღებული შედეგების აღნუსხვის ხასიათი.



სასიამოვნო მოვალეობად ვთვლით მადლობა გადავუხადოთ ა. ბელოკობილსკის ექსპერიმენტების დაგეგმვისა და განხორციელების ხელმძღვანელობისათვის, ე. გინტურს და ა. ხიზანიშვილს – ექსპერიმენტებში მონაწილეობისათვის, ხოლო ა. რჩეულიშვილს – აას-მეთოდით *S. platensis* ნიმუშებში ქიმიური ელემენტების შემცველობის განსაზღვრისათვის [13, 14].

### დამოწმებანი

1. ნ. წიბახაშვილი, ა. რჩეულიშვილი, ე. გინტური, ნ. კუჭავა, ნ. ბაღდავაძე, ვ. გაბუნია. კრ.: 1-ლი საერთ. კონფ. “ნანოქიმია – ნანოტექნოლოგიები” მოხს. თეზ., 2010, თბილისი, წმ. ანდრია პირველწოდებულის სახ. ქართ. უნივ., 37-38.
2. N. Tsibakhashvili, T. Kalabegishvili, V. Gabunia, E. Ginturi, N. Kuchava, N. Bagdavadze, D. Pataraiia, M. Gurielidze, D. Gvardjaladze, L. Lomidze. Nano Studies, 2010, 2, 179-182.
3. T. Kalabegishvili, I. Murusidze, E. Kirkesali, A. Rcheulishvili, E. Ginturi, E. Gelagutashvili, N. Kuchava, N. Bagdavadze, D. Pataraiia, M. Gurielidze, G. Ttsercvadze, V. Gabunia Nano Studies, 2012, 5, 127-136.
4. T. Kalabegishvili, I. Murusidze, E. Kirkesali, A. Rcheulishvili, E. Ginturi, E. Gelagutashvili, N. Kuchava, N. Bagdavadze, D. Pataraiia, M. Gurielidze, L. Lomidze, D. Gvardjaladze. In: Abs. ISTS Int. Sci. Sem. “Neuroplativity: Neuro Substrates for Health & Disease. Nev Approaches for Research”. 2012, Tbilisi, 29-30.
5. T. L. Kalabegishvili, I. G. Murusidze, E. I. Kirkesali, A. N. Rcheulishvili, E. N. Ginturi, E. S. Gelagutashvili, N. E. Kuchava, N. B. Bagdavadze, D. T. Pataraiia, M. A. Gurielidze, M. B. Frontasyeva, I. I. Zinikovskaia, S. S. Pavlov, T. V. Gristina. J. Life Sci., 2013, 7, 2, 110-122.
6. А. В. Грошинский, В. К. Мазо, С. Н. Зорин, Ю. П. Алешко–Ожевский, Е. С. Зарецкая. Вопр. питания, 2004, 2, 28-31.
7. А. В. Грошинский, В. К. Мазо, И. С. Зилова. Вопр. питания, 2004, 1, 45-53.
8. Л. М. Мосулишвили, А. И. Белокобыльский, Е. И. Киркесали, А. И. Хизанишвили, Э. Н. Гинтури, Н. Е. Кучава, М. В. Фронтасьева, С. С. Павлов, Н. Г. Аксенова. В сб.: P18–2008–8, 2008, Дубна, ОИЯИ, 11 стр.
9. ნ. კუჭავა. Nano Studies, 2013, 7, 185-192.
10. ნ. კუჭავა. Nano Studies, 2014, 9, 119-126.
11. ნ. კუჭავა. Nano Studies, 2014, 10, 111-116.
12. А. А. Кист. Феноменология Биохимии и Бионеорганической Химии. 1987, Ташкент, ФАН.
13. A. Khizanishvili, A. Belokobilcky, E. Ginturi, N. Kuchava, A. Rcheulishvili. In: Workbook 8th Int. Conf. Pharmacy & Appl. Phys. Chem. 2004, Ackona, PO24, 26-30.
14. A. Khizanishvili, A. Belokobilcky, E. Ginturi, N. Kuchava, A. Rcheulishvili, L. Mosulishvili. J. Bio. Phys. & Chem., 2006, 6, 1, 9-13.

## МЕХАНИЧЕСКАЯ ПРОЧНОСТЬ ТОНКИХ ПЛЕНОК TmSe, TmS И LaBi

З. У. Джабуа, А. В. Гигинейшвили

Грузинский технический университет  
Департамент инженерной физики  
Тбилиси, Грузия  
Z.Jabua@hotmail.com

Принята 20 мая 2015 года

### Аннотация

Впервые исследована относительная механическая прочность тонких кристаллических пленок TmSe, TmS и LaBi. Все пленки приготовлены методом вакуумно-термического испарения из двух независимых источников на подложках из монокристаллического кремния, ситалла или лейкосапфира. Показано, что относительная механическая прочность пленок зависит от материала подложки. Исследована относительная механическая прочность пленок TmSe, приготовленных методом вакуумного-термического испарения из двух независимых источников и методом вакуумно-термического испарения из предварительно синтезированного соединения. Показано, что пленки, приготовленные методом дискретного испарения, имеют значительно высокую механическую прочность, чем пленки, приготовленные испарением из двух независимых источников.

В последнее время большое внимание уделяется изучению механических свойств тонких пленок соединений редкоземельных элементов, что вызвано тем, что часто пленки, имеющие интересные электрические, оптические и другие свойства, обладают низкими механическими свойствами, что значительно ограничивает их практическое применение в различных приборах.

Существуют различные способы изучения механических свойств пленок. Из них нами выбран метод полного истирания. Сущность метода заключается в том, что о механической прочности пленки и о степени ее прилипания к подложке можно судить по той работе, которую нужно затратить для того, чтобы полностью стереть пленку с поверхности подложки. Схема соответствующей установки приведена на **Рисунке 1**.

Массивная плита 1, на которой крепится исследуемая плунка 2, элетромотором 7 приводится в поступательное движение взад и вперед. По середине плиты в П-образный стояк 3 перемещается стержень 6, на нижнем конце которого закреплена рабочая поверхность, а на верхней – диск 5, на который укладывается соответствующий груз. Между диском и стояком 3 помещена пружина 4, которая подобрана таким образом, чтобы стержень 6 касался поверхности пленки, но не давит на нее, когда стержень не нагружена. Приспособления 8 являются щупальцами, при соприкосновении с которыми плита меняет направление движения. В коробке 9 вмонтирована схема электрического питания устройства. На конце стержня 6 закреплен кусок замшевого материала толщиной не более 1 мм, на который наносится алмазная паста, стирающая пленку с подложки при

движении плиты 1 с закрепленной на ней исследуемой плёнкой 2. Нагрузка на пленку подбирается таким образом, что самая непрочная пленка стирается с подложки после нескольких десятков прохождении нагрузки (при увеличении числа прохождений ошибка эксперимента увеличивается). Таким образом прочность пленки при постоянной нагрузке практически измеряется числом прохождении, которое требуется для полного истирания пленки с подложки.

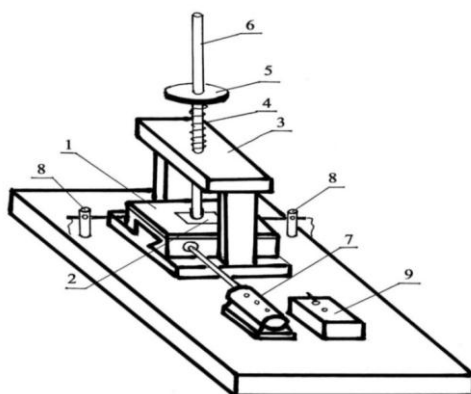


**Рисунок 1.** Схема установки для изучения механической прочности пленок.

Нами изучена относительная механическая прочность тонких пленок TmS, TmSe, LaBi, приготовленных на подложках из монокристаллического кремния, ситалла или лейкосапфира. Все пленки получены методом вакуумно-термического испарения из двух независимых источников на подложках прямоугольной формы из монокристаллического кремния, ситалла и лейкосапфира. Пленки были однофазными и имели поликристаллическую структуру. Поскольку для описанной методики решающим фактором является толщина пленки, все исследуемые нами пленки имели одинаковую толщину – 0.7 мкм, а нагрузка также была одинаковая и составляла 250 г.

**Таблица 1.** Число проходов для полного истирания пленок TmSe, TmS и LaBi, напыленных на различных подложках.

Материал плёнки	Толщина пленки, мкм	Нагрузка, г	Число проходов для полного истирания		
			Подложка из кремний	Подложка из ситалла	Подложка из лейкосапфира
TmSe	0.7	250	29 – 33	42 – 45	50 – 59
TmS	0.7	250	41 – 43	54 – 56	70 – 73
LaBi	0,7	250	49 – 52	65 – 68	81 – 84

Как видно из **Таблицы 1** и **Рисунка 2** относительная механическая прочность одного и того же материала на одной и той же подложке увеличивается с последовательностью TmSe–TmS–LaBi, что, по видимому, вызвано уменьшением разности коэффициентов теплового расширения подложки и материала пленки, напыленной на этой подложке с указанной выше последовательностью. Чем меньше разность между коэффициентами теплового расширения (**Таблица 2**) пленки и подложки, тем меньше дефектов образуются в пленке при охлаждении от температуры напыления до комнатной температуры, что по видимому, существенно влияет на механическую прочность пленки.

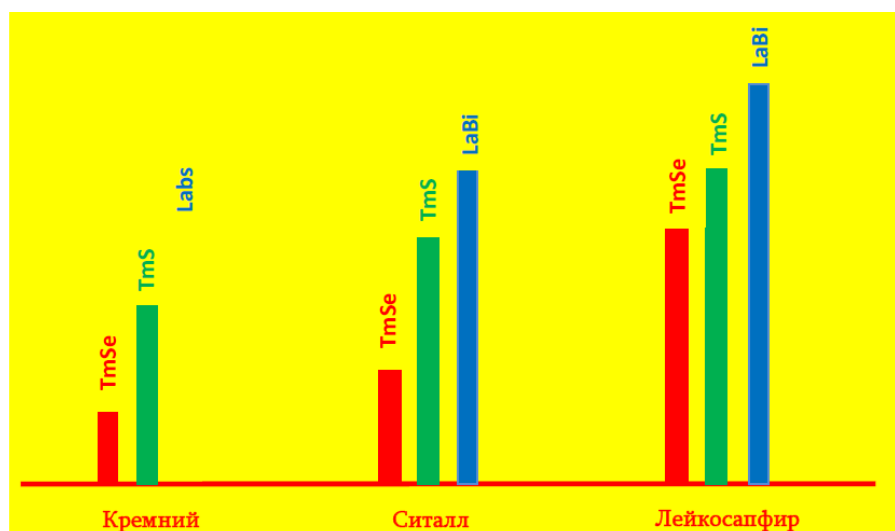


**Рисунок 2.** Относительная механическая прочность пленок TmSe, TmS и LaBi, напыленных на различных подложках.

**Таблица 2.** Коэффициенты теплового расширения пленок TmSe, TmS и LaBi и материалов подложки.

Материал	Коэффициент теплового расширения, $10^{-6}$ , град $^{-1}$	Среднее значение температурного интервала, К	Ссылки
TmSe	18.6	300 – 950	[1]
TmS	14.6	300 – 800	[1]
LaBi	11.9	300 – 980	[2]
Монокристаллический кремний	2.54	300 – 1050	[3]
Ситалл	4.10	300 – 575	[3]
Лейкосапфир	8.10	300 – 575	[3]

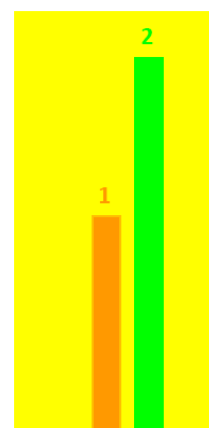
Из **Рисунка 2** также видно, что относительная механическая прочность увеличивается в зависимости от материала подложки с последовательностью монокристаллический кремний – ситалл – лейкосапфир. В частности, механическая прочность пленок напыленных на лейкосапфировую подложку имеют более высокую механическую прочность, чем напыленных на ситалловую подложку, а пленки напыленные на монокристаллический кремний имеют наименьшую прочность. Этот факт, может быть вызван тем, что коэффициент теплового расширения лейкосапфира ближе к коэффициенту теплового расширения напыленного материала, в то время как аналогичная разница для кремния больше, а для ситалла имеет промежуточное значение.

В данной работе также исследована механическая прочность моноселенида тулия, напыленного методом дискретного вакуумно-термического испарения и методом вакуумно-термического напыления из двух независимых источников. В частности на лейкосапфировой подложке приготовили пленки толщиной 0.7 мкм и посчитали количество проходов для полного истирания пленок при нагрузке 250 г (**Таблица 3**).

**Таблица 3.** Относительная механическая прочность пленок TmSe, приготовленных различной методикой на сапфировой подложке.

Метод приготовления пленок	Состав пленки	Толщина пленки, мкм	Нагрузка, г	Число проходов для полного истирания
Испарение из двух независимых источников	TmSe	0.7	250	67
Дискретное испарение Предварительно Синтезированного соединения	TmSe	0.7	250	115

**Рисунок 3.** Относительная механическая прочность пленок TmSe, напыленных на лейкосапфировой подложке (толщина пленок 0.7 мкм, пленки приготовлены методами испарения из 1 – двух независимых источников и 2 – предварительно синтезированного материала).



Как видно из **Таблицы 3** и **Рисунка 3** относительная механическая прочность пленок, приготовленных дискретным вакуумно-термическим испарением предварительно синтезированного материала, почти на 40 % больше механической прочности пленок, приготовленных вакуумно-термическим испарением из двух независимых источников компонентов. Такая разница может быть вызвана тем фактом, что как показали рентгенодифрактометрические исследования, кристаллическая решетка пленок приготовленных дискретным испарением более совершенна, чем структура пленок приготовленных испарением из двух независимых источников. Аналогичную картину мы наблюдали для пленок антимоноидов редкоземельных элементов [4].

#### Ссылки

1. В. Н. Марченко, Г. В. Самсонов. Тепловое расширение некоторых сульфидов РЗМ. ФТТ, 1963, 15, 631-635.
2. С. И. Новикова, Н. Х. Абрикосов. Тепловое расширение некоторых халькогенидов редкоземельных элементов. ФТТ, 1963, 5, 1913-1919.
3. С. И. Новикова. Тепловое расширение твердых тел. 1974, Москва, Наука, 158 стр.
4. З. У. Джабуа. Автореф. дисс. на соиск. уч. степ. докт. техн. наук. 2005, Тбилиси, 16 стр.

## MANAGEMENT OF OCCUPATIONAL RADIATION EXPOSURE IN GEORGIA

G. Nabakhtiani, I. Giorgadze, K. Gorgadze, Sh. Khizanishvili

Georgian Technical University  
Department of Engineering Physics  
Tbilisi, Georgia  
g.nabakhtiani@moe.gov.ge

Accepted June 20, 2015

### Abstract

Georgia has established occupational exposure control system. Further developing of the system is going on. As a first step a new legislation base is elaborating – new national BSS is drafted and agreed among different ministries. The other task is practical implementation of requirements and providing of technical support for them. New approach for occupational exposure gives the possibility to increase effectiveness for implementation of main radiation safety principles.

### 1. Introduction

Georgia is small country situated on the south Caucuses territory was before the part of Soviet Union. After destroying Soviet Union the country had received difficult heritage for control of nuclear and radiation activity: Many enterprises stopped their activity or changed the profile without proper notification sent to state supervising authority. As a result in the first years of the country independence even no register of organizations conducted the nuclear and radiation activity was established. The major problem was s.c. orphan radioactive sources, which were disseminated over the country territory. The situation was changing step by step starting 1996 when Georgia become member of International Atomic Energy Agency (IAEA). Based on the international support the all main activities were focused on two ways: Searching and recovery of orphan radioactive sources and establishment of state regulation. The first important action was adoption of Frame Law “On Nuclear and Radiation Safety” at January 1, 1999 (No. 1674–IS) According to the law requirements Ministry of Environment and Natural Resources Protection (MENRP) was assigned as a state Regulatory Body and Nuclear and Radiation Safety Service (later converted to Department for Nuclear and Radiation Safety – DNRS) was created within the Ministry of practical fulfillment of state regulatory functions. RB started activity to define scope of regulatory area (establishment of state register for facilities and sources) and elaboration regulatory requirements.

Up to 2004 DNRS developed only partially completed inventory covered some main users of radiation sources. The information was kept as a hardcopy and in excels files. According to IAEA standards every state should have inventory of its radioactive sources [1]. Receiving support from US NRC Georgian RA – DNRS had started activity to create full scale inventory of all sources of ionization radiation existed in Georgia. DNRS was granted by



computer code RASOD elaborated by Armenian specialists under US NRC programme to support of some former Soviet country in establishment of inventory of sources of ionization radiation.

Information collection was divided on the two main stages. At the first stage special letters were disseminated to the potential owners asking them to provide information for their radioactive sources. As a Georgian experience showed this type activity was not as effective as it was desired. Therefore special on-site checkings were conducted. So, full scale inventory of ionization radiation sources (not only radioactive sources) and associated activities were created. The sources were grouped in classless according to IAEA requirements what provides base to determine security level for different sources [2] and associated activities.

### 2. Legislative framework

Every activity should be based on clearly defined legal basement. As it was mentioned above the first Frame Law was put in operation at 1999. During the last year a number of changes were incorporated into the law text, so new version of the Frame law (No. 5912-RS) was adopted at 2012. General principles for authorization of nuclear and radiation activity are defined by Law of Georgia No. 1775-RS “On Licenses and Permits” – adopted on June 24, 2005. (License process started at 2001. It was regulated by specials decree before). Georgia has its national basic safety standards s.c. RSL-2000 (Technical regalement No. 28 approved by Georgian government). The text of the regalement contains some old –exhaust requirements, therefore by IAEA support the new national BSS was drafted being fully corresponded to IAEA GSR Part 3. The text of the document is discussed among different ministries and waits its final approval. There are number of other legal documents (for instance technical regalement No. 34 “Main Rules for Handling with Radioactive Sources and other Sources of Ionization Radiation”), which also need to be upgraded. The new document “On Inspection of Nuclear and Radiation Activity” defines general rules and requirements for conducting of regulatory inspection of different types of activity. DNRS has clear action plan for legislation upgrade elaborated together with IAEA experts.

### 3. Occupational radiation management

Defining the standards and norms for occupational radiation three main exposure situations can be considered: Planned exposure, Emergency exposure and Existing exposure.

#### *Planned exposure*

Georgian legislation sets special way for application of graded approach: removing from regulatory control exempted sources and activities, and license all other activity (no simply registration). Up-to-date 667 license holder is fixed in Georgia. **Figure 1** shows dynamics for license issuing at last years.

One important document for authorization of activity is Radiation Protection Programme (RPP). Usually RPP contains description of responsibilities, setting of zones (controlled and supervised areas), working rules, integrated radiation protection functions with other ones, dose monitoring programme, emergency plan, training programme, Quality Assurance programme. RPP considers implementation of three main principles [3]:

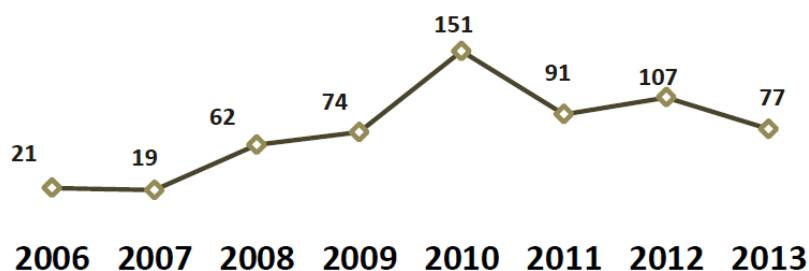


Figure 1. The number of licenses issued at the last years.

- Justification – all activities should be justified;
- Optimization – doses should be As Low As Reachable Achievable (ALARA); and
- Limitation – special dose limits should be set.

RSL-2000 still divides workers in two main groups: Group “a”, who works with ionization radiation sources and, group “b” who supports the activity of group “a” persons. This deviation will be abolished by adoption of new national BSS soon, but now annual dose limit for group “a” is defined as 20 mSv and for group “b” – 5 mSv. Annual optimized dose is assigned as 6 mSv. If annual dose is less than 6 mSv no individual dose monitoring is obliged. In other case individual dose as a ambient dose  $H_p(10)$ ,  $H_p(3)$  and  $H_p(0.07)$ . In measurement the type of exposure should be considered. For instance, during working with neutron sources the neutron flux measured by special detectors. Linear medical accelerators with energy 12 MeV and more are good examples for it. In case of using of unsealed radioactive sources the license should use radiometers for measurement of potential contamination. The doses monitoring programme defines two main actions: individual dose monitoring and workplace monitoring. There are four main reasons to conduct dose monitoring [4]:

- (a) Routine monitoring is associated with continuing operations and is intended to meet regulatory requirements and to demonstrate that the working conditions, including the levels of individual dose, remain satisfactory;
- (b) Special monitoring is investigative in nature and typically covers a situation in the workplace for which insufficient information is available to demonstrate adequate control. It is intended to provide detailed information to elucidate any problems and to define future procedures. It should normally be undertaken at the commissioning stage of new facilities, following major modifications to facilities or procedures, or when operations are being carried out under abnormal circumstances such as an accident;
- (c) Confirmatory monitoring is performed where there is a need to check assumptions made about exposure conditions, for example to confirm the effectiveness of protective measures;
- (d) Task related monitoring applies to a specific operation. It provides data to support the immediate decisions on the management of the operation. It may also support the optimization of protection.

Especial attention is paid for setting of doses constraints and reference levels. Usually all licensee uses recordable, investigation and intrusion levels. The first used as starting (zero) level to record individual doses, the second – to initiate the investigation (why doses become so high?), and third – start investigation simultaneously stopping one or all types of activities. Such approach allows avoiding achieving of dose limit occasionally.

Georgia is not nuclear country. The country had only one research nuclear reactor, which operation was stopped at 1989. The decommissioning of the reactor is going successfully based on IAEA support. The main area for application of ionization sources in Georgia is medicine (Figure 2). Individual dose monitoring is conducted by licensee or special technical support organization having appropriate license. The annual doses for personnel are appr.2.5 – 4.5 mSv. The doses are higher in brachithery and angiography.

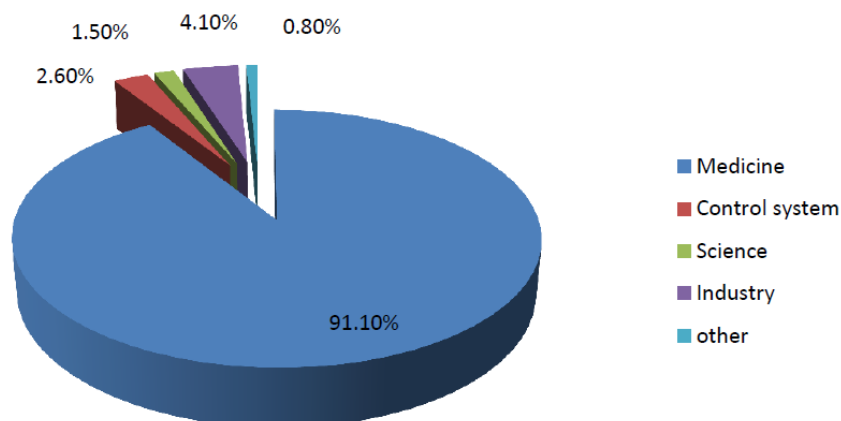


Figure 2. Application of ionization radiation in Georgia.

According to Req.5 of BSS [2] Management System (MS) and Human and Organizational Factor (HOF) together with safety culture are essential elements having influence occupational exposure. Therefore all of them should be considered in authorization documents. Georgian legislation set clear requirements for HOF, but legal bases for others should be developed considered the local features.

Last years especial attention paid to NORM. Georgia has oil excavation and gas transportation industry providing of accumulation NORM. Usually if they amount are less as defined by unconditional clearance level [5], no regulation should be applied for them; other cases can be considered as a planned exposure.

### ***Emergency Exposure***

Emergency workers can be divided into four main groups [4]:

- (a) Emergency workers who have specified duties in response to a nuclear or radiological emergency;
- (b) Workers performing their duties at working places and being not involved in response to a nuclear or radiological emergency;
- (c) Workers who are asked to stop performing their duties at working places and to leave the site;
- (d) Workers who are accidently exposed as a result of an accident or incident at a facility or in an activity and whose exposure is not related to the emergency response.

By the requirement of national frame law every licensee should develop emergency plan and conduct its activity according to the plan including the notification of Regulatory Body. By the decision of RB the facility emergency accident can be assessed as a national radiation accident in solving of what specialists of Civil Defense Department of Ministry of internal Affairs can be also involved. So, exposure situation for workers of groups (b) and (c) can be considered as a planned exposure situation.

A number of emergency recovery operations were conducted in Georgia- the country had great problems with to s.c. orphan radioactive sources. Unfortunately some people (no workers) were overexposed due them. All emergency actions should be conducted according to elaborated plan, which considers transformation of emergency exposure situation to the existing exposure situation according to requirement No. 46 BSS [2]. It is should be emphasized that justification principle should be applied for emergency workers, especially started with the first phase of activity when gathering information and assessment of nature of the event is necessary. At the second phase the situation should be evaluated and recovery operation plan should be developed (**Figure 3**).

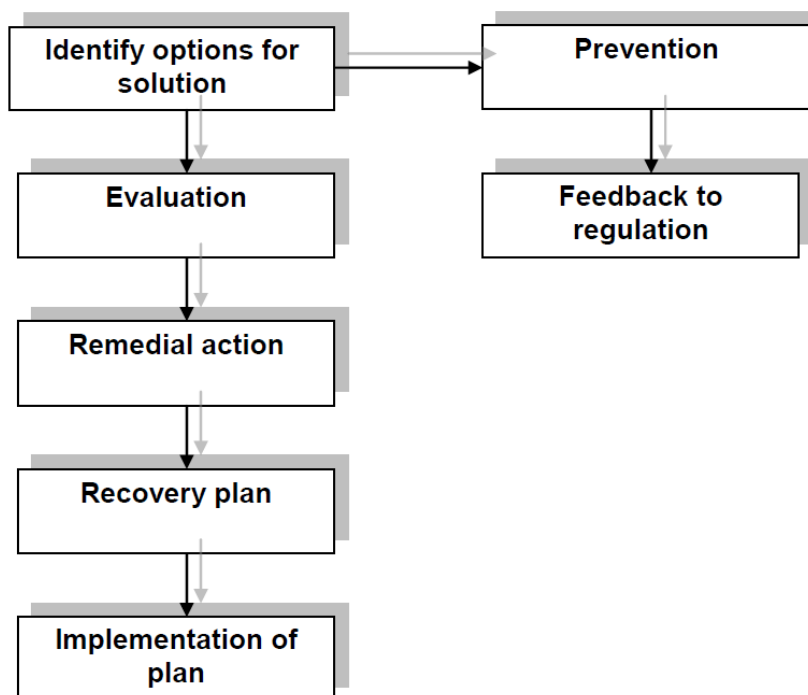


**Figure 3.** Chart for phase two for recovery operation.

It is important also to consider feedback to regulatory requirements for prevention in future of occurring of such situations. Phase three considers implementation of the plan. It is important to implement optimization and limitation principles during the emergency actions. The good example is recovery operation conducted for naked RTG sources (Two radioactive sources. Each of two contains radionuclide  $^{90}\text{Sr}$  with initial activity 1295 TBq) at Georgian village Lia in 2002 [6]. The special trainings were conducted for emergency workers to better identify:

- Emergency workers groups and their collaboration;
- Coordination among emergency workers;
- The tools to be used;
- Options to upgrade emergency (recovery) plan.

These actions allow implementation of optimization principle for workers. Georgian legal base sets the same requirements for doses limitation as defined by international requirements [4], but maximum individual dose received by one person was 1.16 mSv, usually doses were in range 0.05 – 0.95 mSv [6].

### *Existing Exposure*

Existing exposure can be occurred by ending of emergency exposure or due to natural exposure. It contains exposure of workers and population. As usual justification, optimization and limitation principles can be considered for workers. It is important that RB should be satisfied with emergency actions and identify them as an ended. In other case the situation can not be defined as “Existing” (Anaseuli case in Georgia).

### **4. Conclusion**

According to economic development application of ionization radiation in different branches is growing in Georgia, especially in medicine. More attention needs to paid for radioactive waste processing and NORM. So, implementation of new approach for occupational exposure is important task to provide nuclear and radiation safety for all types of activity.

### **References**

1. IAEA. Code of Conduct on Safety and Security of Radioactive Sources. 2004, Vienna.
2. IAEA. Radiation Protection and Safety of Radiation Sources: International Basic Safety Standards. In: IAEA Safety Standards, General Safety Requirements, Part 3. 2011, Vienna.
3. IAEA. Fundamental Safety Principle No. SF-d1. 2006, Vienna.
4. IAEA. Occupational Radiation Protection, IAEA Safety Standards (Draft ds453). 2014, Vienna.
5. IAEA. Application of Concept of Exclusion, Exemption and Clearance. In: IAEA Safety Standards Series, Safety Guide RS-G-1.7. 2004, Vienna.
6. IAEA. The Radiological Accident in Lia, Georgia. 2013, Vienna.

STATEMENT OF BOUNDARY CONDITIONS OF EQUATION  
FOR MAGNETIC FLUID INCLUDING NANOPARTICLES

K. Kotetishvili, E. Iordanishvili, G. Chikhladze

Georgian Technical University  
Department of Engineering Physics  
Tbilisi, Georgia  
ketinooo@hotmail.com  
gurchix@gmail.com

Accepted July 16, 2015

**Abstract**

The statement of boundary conditions of the closed system of equations for the magnetic fluid, which includes nanoparticles, has been carried out. It is shown that these conditions are received from Maxwell's equations and that the surface current at two extreme points may be directed oppositely. It is shown as well that the magnetic field outside the area of the magnetic fluid is zero, i.e. it may exist only within the definite area covered by the magnetic fluid.

After linearization of Langevin's function of the equation for magnetic fluids, the closed system of equations is received for complex amplitudes of magnetization  $\hat{m}_x$ ,  $\hat{m}_y$ , spin-velocity  $\omega_z$  and velocity of the magnetic flux  $v_x$  [1]:

$$\hat{m}_x = \frac{M_0}{\mu_0} \frac{\left(j\Omega\tau + 1 + \frac{M_0}{\mu_0}\right) \hat{h}_x - (\omega_z\tau) \frac{\hat{b}_y}{\mu_0}}{\left(j\Omega\tau + 1\right) \left(j\Omega\tau + 1 + \frac{M_0}{\mu_0}\right) + (\omega_z\tau)^2}, \quad (1)$$

$$\hat{m}_y = \frac{M_0}{\mu_0} \frac{(\omega_z\tau) \hat{h}_x + \left(j\Omega\tau + 1\right) \frac{\hat{b}_y}{\mu_0}}{\left(j\Omega\tau + 1\right) \left(j\Omega\tau + 1 + \frac{M_0}{\mu_0}\right) + (\omega_z\tau)^2}, \quad (2)$$

$$-2\xi \frac{\partial v_x}{\partial y} - 4\xi \omega_z + \langle T_{mag,z} \rangle = 0, \quad (3)$$

$$-2 \frac{\partial p'}{\partial x} + 2\xi \frac{\partial \omega_z}{\partial y} + (\xi + \eta) \frac{\partial^2 v_x}{\partial y^2} = 0, \quad (4)$$

$\hat{b}_y$  and  $\hat{h}_x$  being the fields of the small signal and are known quantities. Analytical solutions of this system of equations may be received, when the boundary conditions will be taken into account. From Maxwell's equations the corresponding boundary conditions for the components of the magnetic field are given as follows:

$$\vec{l}_n (\vec{B}_{int} - \vec{B}_{ext}) = 0, \quad (5)$$

$$\vec{l}_n \times (\vec{H}_{int} - \vec{H}_{ext}) = L_s, \quad (6)$$

where  $\vec{l}_n$  is the unit vector (normal) at the surface between two mediums apart.  $L_s$  is the boundary surface current density in the area from  $y=0$  to  $y=d$  (**Figure 1**), which is the source



of the magnetic field in  $x$  and  $y$  directions. The density of the magnetic flux and the intensity of the magnetic field are given:  $\vec{B}_{int}$  and  $\vec{H}_{int}$  correspond to the internal part of the area of fields of the magnetic fluid, i.e. to  $0 < y < d$  area, while  $\vec{B}_{ext}$  and  $\vec{H}_{ext}$  correspond to external part of the magnetic fluid, i.e. to  $y < 0$  and  $y > d$ .

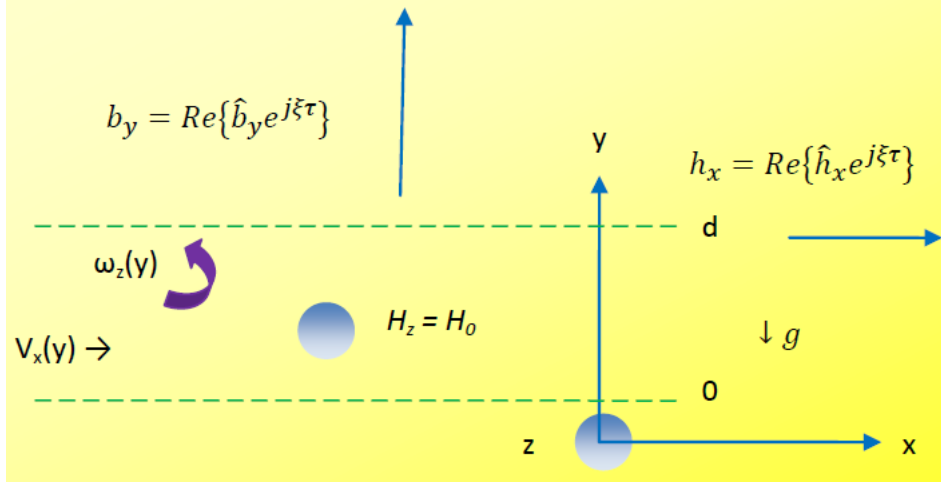


**Figure 1.** Magnetic fluid in the vessel with solid, fixed walls ( $y=0$ , and  $y=d$ ).

The surface current at  $y=0$  and  $y=d$  may be of opposite direction (e.g. generation of the surface current in  $x$  direction with uniformly distributed direct constant current in  $z$  direction and generation of varying in time and in  $z$  direction surface current in  $x$  direction). At that time the magnetic field outside the area of the magnetic fluid is zero. In  $y$  direction for  $\vec{B}$  field the superposition of the field at the area takes place, when the magnetic field is located at  $y=0$  and  $y=d$ . For the spin-velocity  $\omega_z$  the boundary conditions are absent as to the spin-velocity is not taken into account in the formula

$$\vec{T}_{mag} + 2\xi(\vec{\nabla} \times \vec{v} - 2\vec{\omega}) = 0, \quad (7)$$

while  $v_x$  velocity at the stationary border ( $y=0$  and  $y=d$ ) is zero. Taking into account all these conditions, the system of equations for the magnetic fluid should be solved.

## References

1. K. V. Kotetishvili, E. Iordanishvili, N. Kobalia, G. G. Chikhladze. Studying the equation of motion for magnetic fluids with nanoparticle inclusions. J. Appl. Electromagn., 2015 – in press.
2. K. V. Kotetishvili, G. G. Chikhladze. Linearization of the solution of Langevin's equation in magnetic liquids. Nano Studies, 2013, 7, 225-228.
3. R. Rosensweig. Ferrohydrodynamics. 1997, New York.
4. J. Popplewell, R. E. Rosensweig, R. J. Johnston. Magnetic field induced rotations in ferrofluids. IEEE Trans. Magn., 1990, 26, 5, 1852-1854.

A NEW MECHANISM OF “ANOMALIES” OF PHENOMENA  
RELATED TO ATOMIC DISPLACEMENTS IN NANOMATERIALS

A. Gerasimov<sup>1</sup>, G. Chiradze<sup>2</sup>, M. Vepkhvadze<sup>1</sup>, T. Ratiani<sup>1</sup>

<sup>1</sup>Georgian Technical University  
Department of Engineering Physics  
Tbilisi, Georgia

aleksi.gerasimovi@gmail.com

<sup>2</sup>A. Tsereteli State University  
Department of Physics

Kutaisi, Georgia  
gogichiradze@yahoo.com

Accepted July 22, 2015

**Abstract**

It is shown that essentially the change of properties of nanomaterials depending on the nanoparticles size is associated with changing in the location of atoms, which from the standpoint of the molecular-kinetic theory are considered as anomalies, turn into normal when applying a new mechanism of changing the location of atoms in condensed matter, i.e. molecular-potential theory.

It is known that some physical phenomena associated with atom displacements in nanomaterials have “abnormal” character depending on the nanoparticles size compared with same phenomena in conventional material from the same substance [1, 2]. In particular, with decreasing particle size:

1. The microhardness and yield point increases above the law Hall-Petch relation and then it takes place an “anomaly”, i.e. reduction.
2. Superplasticity in nanomaterials is higher and it occurs at lower temperatures than in conventional materials.
3. Coefficient of diffusion in nanomaterials is considerably higher than in bulk of same substances. In nanomaterials, coefficient of diffusion increases with reducing in size of nanoparticles (**Table 1**).
4. Recrystallization is faster at smaller size of nanoparticles.

It should be noted that the notion “anomaly” in the scientific discourse arises only in the case when partially the observed phenomenon defies even qualitative interpretation of those scientific concepts that are used to explain the phenomenon, i.e., anomaly, is contrary to notions accepted at current stage of development of science.

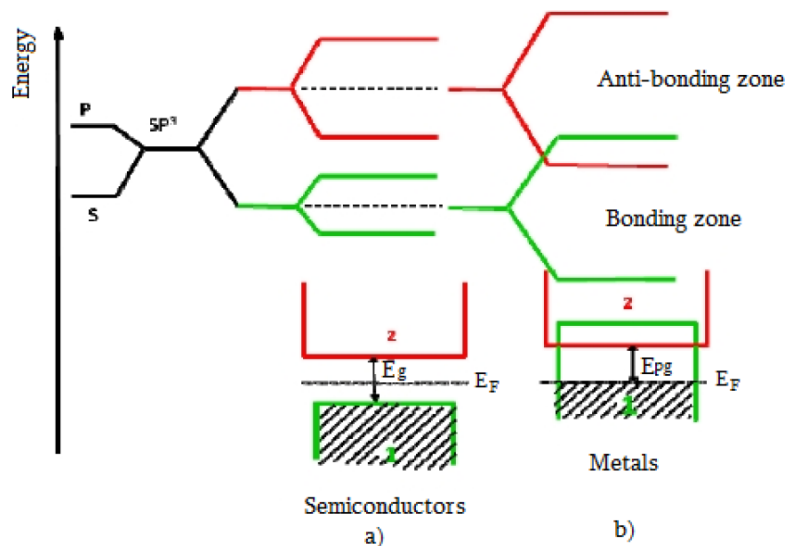
All the physical phenomena related to the easiness of atomic motion are described by the traditional molecular-kinetic theory [3, 4]. There are many attempts to explain them, but all they have failed because all they are based on traditional molecular-kinetic theory, which is suitable only for high temperature region ( $T > 0.7T_m$ , where  $T_m$  is the melting point) [5, 6].

Table 1

Material	Diffusion coefficient (393 K), $m^2 / s$
Nano Cu	$1.8 \cdot 10^{-17}$
Compacted Cu	$1.3 \cdot 10^{-31}$
Granular Cu	$1.7 \cdot 10^{-19}$
Surface Cu	$1.4 \cdot 10^{-16}$
Nano Ni	$1.0 \cdot 10^{-10}$
Compacted Ni	$1.2 \cdot 10^{-25}$
Granular Ni	$3.0 \cdot 10^{-12}$

Here we offer a new concept, which is proved theoretically and experimentally and gives the opportunity to explain any experimental fact related to the atomic displacements in solids and nanomaterials.

According to this conception, all properties of substance are determined by the states of chemical bonds between neighboring atoms in given conditions. It is known that in solids, as well as in molecules, electrons contributing in chemical bonds can occupy two different kinds of quantum states, where they are strengthened or weakened by the inter-atomic binding. In first case, they occupy bonding orbitals, while in second case – anti-bonding ones [7]. In solids and also their melts atomic orbitals are combined into bands (**Figure 1**). Formation of the hybridized orbitals in process of approaching atoms means their splitting into bonding and anti-bonding orbitals and creation of corresponding bonding and anti-bonding bands: in dielectrics and semiconductors bonding (valence) and anti-bonding (conduction) bands are separated by a band gap of a certain width characteristic for given substance, while in metals they are overlapped and transition energy between two states is determined by the energy-difference between the Fermi level and anti-bonding band's lower edge, which is called as pseudo-gap (**Figure 1**).



**Figure 1.** During the approaching atoms, the formation hybridized orbitals (there is shown an example of a IV group element) and their further splitting in binding and anti-bonding orbitals of further forms the bonding and anti-bonding bands. Bonding and anti-bonding energy bands: a) semiconductor or dielectric, b) metal, where  $E_F$  is the Fermi level,  $E_g$  is the band gap in semiconductors and  $E_{pg}$  is the pseudo-gap in metals.

Nanoparticles electronic structure is a kind of discrete spectrum [8, 9] with quite closely located bonding and anti-bonding levels (**Figure 2**). In case of nanoparticles, electron in some way created on the anti-bonding level and corresponding hole on the bonding level freely move if energy-difference between these levels is  $\sim kT$ ,  $T$  is the temperature, whattakes a place even at room temperature.

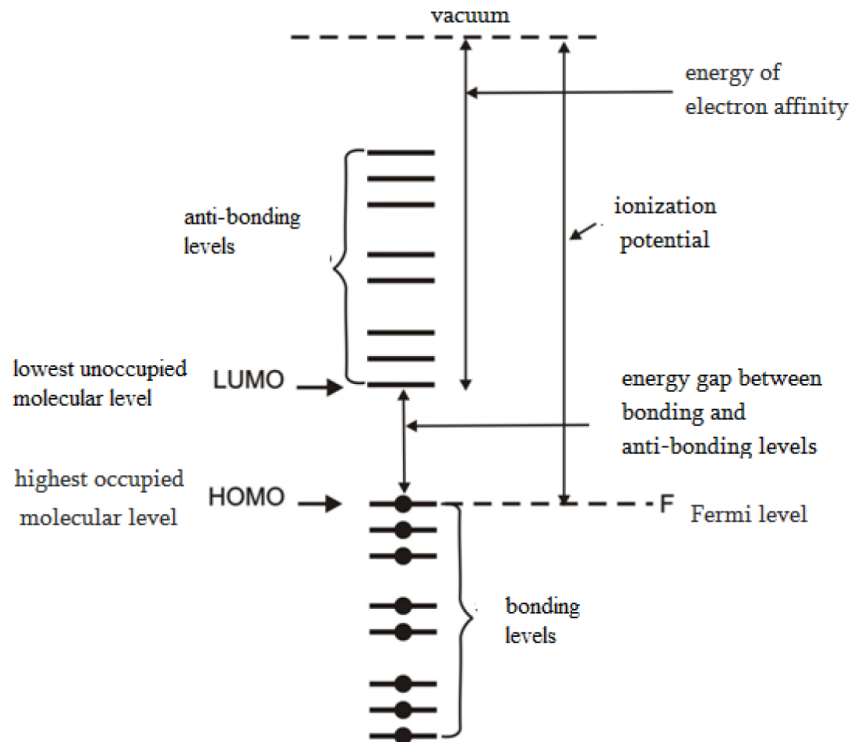


**Figure 2.**The energy structure of a nanoparticle.HOMO – highest occupied molecular orbital and LUMO – lowest unoccupied molecular orbital.

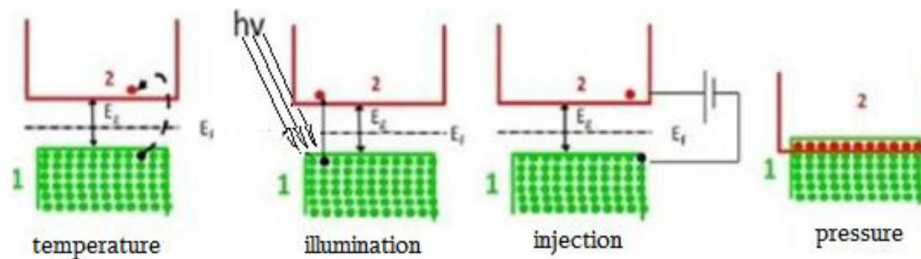


**Figure 3.**Different methods of forming of ABQPs.

Free electron created in the anti-bonding band (levels) by the transition from bonding one or injection and corresponding unoccupied state (hole) in the bonding-band (levels) are anti-bonding quasi-particles (ABQPs). Regardless of the way (temperature, illumination, injection, pressure, etc. – **Figure 3**) of changing in their number, ABQPs weaken chemical bonds between neighboring atoms and facilitates the movement of atoms. The fact that at the higher concentration ABQPs the easier movement of atoms occurs, unambiguously were proved by photomechanical and electromechanical effects (softening, i.e. decrease in microhardness, as a result of exposure, respectively, to light or electric field, which form ABQPs in anti-bonding interband (levels) optical transitions or injection [10, 11]). For example, from the **Figure 4** it is seen that the softening has to occur in those regions of the sample where ABQPs are formed.

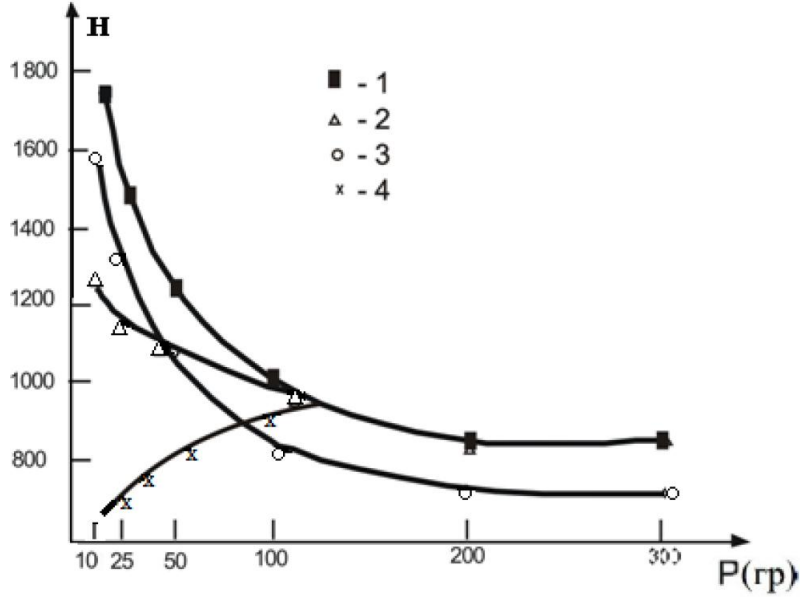


**Figure 4.** Microhardness of Si versus the applied loads on the indenter: 1 – in darkness, under illumination of 2 –laser (with energy of quanta  $h\nu \geq E_g$ ), when a certain concentration of ABQPs is created only on the surface layer, 3 –white light passing through the Si-filter ( $h\nu < E_g$ ), when ABQPs are generated in the bulk, and 4 – laser of high intensity, i.e. when they are ABQPs in high concentration. Surface hardness is smaller than the bulk hardness.

According to these conceptions, the substance energy bands structure, their hierarchy on the energy scale and population by electrons determine all properties of a substance at given temperature (aggregative state, conductivity, mechanical and optical properties.Etc.). Changes in these characteristics, mainly, in numbers of electrons on bonding and anti-bonding levels induced by any influence leads to changes in various properties of a substance [5, 6].

In condensed matters, there is a certain probability (for given ABQPs concentration) that several ABQPs due to their chaotic motion will fall in an atom vicinity, what can distinctly weaken its chemical bonds and then simplify the atom’s displacement within the lattice.The atomic displacements probability has been expressed by the formula:

$$W_A = A W_{ph} \left( \frac{n_{ABQP}}{N_a} \right)^\beta, \quad (1)$$

where  $n_{ABQP}$  is the ABQPs concentration,  $N_a$  is the concentration of atoms in substance,  $W_{ph}$  is the probability of the presence of phonon of certain energy near the given atom,  $A$  is a proportionality coefficient almost independent of temperature,  $\beta$  is the number of ABQPs sufficient for causing an atomic displacement. One can see from this relation that such probability mainly is determined by the concentration and not by the temperature unlike the diffused opinions that it should be an exponential function of temperature:

$$W_A = B \exp\left(-\frac{U}{kT}\right), \quad (2)$$

where  $U$  is the activation energy of atomic displacements and  $B$  is the another proportionality coefficient almost independent of temperature.

ABQPs reaching nanoparticles surface are reflected. This is a reason why they cannot leave nanoparticle unlike to equal volume in the compacted solid (**Figure 5**). Consequently, ABQPs in nanoparticles will be located near larger number of atoms than in the compacted

substance that enhances the effect of weakening the chemical bonds in the nanoparticles. Such effect can be described introducing effective concentration, ratio of which with its real value equals to the ratio of frequencies of ABQPs' appearance near the given atom in nanoparticle and compacted solid during an atomic vibrations cycle.

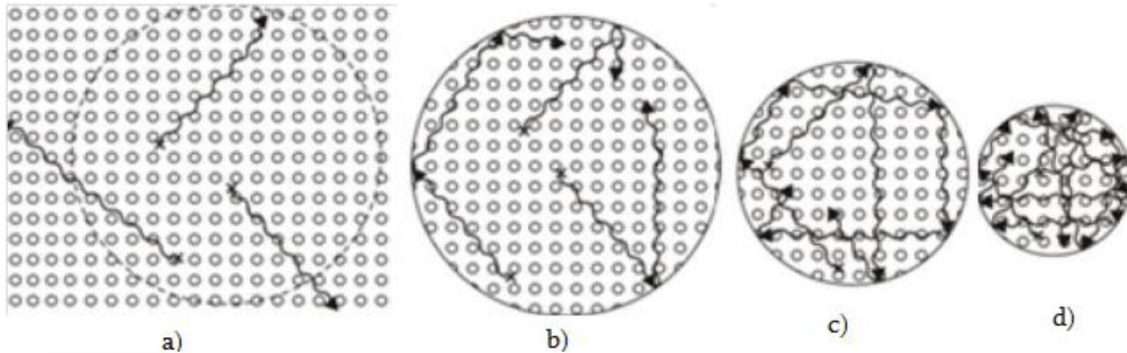


**Figure 5.** Schematic illustration of growth in ABQPs' concentration with reducing in nanoparticles size at given temperature. Increasing in ABQPs effective concentration for fixed real concentration with decreasing in sizes: a) ABQP trajectory in compacted solid's region with volume equal to the nanoparticle volume: two of them are leaving the volume; b) in connection with the reflection from the boundary surface of the nanoparticle: trajectories of three ABQPs are in it and they are around more number of atoms than in the case of a compacted solid body; c) and d) when size of nanoparticles decreases the same three ABQPs are near a larger number of atoms.

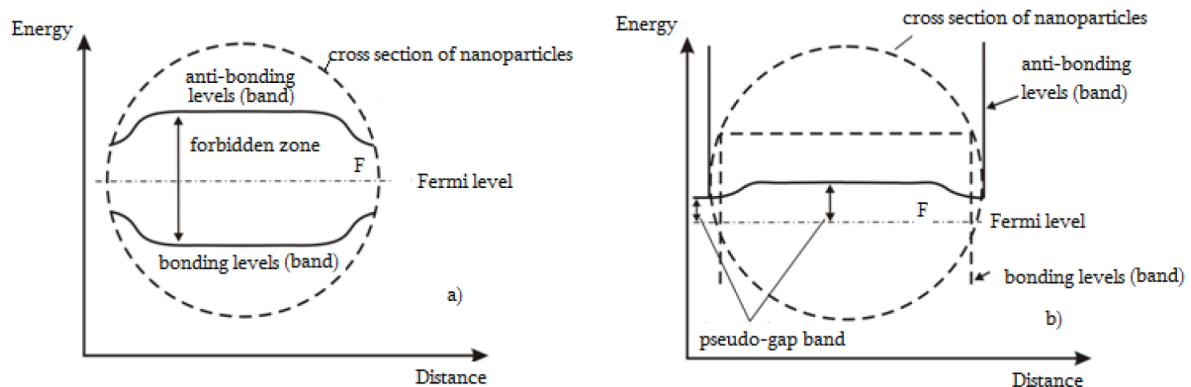


**Figure 6.** Energy levels distributions in nano-particle surface layer and bulk. Due to surface reflection, the probability of ABQPs appearance near the atoms in surface layer is higher than that in bulk, what a) decreases energy-difference between bonding and anti-bonding levels in semiconductor; b) in metals these levels are overlapped and pseudo-gap near the surface is smaller than in bulk and then the concentration is incomparably higher.

Because of small sizes, in nanoparticles with the given concentration of ABQPs they more frequently reach surface and are reflected from it. As a result, inter-atomic bonds in the surface layer are weakened in more degree if compared with those in bulk. Weakening in bonding leads to the decreasing in energy gap width [12] and intensifies electron transitions at given temperature, which causes an excess of the ABQPs concentration in the surface layer and then further decreasing in energy gap value. It yields an interesting energy band structure of substance, which is characterized by the variable energy gap: lower near the surface than in the bulk (Figure 6).



Such kind of electronic structure leads to the ABQPs excess in surface layer and, consequently, to the material softness if compared with that in bulk. From it follows higher mobility of atoms in surface layer than in nanoparticle’s bulk. It is clear that effective concentration increases with decreasing in the nanoparticles’ size. Consequently, in formula (1) describing atomic displacements the real concentration should be substituted for effective concentration, which should be calculated separately for nanoparticles’ given size and process.

Based on the above stated new concept of movement of atoms in condensed matter, let us describe the mechanisms of “anomaly” phenomenon mentioned in the introductory part.

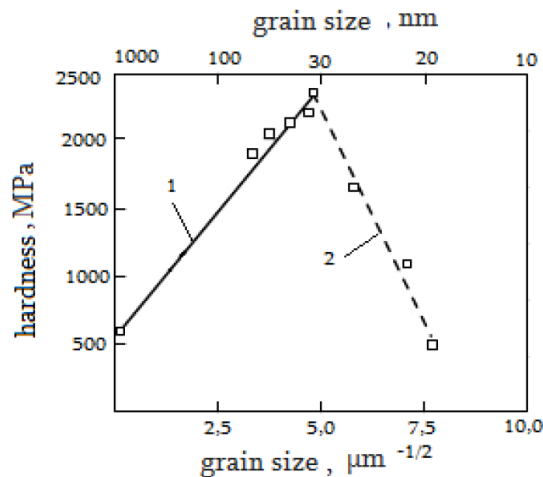


**Figure 7.** Dependence of nanomaterial hardness from size of consistent grain-particles. 1 – Hall–Petch and 2 – anomalous (“anti-Hall–Petch”) regions [7, 8].

Typically, the reduction of grain size to nanometer values causes an increase in the material microhardness (MH) and the yield point in 4 – 5 times. This trend in the case of MH is described by empirical Hall–Petch relation:  $H = H_0 + KL^{-1/2}$ , where  $H$  is the hardness of the nanomaterial,  $H_0$  is the hardness of a bulk substance,  $K$  is a constant individual for each material, so-called coefficient of the Hall–Petch relation, and  $L$  is the average size of nanoparticles [10]. Similarly, the yield point increases with decreasing in the size of nanoparticles at the beginning similarly to the Hall–Petch law:  $\delta_r = \delta_0 + KL^{-1/2}$  ( $\delta_r$  is the yield point and  $\delta_0$  is the internal tension, which prevents the plastic shearing in the material), and then decreases [13]. For many of the investigated nanomaterials, the Hall–Petch relation is valid down to a certain nanoparticles’ size. But, for smaller grains there is observed an opposite effect: hardness and yield point decrease with decreasing in the grain size. Such an “anomaly” phenomenon is called “anti-Hall–Petch” effect (**Figure 7**). Also let us draw attention to the fact that for fragile substances (oxides, nitrides, carbides, intermetallics, etc.) changing in the grain size does not change hardness significantly [14, 15].

The increase of the microhardness and yield point with decreasing in the grain size to the nanoscale typically is explained by a decrease in the number of dislocations in the particles with the reduction of their sizes, what is confirmed by X-ray and electron microscopic studies [1, 2]. It is believed that due to the fact that in the anti-Hall–Petch” effect the dislocation activity is not observed, the deformation is caused by other mechanisms. There are known too many attempts to explain this effect [1, 2]. Existing views on the reducing in the hardness, what is abnormal, give no explanation.

As shown above, the strength of chemical bonds decreases and the mobility of atoms increases with decreasing in the size of nanoparticles. Therefore, one can observe the normal reducing in hardness and yield point of nanomaterials.

The equal concentration of ABQPs in the nanograins explains the fact that for fragile materials (oxides, nitrides, carbides, intermetallics, etc.) the changes in the grains size the substance hardness varies slightly [1, 2] As it has been shown [4, 16] that for the higher melting point of the substance their microhardness is higher, and in semiconductors and metals, respectively, band and pseudo- gaps correlate with the melting temperature. Based on this, the higher forbidden gap is related to lower concentration of ABQPs at given temperature. Nanoparticles contain ABQPs concentration less than the actual and effective concentrations, so the particles of substances with high melting points must be smaller due to effective concentration is reached the corresponding value. From **Figure 8**, it is seen that the anomaly for  $\text{NiZr}_2$  begins with relatively smaller sizes of nanoparticles than in the Fe–Mo–Si–B with melting point lower than that of  $\text{NiZr}_2$  [2].

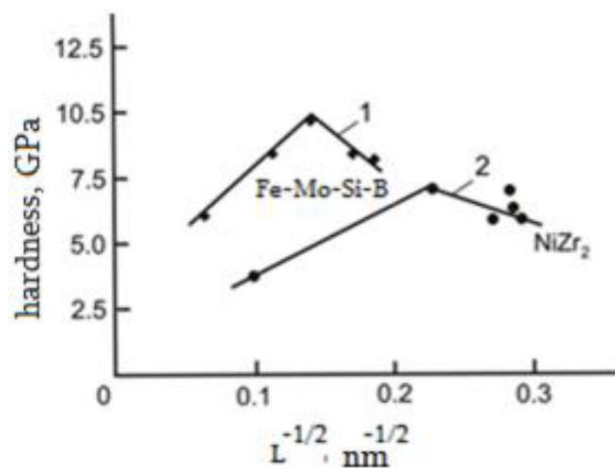


**Figure 8.** Dependence of hardness of nanomaterials with different melting point from their nanoparticles sizes  $T_{m1} < T_{m2}$  [17].

Superplasticity is a too-increased plasticity at given temperature and under the fixed pressure. As is known, plasticity of substances increases with the temperature or the operating pressure and decreases with the sizes of nanomaterial particles. There are proposed some models to explain these experimental data, which indicate that there is no comprehensive mechanism of superplasticity [1, 2]. It is clear that superplasticity, as all types of deformation, due to the easiness of mobility of atoms, which is determined, as is shown above, by the concentration of ABQPs increasing with temperature, operating pressure and decreasing with nanoparticles size.

In nanocrystalline metals Ni, Al [18–20] and fragile nanomaterials TiN, SiC, Si, (Fe,Ni)B $\star$  [21–28], the temperature of the beginning of superplasticity decreases with decreasing in grain size. In materials, e.g. nitrides and oxides, in which bonding and anti-bonding levels are separated from each other significantly, superplasticity takes place at high temperatures – at sufficient number of ABQPs.

Some of authors believe that the plastic deformation in nanomaterials always starts as athermal microsliding of grain boundaries [29, 30]. In nanomaterials, crystallographic orientations of nanoparticles are randomly distributed. When a load is applied to a sample of nanomaterial the pressure acts on nanoparticles. Pressure in certain crystallographic directions

reduces the energy distance between bonding and anti-bonding levels [31 – 33] (i.e. there is an increase in the concentration of ABQPs). Therefore, in those planes, in which there are more nanoparticles, such orientation is real and effective concentration of ABQPs exceeds others. In these planes, it makes possible the microsliding (Figure 9). At this moment, one can easily make melt nanoparticles because the melting temperature is significantly lower [34], while the surface can be melted even at lower temperatures [35].

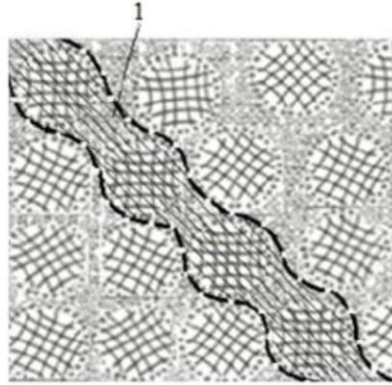


**Figure 9.** Disposition of nanoparticles with different crystallographic orientations in a nanomaterial. 1 – microsliding plane.

As is shown above, the atomic displacements' probability can be expressed by the equation (1). To obtain the diffusion coefficient, it should be multiplied by “speed of mixing”  $v_a d$ , where  $d = 2r_a$  and  $r_a = (3V_a / 4\pi)^{1/3}$ .  $V_a$  is the atomic volume,  $v_a = \sqrt{kT / M_a}$  is the average thermal velocity of an atom of mass  $M_a$  [4]. The increase in the diffusion coefficient with increasing concentration of ABQPs is proved by the experiments on photostimulated diffusion carried out at low temperatures [36]. As we now, concentration of ABQPs increases with decreasing in nanoparticles' size, which decreases the strength of chemical bonds and increases the mobility of atoms: accordingly, diffusion coefficient increases (Table 1).

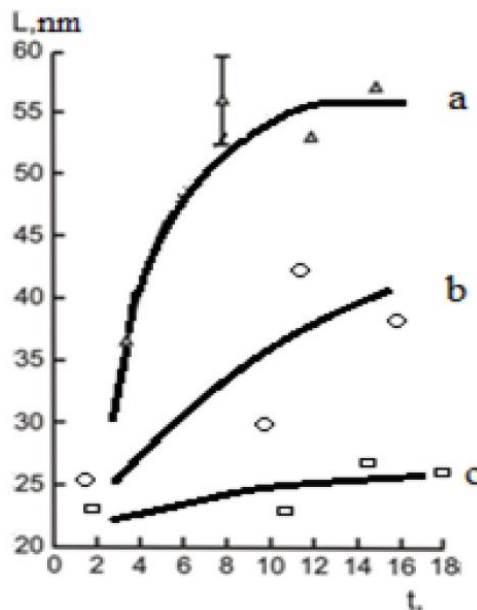


**Figure 10.** Grains growth kinetics in Cu nanosample obtained by Gliter method [37] at room temperature (at pressure 1 GPa). Samples porosities are: a – 7, b – 4 and c – 3 % [38].

Superplastic processing of nanomaterials is accompanied by the propagation of the recrystallization process leading to an increase in the size of the original nanoparticles, what naturally affects the deterioration of parameters of superplasticity [19]. Many nanomaterials are characterized by abnormal grain growth even at room temperature and the influence of porosity on this process [38]. Since recrystallization is determined by a diffusion process, both of them have the same mechanism. As shown above, the atomic displacements' probability is determined by the concentration of ABQPs: at small nanoparticles effective concentration ABQPs is high and the diffusion of atoms of nanoparticles may occur at room temperature, which leads to increase in the size of the nanoparticles and, consequently, reduces the concentration of ABQPs and slows diffusion and recrystallization processes. The pores in nanomaterials increase the rate of diffusion, because diffusion occurs on the surface of the pores, the value of which exceeds the rate of bulk diffusion [39]. Therefore, with increasing the porosity of the nanomaterial it increases the rate of recrystallization (**Figure 10**).

Thus, the above presented material clearly proves that in the context of new ideas about the mechanism of changes in the location of atoms in condensed matter, i.e. molecular-potential theory, there are no anomalies in the phenomena according to the standard molecular-kinetic theory.

## References

1. R. A. Andrievskii, A. M. Glezer. *Phys. Met. & Metallogr.*, 2000, 89, 91.
2. R. A. Andrievskii, A. M. Glezer. *Phys. – Uspekhi*, 2009, 179, 337.
3. J. I. Frenkel. *Kinetic Theory of Liquids*. 1975, Leningrad, Nauka.
4. J. I. Frenkel. *Statistical Physics*. 1948, Moscow, Acad. Sci. USSR.
5. A. Gerasimov. *Fundamentals of Low-Temperature Technology of Production of Semiconductor Devices*. 2005, Tbilisi, Tbilisi Univ. Press.
6. A. B. Gerasimov. In: *Cont. 2nd Int. Conf. “Nanotechnologies” (Nano – 2012)*. 2012, Tbilisi, Neker, 160.
7. W. A. Harrison. *Electronic Structure and the Properties of Solids. The Physics of the Chemical Bond*. 1980, San Francisco, W. H. Freeman & Co.
8. Yu. I. Petrov. *Clusters and Small Particles*. 1986, Moscow, Nauka.
9. S. P. Gubin. *Materials Chemistry. Principles of Classification and Structure*. 1987, Moscow, Nauka.
10. A. B. Gerasimov, G. D. Chiradze, N. G. Kutivadze. *Semicond.*, 2001, 35, 72.
11. A. B. Gerasimov, G. D. Chiradza, N. G. Kutivadze. *Proc. “Intelecti”*, 1998, 3, 24.
12. Yu. I. Ukhanov. *Optical Properties of Semiconductors*. 1977, Moscow, Nauka.
13. G. A. Malygin. *Phys. Solid State*, 2007, 49, 2266.
14. C. C Koch, D. G. Morris, K. Lu, A. Inoue. *MRS Bull.*, 1999, 24, 54.
15. M. A. Morris, M. Leboeuf. *Mater. Sci. & Eng. A*, 1997, 224, 1.
16. A. Gerasimov, E. Kutelia, G. Chiradze, Z. Bokhochadze, D. Kimeridze, T. Ratiani. *Phys. & Chem. Mater. Proc.*, 2003, 4, 5.
17. K. Lu. *Mater. Sci. & Eng.*, 1996, R16, 161.
18. S. X. Mc Fadden, R. S. Mishra, R. Z. Valiev, A. P. Zhilyaev, A. K. Mukherjee. *Nature*, 1999, 398, 684.
19. G. F. Wang, K. C. Chan, K. F. Zhang. *Scr. Mater.*, 2006, 54, 765.

20. R. Z. Valiev, I. V. Alexandrov. Bulk Nanostructured Metal Materials: Preparation, Structure and Properties. 2007, Moscow, Akademkniga.
21. A. M. Glezer. Bull. Russ. Acad. Sci. (Phys.), 2003, 67, 893.
22. K. J. Ma, A. Bloyce. Surf. Eng., 1995, 11, 71.
23. X. D. Han, Y. F. Zhang, K. Zheng, X. N. Zhang, Z. Zhang, Y. J. Hao, X. Y. Guo, J. Yuan, Z. L. Wang. Nano Lett., 2007, 7, 452.
24. X. D. Han, K. Zheng, Y. F. Zhang, X. N. Zhang, Z. Zhang, Z. L. Wang. Adv. Mater., 2007, 19, 2112.
25. Y. Zhang, X. Han, K. Zheng, Z. Zhang, X. Zhang, J. Fu, Y. Ji, Y. Hao, X. Guo, Z. L. Wang. Adv. Funct. Mater., 2007, 17, 3435.
26. A. M. Glezer, S. E. Manaenkov, I. E. Permyakova. Bull. Russ. Acad. Sci. (Phys.), 2007, 71, 1702.
27. V. A. Pozdnyakov. Phys. Met. & Metallogr., 2004, 97, 7.
28. A. M. Glezer, I. E. Permyakova, S. E. Manaenkov. Bull. Russ. Acad. Sci. (Phys.), 2008, 72, 1265.
29. A. M. Glezer. Deform. & Fract. Mater., 2006, 9, 30.
30. V. A. Pozdnyakov. Bull. Russ. Acad. Sci. (Phys.), 2007, 71, 1708.
31. A. L. Polyakova. Phys. Solid State, 1967, 9, 1164.
32. A. L. Polyakova. Acoustic J., 1972, 18, 1.
33. E. G. Melikyan, F. V. Harutyunyan, M. G. Hakobyan. Semicond., 1973, 7, 855.
34. A. Gerasimov, A. Bibilashvili, D. Buachidze, I. Lomidze, R. Kazarov, D. Kimeridze. Bull. Georg. Acad. Sci., 2005, 172, 233.
35. A. Gerasimov. Nano Studies, 2010, 1, 174.
36. A. B. Gerasimov, R. Kazarov. Ukr. J. Phys., 2006, 51, 9.
37. H. Gleiter. In: Proc. 2nd RISO Int. Symp. Metall. & Mater. Sci. 1981, Roskilde, RISO Nat. Lab., 15.
38. V. Y. Gertsman, R. Birringer. Scr. Metal. Mater., 1994, 30, 577.
39. B. I. Boltaks. Diffusion and Point Defects in Semiconductors. 1972, Leningrad, Nauka.

## ВВЕДЕНИЕ ЖИДКИХ $\text{Vi}$ И $\text{Hg}$ В ОДНОМЕРНЫЕ КАНАЛЫ ЦЕОЛИТА $\text{NaM}$

А. А. Капанадзе, Г. Д. Табатадзе, М. С. Тактакишвили

Грузинский технический университет  
Департамент инженерной физики  
Тбилиси, Грузия

Принята 23 июля 2015 года

### Аннотация

Экспериментально изучено введение жидких металлов  $\text{Vi}$  и  $\text{Hg}$  в одномерные каналы цеолита  $\text{NaM}$  с целью получения проводящих атомных цепей. Показано, что после снятия внешнего давления с образца металл частично выходит из каналов. Эффект представлен графически и с помощью соответствующих экспериментальных данных. Проведен рентгеноструктурный анализ образцов.

Получение одномерного металла, т.е. объекта в виде одноатомной проводящей цепочки, представляется задачей исключительно интересной. Одномерный металл, по-видимому, должен обладать уникальными свойствами. Прежде всего, это касается сверхпроводимости. Как было показано в работе [1], можно ожидать резкого увеличения температуры сверхпроводящего перехода для системы взаимодействующих металлических нитей, в которой отсутствует флуктуационное разрушение сверхпроводимости. Однако, в настоящее время, определенно ответить на вопрос о возможности высокотемпературной сверхпроводимости возможно только путем эксперимента. Задача практического получения такой одномерной нити чрезвычайно сложна. В то же время предсказания весьма больших критических магнитных полей ( $> 10^6$  Э) для таких систем более определены, если, конечно, они могут быть сверхпроводящими.

Некоторые надежды в области высокотемпературной сверхпроводимости связывались с солями  $\text{TCNQ}$  – органическими соединениями с большой анизотропией ( $10^2 - 10^3$ ) проводимости. Среди материалов этой группы имеются такие, проводимость которых достаточно велика ( $\text{TCNQ-TTF}$ ), а в структуре имеется достаточно ярко выраженная анизотропия. Однако в этих соединениях, по-видимому, не образуются одномерные нити, хотя целый ряд явлений, связанных с анизотропией, наблюдается довольно хорошо. В них сверхпроводимости не было обнаружено.

Еще в 1973 г. появилось сообщение [2] об экстраординарном увеличении электропроводности (до величины больше, чем у меди) в соли  $\text{TCNQ-TTF}$  в районе 60 – 70 К, которое авторы связывают со сверхпроводимостью. Впоследствии, однако, этот результат воспроизведен не был.

Для создания одномерных металлических нитей путем вдавливания металла в диэлектрическую матрицу идеальными являются структуры типа гмелинита или морденита, в которых каналы имеют размеры, допускающие проникновение металла в виде одноатомных цепочек, располагающихся достаточно близко друг к другу так, чтобы между ними могло существовать взаимодействие. В таких системах взаимодействие



атомов металла с диэлектрической матрицей будет, вероятно, достаточно слабым, обеспечивая требуемую квазиодномерность. Роль физического контакта с матрицей сводится лишь к стабилизации положения металлических нитей в пространстве. Насколько нам известно, такая система является, по-видимому, единственной и наиболее близкой к теоретически рассматриваемой модели [1].

Следует особо подчеркнуть, что попытка практического создания структуры с квазиодномерными металлическими нитями в диэлектрической матрице могла оказаться и безуспешной из-за ряда осложнений, возможность преодоления которых могла быть выяснена только опытным путем. Введение металла могло оказаться невозможным либо по принципиальным соображениям – ввиду малости диаметров каналов, либо – из-за методических осложнений – недостаточной прочности кристаллов или необходимости использования нереально высокого давления. Кроме того, не было ясно, будут ли такие системы, в случае возможности их изготовления, устойчивыми, и будут ли они сохраняться после снятия давления.

В качестве диэлектрической матрицы для получения одномерной нити металла был выбран Na–*Морденит* или NaM. Синтетический цеолит NaM по своей структуре соответствует природному минералу мордениту. В его каркасе отсутствуют пустоты больших диаметров, имеются лишь пересекающиеся каналы с диаметрами  $\sim 2.8$  и  $\sim 6.6$  Å. Поскольку для заполнения ртутью и висмутом каналов диаметром 2.8 Å требуются, по формальным оценкам, критические давления порядка 50 – 60 кбар (хотя, видимо, такие оценки не имеют смысла, т.к. диаметр канала меньше диаметра атома), этот цеолит можно считать обладающим практически одномерной системой каналов. В наших опытах мы использовали промышленно выпускаемый NaM в виде порошка с размерами кристаллов 3 – 10 мм, который спрессовывался в контейнере давлением 7 кбар. Рентгенограмма таким образом спрессованного цеолита практически не отличалась от исходной. Нами был также проведен рентгеноструктурный анализ цеолита NaM, спрессованного (не в гидростатических условиях) давлением 28 кбар, для проверки прочности каркаса цеолита. Заметных отличий в рентгенограмме по сравнению с исходной обнаружено не было.

По сравнению с цеолитом NaX, NaM обладает небольшим объемом пустот, доступных заполнению водой 0.25 – 0.30 см<sup>3</sup> кристалла [3]. В обычных условиях, так же, как и в цеолите NaX, каналы заполнены водой. Режим обезвоживания цеолита NaM весьма схож с режимом для цеолитов типа фожазита (NaX, NaY) [3]. Кривая обезвоживания природного морденита приведена на **Рисунке 1** [3]. Как видно из рисунка, основная массапотеря воды происходит при температуре 200 °С и заканчивается при 400 °С. Вначале обезвоживание проводилось аналогично тому, как это делалось для цеолитов с трехмерной сеткой каналов. Образцы выдерживались в течение трех часов в вакууме 10<sup>-1</sup> мм рт. ст. при температуре 350 °С. Затем образцы NaM заливались жидким металлом. Для таких образцов порограммы или вообще не содержали скачка объема, или скачок был едва заметным. Отсутствие скачка объясняется недостаточным обезвоживанием NaM перед введением металла. Поэтому, в дальнейшем режим обезвоживания был выбран иным. Обезвоживание производилось при температуре  $\sim 400$  °С в вакууме 10<sup>-1</sup> мм рт. ст. в течение 6 ч. Обезвоженные образцы цеолита заливались жидким металлом в вакууме. Такая технология обработки NaM перед введением в его каналы металла позволила получить максимальный скачок объема при снятии порограмм.

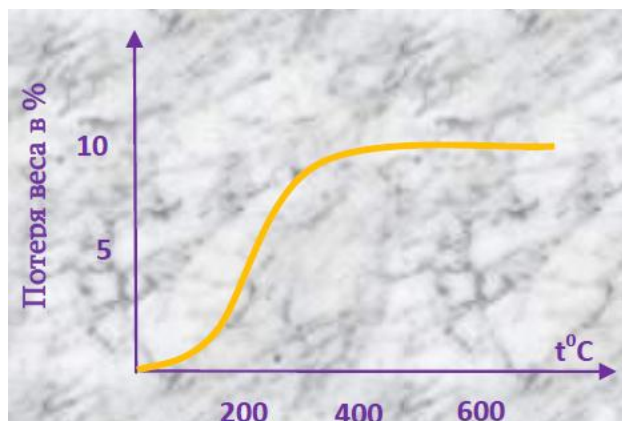


**Рисунок 1.** Кривая обезвоживания морденита при нагревании на воздухе.

Порограммы для системы металл (Hg,Bi)–цеолит снимались обычным способом. Особое внимание было обращено на правильный выбор температуры, при которой производилось вдавливание металла, из-за заметной зависимости температуры плавления металла от величины приложенного давления. Оценка температуры разогрева, при которой металл остается жидким при всех использованных давлениях, производилась следующим образом. Вначале вычислялось критическое давление, при котором металл должен проникнуть в каналы NaM. Вычисление производилось по обычной порометрической формуле [4], применимость которой для каналов даже столь малых размеров ( $\sim 6.6 \text{ \AA}$ ), как это следует из эксперимента, вполне обоснована. Для ртути найденное таким образом критическое давление составляет 29 кбар, для висмута – 23 кбар. Далее по графикам зависимости температуры плавления висмута и ртути от давления определялась температура, при которой металл оставался жидким до давлений, несколько выше критических (до 32 кбар для ртути и до 26 кбар для висмута). Для висмута достаточна температура разогрева  $275 \text{ }^\circ\text{C}$ , для ртути –  $115 \text{ }^\circ\text{C}$ . В разогретой системе создавалось давление и снимались порограммы. Порограммы систем NaM–Bi и NaM–Hg приведены на **Рисунке 2**.

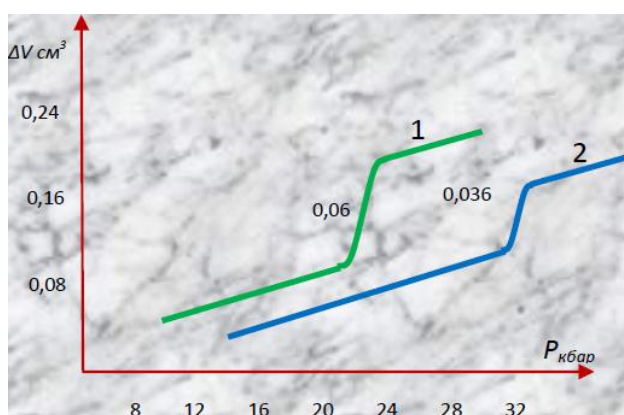


**Рисунок 2.** Изменение объема систем NaM–Bi (1) и NaM–Hg (2) в зависимости от давления.

Критические давления, при которых происходит проникновение металлов висмута и ртути в каналы NaM, величины скачков объема для этих систем, а также расчетные значения скачков приведены в **Таблице 1**. После снятия внешнего давления ртуть,

введенная в каналы цеолита NaM, по-видимому, полностью вытекает наружу (как это имело место и в случае цеолитов с трехмерной сеткой каналов). Это следует из измерения плотности образцов, обработанных давлением в жидкой ртути при давлении, превышающем критическое (первая группа образцов) и при давлении, меньшем критического (вторая группа образцов). Очевидно ртуть вводилась в каналы образцов только первой группы, а в образцах второй группы каналы не заполнялись, а создавалась только обмазка.

**Таблица 1.**

Тип цеолита	Вводимый металл	Расчетное $P_{кр}$ , кбар	Экспериментальное $P_{кр}$ , кбар	Расчетное $P_{кр}$ / Экспериментальное $P_{кр}$	Расчетный скачок объема		Экспериментальный скачок объема		Расчетное заполнение объема каналов металлом, %	Фактическое заполнение объема каналов металлом, %
					см <sup>3</sup> / см <sup>3</sup>	%	см <sup>3</sup> / см <sup>3</sup>	%		
NaM	Bi	22.8	20	1.14	0.056	5.6	0.060	6.0	22.4	24.0
NaM	Hg	28.2	29	0.97	0.043	4.3	0.036	3.6	17.2	14.5

Для удаления избыточной ртути образцы отжимались давлением 20 кбар. Плотность образцов второй группы была равна 1.9 г / см<sup>3</sup>, т.е. в обмазке находилось 0.15 г / см<sup>3</sup> ртути, так как плотность просто обезвоженного цеолита – 1.75 г / см<sup>3</sup>. Плотность образцов первой группы оказалась примерно равной 1.95 г / см<sup>3</sup>. Таким образом плотности образцов обеих групп примерно равны. Этот результат говорит о том, что по-видимому, ртуть полностью вытекает из каналов цеолита после снятия внешнего давления.

По данным **Таблицы 1** ртутью заполняется 3.6 % объема кристаллов NaM, т.е. в каналы проникает  $13.6 \times 0.36 \approx 0.49$  г / см<sup>3</sup> ртути. Если бы вся вдавленная ртуть оставалась в каналах цеолита, после снятия внешнего давления, плотность образцов первой группы должна была бы быть равной  $1.90 + 0.49 = 2.39$  г / см<sup>3</sup>.

На образцах обеих групп был произведен рентгеноструктурный анализ, который не обнаружил существенных различий. Рентгенограммы образцов содержали линии цеолита NaM и отдельно линии ртути, которая находилась в обмазке.

### Ссылки

1. А. И. Ларкин, К. Б. Ефетов. ЖЭТФ, 1974, 66, 2290.
2. L. V. Coleman, H. J. Cohen, D. J. Sandman, F. G. Yamagishi, A. C. Garito, A. J. Heeger. Solid State Commun., 1973, 12, 1125.
3. Э. Э. Сандаров, Н. И. Хитаров. Цеолиты, их синтез и условия образования в природе. 1970, Москва, Наука.
4. А. А. Капанадзе, Г. В. Ртвелишвили, Г. Д. Табатадзе. Nano Studies, 2013, 7, 207.

THE SPATIALLY SEPARATED PROCESS OF THE FORMATION OF  
NANOSIZED IRON–OXYGEN STRUCTURES ON THE STEEL  
SURFACE CONTACTING WITH WATER DISPERSION MEDIUM

O. M. Lavrynenko

National Academy of Science of Ukraine  
F. D. Ovcharenko Institute of Bio-Colloid Chemistry  
Kyiv, Ukraine  
alena-lavry@yandex.ru

Accepted July 29, 2015

**Abstract**

The study of the process of the iron–oxygen nanoparticle formation on the steel surface alternately contacting with water dispersion medium and air has been significantly expanded with complex usage of the scanning electron microscopy data together with the analysis of the electrochemical processes in the local anodal and cathodal areas. The acidic local pH value in the anodal areas and the presence of ferrous iron that is catalytically active with respect to iron–oxygen mineral phases lead to the formation of the well-ordered needle- or rod-like goethite particles via dissolution-re-precipitation process. The alkaline medium in the cathodal areas and oxygen depolarization causes the formation and solid-state oxidation of Green Rust particles accompanied by the obtaining of randomly oriented plate-like Fe(III)–Green Rust and lepidocrocite particles.

**Introduction**

Nowadays the interest in the development of new methods for obtaining finely-dispersed iron–oxygen mineral phases is related to their application in different medical and biological processes [1, 2]. The electrochemical formation of nanosized iron oxyhydroxides and oxides as well as 3d-metal spinel ferrites on the surface of iron (steel) [3] or precious metal electrodes is realized under potentiostatic and galvanostatic conditions [4, 5]. Recently we have proposed a new method for obtaining nanosized iron oxide and oxyhydroxide particles, non-stoichiometric spinel ferrites and *core & shell* composites that include a ferrimagnetic (magnetite or maghemite) core and a precious metal shell (silver, gold, platinum, palladium) that has been called the rotation-corrosion dispergation (the RCD) [6]. The main principles of the RCD method include: 1. the anodal dissolution of iron bearing components and cathodal depolarization of oxygen; 2. the chemical interaction of the dissolved products of electrochemical processes; 3. the formation of the primary iron–oxygen structures such as Fe(II)-Fe(III) layered double hydroxides (Green Rust) or ferrihydrite; 4. the dissolution or the phase transformation of the primary particles, and 5. the formation of spinel ferrite and ferric oxyhydroxide particles [7]. The phase formation process takes place on the steel surface, in the near-surface layer (thin water film) and in the dispersion medium [8]. We showed that the pH

value in the water layer adjoining the electrode surface ( $\sim 400 \mu\text{m}$ ) averages in the range from 7.0 to 9.0 [7] and we supposed that the phase formation process on the steel surface was realized under equal physical-chemical conditions and it did not depend on the structures and defects of the steel surface.

At the same time the following fact draws our attention: the structures related to the primary metastable phases together with the well crystallized disperse minerals obtained within the same period of time are present in the SEM images from the different areas of the steel surface. Moreover, as a rule the same disperse mineral is characterized by a various particle morphology. We suppose that the explanation of such phenomenon is closely connected with the spatial separation of the phase formation process on the heterogeneous areas on the steel surface.

The aim of the study is to describe the phase formation process on the steel electrode alternately contacting with air and water dispersion medium according to the differences of the physical-chemical conditions created in the anodal and cathodal areas on the heterogeneous steel surface.

### Materials and methods

The process of the iron–oxygen particles formation was realized on the surface of the rotating disk electrode that was made of Steel 3 materials [9]. The method of the iron–oxygen surface structure formation was described in our previous work [10]. A steel electrode was exposed to mechanical and chemical treatment. The oxidized layer was mechanically removed from the steel electrode. A concentrated sulfur acid was used for activation of the electrode surface. Distilled water as well as  $\text{Fe}_2(\text{SO}_4)_3$  and  $\text{FeSO}_4$  water solutions at  $\text{pH} = 6.5$  with concentration of ferric and ferrous cations 100 and 1000  $\text{mg} / \text{dm}^3$  were chosen as the dispersion medium contacting with the electrode surface. The phase formation process was performed at around  $T = 20 \text{ }^\circ\text{C}$ . The temperature condition was provided by application of TS–1/80–SPU thermostat. The duration of the phase formation process lasted about 24 h.

A scanning electron microscopy (SEM) using JOEL–6700 microscope equipped by energy-dispersive and cathode-luminescence attachment was determined as a main method of the research. X-ray diffraction (XRD) *in situ* and Fourier transform infrared spectroscopy (FTIR) were used as additional methods. The obtaining of the XRD patterns was performed on computer-aided equipment (DRON 3) with filtered emission of cobalt anode in the  $2\Theta$  range from 0 to 85 degrees. The additional module was applied for recording XRD data *in situ* [10]. Thermo Nicolet FTIR spectrometer in the range  $4000 - 400 \text{ cm}^{-1}$  with 50 scan collection was used for obtaining the IR spectra.

### Result and discussion

#### *XRD and FTIR studies of the mineral phases obtained on the steel surface contacting with water dispersion medium in the open-air systems*

According to the analysis of X-ray diffraction patterns the typical mineral phases formed on the steel surface contacting with water dispersion medium are the following: Fe(II)–Fe(III) LDH (Green Rust), magnetite, lepidocrocite and / or goethite. Depending on the anion



composition of the dispersion medium ferric and ferrous hydroxide layers can be coordinated in the Fe(II)–Fe(III) LDH structures such as Green Rust I (hydroxycarbonate) or Green Rust II (hydroxysulfate). The usage of X-ray diffraction method *in situ* permits to follow the development of the surface structures and to make the supposition about their transformation.

The typical XRD patterns of the surface structures formed within 24 h are present in **Figure 1**. We can see the reflexes related to lepidocrocite and magnetite mineral phases when the sample was formed on the steel surface contacting with distilled water (**Figure 1a**). Lepidocrocite, magnetite and goethite are the commonly mineral phases of the near surface layer that was obtained under the same conditions (**Figure 1b**). On the contrary, hydroxysulfate Green Rust, goethite and ferrihydrite reflexes are clearly seen in the patterns of the surface structures formed when the steel was contacting with water ferrous (**Figure 1c**) and ferric (**Figure 1d**) sulfate solutions.

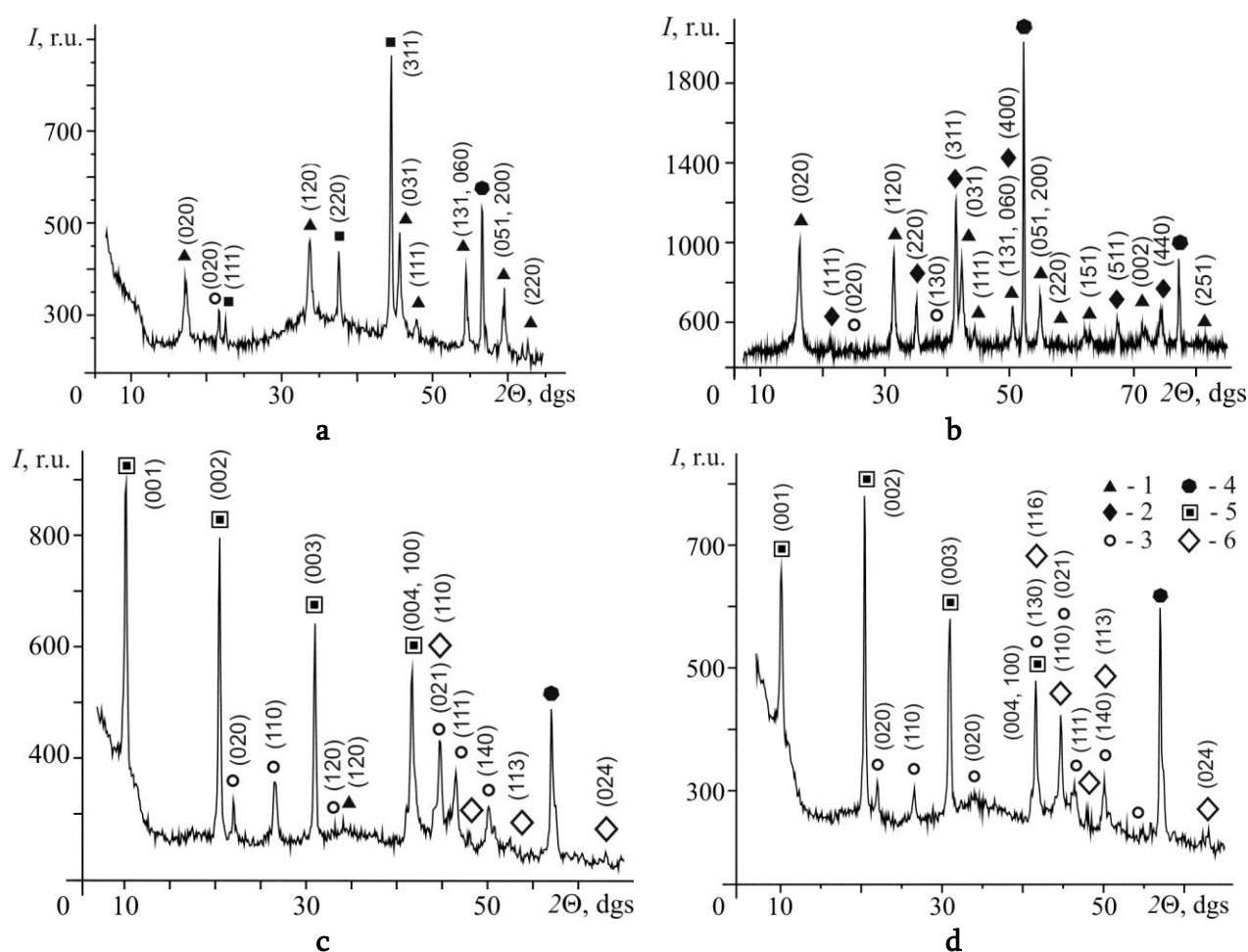


**Figure 1.** XRD patterns of the iron–oxygen mineral phases obtained on the steel surface contacting within 24 h with: a – distilled water (surface layer), b – distilled water (surface and near-surface layers), c –  $\text{FeSO}_4$  water solution ( $c_{\text{Fe(II)}} = 1000 \text{ mg / dm}^3$ ), d –  $\text{Fe}_2(\text{SO}_4)_3$  water solution ( $c_{\text{Fe(III)}} = 1000 \text{ mg / dm}^3$ ). The numbers correspond to mineral phases: 1 – lepidocrocite  $\gamma\text{-FeOOH}$ , 2 – magnetite  $\text{FeFe}_2\text{O}_4$ , 3 – goethite  $\alpha\text{-FeOOH}$ , 4 – iron  $\text{Fe}^0$  (the steel surface), 5 – hydroxysulfate Green Rust  $\text{GR}(\text{SO}_4^{2-})$ , 6 – ferrihydrite  $\text{Fe}_5\text{O}_3(\text{OH})_9$ .

The analysis of the FTIR spectra of the hydroxysulfate and hydroxycarbonate Green Rust obtained on the steel surface contacting with ferrous sulfate solution and distilled water, respectively, shows the presence of both anions on the surface of every disperse mineral [11].



The following study permits to define more precisely the chemical composition of the Fe(II)–Fe(III) layered double hydroxide (Green Rust) sediments formed on the steel surface (**Figure 2**). So, the band  $420\text{ cm}^{-1}$  is present on the both spectra and corresponds to Fe–O chemical bond in oxides. The intensive bands at  $455\text{ cm}^{-1}$  are related to  $\delta$ -FeOOH and the bands at  $482$  and  $542\text{ cm}^{-1}$  correspond to hematite  $\alpha$ -Fe<sub>2</sub>O<sub>3</sub>. The IR bands at  $896$  and  $790\text{ cm}^{-1}$  are typical reflexes for goethite  $\alpha$ -FeOOH whereas the bands at  $1022$  and at  $744\text{ cm}^{-1}$  are related to other iron oxyhydroxide – lepidocrocite  $\gamma$ -FeOOH. But the band at  $1022\text{ cm}^{-1}$  can correspond to the vibration of C–O bond. The  $3401$  and  $3189\text{ cm}^{-1}$  regions point to the stretching vibrations of the water molecules and OH groups, respectively. The indicative reflexes for hydroxysulfate Green Rust bands are the following: the band at  $975$  ( $980$ )  $\text{cm}^{-1}$  points to free sulfate (SO<sub>4</sub>) and the band at  $1137\text{ cm}^{-1}$  corresponds to vibration of the adsorbed SO<sub>4</sub><sup>2-</sup>. The band at  $1022\text{ cm}^{-1}$  coupled with band at  $880\text{ cm}^{-1}$  point to C–O–C stretching whereas the bands at  $1369$  and  $1504\text{ cm}^{-1}$  are typical for CO<sub>3</sub><sup>2-</sup> anion vibration. The band at  $1970\text{ cm}^{-1}$  denotes the existence of C=O bond. A band at  $1369\text{ cm}^{-1}$  may be related to COO-groups. The vibration of carbonate group at  $1430$ ,  $853$ ,  $695\text{ cm}^{-1}$  is not seen in the spectra but the strong band at  $1508\text{ cm}^{-1}$  probably points to C–O stretching vibrations.

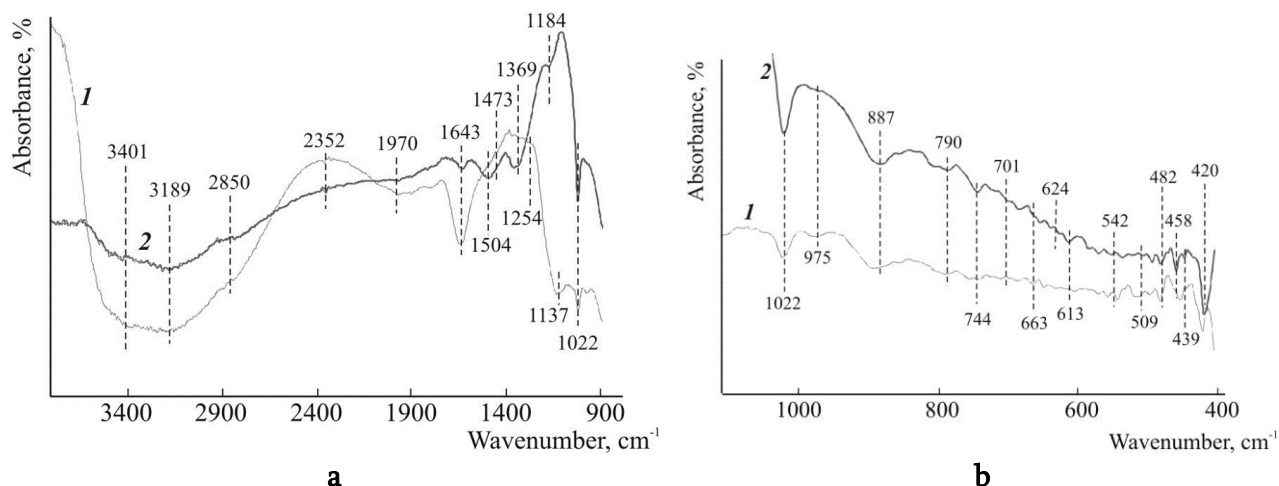


**Figure 2.** The FTIR spectra of the hydroxysulfate (1) and hydroxycarbonate (2) Green Rust formed on the steel surface contacting with ferrous sulfate solution and distilled water, respectively.

Whereas the arising of the following bands,  $\text{cm}^{-1}$ :  $755$  ( $\nu_4\text{CO}_3$ ),  $856$  ( $\nu_2\text{CO}_3$ ),  $879$  ( $\text{CO}_3^{2-}$ ), weak  $1022$  (C–O) on the GR(SO<sub>4</sub><sup>2-</sup>) spectra and, respectively, other bands,  $\text{cm}^{-1}$ :  $613$  ( $\square_4\text{SO}_4$ ),  $624$ ,  $640$  and  $744$  (SO<sub>4</sub><sup>2-</sup>), weak  $663$  peak and splitted  $701$  ( $\nu_4\text{SO}_4$ ),  $1184$  ( $\nu_3\text{SO}_4$ ) on the GR(CO<sub>3</sub><sup>2-</sup>) spectra clearly points to the complication and heterogeneity of the phase composition of the surface Fe(II)–Fe(III) LDH structures.

The inconsistency between chemical and phase composition of the disperse minerals formed on the steel surface is confirmed by the scanning electron microscopy images. So, it is well known, that some of disperse iron–oxygen minerals are characterized by a unique morphology of the particles and aggregates. For example, a recently found disperse mineral schwertmannite (Sh) belongs to similar structures. The schwertmannite is poorly (nano) crystalline iron oxyhydroxysulfate that consists of spherical or ellipsoidal particles. The average width of such particles amounts to  $2 - 4\text{ nm}$  and their length makes up  $60 - 90\text{ nm}$ . The typical morphology of the aggregates corresponds to ‘hedge-hog’, ‘pincushion’ or ‘web-like’ structures.

[12]. The chemical composition of schwertmannite includes  $\text{SO}_4^{2-}$  anions and its formula averages  $\text{Fe}_8\text{O}_8(\text{OH})_{8-2x}(\text{SO}_4)_x$  where  $1 \leq x \leq 1.75$ . The formation of such disperse mineral is possible under the given chemical conditions: the concentration of  $\text{SO}_4^{2-}$  is found in the range 1000 – 3000 mg/dm<sup>3</sup> and the pH value equals 2.5 – 4.5 [13]. The appearance of ‘hedge-hogs’ schwertmannite aggregates on the SEM images of the structures obtained on the steel surface contacting with distilled water at  $T = 35\text{ }^\circ\text{C}$  within 10 h (**Figure 3a**) and at  $T = 70\text{ }^\circ\text{C}$  within 4 h (**Figure 3b**) disproves the supposition about neutral medium in the reaction area and it needs to be explained.

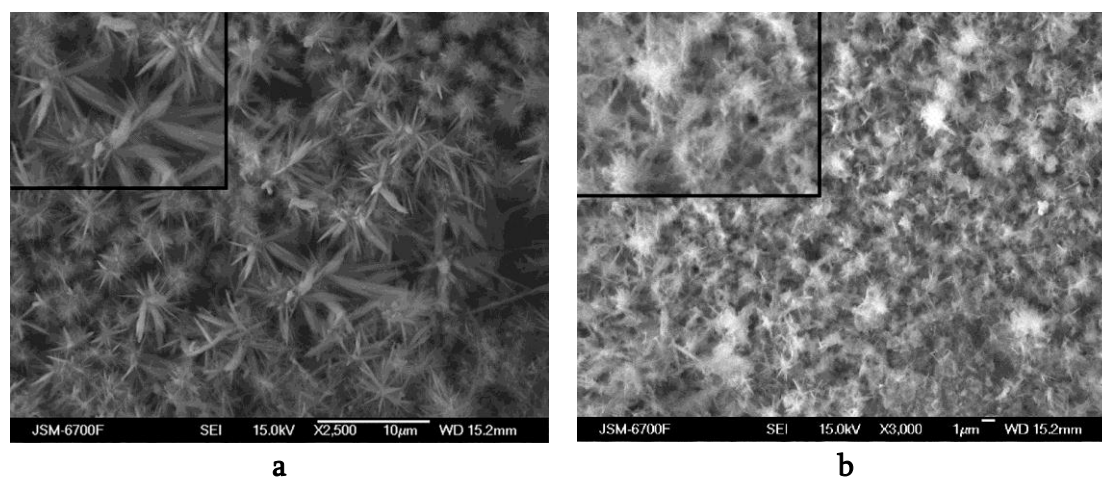


**Figure 3.** The ‘hedge-hogs’ schwertmannite structures formed on the steel surface contacting with distilled water: a – intact aggregates obtained at  $T = 35\text{ }^\circ\text{C}$  within 10 h; b – partially dissolved aggregates obtained at  $T = 70\text{ }^\circ\text{C}$  within 5 h.

In fact the steel belongs to carbon alloys of iron and it consists of the following chemical components: metal ferrites  $\text{MeFe}_2\text{O}_4$ , graphite C, cementite  $(\text{Fe},\text{Ni},\text{Co})_3\text{C}$  etc. So, a large number of micro galvanic couples such as *ferrite – graphite* and *ferrite – cementite* spontaneously appear on the heterogeneous steel surface where anodal and cathodal areas are clearly distinguished. The ferrite particles play the role of anodes whereas graphite and cementite particles, correspondingly, are cathodes. The differences in the value of standard electrode potentials of half-cells lead to electrochemical red-ox reactions under corrosion conditions when the steel surface contacts with water dispersion medium and air oxygen. The primary micellar species in the reaction area interact with each other and form nuclear iron–oxygen structures and primary mineral phases [7]. At the same time the phase formation process and the structure of every mineral phase strongly depend on the physicochemical conditions in the local surface areas.

Also the physical limitation of XRD method does not permit to identify the metastable phase formed on the heterogeneous areas of steel. Analysis of the XRD patterns gives the information about the composition of the bulk mineral phases and greatly simplifies the understanding of local processes in the system. On the contrary, FTIR analysis displays chemical linkages on mineral surfaces and partially points to structural elements belonging to various iron-containing mineral phases.

We consider that our conception of the phase formation processes on the steel surface in the open-air systems [14] can be significantly supplemented with complex usage of the scanning electron microscopy data together with the analysis of the electrochemical processes on the local anodal and cathodal areas.

*The phase formation process on defects of the steel surface  
(in pittings) when it contacted with water dispersion medium*

A reusable steel electrode is exposed to crude workmanship without buffing operation that leads to the presence of different inequalities, defects, deep-seated rust and pittings on its surface and prevents from removing the ‘trace’ quantity of sulfur acid when the electrode is flushed after activation procedure. According to the classical corrosion study [15] the pH value in the pittings on the steel surface changes from 1.5 (at the bottom) to 6.5 – 7.0 on the surface where it plays the role of a peculiar galvanic couple with an anodal area at the bottom and a cathodal area at the top. Moreover, the corrosion process in the pittings is accompanied by hydrogenous polarization and characterized by enhanced concentration of  $\text{SO}_4^{2-}$  and  $\text{Cl}^-$ . The products of the phase formation process on the defects of the steel surface contacting with water dispersion medium within 25 h are shown in **Figure 4a**. Redistribution of the material and the formation of roller-like structures around corrosion caves are clearly seen in **Figure 4b**.

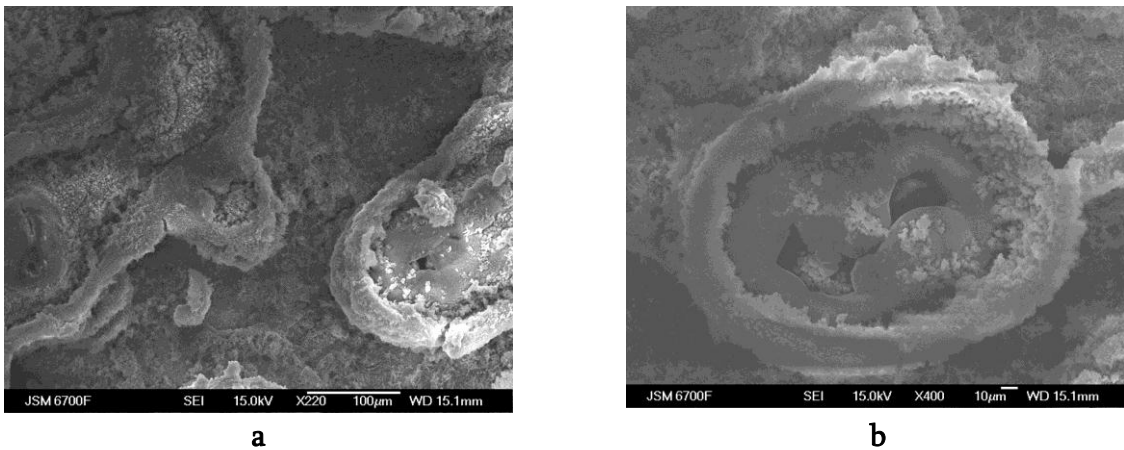
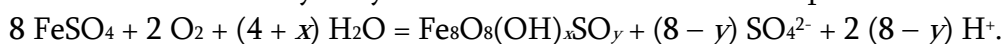


**Figure 4.** The phase formation process on the surface defects fixed when the steel surface was contacting with distilled water at 25 °C within 10 h.

Due to hydrolysis of dilute sulfur acid two anion types  $\text{HSO}_4^-$  and  $\text{SO}_4^{2-}$  can be present in an anodal area. The analysis of FTIR data suggested [16] that sulfate may form complexes both through hydrogen-bonding and direct binding to the iron structure in schwertmannite. The slow oxidation of ferrous cations in the acidic medium and the presence of  $\text{SO}_4^{2-}$  and  $\text{HSO}_4^-$  anions leads to their coordination where  $\text{SO}_4^{2-}$  is bonding to the inner shell of  $\text{Fe}^{2+}$  and during the oxidation process it results in the formation of ferric sulfate complex  $\text{FeSO}_4^+$  [17]. Hydroxyl species coordinate with sulfate anions via polymerization process, and schwertmannite ‘hedgehog’ structures appear as a favor product of the phase formation process.

At the same time, the work [17] contends that schwertmannite is the first mineral formed after oxidation and hydrolysis of ferrous sulfate solution at pH 5 – 6:



It is known that dimer  $\text{Fe}_2(\text{OH})_2^{4+}$  belongs to precursor species of 6-line ferrihydrite [18]. But dimer  $\text{Fe}_2(\text{OH})_2^{4+}$  associates with  $\text{SO}_4^{2-}$  in highly concentrated sulfate solutions and forms the sulfato-dimer complex  $\text{Fe}_2(\text{OH})_2(\text{SO}_4)_{x-2x}$ , its appearance explains the formation of schwertmannite but not ferrihydrite [19]. So, we can state that the physical-chemical conditions at the bottom of pittings on the steel surface are suitable for the formation of schwertmannite mineral. The morphology of schwertmannite can be changed due to the velocity of ferrous iron oxidation as well as the presence dissolved ferrous or ferric species [17].



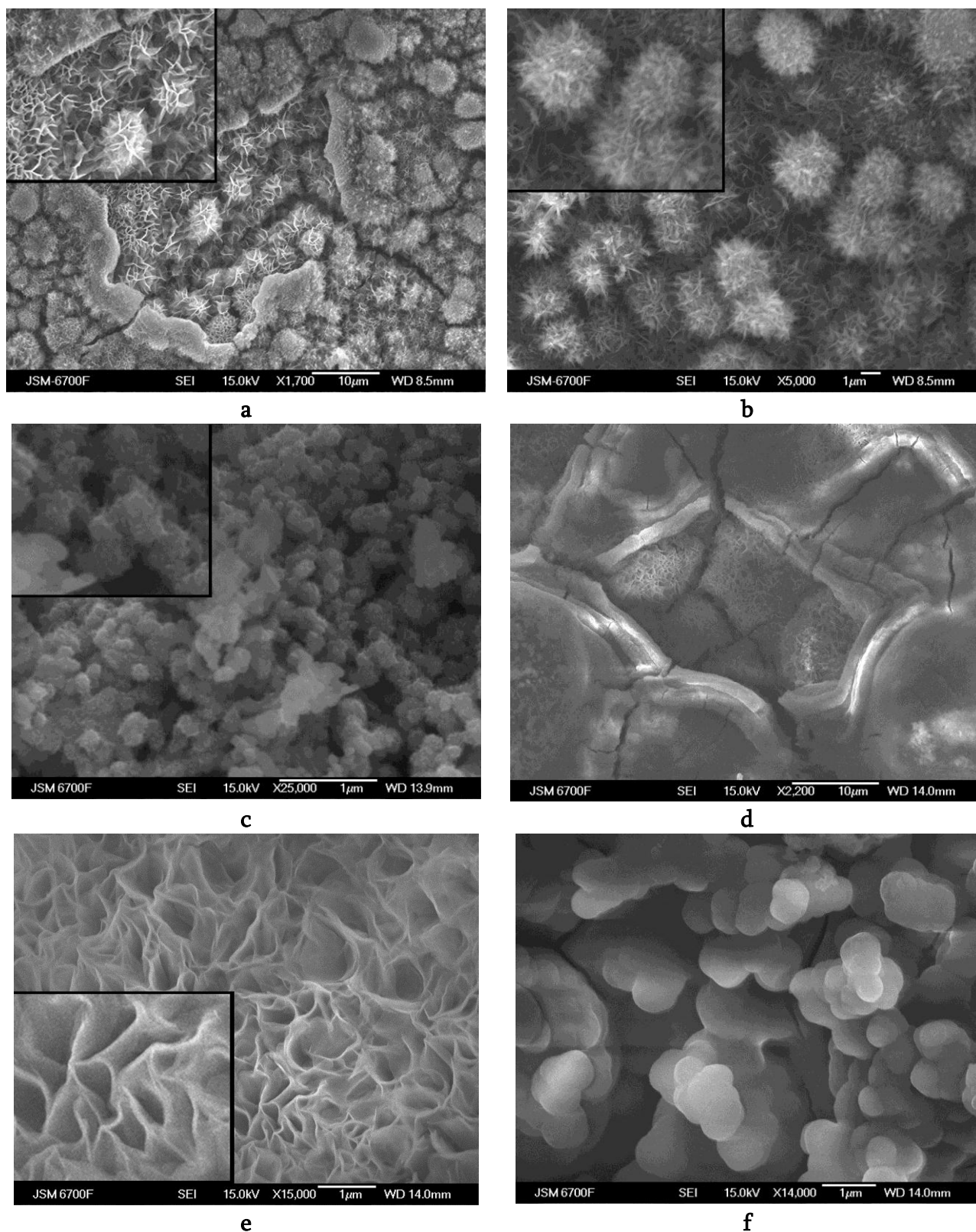
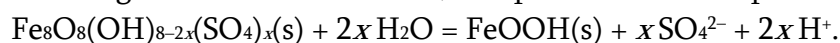


**Figure 5.** The disperse mineral phases formed in the pitting on the steel surface contacting with  $\text{FeSO}_4$  water solution ( $c\text{Fe(II)} = 100 \text{ mg / dm}^3$ ): a – schwertmannite in the pitting, b – ‘hedge-hogs’ of schwertmannite, c – spherical goethite aggregates as the product of phase transformation and with  $\text{Fe}_2(\text{SO}_4)_3$  solution ( $c\text{Fe(III)} = 100 \text{ mg / dm}^3$ ): d – schwertmannite in the pitting, e – ‘web-like’ chwertmannite, f – probably pseudomorphic goethite from schwertmannite.

The differences of the schwertmannite (Sh) morphology depending on the chemical composition of the dispersion medium that contacted with the steel surface within 24 – 25 h are seen in **Figure 5**. When the steel surface interacted with FeSO<sub>4</sub> water solutions (cFe(II) = 100 mg / dm<sup>3</sup>) the schwertmannite in the pitting has the shape of ‘hedge-hogs’ (**Figure 5a**). Their enlarged section is present in **Figure 5b**. The partially dissolved and transformed Sh (**Figure 5c**) becomes spherically shaped. The pitting with the ‘web-like’ schwertmannite formed on the steel surface which contacted with Fe<sub>2</sub>(SO<sub>4</sub>)<sub>3</sub> water solution (cFe(III) = 100 mg / dm<sup>3</sup>) is present in the **Figure 5d**. The enlarged view of initial Sh structure is seen in **Figure 5e** and the destructed structure is shown in **Figure 5f**.

Probably the structures presented in **Figure 5c** and **Figure 5f** can be related to a spherical goethite. The mechanisms of such transformation were widely discussed by scientists and the following versions were proposed: 1. via dissolution of schwertmannite inside spheres [20], 2. goethite adopts the Sh shape and morphology [21 – 23], 3. pseudomorphic goethite morphology from Sh that was preserved during re-crystallization process, 4. preservation of spherical schwertmannite structure in goethite due to the influence of adsorbed sulfate [24].

The pH value of the dispersion medium alongside with the temperature is the most important parameters that determine the phase stability of the schwertmannite structure [22, 23]. The rate of the phase transformation of schwertmannite to goethite, according to [22] is slower for high sulfate concentration, low pH value and temperature:



Two stages of the schwertmannite transformation to goethite were shown in [25]: the release of the sulfate anions from the structure of schwertmannite, and the change of the squared schwertmannite structure to the rectangular one present in goethite. A close structural relationship between schwertmannite and goethite was determined in [26], where the structural elements of goethite can be included into schwertmannite aggregates depending on the temperature and synthesis method.

The change of the phase composition of disperse minerals throughout the height of the pitting, redistribution of the iron–oxygen substance and agglomeration of the iron–oxygen disperse minerals around the pitting (cathodal area) on the steel surface are the important aspects of the phase formation process in the open-air system on the steel.

The phase transformation of schwertmannite in the presence of dissolved ferrous iron under condition of the pH increase was described for the water suspensions [27]. The obtained results can be related to the processes in the pittings on the steel surface. So, the schwertmannite structure is formed at pH < 5.0 at the bottom of pittings (in the anodal area). Ferrous cations are adsorbed on the schwertmannite surface at pH > 5.0, and then catalyze the schwertmannite dissolution and the following precipitation of the nanosized goethite or ferrihydrite particles in the middle area of the pitting. The increase of pH value to 7.0 on the top of pitting (the cathodal area) is the cause of the decrease in the ferrous iron dissolution rate and Fe<sup>2+</sup> cations can incorporate into goethite lattice and lead to α-FeOOH transformation into the mixed ferric / ferrous hydroxide layers that are the primary structure unit of Green Rust. Sulfate-anions as a component of a schwertmannite crystal lattice at first are adsorbed on the goethite surface and then incorporate into the interlayer space of Green Rust.

At the same time the formation of Green Rust phase on the steel surface can be performed as a result of the interaction of hydroxyl and ferrous cations in the presence of air

oxygen. It is especially true for hydroxycarbonate Green Rust which structure is similar to the structure of  $\text{Fe}(\text{OH})_2$ .

So, we have followed the chain of the phase transformation *schwertmannite* – *nanogoethite* / *ferrihydrite* – *Green Rust* when the pH value is changed from acid to weak alkaline medium under limited oxidation in pittings and *ferrous iron hydroxide* – *Green Rust* on the steel surface under oxidative conditions.

***The phase formation process in the anodal areas on the steel surface contacting with water dispersion medium***

The anodal dissolution of the iron-bearing components leads to the formation of ferrous cations and can be accompanied by hydrogen depolarization [28]. Also, the local pH in anodal areas is acidic. Under the following conditions the main phase formation process can be dissolution–re-precipitation of primary iron–oxygen species (Green Rust). The permanent entrance of ferrous iron characterized by high catalytical activity in respect to iron–oxygen mineral phases [29, 30] leads to acceleration of the dissolution process. The feature of the particle morphology related to the formation of needle- or rod-like particles of iron oxyhydroxides that are well ordered and are usually oriented along the direction [001] [31]. The selective formation of either lepidocrocite or goethite particles strongly depends on the iron species oxidation [32]. Such supposition was confirmed by [29] where the formation of lepidocrocite particles had been explained via direct precipitation of ferric iron monomers  $\text{Fe}(\text{OH})^{2+}$  or / and dimers  $\text{Fe}(\text{OH})_2^+$ , whereas the formation of the goethite particles is realized during the following stages of the polymerization process when ferrous iron formed dimers, trimers ... polymers and finally  $\alpha\text{-FeOOH}$ . Temperature is the key parameter for the polymerization rate and hence for mineral composition of iron oxyhydroxides: lepidocrocite is formed at low temperature and goethite favorably appears at high temperature. Moreover the anion composition of the dispersion medium influences mineral composition of ferric oxyhydroxides as well as their particle shape [33]. In general lepidocrocite precipitates in the presence of chlorides, and goethite is formed in the sulfate solutions via dissolution of intermediate phase of ferrihydrite under standard conditions. The quantity of the lepidocrocite re-precipitated in the sulfate solutions is strongly limited. A typical shape of lepidocrocite particles formed in chloride-containing medium is plate-like and a typical goethite shape is star-like, respectively, but the shape of goethite particles that are grown in sulfate medium after ferrihydrite dissolution is needle-like and rod-like.

Green Rust particles dissolve in the anodal area and re-precipitate as the iron oxyhydroxides that as well as Green Rust undergo the repeated dissolution–re-precipitation process. The dissolution process is catalyzed by  $\text{Fe}^{2+}$  cations that are adsorbed on the surface of the mineral phase, reduce ferric iron in the crystal lattice and convert iron species to the transportable state. Ferrous iron cations are oxidized in the dispersion medium and precipitated as a new mineral phase. A low temperature and pH values are favorable for dissolution–re-precipitation process and it leads to the formation of well crystalline lepidocrocite and goethite particles [29]. The velocity of ferrous iron oxidation determines the phase composition of the iron–oxygen precipitates. So, when the oxidation velocity is low well crystalline goethite or lepidocrocite particles are obtained [34]. When oxidation process is faster than the dissolution process ferrihydrite particles are formed in the system. But when the oxidation velocity is extremely fast  $\text{Fe}(\text{III})\text{-GR}$  is the main product of the phase formation [34].



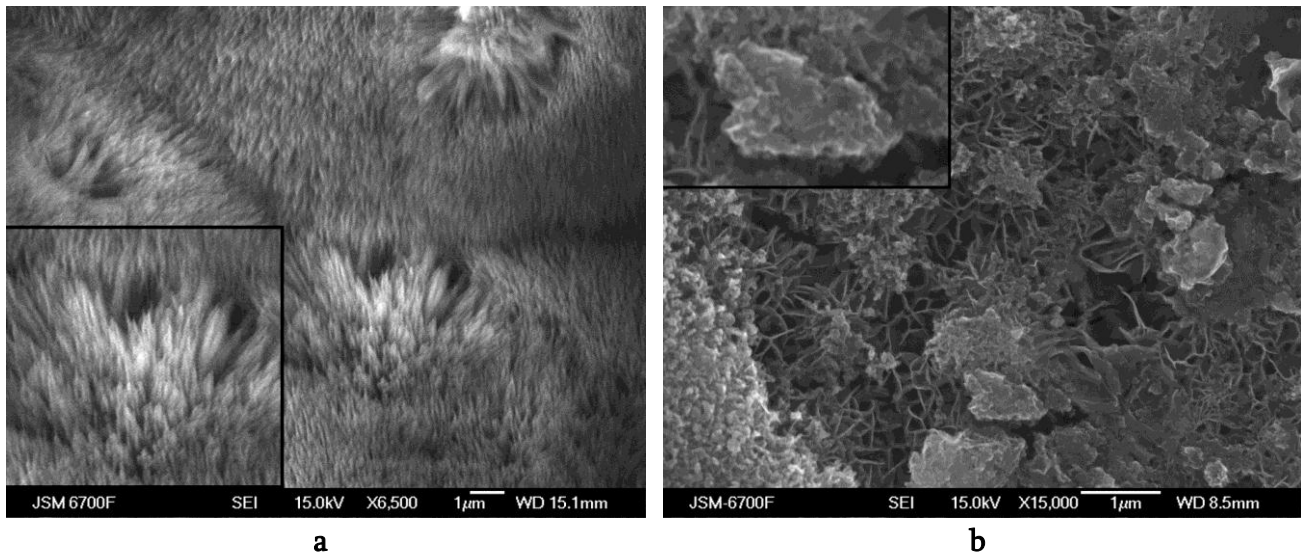
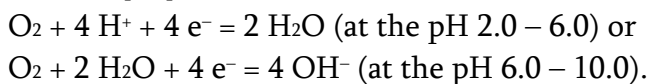


**Figure 6.** The iron–oxygen mineral phases formed via dissolution–re-precipitation process: a – goethite  $\alpha$ -FeOOH needles, b – lepidocrocite  $\gamma$ -FeOOH plates on the schwertmannite surface.

**Figure 6** shows the products of the dissolution – re-precipitation of primary structures: ferrihydrite into needle-like goethite in  $\text{FeSO}_4$  water solutions  $c\text{Fe(II)} = 100 \text{ mg / dm}^3$  (24 – 25 h) (**Figure 6a**) and Green Rust into plate-like lepidocrocite (**Figure 6b**) in  $\text{Fe}_2(\text{SO}_4)_3$  water solutions  $c\text{Fe(III)} = 10 \text{ mg / dm}^3$ .

***The phase formation process in the cathodal areas on the steel surface contacting with water dispersion medium***

The oxygen depolarization accompanied by hydroxyl generation is the main process that takes place in the cathodal areas on the steel surface. It leads to the increase in the local pH value up to alkalization of the medium. Depending on the initial pH value cathodal process can be described as [28]:



Under the following conditions the solid state transformation is confirmed as a main phase formation process. The feature of particle morphology is the preservation of the shape and orientation of the phase-precursor particles, their chaotic arrangement [4]. Green Rust particles play the role of the precursor species in our case.

Analysis of the SEM images (**Figure 7**) permits us to find the following phase transformation processes: solid-state Green Rust oxidation when its structure does not change and formation of Fe(III)–GR or lepidocrocite. The phase composition of the products of the solid-state transformation is determined by local pH values, as it was shown in the corrosion study [35]. So only lepidocrocite can be formed at  $\text{pH} = 8$ , the coexistence of both phases Fe(III)–GR and  $\gamma$ -FeOOH is typical in the pH range from 8 to 8.9 and the single phase of Fe(III)–GR is dominant at  $\text{pH} > 8.9$  [35]. The solid-state transformation hydroxysulfate Green Rust in the lepidocrocite was mentioned in the early work [36] where the duration of the oxidation process played the determining role. All listed conditions can take place in the cathodal areas on the steel surface. The chaotic arrangement of Fe(III)–GR (**Figures 7a – c, e, and f**) as well as  $\gamma$ -FeOOH (**Figure 7d**) is clearly seen on the SEM images.

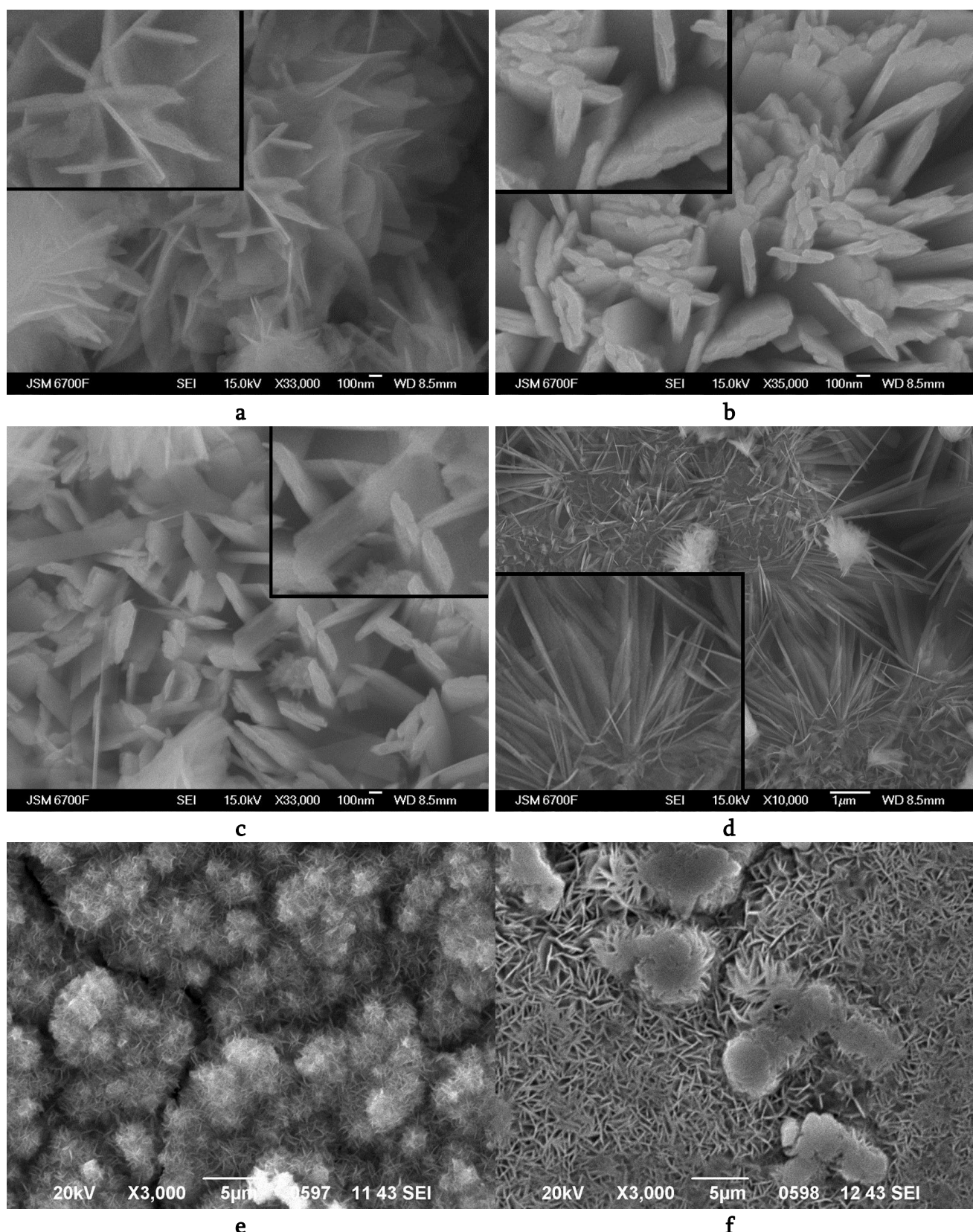


**Figure 7.** The products of the solid state transformation in the cathodal areas of the steel surface contacting with  $\text{FeSO}_4$  water solution  $c\text{Fe(II)} = 1000 \text{ mg / dm}^3$ : a – hydroxylsulfate Green Rust (the intact plate-like particles), b –  $\text{Fe(III)-GR(SO}_4^{2-})$  (the oxidized plate-like particles), c – plate-like particles of  $\text{Fe(III)-GR(SO}_4^{2-})$  and rod-like crystals of lepidocrocite, d – lepidocrocite needle-like particles and with  $\text{Fe}_2(\text{SO}_4)_3$  water solution  $c\text{Fe(III)} = 1000 \text{ mg / dm}^3$ : e –  $\text{GR(SO}_4^{2-})$ , f –  $\text{Fe(III)-GR(SO}_4^{2-})$ .



So, we suppose that the formation of  $\text{Fe}(\text{OH})_2$  and its following oxidation in Green Rust coupled with solid-state transformation in Fe(III)-Green Rust or lepidocrocite is the main phase formation processes in the cathodal areas of the steel surface contacting with water solution and air oxygen.

### Conclusions

The process of the formation of the iron–oxygen mineral phases on the steel surface has been recently described by usage of X-ray diffraction study *in situ*, and now it has been considered in the view of heterogeneity of the high carbon iron bearing alloy. The presence of spinel ferrites, graphite and cementite components in the structure of the steel leads to the appearance of cathodal and anodal areas on its surface. Moreover the multiple usage of steel electrode without buffing operation causes the formation of different inequalities, defects, deep-seated rust and pittings on its surface. Such heterogeneity of the steel surface influences the local physical-chemical conditions and as a result it determines the phase formation processes under galvanostatic conditions on the small parts of the electrode surface.

The SEM images of the steel surface obtained after its contact with distilled water as well as ferric and ferrous sulfate solutions within 24–25 h clearly show the mineral particles that are characterized by various size, shape and morphology. The analysis of the physical-chemical conditions in the local areas under corrosion conditions permits to determine the mechanisms of the formation and development of iron–oxygen mineral phases on the steel surface.

The development of the mineral phases in pittings on the steel surface is realized via dissolution–re-precipitation process that takes place when the pH value is increased throughout the height of the pitting. We have followed the chain of the phase transformation schwertmannite – nanogoethite / ferrihydrite – Green Rust when the pH value is changed from acid to weak alkaline medium under the limited oxidation in pittings.

The dissolution of the iron bearing component of the steel accompanied by hydrogen depolarization leads to the formation of the following physical-chemical conditions on the anodal areas: the acidic local pH and the presence of ferrous cations that are catalytically active with respect to iron–oxygen mineral phases. The well-ordered needle- or rod-like goethite particles are the main product of the phase formation process.

The depolarization of oxygen accompanied by hydroxyl generation is the main mechanism in the cathodal areas of the steel. The phase formation process is carried out in alkaline medium and is associated with solid-state oxidation of Green Rust particles. The randomly oriented plate-like Fe(III)–Green Rust and lepidocrocite particles are the main mineral phases formed under such conditions.

### Acknowledgments

We gratefully acknowledge the support from PhD Yu. M. Bolbukch from O. O. Chuiko Institute of Surface Chemistry of NAS of Ukraine for the obtaining and interpretation of IR–FT data. We express our gratitude to PhD O. A. Vishnevskij from M. P. Semenenko Institute of Geochemistry, Mineralogy and Ore Formation of NAS of Ukraine for preparing the SEM photos.

## References

1. I. V. Uvarova, P. P. Gorbyk, S. V. Gorobets, O. A. Ivashchenko, N. V. Ulianchych. In: *Nanomaterials of Medical Application* (Ed. V. V. Skorokhod) – Scientific Book Project. 2014, Kyiv, Naukova dumka. – *in Ukrainian*
2. M. Mohapatra, S. Anand. *Int. J. Eng. Sci. & Technol.*, 2010, 2, 127.
3. H. Park, P. Ayala, M. A. Deshusses, A. Mulchandani, H. Choi, N. V. Myung. *Chem. Eng. J.*, 2008, 139, 208.
4. S. Peulon, H. Antony, L. Legrand, A. Chausse. *Electrochem. Acta*, 2004, 49, 2891.
5. D. Ramimoghadam, S. Bagheri, Sh. B. A. Hamid. *J. Magn. & Magn. Mater.*, 2014, 368, 207.
6. O. M. Lavrynenko, V. I. Kovalchuk, S. V. Netroba, Z. R. Ulberg. *Nano Studies*, 2013, 7, 295.
7. O. M. Lavrynenko. *The Obtaining of the Composition Structured Systems Based on the Iron–Oxygen Minerals, Their Structure and Properties* (Autoref. Diss. Doctor in Chem. – Colloid Chem.), 2013, Kyiv. – *in Ukrainian*.
8. V. A. Prokopenko, O. M. Lavrynenko, S. V. Mamunya. *Nanosyst. & Nanomater. Nanotechnol.*, 2005, 3, 513. – *in Russian*
9. Stali i splavy vysokolegirovannye, korrozionnostojkie, zharostojkie i zharoprochnye (deformiruemye). Marki : GOST 5632-61., 1962, Moskva: Standartgiz. – *In Russian*
10. O. M. Lavrynenko, Ya. D. Korol, S. V. Netroba, V. A. Prokopenko. *Chem. Phys. & Technol. Surf.*, 2010, 1, 338.
11. O. M. Lavrynenko, Yu. M. Bolbukh. *Nano Studies*, 2014, 9, 127.
12. A. Goswami, M. K. Purkait. *Int. J. Chem. Nucl. Metall. & Mater. Eng.*, 2013, 7, 46.
13. J. M. Bigham, L. Carlson, E. Murad. *Mineralog. Mag.*, 1994, 58, 641.
14. O. M. Lavrynenko. *Nano Studies*, 2011, 4, 5.
15. U. R. Evans. *The Corrosion and Oxidation of Metals. Scientific Principles and Practical Applications*. 1960, London, Edward Arnold Publ. Ltd.
16. J. F. Boily, P. L. Gassman, T. Peretyazhko, J. Szanyi, J. M. Zachara. *Environ. Sci. & Technol.*, 2010, 44, 1185.
17. S. Regenspurg, A. Brand, S. Peiffer. *Geochim. et Cosmochim. Acta*, 2004, 68, 1185.
18. R. M. Cornell, U. Schwertmann. *The Iron Oxides*. 2003, Weinheim, VCH Verlag.
19. U. Schwertmann, J. Friedll, H. J. Stanjek. *Coll. Int. Sci.*, 1999, 209, 215.
20. S. H. Yu, H. Colfen, M. Antonietti. *J. Phys. Chem. B*, 2003, 107, 7396.
21. L. A. Sullivan, R. T. Bush. *Mar. & Freshwater Res.*, 2004, 55, 727.
22. J. Jonsson, P. Persson, S. Sjoberg, L. Lovgren. *Appl. Geochem.*, 2005, 20, 179.
23. U. Schwertmann, L. Carlson. *Clay Minerals*, 2005, 40, 63.
24. T. Peretyazhko, J. M. Zachara, J.-F. Boily, Y. Xia, P. L. Gassman, B. W. Arey, W. D. Burgos. *Chem. Geology*, 2009, 262, 169.
25. A. Fernandez–Martinez, V. Timon, G. Roman–Ross, G. J. Cuello, J. E. Daniels, C. Ayora. *Am. Mineralogist*, 2010, 95, 1312.
26. R. A. French, N. Monsegue, M. Murayama, M. F. Hochella. *Phys. Chem. Miner.*, 2014, 41, 237.

27. I. A. M. Ahmed, L. G. Benning, G. Kakonyi, A. D. Sumoondur, N. J. Terrill, S. Shaw. *Langmuir*, 2010, 26, 6593.
28. L. I. Antropov. *Theoretical electrochemistry*. 1984, Kyiv, Vysshaya shkola. – *in Russian*
29. H. Liu, P. Li, M. Zhu, Y. Wei, Y. Sun. *J. Solid State Chem.*, 2007, 180, 2121.
30. H. Liu, Y. Wei, Y. Sun. *J. Mol. Catal. A*, 2005, 226, 135.
31. H. Antony, S. Peulon, L. Legrand, A. Chausse. *Electrochem. Acta*, 2004, 50, 1015.
32. K. Kimijima, K. Kiyoshi, S. Suzuki, A. Muramatsu. *Current Adv. Mater. & Proc.*, 2005, 18, 1673.
33. H. Liu, H. Guo, P. Li, Y. Wei. *J. Solid State Chem.*, 2008, 181, 2666.
34. Ph. Refait, O. Bernali, M. Abdelmoula, J.-M. R. Genin. *Corros. Sci.*, 2003, 45, 2435.
35. L. Legrand, L. Mazerolles, A. Chausse. *Geochim. Cosmochim. Acta*, 2004, 68, 3497.
36. R. Lin, R. L. Spicer, F. L. Tungate, B. H. Davis. *Coll. & Surf. A*, 1996, 113, 79.

THE STATE-OF-THE-ART CHEMICAL ANALYTICAL METHOD FOR  
DETECTION OF SODIUM AZIDE BY  $^{14}\text{N}$  NMR SPECTROSCOPY

T. Chachibaia <sup>1,2</sup>, M. M. Pastor <sup>3</sup>

<sup>1</sup> University of Santiago de Compostela  
Faculty of Pharmacy  
Department of Analytical Chemistry, Food Science & Nutrition  
Santiago de Compostela, Spain  
nanogeorgia@gmail.com

<sup>2</sup> I. Javakhishvili Tbilisi State University  
Faculty of Medicine  
Department of Public Health & Epidemiology  
Tbilisi, Georgia

<sup>3</sup> University of Santiago de Compostela  
Center of Technology Innovation & Transfer (CACTUS)  
Magnetic Resonance Unit  
Santiago de Compostela, Spain

Accepted August 19, 2015

### Abstract

Sodium azide is acute poison similar to cyanide. Due to its attractive chemical and physical properties it is widely used in many spheres including automotive industry, medicine, pharmaco-chemistry, agriculture and even everyday life. Detection of sodium azide becomes more demanding nowadays than several decades ago. We propose to use of  $^{14}\text{N}$  NMR spectroscopy to detect and quantify sodium azide in aqueous solutions and extrapolate calibration results for real time detection of unknown concentrations. The results of this methodology relying in measurement of 1D  $^{14}\text{N}$  NMR spectra at the lowest concentration of sodium azide aqueous solutions.

### Introduction

Sodium azide is acute poison similar to cyanide. Sodium azide is in the group of alkali metal azides, it is water soluble and currently used in many applications, from industry to everyday life.

The Organization for Economic Co-operation and Development (OCDE) has included sodium azide in the list of 5,235 High Production Volume Chemicals (HPV) with a production or import greater than 1,000 tons per year [1].



One particular important area of use of sodium azide is in the agricultural sector. Sodium azide is among the great variety of chemicals which are frequently used as fermentation inhibition in wine production.

Since 2000s sodium azide started to be used as pesticide, herbicide and insecticide [2]. In one study during eight year period usage of sodium azide in soil reached the impressive value of 336 kg / ha [3].

In 2014, International Organization of Vine and Wine (OIV) released the revised “Compendium of International Methods of Analysis” for the detection of preservatives and fermentation inhibitors. They proposed two methods of detection sodium azide which are HPLC and colorimetric method. This methods are relative obsolete despite the fact that it was modified in 2006, based on originally developed works Swaring & Waldo [4] and Battaglia & Mitiska [5]. The colorimetric method proposed is also very obsolete and neither specific nor sensitive. While, in recent years was discovered possibility of reaction based detection of sodium azide at small quantities as 21 ppb [6].

In parallel, concern was raised by environmentalist and atmospheric scientists about the safety of the use of sodium azide. Despite the widespread opinion of sodium azide proponents for its use in water and soil, arguing that this chemical undergoes rapid hydrolysis and degradation (Rodrigues–Kabana et al.) [7 – 10], their opponents (Betterton et al.) [11 – 13] claimed that it is not exactly what it can be anticipated, since they discovered water and soil samples containing residual amounts of sodium azide.

In the recommendations for disposal of sodium azide in industry or workplace, the standard method for its neutralization is manifold dissolution in water and release in sewage by the Royal Society of Chemistry [14], at the same time, American Azide Corporation strictly require a chemical reaction for the inactivation of wastes of sodium azide before draining [15].

In this context, it is clear that the detection of sodium azide becomes more demanding nowadays than several decades ago.

We propose to use of  $^{14}\text{N}$  NMR spectroscopy to detect and quantify sodium azide in aqueous solutions and extrapolate calibration results for real time detection of unknown concentrations. The results of this methodology relying in measurement of 1D  $^{14}\text{N}$  NMR spectra at the lowest concentration of sodium azide aqueous solutions.

### **Aims and objective**

The aim of the study is to apply  $^{14}\text{N}$  NMR spectroscopy to detect  $^{14}\text{N}$  spectra of the sodium azide at several concentrations to determine minimum detection limit.

We followed to fulfill the following objectives:

- 1) We studied the detection limit of  $\text{NaN}_3$  with  $^{14}\text{N}$  NMR. The minimum concentration of  $\text{NaN}_3$  that can be measured with  $^{14}\text{N}$  NMR in the spectrometer in a standardized and reasonable amount of time.
- 2) We determined the concentration of any unknown sample of  $\text{NaN}_3$  prepared under analogue conditions in water, as far as it is equal or greater than the  $^{14}\text{N}$  NMR detection limit of  $\text{NaN}_3$ .
- 3) The next is to perform calibration of  $\text{NaN}_3$  samples with dilution experiments and calculate calibration curve for  $^{14}\text{N}$  NMR sensitivity for detection of sodium azide of unknown concentration.

To estimate the minimum detectable concentration of sodium-azide, we need to prepare a sample with known concentration. To acquire the spectrum under some standardized conditions (in particular the total measurement time) and repeat the spectrum 5 or more times diluting the sample.

Then we extrapolated the calibration curve of NMR sensitivity (signal-over-noise ratio S/N) with the respect to  $\text{NaN}_3$  concentration to determine the minimum required concentration, which is detectable in the spectrometer.

### **Materials and Methods**

The experimental part of this project is performed in the Magnetic Resonance Unit at the Center of Technology Innovation and Transfer (CACTUS) of the University of Santiago de Compostela. Experiments were conducted during 2012–2014 and obtained results analyzed.

University of Santiago de Compostela (USC) is equipped with NMR spectroscopy and propriety technology of MESTRE Labs, which is the software used worldwide.

The Magnetic Resonance Unit at the University of Santiago de Compostela, provides the optimum research instrumentation required for this part of the project. The NMR facility provides three state-of-the-art high magnetic field NMR spectrometers of 500 and 750 MHz.

### **Experimental**

Sodium azide and deuterated water ( $\text{D}_2\text{O}$ ) were obtained from Sigma-Aldrich. Azide standards were prepared using sodium azide in  $\text{D}_2\text{O}$ , in which target concentrations were set relative to free azide concentration. Test samples were prepared at descending target concentration in  $\text{D}_2\text{O}$ . Stock sample of 100 mM concentration solution of sodium azide 0.5 ml was transferred into an NMR tube. The sample NMR tube is placed into a magnetic field. A radio frequency pulse is then sent through the sample solution in order to orient the magnetic moments of the nuclei in the solution. As the magnetic moments relax, they exhibit free induction decay (FID). The free induction decay is Fourier transformed into a NMR spectrum. The NMR spectrum displays chemical shifts for the individual nuclei of nitrogen; and from these chemical shifts, the structure of the compound was determined.

### **Standard and test sample preparation**

- 1) Preparation of reference standard sample with a compound, which  $^{14}\text{N}$  NMR signal is used as the reference of concentration. This sample is important because it allows measuring the unknown concentration of  $\text{NaN}_3$  in any sample that we prepare in the future.
- 3) Reference compound: 100 %  $\text{CH}_3\text{NO}_2$  total volume of 700 microliters.

Reference compound 100 % Nitromethane ( $\text{CH}_3\text{NO}_2$ ) 600 microliters was placed in a standard NMR tube and the remaining 100 microliters in a special capillary. The capillary with the reference compound is inserted inside of standard NMR tube. We prepared the initial sample of  $\text{NaN}_3$  in solution in a "narrow wall" NMR tube.

The starting concentration of  $\text{NaN}_3$  is 100 mM in this sample. Then the capillary is inserted with the reference sample inside this standard NMR tube. We measure the  $^{14}\text{N}$  spectrum of the sample by 4 or 5 dilutions of the original  $\text{NaN}_3$  concentration using dilution 5 times.

### Results:

A preliminary test was carried out in our lab for the measurement of the 1D  $^{14}\text{N}$  NMR spectrum of sodium azide in water solution. The spectrum was obtained with very good quality in only 30 s of measurement time. The sample 100 mM gave the expected three peaks in  $^{14}\text{N}$  NMR (two peaks for  $\text{NaN}_3$  and one peak for  $\text{CH}_3\text{NO}_2$ ). The assignment of the peaks of the 1D  $^{14}\text{N}$  spectrum of sodium azide in water is provided in **Figure 1**.

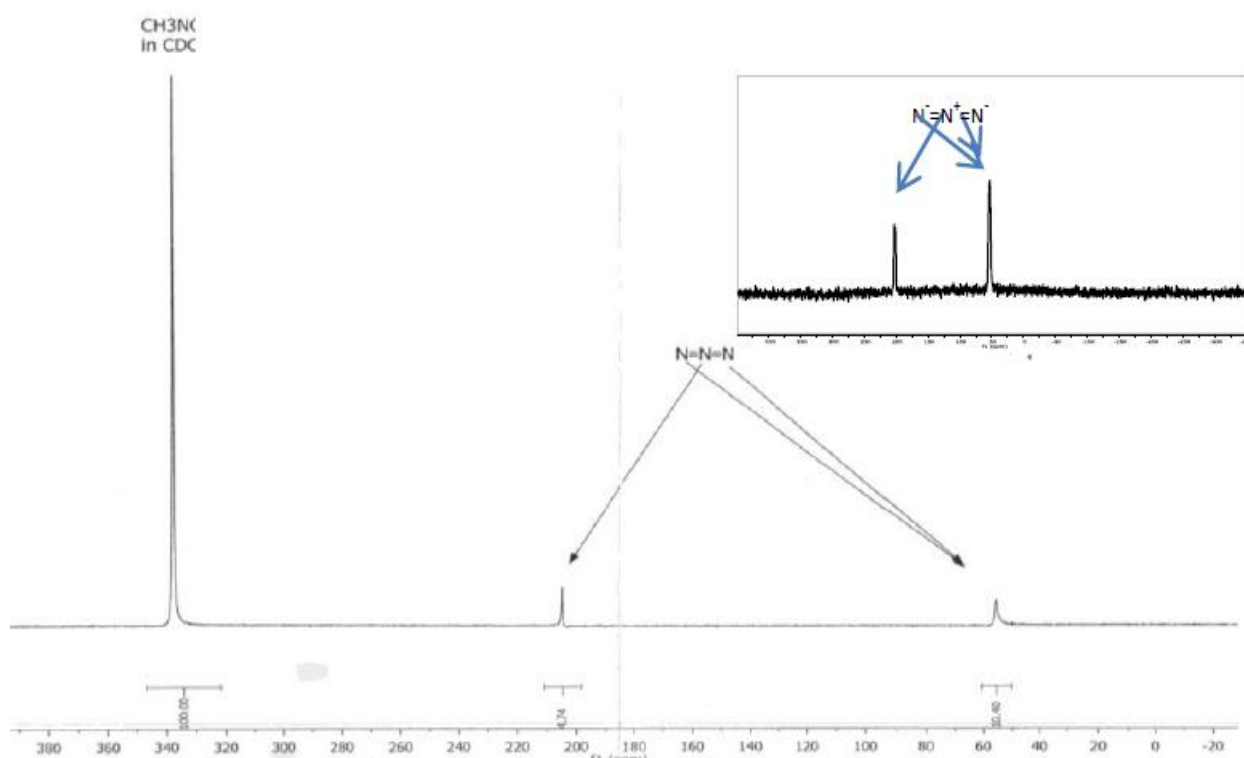


**Figure 1.**  $^{14}\text{N}$  NMR spectrum of 100 %  $\text{CH}_3\text{NO}_2$  and 100 mM Sodium azide ( $\text{NaN}_3$  in  $\text{D}_2\text{O}$ ).

The chemical shifts obtained are in excellent concordance with those described for this molecule in the NMR spectral databases, and also in concordance with those expected for its structure. The 1D  $^{14}\text{N}$  NMR spectrum of sodium azide shows just two peaks corresponding to the two types of nitrogen atoms of this molecule. The two external nitrogen atoms resonate at  $\sim 50$  ppm, and the central nitrogen atom at  $\sim 200$  ppm. As expected, the former peak has double intensity than the later one since it corresponds to two nitrogen atoms.

The  $^{14}\text{N}$  chemical shifts resonances are spread out in an extremely broad range that covers 900 ppm. Such dispersion is favorable for our purposes of detecting sodium azide in mixtures, since it reduces the chances of accidental signal overlapping with the  $^{14}\text{N}$  signals of other nitrogenated compounds. As the  $^{14}\text{N}$ -spectrum of sodium azide has two peaks, and the

same happens with its  $^{15}\text{N}$ -spectrum. In both cases the peaks are easily to interpret; the less intense one correspond to the central N atom, and the double intense one corresponds to the two external nitrogen atoms.

1D  $^{14}\text{N}$  NMR spectrum of sodium azide 100 mM in  $\text{H}_2\text{O}$  obtained at 300 K in a Bruker Avance I NMR 11.7 T spectrometer. The spectrum was obtained in 30 s with 64 scans. The assignment of the peaks to the azide molecule and  $\text{CH}_3\text{NO}_2$  are shown of the **Figure 2** (Magnetic Resonant Unit, CACTUS, University of Santiago de Compostela).

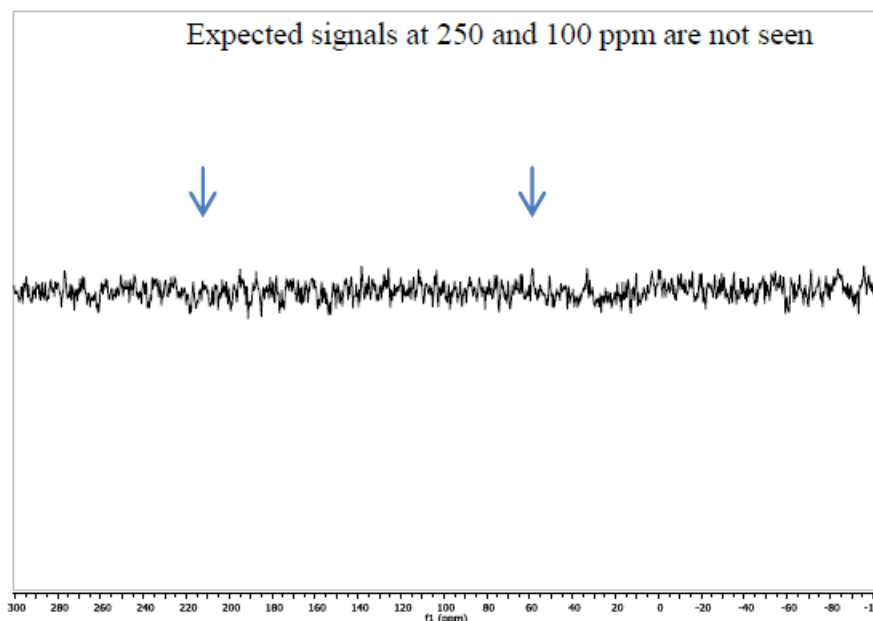


**Figure 2.**  $^{15}\text{N}$  NMR spectra of 100 mM sodium azide.

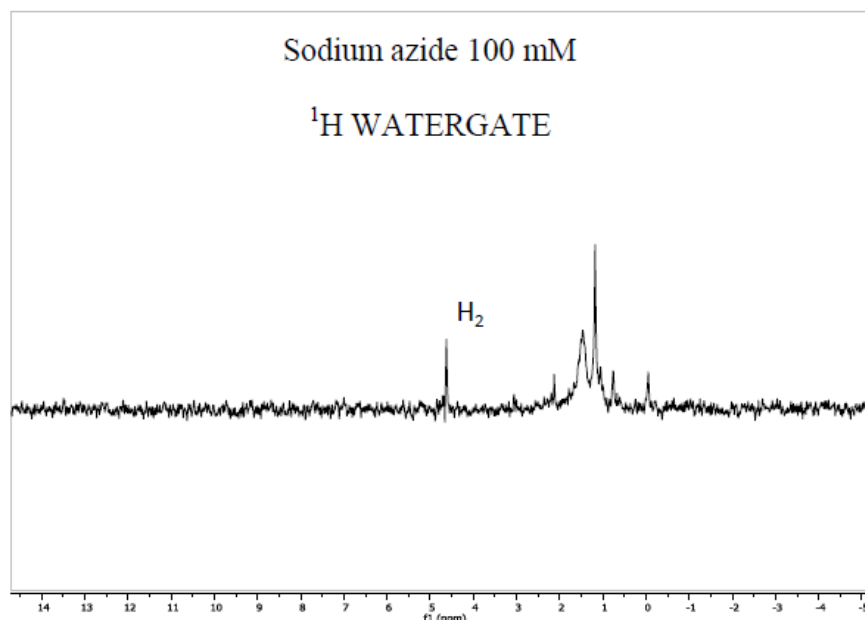


**Figure 3.** Proton  $^1\text{H}$  NMR spectroscopy of  $\text{NaN}_3$ .

The  $^{15}\text{N}$  peaks of sodium azide are not visible because they are below the noise level (S/N). To observe them, it is sure that a longer measurement time is needed; it means to use many more scans to average the noise to a lower level, or alternatively, to increase the

concentration of sodium azide in the sample so as to get a higher amount of signal per scan. With that sample of sodium azide, it would probably require at least 12 hours of measurement time (or even more) to make the expected  $^{15}\text{N}$  peaks appear over the noise level.

The  $^{14}\text{N}$ -spectrum of  $\text{NaN}_3$  is highly sensitive, much better than the equivalent experiments with  $^{15}\text{N}$  in the same molecule. The measurement of the 1D  $^1\text{H}$  NMR spectrum of sodium azide solutions in water is not practical. Depending of pH, protonated forms of sodium azide could be formed and in principle detected with proton NMR, however those forms do not lead to distinguishable peaks in the  $^1\text{H}$  spectrum because they overlap with the strong water solvent peak due to their undergoing fast exchange equilibrium with the water. (**Figure 3**).

Under the conditions of measurement, the  $^{14}\text{N}$  spectrum of sodium azide had a considerably much better sensitivity than the alternative  $^{15}\text{N}$  NMR. Although the concentration of sodium azide in this test sample was considerably high (100 mM), it would be possible to adjust the experimental conditions for the detection of lower concentrations of sodium azide (e.g. 1 mM) within still a reasonable NMR measurement time (e.g. from 30 min. to a few hours). For the next sample we diluted the 100 mM sample by a factor of 4 (concentration of 25 mM of  $\text{NaN}_3$ ) and repeat the spectrum.

To estimate the minimum detectable concentration of the water solution of sodium-azide we need to prepare a sample with known concentrations. To acquire the spectrum under some standardized conditions (in particular the total measurement time) and repeat the spectrum 4 or 5 times diluting the sample. We obtained  $^{14}\text{N}$  NMR spectra of 5 different concentrations of  $\text{NaN}_3$  water solution, reducing the concentration by factor of 2 each time (**Figure 4**).  $^{14}\text{N}$  peaks are observed at 4 mM. Calibration curve was calculated using least squares linear regression method. As an external reference standard was used nitromethane 100 %.

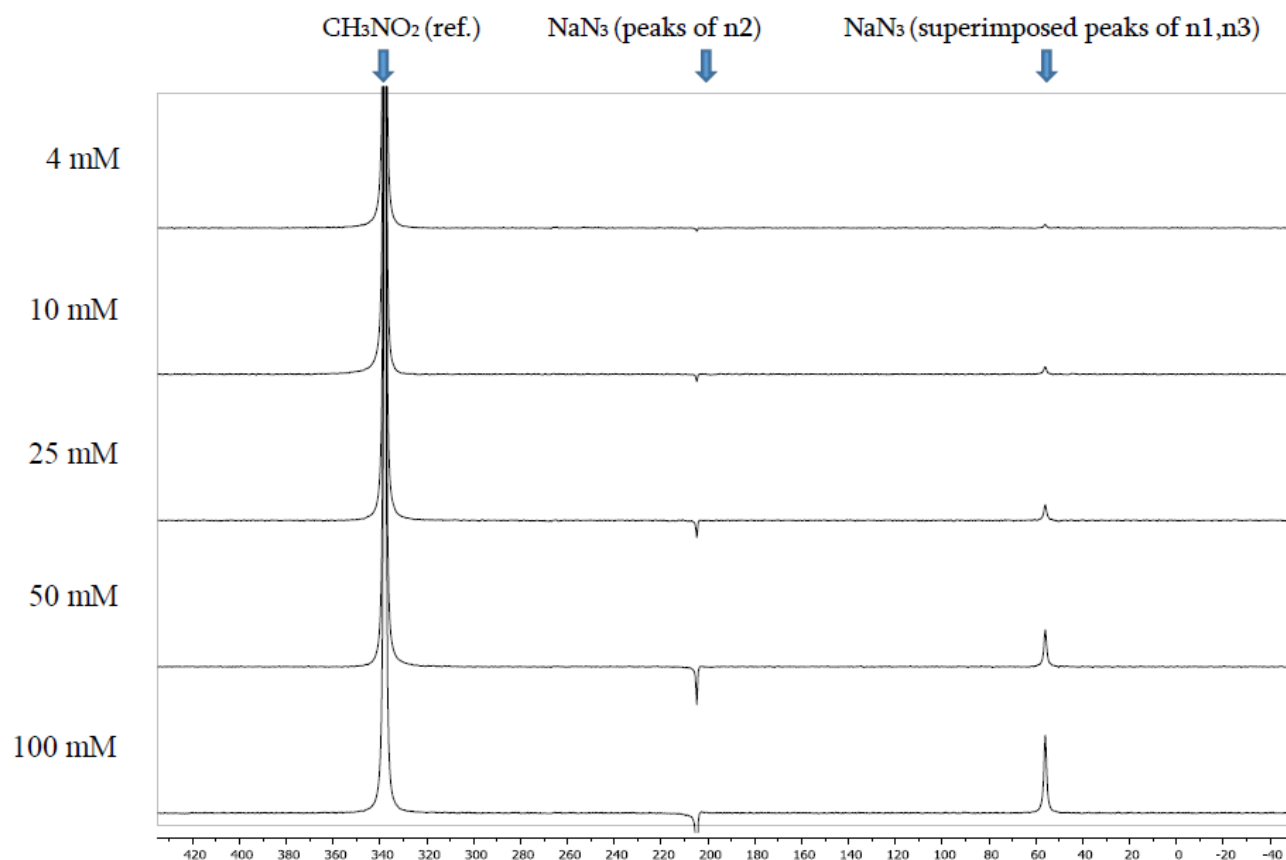
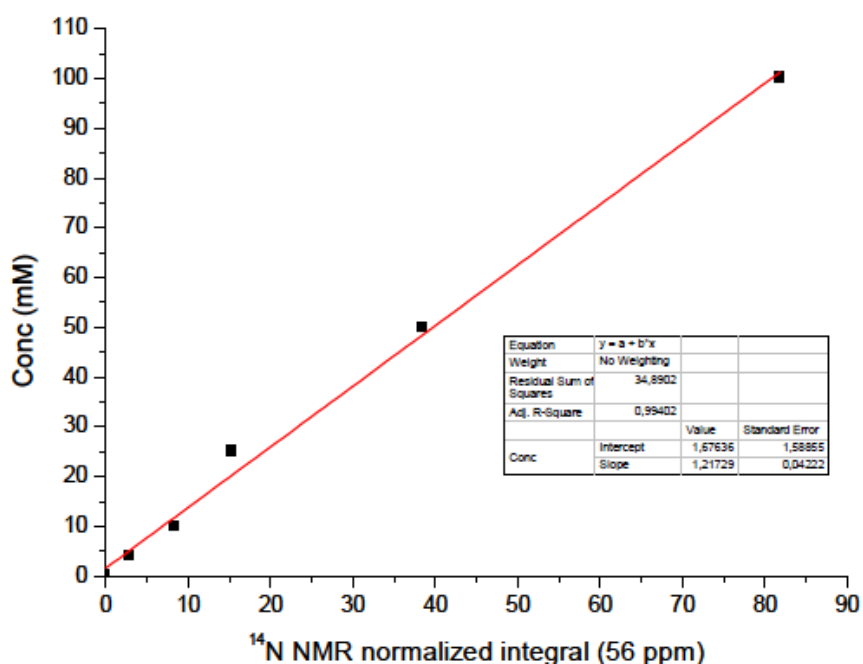
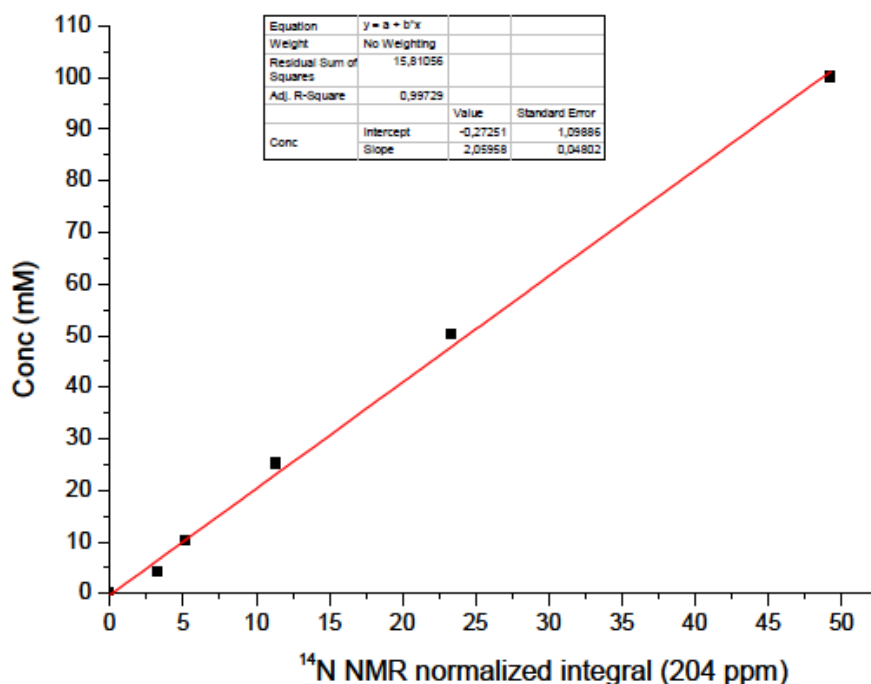


**Figure 4.**  $^{14}\text{N}$  NMR spectra of different concentrations of  $\text{NaN}_3$  water solution.

Calibration curve allows using this method for calculation even lower concentration of  $\text{NaN}_3$  indirectly. Particularly, we propose to lyophilize analyte sample by following protocol:  $^{14}\text{N}$  NMR can be measured with lower concentrations by following standard protocol. As the amount of sodium azide in the sample is only 0.5 mL for NMR assay, we recommend concentrating the analyte sample by liophilization of the water, to get a higher effective concentration of sodium azide for the NMR measurement.



(a)



(b)

Figure 5. Calibration curves (a) and (b).



Liophilization requires freezing under high vacuum a given amount of the analyte sample. The water will sublime during the liophilization process while the organic molecules and likely sodium azide will remain in the residual frozen solid. After liophilization to resuspend the residual solid in water, and then perform the  $^{14}\text{N}$  NMR analysis at 25 °C. For testing of proposed method of liophilization for detection of sodium azide is needed preparation of the sample at a known concentration and measurement by  $^{14}\text{N}$  NMR. We evaporate 5 ml of analyte solution and then resuspend up to 0.5 ml we will be able to detect 0.4 mM concentration of  $\text{NaN}_3$  in solution using obtained by us calibration curve standard (Figure 5) greater by factor of 10 compared to LOD obtained in our experiment.

## Discussion

Liquid Nuclear Magnetic Resonance (NMR) spectroscopy is nowadays a well-established, widespread and recognized analytical technique for the identification and quantification of molecules in a mixture. The technique is available in many recognized centers of research and development excellence. Despite the relative insensitivity of NMR compared to other analytical techniques such as Mass Spectrometry (MS), it has the unique capacity of being sensitive to the finest and subtle details of the structure of each molecule in the sample. In particular, the NMR spectrum is sensitive both to the three-dimensional structure of a molecule in solution and to the topology of each one of its covalent bonds.

Moreover, NMR is amenable for detection and quantitative analysis of specific molecules in a mixture without requiring any previous step of separation.

NMR sample preparation is simple and only requires a volume of 0.5 mL. It is also very versatile regarding the type of solvents and temperature that can be chosen. The NMR sample is studied directly under the relevant experimental conditions (e.g. in water solvent, at room temperature, etc.).

The only caution specific for the preparation of NMR samples containing relative concentrated solutions of sodium azide in water, is to handle them with care in a chemical hood and immediately seal the NMR tube after preparation since it changes rapidly to a toxic gas with a pungent (sharp) odor.

A better alternative to detect sodium azide with NMR is to rely in other nuclei such as  $^{14}\text{N}$  NMR or  $^{15}\text{N}$  NMR spectroscopy. From these two isotopes,  $^{14}\text{N}$  is the most abundant in nature (the natural abundance of  $^{14}\text{N}$  and  $^{15}\text{N}$  is 99.63 and 0.37 %, respectively) and in favorable case molecules, the higher natural abundance of  $^{14}\text{N}$  positively correlates with a remarkable higher experimental sensitivity in NMR than  $^{15}\text{N}$ .

Nevertheless, such favorable situation of  $^{14}\text{N}$  is not always the case; one aspect to consider is that  $^{14}\text{N}$  is a quadrupolar nucleus (spin  $I = 1$ ) while  $^{15}\text{N}$  has spin  $1/2$ .

The NMR sensitivity of quadrupolar nuclei is strongly affected not only by its isotopic abundance, but also by its characteristic transversal relaxation rate ( $R_2$ ). The relaxation rate  $R_2$  affects the appearance of the peak that is generated in the NMR spectrum (peak height and broadening depend on  $R_2$ ).

According to NMR theory, the expected trend is that  $^{14}\text{N}$  nucleus placed in an asymmetric (molecular) environment usually experiences a very efficient transversal relaxation

rate (a high value of  $R_2$ ), leading to a reduction of the peak height and enhanced line-broadening that severely degrades its NMR sensitivity. The situation is the opposite for  $^{14}\text{N}$  nuclei in symmetric (molecular) environments.

### Conclusions:

Considering together the large signal dispersion of  $^{14}\text{N}$  NMR resonances and the good sensitivity obtained in our preliminary  $^{14}\text{N}$  NMR study of sodium azide in water solution, we propose to use of  $^{14}\text{N}$  NMR spectra to detect and quantify sodium azide in real case samples e.g., contaminated water or soil extracts, wine, milk, biological fluids, e.g. urine and blood.

The methodology relying in measurement of 1D  $^{14}\text{N}$  NMR spectra at the lowest concentration compared to methods described previously with other analytical techniques.

The method has significance to apply in the fields of medicine, pharmaco-chemistry, toxicology, which should open the way for the various possible applications, including neurodegenerative disorders and ageing.

### References

1. Ed. S. McKeen. High Production Volume (HPV) Chemicals. 2010, Paris, OECD (Environ. Direct.).
2. R. Rodríguez-Kábana. An azide method and composition for controlling deleterious organisms. 2001, US Patent # PCT/US01/31669.
3. J. A. Cabrera, D. Wang, S. M. Schneider, B. D. Hanson. Effect of methyl bromide alternatives on plant parasitic nematodes and grape yield under vineyard replant conditions. *Am. J. Enology & Viticulture*, 2011, 62, 42.
4. S. J. Swaring, R. S. Waldo. Liquid chromatographic determination of azide as the 3,5-dinitrobenzoyl derivative. *J. Liq. Chromatogr.*, 1982. 5, 597.
5. R. Battaglia, J. Mitiska. Specific detection and determination of azide in wine. *Z. Lebensm. Unters Forsch*, 1986, 182, 501.
6. L. Wang, C. Dai, W. Chen, S. L. Wan, B. Wang. Facile derivatization of azide ions using click chemistry for their sensitive detection with LC-MS. *Chem. Commun.*, 2011, 47, 10377.
7. R. Rodríguez-Kábana, D. G. Robertson. Nematicidal and herbicidal properties of potassium azide. *Nematropica*, 2000, 30, 146.
8. R. Rodríguez-Kábana. Pre-plant applications of sodium azide for control of nematodes and weeds in eggplant production. In: *Proc. Ann. Int. Res. Conf. Methyl Bromide Alternatives & Emissions Reductions*. 2001, San Diego, 6-1.
9. R. Rodríguez-Kábana. Efficacy of aqueous formulations of sodium azide with amine-protein stabilizers for control of nematodes and weeds in tomato production. In: *Proc. Ann. Int. Res. Conf. Methyl Bromide Alternatives & Emissions Reductions*. 2001, San Diego, 7-1.
10. R. Rodríguez-Kábana, H. Abdelhaq. Sodium azide for control of root-knot nematodes and weeds in green pepper and tomato production in the Souss valley. In: *Proc. Ann. Int. Res. Conf. Methyl Bromide Alternatives & Emissions Reductions*. 2001, San Diego, 8-1.

11. E. A. Betterton. Environmental fate of sodium azide derived from automobile airbags. *Critical Rev. Environ. Sci. & Technol.*, 2003, 33, 423.
12. E. A. Betterton, J. Lowry, R. Ingamells, B. Venner. Kinetics and mechanism of the reaction of sodium azide with hypochlorite in aqueous solution. *J. Hazard. Mater.*, 2010, 182, 716.
13. E. A. Betterton, D. Craig. Kinetics and mechanism of the reaction of azide with ozone in aqueous solution. *J. Air & Waste Manag. Assoc.*, 1999, 49, 1347.
14. Ed. L. Bretherick. *Hazards in the Chemical Laboratory*. 1986, London, Roy. Soc. Chem., 491.
15. American Azide Corporation MSDS. Sodium Azide. 9.19.2003.

## SOME OPTICAL METHODS OF DETECTING PATHOGENIC NANO-BIO-PARTICLES

K. Kapanadze, G. Kakabadze, V. Kvintradze

Georgian Technical University  
Tbilisi, Georgia  
vakho710@gmail.com

Accepted August 22, 2015

### Abstract

For detecting and identification of nano-bio-particles (NBP) different optical methods of contact as well as non-contact types are considered. There was said that, contact systems would be suitable for collecting physical data (size, shape, mass, binding energy, electric magnetic and optical characteristics, etc.) of NBP for application them to stand-off detection systems. Both type of methods are very useful, they have their positive and negative sides, and in the case of acting together would better solve the problems of detection of pathogenic NBP.

### 1. Introduction

Rapid, early, and accurate detection and identification of pathogenic nano-bio-particles (NBP) is an important problem of healthcare. Detection and identification in general is complex processes and consists of several procedures (triggering, rapid identification, and laboratory confirmation). Applying the classical methods (to get final result) takes from several hours to several days. Rapid, early and accurate detection means to save time from propagation of illness. For the solution this tusk, the nanotechnologies are applied.

Particles that are smaller than the characteristic lengths associated with the specific phenomena often display new chemistry and new physics that lead to new properties that depend on size. When the size of the structure is decreased, surface to volume ratio increases considerably and the surface phenomena predominate over the chemistry and physics in the bulk. The reduction in the size of the sensing part and / or the transducer in a sensor is important in order to better miniaturize the devices. Science of nanomaterials deals with new phenomena, and new sensor devices are being built that take advantage of these phenomena. Sensitivity can increase due to better conduction properties, the limits of detection can be lower, very small quantities of samples can be analyzed, direct detection is possible without using labels, and some reagents can be eliminated [1].

A sensor is an instrument that responds to a physical stimulus (such as heat, light, sound, pressure, magnetism, or motion). It collects and measures data regarding some property of a phenomenon, object, or material. Sensors are an important part to any measurement and automation application. The sensor is responsible for converting some type of physical

phenomenon into a quantity measurable by a data acquisition (DAQ) system. Nano-sensors are any biological, chemical, or surgical sensory points used to convey information about nanoparticles to the macroscopic scale [1].

The methods for detection and identification of NBP can be based on different ways: physical, chemical, biological etc. All of them have as positive also negative (preparing procedures, separation pathogens from surrounding environment, i.e., sampling, too long time to get result, they can damage analyte and so on) sides. It is well-known that most appropriate (non-invasive, precise) way is optical method (contact or non-contact-remote) of detection and identification of NBP *in situ*, i.e., at given time and place. For execute this, is necessary to know physical characteristics (such as a size, shape, mass, density of particle it's frequency, index of refraction, dielectric constant etc.) of NBP.

## 2. Optical methods

The optical methods are of different kinds (flow cytometry, fluorescence, fiber optics, surface plasmon resonance, mass-spectrometry, Raman spectroscopy, etc.). In general, they are contact and non-contact types. For the contact (i.e. point) methods, is necessary the enough quantity of bio-particles (i.e., concentration), separated from environment for sensitive measurements. Below, contact type optical methods are considered.

### 2.1. Evanescent wave fiber optic bio-sensors (EWAB)

When light propagates through a fiber optic (**Figure 1**) on the basis of total internal reflection (TIR), a thin electromagnetic field (the “evanescent wave”) generated decays exponentially with the distance from the interface with a typical penetration depth of up to several hundred nanometer [2]:

$$E(z) = E_0 \exp(-\delta/d_p).$$

Here  $\delta$  is the distance from the interface, the penetration depth ( $d_p$ ) is given by the expression

$$d_p = \frac{\lambda_{ex}}{2\pi} [(n_2)^2 \sin^2 \alpha - (n_1)^2]^{-1/2},$$

where  $\lambda_{ex}$  is the wavelength of the light,  $n_1$  is the refractive index of the cladding region and  $n_2$  is the refractive index of the core, and  $\alpha$  is the angle of incidence measured from the normal at the interface of the core and cladding.

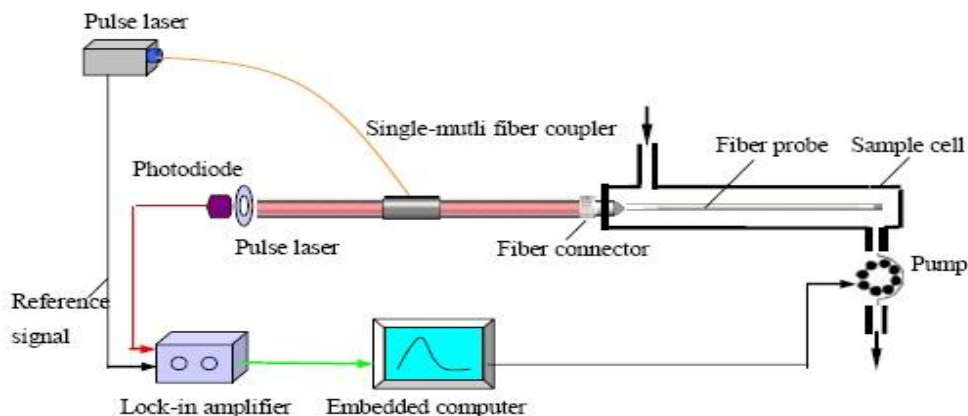


**Figure 1.** Principle scheme of the portable optical fiber biosensor [2].

This evanescent wave can excite fluorescence in the proximity of the sensing surface, e.g., in fluorescently labeled biomolecules bound to the optical sensor surface through affinity recognition interactions. The short range of the evanescent wave enables it to discriminate between unbound and bound fluorescent complexes, hence eliminating the normally required washing procedures. Moreover, evanescent field-based waveguides are well suited for study and detection of bio-molecular interaction. Ultrasensitive DNA detection was achieved by the EWAB based on quantum dots (QDs) [2].

## 2.2. SPR biosensors

Surface plasmon resonance (SPR) is a surface-sensitive optical technique that is associated with the evanescent electromagnetic field generated on the surface of a thin metal film when excited by an incident light under total internal reflection conditions. Due to the fact the evanescent field diminishes exponentially with increasing distance of penetration from the interface, SPR promotes monitoring of only surface-confined molecular interactions occurring on the transducer surface. SPR biosensors allow real-time detection of minute changes in the refractive index when bio-recognition molecules (e.g., antibodies) immobilized on a transducer surface bind with their bio-specific targets (e.g., analytes) in solution [2].

The use of SPR to detect environmental contaminants, including atrazine, dichlorodiphenyl-trichloroethane (DDT), 2,3,7,8-tetrachlorodibenzo-*p*-dioxin, carbaryl, 2,4-D, benzo[a]pyrene (BaP), biphenyl derivatives, and trinitrotoluene (TNT), has recently gained considerable interest [2].

## 2.3. Optical micro-resonators

Here, it has been developed [3] the highly sensitive, miniaturized, optical-sensing component that allows detection of single pathogens or disease biomarkers without having to label them.

This bio-sensing component derives its unprecedented sensitivity from the use of micro-sphere optical resonators. The optical resonance is created by launching and confining coherent light inside the microsphere, where it interferes constructively due to total-internal reflection.

Detection of single particles relies on the ability to discriminate the wavelength-shift signal against background noise, a task that requires narrow line-width, high-quality ( $Q$ ) optical resonance and the use of nanoparticles that produce an observable resonance shift. Unfortunately, most important biological pathogens are virus nanoparticles in the 50 – 1000 nm size range, and discerning the resulting wavelength-shift signal is extremely challenging (its magnitude scales inversely with the virus size to the third power). Fortunately, the magnitude of the wavelength-shift signal can be sufficiently enhanced by making the microsphere resonator smaller. We confirmed a reactive sensing mechanism with inverse dependence on mode volume in experiments with virus-sized polystyrene Nano-particles. By comparing the electromagnetic theory for this reactive effect with experiments, we can determine the size ( $\sim 100$  nm) and mass ( $\sim 5.2 \cdot 10^{-16}$  g) of a bound influenza A virion directly from the optimal resonance wavelength shift [3].

The non-contact (remote or stand-off) detection systems (LIDAR – Light detection and ranging) are not so precisely as point systems. They are long distance (1 – 5 km) operate systems,



they are used for atmospheric research and monitoring, they distinguish organic from nonorganic, but don't distinguish organic particles from each other, and they are used for early (alarm) warning, so they aren't discussed here.

Most interesting is detection of pathogenic nanoparticles indoor (for example: schools, cinemas, hospitals, etc.) for the short (1 – 50 m) distances. For this case, most valuable method is based on Raman scattering.

### 2.4. Raman spectroscopy

Raman spectroscopy has become a powerful instrument for study biological samples. This technique rapidly characterizes the tissue and bodily fluids in nondestructive and noninvasive fashion. Raman Spectroscopy used to identify different molecules and even functional groups within larger molecules. The bonds formed between atoms have specific vibrational frequencies that correspond to the atom's masses and the strength of the bond between them. Complex molecules therefore exhibit many peaks and can be readily identified by the pattern or "fingerprint" created by those peaks. Besides, the spectroscopy of Raman allows very sensitive for the discrimination of bacteria. Raman scattering of light has interacted with vibrational modes of the molecule, a vibrational spectrum may be obtained allowing for identification of molecules and their functional groups. Raman spectroscopy is sensitive to analyze molecular changes such as protein structures and concentrations. Raman spectroscopy has capability to detect molecules alternation and to analyze some difference at molecules level and its tool are possible to open many new factors in studying of viruses [4].

The idea of Raman spectroscopy stand-off detection is based on the features of Raman scattering. Raman scattering is a two-photon process that conveys information about the vibrational mode-structure of the scattering molecule. In normal Raman scattering, an incident photon of frequency  $\nu_0$  excites a molecule from its ground electronic level to a "virtual" energy level. If the energy of this virtual level is sufficiently different from that of the nearest real level, the molecule returns quickly back to its ground level; a second photon is emitted almost instantly. If the emitted photon has the same frequency as the incident one, the process is called Rayleigh scattering. However, interaction of the incident photons with the vibrations of a molecule can shift the frequencies of the scattered photons. The shifts are equal to the frequencies of the discrete vibrational modes of the molecule. This unique set of frequency-shifts produces a spectrum that is a vibrational "fingerprint" of the interacting molecule [5].

Raman scattering is strongest when vibrations cause a change in the polarizability of the electron cloud around the molecule. Therefore, the difference in energy between the incident and scattered photons is a characteristic of and provides structural information about the irradiated molecule [6]. The mathematical expression of Raman scattering is as following. When the light interacts with non-oscillating molecule it gives part of energy to molecule and therefore its frequency decreases (Stokes effect)

$$h\nu' = h\nu_0 - h\nu_m \quad \text{or} \quad \nu' = \nu_0 - \nu_m$$

Here  $\nu_0$  is the frequency of incident light and  $\nu_m$  is the frequency of oscillating molecule. When the light interacts with oscillating molecule with energy of  $h\nu_m$ , it can take away energy of molecule and became of radiation of high frequency (anti-Stokes effect) [7]:

$$h\nu' = h\nu_0 + h\nu_m,$$

or

$$\nu' = \nu_0 + \nu_m.$$

Further, due to its narrow spectral lines and unique signatures, Raman spectroscopy enables selective identification of individual analytes in a complex, multicomponent mixture without the need for chemical separations. In addition, the technique requires little or no sample preparation, is nondestructive, and can use water as a solvent (since water is a poor Raman scatterer). The intensity of the scattering is related to the power of the laser used to excite the scattering, the square of the polarizability of the molecule, and the fourth power of the frequency of the exciting laser. Therefore, the most common choice for excitation is a visible laser [6].

Unfortunately, Raman scattering is an inherently weak process, precluding the possibility of remote trace analysis without some form of enhancement. However, surface-enhanced Raman scattering (SERS) can give an enhancement of up to about  $10^6 - 10^7$  in scattering efficiency over normal Raman scattering. Even stronger enhancements of order of  $10^{11} - 10^{13}$  come from sharp features or “hot spots”, such as are found in nanostructures. Such extremely large enhancements can produce a total SERS cross-section comparable to that of fluorescence [6].

### 3. Conclusions

As it was mentioned above, the goal was to find proper characteristics among NBP and sensors to detect and identification of NBP, especially, remote, stand-off detection indoor pathogens. For this, are considered different types of optical methods (contact, non-contact) of detection of pathogen particles. It is seen, that some of them are well suited for study and detection of bio-molecular interaction, real-time detection changes in the refractive index when bio-recognition molecules (e.g., antibodies) bound on a transducer surface with their biospecific targets, allow detection of single pathogens or disease biomarkers without having to label them, detecting even virus nanoparticles.

All of these methods are contact methods (the pathogen particles must be separated from environment and concentrated in the small volume). They are applied mostly in the laboratory, but not *in situ*. These methods also are useful for collecting of experimental data about physical properties of bio-particles (size, shape, mass, binding energy, electric magnetic and optical characteristics, etc.). This data base will be fundament for the detection pathogens *in situ*.

One of the most suitable ways for remote (non-contact) detection of pathogens (*in situ*) is Raman spectroscopy. This method identifies pathogens by their own pattern of “fingerprints”. There is no need to separate and collect pathogens in the small volume. These “fingerprints” are independent of initial wavelength. It’s truth, that Raman scattering is weak process, but it can be enhanced by SERS. So at the presence of high resolution advanced technique (or their combination) the problem of detecting and discrimination of NBP will be decided with high probability.

### Acknowledgment

The work is carrying out in Georgian Technical University supported by Shota Rustaveli National Science Foundation (SRNSF) under Grant Agreement (FR/430/3–250/13).

## References

1. E. L. Wolf. Introduction to Nanotechnology. Nanophysics and Nanotechnology (Textbook). [http://www.phys.sinica.edu.tw/TIGP-NANO/Course/2013\\_Fall/classnote/NanoB-Electronic-2.pdf](http://www.phys.sinica.edu.tw/TIGP-NANO/Course/2013_Fall/classnote/NanoB-Electronic-2.pdf).
2. F. Long, A. Zhu, H. Shi. Recent Advances in Optical Biosensors for Environmental Monitoring and Early Warning. File: sensors-13-13928-v3.pdf.
3. F. Vollmer. Optical microresonators: label-free detection down to single viral pathogens. SPIE Newsroom, 4 February 2010, <http://spie.org/x39030.xml>.
4. K. Moor, H. Kitamura K. Hashimoto, M. Sawa, B. B. Andriana, K. Ohtani, T. Yagura, H. Sato. Study of virus by raman spectroscopy. SPIE Conf. Vol. 8587. 2013, Gakuen: Kwansai Gakuin Univ. <http://proceedings.spiedigitallibrary.org/proceeding.aspx?articleid=1656077>.
5. M. D. Ray, A. J. Sedlacek. Mini-lidar sensor for the remote stand-off sensing of chemical / biological substances and method for sensing same. US Pat. # 6608677 B1. 19 August 2003.
6. W. C. Sweatt, J. D. Williams. Laser remote sensing of backscattered light from a target sample. US Pat. # 7336351 B1. 26 February 2008.
7. G. S. Landsberg. Optics. 1976, Moscow: Nauka, 603-604.

THE UPTAKE OF Cr(III) IN THE PRESENCE OF Mn(II)  
DURING GROWTH OF *Arthrobacter* SPECIES

E. Gelagutashvili, A. Rcheulishvili

I. Javakhishvili Tbilisi State University  
E. Andronikashvili Institute of Physics  
Tbilisi, Georgia  
eterige@gmail.com

Accepted September 14, 2015

**Abstract**

The uptake of Cr(III) by *Arthrobacter* species (*Arthrobacter globiformis* 151B and *Arthrobacter oxidas* 61) were studied without and in the presence of Mn(II) ions during growth of *Arthrobacter* species using simultaneous application dialysis and atomic absorption analysis. It was shown, that when added Cr(III) concentration is increased, the interaction of Cr(III) with *Arthrobacter* species are increased too and approximately it is equal to  $10^{13}$  atom Cr per *Arthrobacter* species. It was shown, that biosorption characteristics did not change in the presence of Mn(II) ions during growth of *Arthrobacter* species. This means, that Mn(II) did not significantly affect the biosorption of Cr (III) ion-*Arthrobacter* species, i.e. Mn(II) essentially did not displace Cr(III) from bacteria.

**Introduction**

Nanotechnology has been identified as a technology that could play an important role in resolving many of the problems related to water purification and water quality [1]. Bioremediation is an ecologically sound natural process where natural strains of bacteria breakdown organic wastes most effectively. The field of nanotechnology is an immensely developing field as a result of its wide-ranging applications in different areas of science and technology [2]. Synthesis of nanoparticles using microbes is a new and emerging in nanotechnology science. Nanoparticles are metal particles. Research on synthesis of nanoparticles is the current area of interest. Nanoparticles are biosynthesized when the microorganisms grab target ions from their environment and then turn the metal ions into the element metal through enzymes generated by the cell activities. The modes by which the microorganisms remove metal ions from solution are: extracellular accumulation/ precipitation, cell surface sorption or complexation.

Gram-positive *Arthrobacter* species bacteria can reduce Cr(VI) to Cr(III) under aerobic growth and there is a large interest in Cr-reducing bacteria. The exact mechanism by which microorganisms take up the metal is relatively unclear. The inhibitive effect of FeS on Cr(III) oxidation by biogenic Mn-oxidas that were produced in the culture of a known species of Mn(II) oxidizers, *Pseudomonas putida*. In soils containing manganese oxides, the immobilized form of chromium Cr(III) could potentially be reoxidized [3, 4]. Equilibrium data, commonly known as adsorption isotherms, provide information on metal binding capacity of the adsorbent [5]. In the literature, there are some reports evaluating biosorption of chromium(III) *Spirulina platensis* [6], *Chlorella miniata* [7]).

In the present work, chromium(III) uptake by *Arthrobacter* species without and in the presence of Mn(II) during growth of *Arthrobacter* species were studied using simultaneous application dialysis and atomic absorption analysis.

### Materials and methods

Organisms, culture techniques, cell dry weight measurement, metal analysis methods, data analysis are the same as have been described previously [8].

### Results and discussions

Cr(III) uptake by cells of *Arthrobacter globiformis* 151B and *Arthrobacter oxidas* 61B and in the presence of Mn(II) ions and without it during growth of *Arthrobacter* species were studied as a function of metal concentration. The linearized adsorption isotherms of Cr-bacterium and in the presence Mn during growth bacterium species at room temperature are shown in **Figures 1** and **2** by fitting experimental points. The adsorption yields determined for each *Arthrobacter* were compared in table 1. The data in **Table 1** are not show a significant difference between the binding constants for Cr(III)-*Arthrobater oxidas* and Cr(III)-*Arthrobater globiformis*. (Biosorption constants for *Arthrobacter oxidas* and *Arthrobacter globiformis* are:  $2.60 \cdot 10^{-3}$  and  $2.02 \cdot 10^{-3}$ , respectively). Insignificant decrease in bioavailability has been observed experimentally for Cr(III)-*Arthrobacter globiformis* as compared with *Arthrobacter oxidas*. As seen from **Table 1** for both *Arthrobacter* species  $n$  (1.37 and 1.23) values are not significantly different and their sorption intensity indicator are generally small. It was shown also, that when added Cr(III) concentration is increased, the interaction of Cr(III) with *Arthrobacter* species are increased too and approximately it is equal to  $10^{13}$  atom Cr per *Arthrobacter* species.

Uptake of metals by microorganisms is substantially influenced by the following parameters: nature of biosorbent, age of culture and origins of biomass, the nature of interactions of metals with functional groups native to the biomass cell wall, concentration of biosorbent, properties of metals and their concentrations, pH, temperature and presence of other cations. pH strongly influenced protonation of metal binding sites exposed by cell surface. If pH increased, more ligands such as carboxyl, phosphate, imidazole and amino group would become deprotonated and thus available of positively charged metal cations. *Pyrobaculum islandicum*, an anaerobic hyperthermophilic microorganism, was reported to reduce many heavy metals including U(VI), Tc(VII), Cr(VI), Co(III), and Mn(IV) with hydrogen as the electron donor [9].

The role of presence Mn(II) cations in biosorption Cr(III)-*Arthrobacter* species were discussed by us. Biosorption characteristics  $K$  and  $n$  for *Arthrobater oxidas* in the presence of Mn(II) are  $2.43 \cdot 10^{-3}$  ( $K$ ) and 1.41 ( $n$ ), respectively, for *Arthrobacter globiformis* in the presence of Mn(II)  $1.94 \cdot 10^{-3}$  ( $K$ ) and 1.47 ( $n$ ), respectively. The correlations between experimental data and the theoretical equation were extremely good, with  $R$  above 0.93 (**Table 1**) for all the cases. The higher correlation coefficient shows that the Freundlich model is very suitable for describing the biosorption equilibrium of Chromium by the *Arthrobacter* species in the studied concentration range.

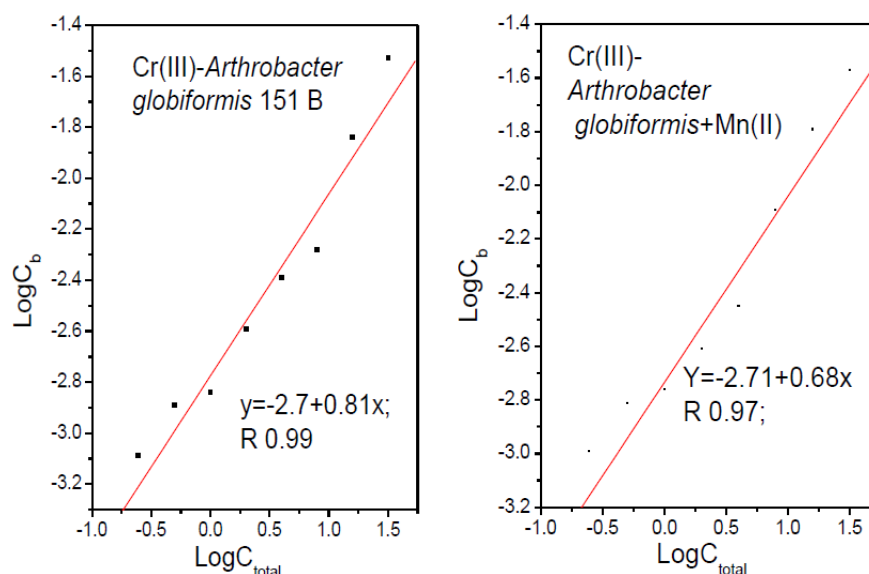


**Figure 1.** The linearized Freundlich adsorption isotherms of Cr(III) ion–*Arthrobacter globiformis* without and in the presence of Mn(II) ions during growth of bacterium. ( $C_b$  is the binding metal concentration (mg / g) and  $C_{total}$  is initial Cr concentration (mg / l).

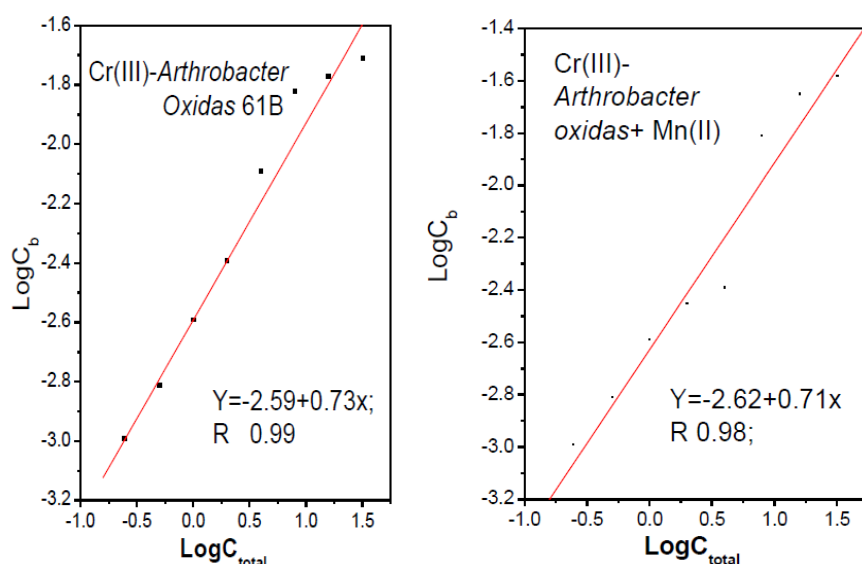


**Figure 2.** The linearized Freundlich adsorption isotherms of Cr(III) ion–*Arthrobacter oxidas* without and in the presence of Mn(II) ions during growth of bacterium. (The parameters are the same as in **Figure 1**).

**Table 1.** Biosorption characteristics for Cr(III)–*Arthrobacter* species in the presence of Mn(II) during growth of bacterium and without it at 23 °C.

Biosorption characteristics ( $K$ and $n$ )	Cr(III)		
	$K \cdot 10^{-3}$	$n$	$R^2$
<i>Arthrobacter oxidas</i>	2.60	1.37	0.98
<i>Arthrobacter globiformis</i>	2.02	1.23	0.98
<i>Arthrobacter oxidas</i> + Mn(II)	2.43	1.41	0.96
<i>Arthrobacter globiformis</i> + Mn(II)	1.94	1.47	0.94



It is seen, that biosorption characteristics did not change in the presence of Mn(II) ions. This means, that Mn(II) did not significantly affect the biosorption of Cr(III) ion–*Arthrobacter* species, i.e. Mn(II) essentially did not displace Cr(III) from bacteria. This fact leads us to speculate that primary binding site for Cr(III) is different than the binding site for Mn(II). The distorted octahedral coordination sphere proposed for Cr(III) and strong tendency to coordinate donor atoms equatorially may be responsible for the specific interaction with *Arthrobacter* species.

Comparative Cr(VI)–*Arthrobacter species* [8] and Cr(III)–*Arthrobacter* species shown, that Cr(III) was more effectively adsorbed by both bacterium than Cr(VI). The adsorption capacity is the same for both the Chromium–*Arthrobacter* systems. The biosorption constants for Cr(III) is higher than for Cr(VI) 5.65 – 5.88 fold for both species. Cr(VI) is one of the more stable oxidation states, the others being chromium(II), chromium (III). Cr (VI) can be reduced to Cr(III) by the biomass through two different mechanisms [10]. The first mechanism, Cr(VI) is directly reduced to Cr(III) in the aqueous phase by contact with the electron–donor groups of the biomass. The second mechanism consists of three steps. The binding of anionic Cr(VI) ion species to the positively charged groups present on the biomass surface, the reduction of Cr(VI) to Cr(III) by adjacent electron-donor groups and the release of the Cr(III) ions into the aqueous phase due to electronic repulsion between the positively charged groups and the Cr(III) ions. The “uptake–reduction” model for chromium (VI) carcinogenicity is, that tetrahedral chromate is actively transported across the cell membrane via mechanisms in place for analogous such as sulfate,  $\text{SO}_4^{2-}$ . Chromium (III) is not actively transported across the cell membrane to lack of transport mechanisms for these octahedral complexes. Comparative our results for Cr(VI) [8] and present work shown, that Cr(VI) may be adsorbed to bacterium a much lower degree than Cr(III).

Uptake of metal ions by bacterium may be associated not only to physico-chemical interactions between the metal and the cell wall, but also with other mechanisms, such as the microprecipitation of the metal [11] or the metal penetration through the cell wall [12].

### References

1. R. Sen, Sh. Chakrabarti. *Curr. Sci.*, 2009, 97, 768-775.
2. Eds. M. Rai, N. Duran. *Metal Nanoparticles in Microbiology*. 2011, Berlin–Heidelberg Springer–Verlag.
3. Y. Wu, B. Deng. *Environ. Eng. Sci.*, 2006, 23, 552-560.
4. Y. Wu, B. Deng, H. Xu, H. Kornishi. *Geomicrobiol. J.*, 2005, 22, 161-170.
5. D. Kratochvil, P. Pimentel, B. Volesky. *Environ. Sci. & Technol.*, 1998, 32, 2693-2698.
6. Z. Y. Li, S. Y. Guo, L. Li. *J. Food Eng.*, 2006, 75, 129-136.
7. X. Han, Y. S. Wong, N. F. Y. Tam. *J. Colloid Interface Sci.*, 2006, 303, 365-371.
8. E. Gelagutashvili, E. Ginturi, A. Rcheulishvili. *Nano Studies*, 2014, 9, 163-166.
9. K. Kashefi, D. R. Lovley. *Appl. & Environ. Microbiol.*, 2000, 66, 1050-1056.
10. D. Park, Y.-S. Yun, J. M. Park. *Chemosphere*, 2005, 60, 1356-1364.
11. J. Scott, S. J. Palmer. *Appl. Microbiol. & Biotechnol.*, 1990, 33, 221-222.
12. T. Y. Peng, T. W. Koon. *Microbial Utilisation Renewable Resources*, 1993, 8, 494-504.

## МАТЕРИАЛ ДЛЯ ПОГЛОЩЕНИЯ ТЕПЛОВЫХ И РЕЗОНАНСНЫХ НЕЙТРОНОВ

Н. В. Багдавадзе, А. В. Рустамбеков,  
Т. И. Зедгинидзе, Т. Г. Петриашвили

Тбилисский государственный университет им И. Джавахишвили  
Институт физики им. Э. Андроникашвили  
Тбилиси, Грузия  
tamuna777petriashvili@yahoo.com

Принята 29 сентября 2015 года

### Аннотация

Разработана технология получения материала, поглощающего тепловые и резонансные нейтроны, содержащего кадмий в виде бромистого кадмия и дополнительно – жидкого стекла при соотношениях исходных компонентов: бромистый кадмий 90.0 – 97.5 и жидкое стекло 2.5 – 10.0 вес. %. Материал предназначен для поглощения тепловых и резонансных нейтронов в различных ядерно-физических источниках нейтронов.

Существует очень много задач в науке и технике, в промышленности и в сельском хозяйстве, которые требуют знания элементного состава веществ как для его основных составляющих, так и для примесей. Широкий набор разнообразных методов для проведения необходимых анализов. Каждый из этих методов имеет свои преимущества и недостатки, определяющие наиболее целесообразные области их применения. Исключением не является и нейтронноактивационный анализ. Одно из направлений, в котором целесообразно этот метод использовать, относится к анализу образцов с малым содержанием примесей при небольшом количестве анализируемого вещества. Такие требования, в частности, встречаются в медико-биологических исследованиях. Желание перейти в таких исследованиях к выяснению роли тяжелых элементов в жизнедеятельности организмов и растений на клеточном и молекулярном уровне резко снижает массу вещества, которую можно представить для анализа. Накладываются ограничения и на пробоподготовку и условия проведения анализа, чтобы избежать загрязнений образца и потерь элементов из него. Предпочтительна в этом случае более инструментальная методика, которой является нейтронно-активационный анализ.

Высокие потоки нейтронов в активной зоне реактора и ядерные константы определяют только принципиальную возможность низких пределов обнаружения некоторых элементов. Реальные образцы и условия анализа создают трудности достижения этих пределов из-за сильной активации основы или отдельных элементов с нехорошими периодами полураспада или из-за потерь элементов. Преодоление теми или

иными способами этих трудностей, чтобы снизить реальные пределы обнаружения, может привести, по сути дела, к созданию новой методики анализа. Введенные и разработанные авторами способы снижения влияния мешающей активности брома путём Cd, Cd + В и CdBr фильтров, фактически приводят к созданию новой методики анализа.

Разработанная технология относится к области прикладной ядерной физики и может быть использована в качестве материала защитного фильтра-экрана в гамма-спектрометрическом инструментальном нейтронно-активационном анализе и, в частности, резонансном в нейтронно-активационном анализе для избирательной активации биологических образцов.

В настоящее время для устранения интерференционных помех, создаваемых различными радиоизотопами в гамма-спектрометрических измерениях биологических материалов, активируемых нейтронами, используется избирательная активация образцов, осуществляемая с помощью защитных экранов на основе бора [1].

Наиболее близким техническим решением является материал для поглощения тепловых и резонансных нейтронов, содержащий кадмий [2]. Однако, вышеупомянутые экраны не в состоянии поглотить поток резонансных нейтронов с энергиями 35, 54, 104 и 136 эВ, на которых происходит образование радиоизотопа  $^{82}\text{Br}$ .

Так, в биологических образцах, защищенных экраном из металлического кадмия, в процессе активации надкадмиевыми нейтронами, происходит индуцирование радиоизотопа  $^{82}\text{Br}$ , являющегося источником гама-излучения с энергиями 564 – 798 кэВ, что, в свою очередь, вызывает затруднения в идентификации радиоизотопов  $^{76}\text{As}$  и  $^{122}\text{Sb}$ , энергии гама-излучения которых соответственно равны 559 и 564 кэВ.

Целью настоящей работы является повышение эффективности поглощения тепловых и резонансных нейтронов с энергиями 35, 54, 104 и 136 кэВ.

Поставленная цель достигается тем, что материал для поглощения резонансных нейтронов, содержащий кадмий, содержит бром в виде бромистого кадмия  $\text{CdBr}_2$  и раствор жидкого стекла  $\text{Na}_2\text{SiO}_3$  при следующих соотношениях исходных компонентов (вес. %): бромистый кадмий 90.0 – 97.5 и жидкое стекло 2.5 – 10.0. Поглощающий материал изготавливают по следующей технологии: к порошку бромистого кадмия добавляют необходимое количество, предпочтительно 5 вес. %, 25 % водного раствора жидкого стекла, смесь тщательно перемешивают и формуют гранулы – брикеты под давлением 100 кг / см<sup>2</sup>. Брикеты термически обрабатывают при 200 – 300 °С в течение 0.5 – 1.0 ч, а затем размалывают в порошок с удельной поверхностью 2500 см<sup>2</sup> / г. Порошок увлажняют 3 – 5 % воды и формуют изделие необходимой формы под давлением 500 кг / см<sup>2</sup>, которое затем обжигают в электрической муфельной печи при температуре 500 °С в течение 1 – 2 ч. Охлаждение изделия производят на воздухе.

Применение 2.5 – 10.0 вес. % и 25 % водного раствора жидкого стекла обусловлено следующим: гомогенно распределенное в массе бромистого кадмия, жидкое стекло выполняет роль связки, которая придает брикету необходимую прочность, причём количество 2.5 вес. % является тем минимальным пределом, при котором наблюдается прочность брикета. Применение жидкого стекла выше 10 вес. % нежелательно, т.к. смесь получается излишне влажной и требует дополнительную сушку, а также уменьшается содержание основного материала – поглотителя  $\text{CdBr}_2$  в единице объема. Оптимальным количеством добавляемого жидкого стекла является 5.0 вес. %. При этом сырьевая смесь формуется удовлетворительно, и брикет обладает достаточной механической прочностью.

В процессе термической обработки жидкое стекло полностью обезвоживается, скрепляя зерна бромистого кадмия в монолитное тело. Например, к 9.75 г порошка бромистого кадмия добавляют 0.25 мл 25 % водного раствора жидкого стекла, смесь перемешивают и формируют брикет размером  $10 \times 40 \times 10$  мм под давлением  $100 \text{ кг / см}^2$ , который обжигают при температуре  $300 \text{ }^\circ\text{C}$  в течение 1.0 ч. По окончании обжига брикет размалывают в порошок с удельной поверхностью  $2500 \text{ см}^2 / \text{г}$ , увлажняют 5 % воды и формируют изделие в виде диска с  $d = 28$  мм и  $h = 5$  мм с центральным углублением для закладки образца диаметром 5 мм и высотой 1.5 мм. Изделие обжигают при температуре  $500 \text{ }^\circ\text{C}$  в течение 2 ч. Аналогичным образом готовят материал и с большим содержанием жидкого стекла, т.е. составы с 5 и 10 вес. %.

Предлагаемая композиция обладает необходимыми для резонансного нейтронно-активационного анализа биологических материалов комбинированными свойствами поглощать тепловые нейтроны с энергией  $\leq 0.4$  эВ благодаря наличию в ней элемента кадмия и резонансные нейтроны с энергией 35, 54, 104 и 136 эВ, при которых происходит образование радиоизотопа  $^{82}\text{Br}$  за счет присутствия элемента Br (Рисунки 1 и 2).

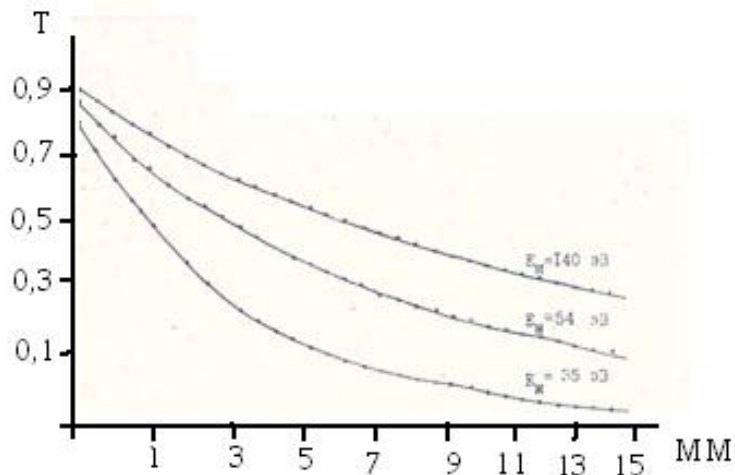


Рисунок 1. Зависимость фактора пропускания  $T$  от толщины  $\text{CdBr}_2$  экрана.

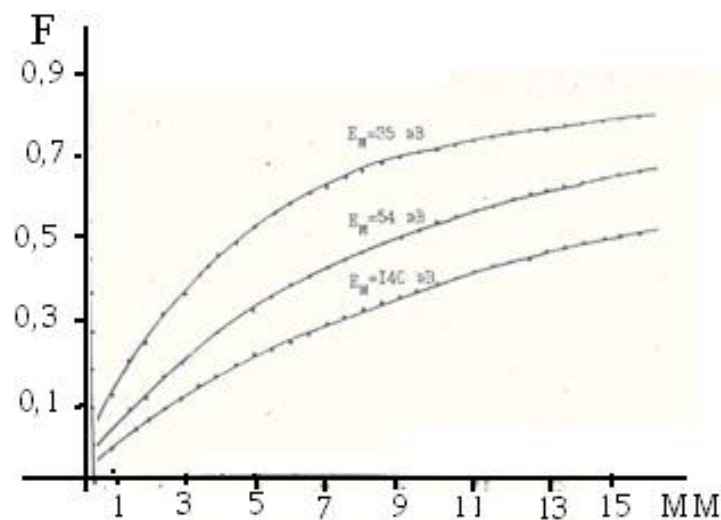


Рисунок 2. Зависимость фактора поглощения  $F$  от толщины  $\text{CdBr}_2$  экрана.

Полученная композиция обладает значительной плотностью, механической прочностью, работоспособна в окислительной атмосфере при температурах до 500 °С, радиационностойка до интегрального потока  $10^{20}$  н / см<sup>2</sup>.

Полученный материал для поглощения тепловых и резонансных нейтронов, содержащий кадмий, отличается тем, что, с целью повышения эффективности поглощения резонансных нейтронов с энергиями 35, 54, 104 и 136 эВ, содержит кадмий в виде бромистого кадмия и дополнительно жидкое стекло при следующих соотношениях исходных компонентов (вес. %): бромистый кадмий 90.0 – 97.5 и жидкое стекло 2.5 – 10.0.

Зависимость эффективности подавления активности <sup>82</sup>Br от композиции состава экрана приводится в **Таблице 1**.

**Таблица 1.**

№	Экран	Активность <sup>82</sup> Br в относительных единицах, %
1	Без экрана	4000 (100)
2	Металлический кадмий	700 (42)
	97.5 вес. % CdBr <sub>2</sub>	290 (7)
	2.5 вес. % Na <sub>2</sub> SiO <sub>3</sub>	
	95.0 вес. % CdBr <sub>2</sub>	300 (7.5)
3	5.0 вес. % Na <sub>2</sub> SiO <sub>3</sub>	
4	90.0 вес. % CdBr <sub>2</sub>	400 (10)
	10.0 вес. % Na <sub>2</sub> SiO <sub>3</sub>	

Расчет толщины поглотителя необходимого для эффективного подавления мешающей активности получали определением критерия фактора пропускания  $T$  и поглощения  $F$  различных энергетических групп нейтронов. Для предлагаемого материала результаты приводятся в [1, 2].

### Ссылки

1. Н. В. Багдавадзе, А. В. Рустамбеков. Материал для поглощения тепловых и резонансных нейтронов. Авт. свид. СССР № 795275, 1980.
2. Н. В. Багдавадзе, О. И. Джавахишвили. Устройство для облучения эпитеpmальными нейтронами. Авт. свид. СССР № 1450639, 1988.

## ОБ ИСТОРИИ РАЗВИТИЯ ТЕОРИИ РАСШИРЯЮЩЕЙСЯ ВСЕЛЕННОЙ

Дж. В. Церцвадзе

Грузинский технический университет  
Департамент инженерной физики  
Тбилиси, Грузия

Принята 12 октября 2015 года

### Аннотация

Рассказано об истории становления, развития, а также основных выводах теории расширяющейся Вселенной.

Как-то один известный ученый (говорят, это был Бертран Рассел) читал публичную лекцию об астрономии. Он рассказывал, как Земля обращается вокруг Солнца, а Солнце в свою очередь обращается вокруг центра огромного скопления звезд, которое называют нашей Галактикой. Когда лекция подошла к концу, из последних рядов зала поднялась маленькая пожилая леди и сказала: «Все, что Вы нам говорили – чепуха. На самом деле наш мир – это плоская тарелка, которая стоит на спине гигантской черепахи». Снисходительно улыбнувшись, ученый спросил: «А на чем держится черепаха?» – «Вы очень, очень умны, молодой человек, – ответила пожилая леди, – Черепаха – на другой черепахе, та – тоже на черепахе, и так все ниже и ниже».

Что нам известно о Вселенной, и как мы это узнали? Откуда взялась Вселенная, и что с ней станет? Было ли у Вселенной начало, а если было, то что происходило до начала? Какова сущность времени? Кончится ли оно когда-нибудь? Достижения физики последних лет, которыми мы частично обязаны фантастической новой технике, позволяют, наконец, получить ответы хотя бы на отдельные из таких давно поставленных вопросов.

Если в ясную безлунную ночь посмотреть на небо, то, вы увидите огромное количество звезд, похожих на наше Солнце, но находящихся гораздо дальше от нас. При обращении Земли вокруг Солнца некоторые из этих «неподвижных» звезд чуть-чуть меняют свое положение относительно друг друга, т.е. на самом деле они вовсе не неподвижны! Дело в том, что они несколько ближе к нам, чем другие. Поскольку же



Земля вращается вокруг Солнца, близкие звезды видны все время в разных точках фона более удаленных звезд. Благодаря этому можно непосредственно измерить расстояние от нас до этих звезд: чем они ближе, тем сильнее заметно их перемещение. Самая близкая звезда, называемая Проксимой Центавра, находится от нас на расстоянии приблизительно четырех световых лет (т.е. свет от нее идет до Земли около четырех лет), или около 37 миллионов миллионов километров. Большинство звезд, видимых невооруженным глазом, удалены от нас на несколько сотен световых лет. Сравните это с расстоянием до нашего Солнца, составляющим всего восемь световых минут! Видимые звезды рассыпаны по всему ночному небу, но особенно густо в той полосе, которую мы называем Млечным Путем.

Еще в 1750 г. некоторые астрономы высказывали мысль, что существование Млечного Пути объясняется тем, что большая часть видимых звезд образует одну дискообразную конфигурацию – пример того, что сейчас называется спиральной галактикой. Лишь через несколько десятилетий астроном Уильям Гершель подтвердил это предположение, выполнив колоссальную работу по составлению каталога положений огромного количества звезд и расстояний до них. Но даже после этого представление о спиральных галактиках было принято всеми лишь в начале прошлого века.

Современная картина Вселенной возникла только в 1924 г., когда американский астроном Эдвин Хаббл показал, что наша Галактика не единственная. На самом деле существует много других галактик, разделенных огромными областями пустого пространства. Для доказательства Хаббл требовалось определить расстояния до этих галактик, которые настолько велики, что, в отличие от положений близких звезд, видимые положения галактик действительно не меняются. Поэтому для измерения расстояний Хаббл был вынужден прибегнуть к косвенным методам. Видимая яркость звезды зависит от двух факторов: от того, какое количество света излучает звезда (ее светимость), и от того, где она находится. Яркость близких звезд и расстояние до них мы можем измерить; следовательно, мы можем вычислить и их светимость. И наоборот, зная светимость звезд в других галактиках, мы могли бы вычислить расстояние до них, измерив их видимую яркость. Хаббл заметил, что светимость некоторых типов звезд всегда одна и та же, когда они находятся достаточно близко для того, чтобы можно было производить измерения. Следовательно, рассуждал Хаббл, если такие звезды обнаружатся в другой галактике, то, предположив у них такую же светимость, мы сумеем вычислить расстояние до этой галактики. Если подобные расчеты для нескольких звезд одной и той же галактики дадут один и тот же результат, то полученную оценку расстояния можно считать надежной.

Таким путем Хаббл рассчитал расстояния до девяти разных галактик. Теперь известно, что наша Галактика – одна из нескольких сотен тысяч миллионов галактик, которые можно наблюдать в современные телескопы, а каждая из этих в свою очередь содержит сотни тысяч миллионов звезд. Наша Галактика имеет около ста тысяч световых лет в поперечнике. Она медленно вращается, а звезды в ее спиральных рукавах в каждые несколько сотен миллионов лет делают примерно один оборот вокруг ее центра. Наше

Солнце представляет собой обычную желтую звезду средней величины, расположенную на внутренней стороне одного из спиральных рукавов.

Звезды находятся так далеко от нас, что кажутся просто светящимися точками в небе. Мы не различаем ни их размеров, ни формы. Но в таком случае как же можно говорить о разных типах звезд? Для подавляющего большинства звезд существует только одно характерное свойство, которое можно наблюдать – это цвет идущего от них света. Настроив телескоп на какую-нибудь отдельную звезду или галактику, можно разложить в спектр свет, испускаемый этой звездой или галактикой. Разные звезды имеют разные спектры, но относительная яркость разных цветов всегда в точности такая же, как в свете, который излучает какой-нибудь раскаленный докрасна предмет. (Свет, излучаемый раскаленным докрасна непрозрачным предметом, имеет очень характерный спектр, зависящий только от температуры предмета – т.н. тепловой спектр. Поэтому мы можем определить температуру звезды по спектру излучаемого ею света.) Кроме того, мы обнаружим, что некоторые очень специфические цвета вообще отсутствуют в спектрах звезд, причем отсутствующие цвета разные для разных звезд. Поскольку, как мы знаем, каждый химический элемент поглощает свой определенный набор характерных цветов, мы можем сравнить их с теми цветами, которых нет в спектре звезды, и таким образом точно определить, какие элементы присутствуют в ее атмосфере.

В 20-х годах прошлого столетия, когда астрономы начали исследование спектров звезд других галактик, обнаружилось нечто еще более странное: в нашей собственной Галактике оказались те же самые характерные наборы отсутствующих цветов, что и у звезд, но все они были сдвинуты на одну и ту же величину к красному концу спектра. Чтобы понять смысл сказанного, следует сначала разобраться с эффектом Доплера. Как известно, видимый свет – это колебания или волны электромагнитного поля. Частота (число волн в одну секунду) световых колебаний чрезвычайно высока – от четырехсот до семисот миллионов миллионов волн в секунду. Человеческий глаз воспринимает свет разных частот как разные цвета, причем самые низкие частоты соответствуют красному концу спектра, а самые высокие – фиолетовому.

Представим себе источник света, например, звезду, расположенный на фиксированном расстоянии от нас излучающий с постоянной частотой волны. Очевидно, что частота приходящих волн будет такой же как та с которой они излучаются (пусть гравитационное поле галактики невелико и его влияние несущественно). Предположим теперь, что источник начинает двигаться в нашу сторону. При испускании следующей волны источник окажется ближе к нам, а потому время, за которое гребень этой волны до нас дойдет, будет меньше, чем в случае неподвижной звезды. Стало быть, время между гребнями двух пришедших волн будет меньше, а число волн, принимаемых нами за одну секунду (т.е. частота), будет больше, чем когда звезда была неподвижна. При удалении же источника частота приходящих волн будет меньше. Это означает, что спектры удаляющихся звезд будут сдвинуты к красному концу (красное смещение), а спектры приближающихся звезд должны испытывать фиолетовое смещение. Как известно, такое соотношение между скоростью и частотой называется эффектом Доплер

Доказав, что существуют другие галактики, Хаббл все последующие годы посвятил составлению каталогов расстояний до этих галактик и наблюдению их спектров. В то время большинство ученых считали, что движение галактик происходит случайным образом и поэтому спектров, смещенных в красную сторону, должно наблюдаться столько же, сколько и смещенных в фиолетовую. Каково же было удивление, когда у большей части галактик обнаружилось красное смещение спектров, т.е. оказалось, что все галактики удаляются от нас! Еще более удивительным было открытие, опубликованное Хабблом в 1929 г.: он обнаружил, что даже величина красного смещения не случайна, а прямо пропорциональна расстоянию от нас до галактики. Иными словами, чем дальше находится галактика, тем быстрее она удаляется! А это означало, что Вселенная не может быть статической, как думали раньше, что на самом деле она непрерывно расширяется и расстояния между галактиками все время растут.

Открытие расширяющейся Вселенной было одним из великих интеллектуальных переворотов двадцатого века. Задним числом мы можем лишь удивляться тому, что эта идея не пришла никому в голову раньше. Ньютон и другие ученые должны были бы сообразить, что статическая Вселенная вскоре обязательно начала бы сжиматься под действием гравитации. Но предположим, что Вселенная, наоборот, расширяется. Если бы расширение происходило достаточно медленно, то под действием гравитационной силы оно в конце концов прекратилось бы и перешло бы в сжатие. Однако если бы скорость расширения превышала некоторое критическое значение, то гравитационного взаимодействия не хватило бы, чтобы остановить расширение, и оно продолжалось бы вечно. Все это немного напоминает ситуацию, возникающую, когда с поверхности Земли запускают вверх ракету. Если скорость ракеты не очень велика, то из-за гравитации она в конце концов остановится и начнет падать обратно. Если же скорость ракеты больше некоторой критической (около одиннадцати километров в секунду), то гравитационная сила не сможет ее вернуть и ракета будет вечно продолжать свое движение от Земли.

Расширение Вселенной могло быть предсказано на основе ньютоновской теории тяготения в XIX, XVIII и даже в конце XVII века. Однако вера в статическую Вселенную была столь велика, что жила в умах еще в начале двадцатого века. Даже Эйнштейн, разрабатывая в 1915 г. общую теорию относительности, был уверен в статичности Вселенной. Чтобы не вступать в противоречие со статичностью, Эйнштейн модифицировал свою теорию, введя в уравнения так называемую космологическую постоянную. Он ввел новую «антигравитационную» силу, которая в отличие от других сил не порождалась каким-либо источником, а была заложена в саму структуру пространства–времени. Эйнштейн утверждал, что пространство–время само по себе всегда расширяется и этим расширением точно уравновешивается притяжение всей остальной материи во Вселенной, так что в результате Вселенная оказывается статической.

По-видимому, лишь один человек полностью поверил в общую теорию относительности: пока Эйнштейн и другие физики думали над тем, как обойти нестатичность Вселенной, предсказываемую этой теорией, российский физик и математик А. А. Фридман, наоборот, занялся ее объяснением. Фридман сделал два очень простых исходных предположения: во-первых, Вселенная выглядит одинаково, в каком бы

направлении мы ее ни наблюдали, и, во-вторых, это утверждение должно оставаться справедливым и в том случае, если бы мы производили наблюдения из какого-нибудь другого места. Не прибегая ни к каким другим предположениям, Фридман показал, что Вселенная не должна быть статической. В 1922 г., за несколько лет до открытия Хаббла, Фридман в точности предсказал его результат!

Предположение об одинаковости Вселенной во всех направлениях на самом деле, конечно, не выполняется. Как мы, например, уже знаем, другие звезды в нашей Галактике образуют четко выделяющуюся светлую полосу, которая идет по всему небу ночью – Млечный Путь. Но если говорить о далеких галактиках, то их число во всех направлениях примерно одинаково. Следовательно, Вселенная действительно «примерно» одинакова во всех направлениях – при наблюдении в масштабе, больших по сравнению с расстоянием между галактиками, когда отбрасываются мелкомасштабные различия.

Долгое время это было единственным обоснованием гипотезы Фридмана как «грубого» приближения к реальной Вселенной. Но потом по некоей случайности выяснилось, что гипотеза Фридмана и на самом деле дает удивительно точное описание нашей Вселенной.

В 1965 г. два американских физика, Арно Пензиас и Роберт Вильсон испытывали очень чувствительный «микроволновый», точнее сверхвысокочастотный (СВЧ) детектор. Пензиас и Вильсон заметили, что уровень шума, регистрируемого их детектором, выше, чем должно быть. Этот шум не был направленным, приходящим с какой-то определенной стороны. Они знали, что любой шум, приходящий из атмосферы, всегда сильнее не тогда, когда детектор направлен прямо вверх, а когда он наклонен, потому что лучи света, идущие из-за горизонта, проходят через значительно более толстые слои атмосферы, чем лучи, попадающие в детектор прямо сверху. «Лишний» же шум одинаков, куда бы ни направлять детектор. Следовательно, источник шума должен находиться за пределами атмосферы. Шум был одинаковым и днем, и ночью, и вообще в течение года, несмотря на то что Земля вращается вокруг своей оси и продолжает свое вращение вокруг Солнца. Это означало, что источник излучения находится за пределами Солнечной системы и даже за пределами нашей Галактики, ибо в противном случае интенсивность излучения изменялась бы, поскольку в связи с движением Земли детектор меняет свою ориентацию. Как мы знаем, по пути к нам излучение проходит почти через всю наблюдаемую Вселенную. Коль скоро же оно одинаково во всех направлениях, по крайней мере в крупном масштабе. Теперь нам известно, что, в каком бы направлении мы ни производили наблюдения, этот шум изменяется не больше, чем на одну десятитысячную. Так Пензиас и Вильсон, ничего не подозревая, дали удивительно точное подтверждение первого предположения Фридмана.

Правда, на первый взгляд, тот факт, что Вселенная кажется нам одинаковой во всех направлениях, может говорить о какой-то выделенности нашего местоположения во Вселенной. В частности, раз мы видим, что все остальные галактики удаляются от нас, значит, что мы находимся в центре Вселенной. Но есть и другое объяснение: Вселенная будет выглядеть одинаково во всех направлениях и в том случае, если смотреть на нее из

какой-нибудь другой галактики. Это, как мы знаем, вторая гипотеза Фридмана. У нас нет научных доводов ни за, ни против этого предположения, и мы приняли его, так сказать, из скромности: было бы крайне странно, если бы Вселенная казалась одинаковой во всех направлениях только вокруг нас, а в других ее точках этого не было! В модели Фридмана все галактики удаляются друг от друга. Это вроде бы как надутый шарик, на который нанесены точки, если его все больше надуть. Расстояние между любыми двумя точками увеличивается, но ни одну из них нельзя назвать центром расширения. Притом, чем больше расстояние между точками, тем быстрее они удаляются друг от друга. Но и в модели Фридмана скорость, с которой любые две галактики удаляются друг от друга, пропорциональна расстоянию между ними. Таким образом, модель Фридмана предсказывает, что красное смещение галактики должно быть прямо пропорционально ее удаленности от нас в точном соответствии с открытием Хаббла. Несмотря на успех этой модели и на согласие ее предсказаний с наблюдениями Хаббла, работа Фридмана оставалась неизвестной на Западе, и лишь в 1935 г. американский физик Говард Робертсон и английский математик Артур Уолкер предложили сходные модели в связи с открытием Хаббла.

Сам Фридман рассматривал только одну модель, но можно указать три разные модели, для которых выполняются оба фундаментальных предположения Фридмана. В модели первого типа (открытой самим Фридманом) Вселенная расширяется достаточно медленно для того, чтобы в силу гравитационного притяжения между различными галактиками расширение Вселенной замедлялось и в конце концов прекращалось. После этого галактики начинают приближаться друг к другу, и Вселенная начинает сжиматься. В модели второго типа расширение Вселенной происходит так быстро, что гравитационное притяжение, хоть и замедляет расширение, не может его остановить. Есть, наконец, и модель третьего типа, в которой скорость расширения Вселенной только-только достаточна для того, чтобы избежать сжатия до нуля (коллапса). В этом случае расстояние между галактиками тоже сначала равно нулю, а потом все время возрастает. Правда галактики «разбегаются» все с меньшей и меньшей скоростью, но она никогда не падает до нуля.

Модель Фридмана первого типа удивительна тем, что в ней Вселенная не бесконечна в пространстве, хотя пространство не имеет границ. Гравитация настолько сильна, что пространство, искривляясь, замыкается с самим собой, уподобляясь земной поверхности. Ведь, перемещаясь в определенном направлении по поверхности Земли, вы никогда не натолкнетесь на абсолютно непреодолимую преграду, не вывалитесь через край и в конце концов вернетесь в ту же самую точку, откуда вышли. В первой модели Фридмана пространство такое же, но только вместо двух измерений поверхности Земли имеет три измерения. Четвертое измерение, время, также имеет конечную протяженность, но оно подобно отрезку прямой, имеющему начало и конец. Мы сможем увидеть, что, если общую теорию относительности объединить с квантово-механическим принципом неопределенности, то окажется, что и пространство, и время могут быть конечными, не имея при этом ни краев, ни границ.

Мысль о том, что можно обойти вокруг Вселенной и вернуться в то же место, годится для научной фантастики, но не имеет практического значения, ибо, как можно показать, Вселенная успеет сжаться до нуля до окончания обхода. Чтобы вернуться в исходную точку до наступления конца Вселенной, пришлось бы передвигаться со скоростью, превышающей скорость света, а это невозможно!

В первой модели Фрийдмана (в которой Вселенная расширяется и сжимается) пространство искривляется, замыкаясь само на себя, как поверхность Земли. Поэтому размеры его конечны. Во второй же модели, в которой Вселенная расширяется бесконечно, пространство искривлено иначе, как поверхность седла. Таким образом, во втором случае пространство бесконечно. Наконец, в третьей модели Фрийдмана (с критической скоростью расширения) пространство плоское (и, следовательно, тоже бесконечное).

Но какая же из моделей Фрийдмана годится для нашей Вселенной? Перестанет ли Вселенная наконец расширяться и начнет сжиматься или же будет расширяться вечно? Чтобы ответить на этот вопрос, нужно знать нынешнюю скорость расширения Вселенной и ее среднюю плотность. Если плотность меньше некоторого значения, зависящего от скорости расширения, то гравитационное притяжение будет слишком мало, чтобы остановить расширение. Если же плотность больше критической, то в какой-то момент в будущем из-за гравитации расширение Вселенной прекратится и начнется сжатие.

Сегодняшнюю скорость расширения Вселенной можно определить, измеряя (по эффекту Доплера) скорости удаления от нас других галактик. Такие измерения можно выполнить очень точно. Но расстояния до других галактик нам плохо известны, потому что их нельзя измерить непосредственно. Мы знаем лишь, что Вселенная расширяется за каждую тысячу миллионов лет на 5 – 10 %.

Однако неопределенность в современном значении средней плотности Вселенной еще больше. Если сложить массы всех наблюдаемых звезд в нашей и в других галактиках, то даже при самой низкой скорости расширения сумма окажется меньше одной сотой той плотности, которая необходима для того, чтобы расширение Вселенной прекратилось. Однако и в нашей и в других галактиках должно быть много «темной материи», которую нельзя видеть непосредственно, но о существовании которой мы узнаем по тому, как ее гравитационное притяжение влияет на орбиты звезд в галактиках. Кроме того, галактики в основном наблюдаются в виде скоплений, и мы можем аналогичным образом сделать вывод о наличии еще большего количества межгалактической темной материи внутри этих скоплений, влияющего на движение галактик. Сложив массу всей темной материи, мы получим лишь одну десятую того количества, которое необходимо для прекращения расширения. Но нельзя исключить возможность существования и какой-то другой формы материи, распределенной равномерно по всей Вселенной и еще не зарегистрированной, которая могла бы довести среднюю плотность Вселенной до критического значения, необходимого, чтобы остановить расширение.

Таким образом, имеющиеся данные говорят о том, что Вселенная, вероятно, будет расширяться вечно. Единственное, в чем можно быть совершенно уверенным, так это в



том, что если сжатие Вселенной все-таки произойдет, то никак не раньше, чем через десять тысяч миллионов лет, ибо по крайней мере столько времени она уже расширяется. Но это не должно нас слишком сильно тревожить: к тому времени, если мы не переселимся за пределы солнечной системы, человечества давно уже не будет – оно угаснет вместе с Солнцем!

Все варианты модели Фридмана имеют то общее, что в какой-то момент в прошлом (десять-двадцать тысяч миллионов лет назад) расстояние между соседними галактиками должно было равняться нулю. В этот момент, который называется большим взрывом, плотность Вселенной и кривизна пространства-времени должны были быть бесконечными. Поскольку математически невозможно обращаться с бесконечно большими величинами, это означает, что, согласно общей теории относительности (на которой основаны решения Фридмана), во Вселенной должна быть точка, в которой сама эта теория неприменима. Такая точка в математике называется особой (сингулярной). Все наши научные теории основаны на предположении, что пространство-время гладкое и почти плоское, а потому все эти теории неверны в сингулярной точке большого взрыва, в которой кривизна пространства-времени бесконечна. Следовательно, даже если бы перед большим взрывом происходили какие-нибудь события, по ним нельзя было бы спрогнозировать будущее, так как в точке большого взрыва возможности предсказания свелись бы к нулю. Точно так же, зная только то, что произошло после большого взрыва (а мы знаем только это), мы не сможем узнать, что происходило до него. События, которые произошли до большого взрыва, не могут иметь никаких последствий, касающихся нас, и поэтому не должны фигурировать в научной модели Вселенной. Следовательно, нужно исключить их из модели и считать началом отсчета времени момент большого взрыва.

Мысль о том, что у времени было начало, многим не нравится, возможно, тем, что в ней есть намек на вмешательство божественных сил. (В то же время за модель большого взрыва ухватилась католическая церковь и в 1951 г. официально провозгласила, что модель большого взрыва согласуется с Библией). В связи с этим известно несколько попыток обойтись без большого взрыва. Наибольшую поддержку получила модель стационарной Вселенной. Ее авторами были Х. Бонди и Т. Гоулд (1948), бежавшие из оккупированной нацистами Австрии, и англичанин Ф. Хойл, который во время войны работал с ними над проблемой радиолокации. Их идея состояла в том, что по мере разбегания галактик на освободившихся местах из нового непрерывно рождающегося вещества все время образуются новые галактики. Следовательно, Вселенная должна выглядеть примерно одинаково во все моменты времени и во всех точках пространства. Конечно, для непрерывного «творения» вещества требовалась некоторая модификация теории относительности, но нужная скорость творения оказывалась столь малой (одна частица на кубический километр в год), что не возникало никаких противоречий с экспериментом. Стационарная модель – это пример хорошей научной теории в смысле, что она дает определенные предсказания, которые можно проверять путем наблюдений. Одно из ее предсказаний таково: должно быть постоянным число галактик и других аналогичных объектов в любом заданном объеме пространства независимо от того, когда и где во Вселенной производятся наблюдения. В конце 50-х – в начале 60-х годов двадцатого века астрономы из Кембриджского университета под руководством М. Райла

составили каталог источников радиоволн, приходящих из внешнего пространства. Эта кембриджская группа показала, что большая часть этих радиоисточников должна находиться вне нашей Галактики и, кроме того, что слабых источников гораздо больше, чем сильных. Слабые источники интерпретировались как более удаленные, а сильные – как те, что находятся ближе. Далее, оказалось, что число обычных источников в единице объема в удаленных областях больше, чем вблизи. Это могло означать, что мы находимся в центре огромной области Вселенной, в которой меньше источников, чем в других местах. Но возможно было и другое объяснение: в прошлом, когда радиоволны начали свой путь к нам, источников было больше, чем сейчас. Оба эти объяснения противоречат предсказаниям теории стационарной Вселенной. Кроме того, микроволновое излучение, обнаруженное в 1965 г. Пензиасом и Вильсоном, тоже указывало на большую плотность Вселенной в прошлом, и поэтому от модели стационарной Вселенной пришлось отказаться.

В 1963 г. два советских физика, Е. М. Лифшиц и И. М. Халатников, сделали еще одну попытку исключить большой взрыв, а с ним и начало времени. Лифшиц и Халатников высказали предположение, что большой взрыв – особенность лишь моделей Фридмана, которые в конце концов дают лишь приближенное описание реальной Вселенной. Не исключено, что из всех моделей, в какой-то мере описывающих существующую Вселенную, сингулярность в точке большого взрыва возникает только в моделях Фридмана. Согласно Фридману, все галактики удаляются в прямом направлении друг от друга, и поэтому нет ничего удивительного в том, что когда-то в прошлом все они находились в одном месте. Однако в реально существующей Вселенной галактики никогда не расходятся точно по прямой: обычно у них есть еще и небольшие составляющие скорости, направленные под углом. Поэтому на самом деле галактикам не нужно находиться точно в одном месте – достаточно, чтобы они были расположены очень близко друг к другу. Тогда нынешняя расширяющаяся Вселенная могла возникнуть не в сингулярной точке большого взрыва, а на какой-нибудь более ранней фазе сжатия; может быть, при сжатии Вселенной столкнулись друг с другом не все частицы. Какая-то доля их могла пролететь мимо друг друга и снова разойтись в разные стороны, в результате чего и происходит наблюдаемое сейчас расширение Вселенной. Как тогда определить, был ли началом Вселенной большой взрыв? Лифшиц и Халатников занялись изучением моделей, которые в общих чертах были бы похожи на модели Фридмана, но отличались бы от фридмановских тем, что в них учитывались нерегулярности и случайный характер реальных скоростей галактик во Вселенной. В результате Лифшиц и Халатников показали, что в таких моделях большой взрыв мог быть началом Вселенной даже в том случае, если галактики не всегда разбегаются по прямой. Но это могло выполняться лишь для очень ограниченного круга моделей, в которых движение галактик происходит определенным образом. Поскольку же моделей фридмановского типа, не содержащих большой взрыв, бесконечно больше, чем тех, которые содержат такую сингулярность, Лифшиц и Халатников утверждали, что на самом деле большого взрыва не было. Однако позднее они нашли гораздо более общий класс моделей фридмановского типа, которые содержат сингулярности и в которых вовсе не требуется, чтобы галактики двигались каким-то особым образом. Поэтому в 1970 г. Лифшиц и Халатников отказались от своей теории.

Тем не менее их работа имела очень важное значение, ибо она показала, что если верна общая теория относительности, то Вселенная могла иметь особую точку, большой взрыв. Но эта работа не давала ответа на главный вопрос: следует ли из общей теории относительности, что у Вселенной должно было быть начало времени – большой взрыв?

Ответ на этот вопрос был получен при совершенно другом подходе, предложенном в 1965 г. английским математиком и физиком Роджером Пенроузом. Исходя из поведения световых конусов в общей теории относительности и того, что гравитационные силы всегда являются силами притяжения, Пенроуз показал, что когда звезда сжимается под действием собственных сил гравитации, она ограничивается областью, поверхность которой в конце концов сжимается до нуля. А раз поверхность этой области сжимается до нуля, то тоже самое должно происходить и с ее объемом. Все вещество звезды будет сжато в нулевом объеме, так что ее плотность и кривизна пространства–времени станут бесконечными. Иными словами, возникнет сингулярность в некоей области пространства–времени, называемая черной дырой.



*ელეფთერ ანდრონიკაშვილის 100 წლისთავის იუბილე საკმაოდ თბილად აღინიშნა საქართველოს მეცნიერებათა აკადემიაში 2010 წლის 25 დეკემბერს. ეს წერილი იმ დღეების გამოძახილია. 2015-ც საიუბილეოა – ბატონ ელეფთერს 105 წელი შეუსრულებოდა.*

### იუბილესუმფობოგი ვნებანი

#### ვ. კვაჭაძე

ი. ჯავახიშვილის სახ. თბილისის სახელმწიფო უნივერსიტეტი  
ე. ანდრონიკაშვილის სახ. ფიზიკის ინსტიტუტი  
თბილისი, საქართველო  
vkvatchadze@gmail.com

მიღებულია 2015 წლის 28 სექტემბერს

მეტად უღიმღამოდ ჩაიარა ელეფთერ ანდრონიკაშვილის საიუბილეო დღეებმა ანდრონიკაშვილისავე ფიზიკის ინსტიტუტში. მიზეზთა მოძიება შეიძლება, რა თქმა უნდა, ოღონდ ნუ მოვიძიებთ.

სულიერებას თითქოს რა უნდა, მაგრამ რომ ვერაფერი მოვიფიქრეთ სასულიერო, არც შედარებით ახალგაზრდებმა და არც ჩვენ, ვისაც ანდრონიკაშვილის შთამომავლებად მოგვაქვს თავი ჩვენი საქმიანობითა.

ისიც როგორ დაამთხვია აზრთაგამრიგემ და სწორედ იმ საიუბილეო შემოდგომას შეუერთა ანდრონიკაშვილის ნალოლიავები ინსტიტუტი დედა უნივერსიტეტსა. დედასა, რამეთუ ყველანი იქიდან მოვდივართ და ანდრონიკაშვილმაც იქიდან დაიწყო ქართული საქმის ქმნა. თავის დროზე ხომ ამ უნივერსიტეტში უხმო იმ სულკურთხეულმა რექტორმა იმედისმომცემ ახალგაზრდა მკვლევარს.

შეერთებაში რა უნდა იყოს ცუდი და მიუღებელი? ერთია, შეიძლება ძველებს გაგვიჭირდეს ახალთან შეგუება, თორემ ახალგაზრდებისთვის ბუნებრივად მოხდება ყოველივე. უბრალოდ, ფაქტი აღვნიშნე დამთხვევისა და ეჭვი არ შემიტანია მომავლის წარმატებაში.

ისიც როგორ დაემთხვა – პატივცემულ რექტორს ახლად შეერთებული ინსტიტუტების დირექტორების თათბირი მოეწვია სწორედ იმ დღესა, როცა აკადემია საიუბილეო სხდომას უძღვნიდა ანდრონიკაშვილსა. ნეტა თუ აცნობეს და მიიპატიყეს ახალგაზრდა რექტორი ამ იუბილეზე? მოსულიყო და ხომ დიდებული იქნებოდა ყოველმხრივ; არ მოვიდოდა და ამასაც გადაუდებელი საქმეებით ავხსნიდით და დაველოდებოდით ახალ იუბილეებსა.

ანდრონიკაშვილს არაფერი დაჰკლებია ჩვენი უნიათობითა. ჩვენ ვკარგავთ რაღაცეებსა ...

რკინას ცეცხლი აწრობს, ადამიანს – განსაცდელით. ანდრონიკაშვილსაც შეხვდა სამყოფი განსაცდელი და არ წაქცეულა. არ წაქცეულა, რაკი ოჟიოში ჰქონდა ფესვები გამდგარი. წარმატებულიც იმიტომ იყო, ალბათ.

იმპერიის აკადემიამ არ აირჩია ის თავის წევრად ... ისე, ამ საქმეში აქეთურებიც მივეხმარეთ იმპერიასა. მეცნიერების მწვერვალს თითქმის უკვე მიღწეულ ახალგაზრდა სწავლულს აქეთ ვუხმეთ და გამოვიძახეთ ქართული ექსპერიმენტული ფიზიკის შესაქმნელად. შეიძლება იფიქრეს კიდევ, რაკი დატოვა იმპერიის უპირველესი სამეცნიერო-კვლევითი დაწესებულების პალატები, ამით დიდი მეცნიერებიდანაც წავიდაო. ანდრონიკაშვილი მომავალში დაამტკიცებს, რომ არც ერთი წამით არ დაუტოვებია დიდი მეცნიერება.

“წამოსვლა” კი ნამდვილად მძიმე და მტკივნეული იყო ანდრონიკაშვილისთვის, მაგრამ, როცა დამშვიდდა და მიხვდა, რომ სამშობლოს ალტერნატივა არ გააჩნია, დაბრუნდა კიდევ მამაპაპეულ ქვეყანაში. ის უკვე ავტორია ბრწყინვალე ექსპერიმენტისა, რომლითაც გამჟღავნდა ერთდროულად მოძრავი და უძრავი მატერიის არსებობა. მარტოოდენ “ანდრონიკაშვილის ექსპერიმენტიც” საკმარისია, რომ მისი ავტორი მუდმივად დარჩენილიყო დიდ მეცნიერებაში. სულ ახლახან არ იყო, გასულმა საუკუნემ რომ გადაულოცა იგი (“ანდრონიკაშვილის ექსპერიმენტი”) XXI საუკუნეს, როგორც მუდმივად მნათი კელაპტარი (The New PHYSICS for the Twenty-First Century. Ed. G. Fraser, Cambridge, 2009).

ანდრონიკაშვილმა მართლაც და სასწაული მოახდინა. ხომ შექმნა ბრწყინვალე ინსტიტუტი მთელი თავისი მაღალმთიანი (იალბუზი, ცხრა-წყარო) თუ დაბალმთიანი (მუხათგვერდი, ბოტანიკური ბაღის მიდამოები) ბაზებითა; ინსტიტუტი, რომელიც რუსეთის დედაქალაქებისა (მოსკოვი, ლენინგრადი) და უკრაინის დედაქალაქების (კიევი, ხარკოვი) წამყვან ინსტიტუტებს შორის მოიაზრებოდა. დიდი მეცნიერების ღირსი აღმოჩენებიც აქ გააკეთა. გააკეთა ადგილობრივ ახალგაზრდა მეცნიერებთან ერთად, ანუ ძალიან მოკლე ხანში ქართული ექსპერიმენტული ფიზიკა შესდგა(!). ამ გოგო-ბიჭებთან ერთად (ვახსენოთ ასე მოფერებითა ის ყმაწვილები) შექმნა ანდრონიკაშვილმა ის კრიტერიუმი, რომლითაც განირჩევა ცოცხალი და მკვდარი მატერია. ვერაფერს იტყვი, იმპერიის გამოცემაც აღიარებს ამ ფაქტს: «Инициировал новое направление биотермодинамики. Под его руководством были созданы уникальные сканирующие дифференциальные микрокалориметры адиабатического типа, с помощью которых впервые измерена теплота внутримолекулярного плавления ДНК, РНК, фибриллярных и глобулярных белков в норме и патологии» (Большая биографическая энциклопедия, 2009).

ახლა უკვე მოწაფეების სხვა ჯგუფზე გადავინაცვლოთ. აკი წერს იგივე გამოცემა, რომ «... работы (Андроникашвили – ვ.კ.) посвящены физике низких температур, физике космических лучей, радиационной физике твердого тела, биофизике». და აი, მყარი სხეულების რადიაციულ ფიზიკაში მომუშავე ახალგაზრდა მეცნიერებთან ერთად ანდრონიკაშვილი ავტორია პლასტიფიკაციის ეფექტისა, კრისტალებზე რადიაციისა და გარე ველის ერთდროული მოქმედების შედეგისა (თვით იმპერია აპირებდა ამ შედეგის აღმოჩენად აღიარებას, მაგრამ არ დასცალდა ბეჩავს). ყველა იმ დიდებულ მეცნიერთათვის (ნობელიანტისთვისა თუ არანობელიანტისთვისა), ვინც კი სწვევია ინსტიტუტს, ეს შედეგი იყო მასპინძლების ერთ-ერთი სავიზიტო ბარათი. ამის შემდეგ იყო პროხოროვმა რომ სთხოვა ანდრონიკაშვილს: კეთილო ხალხო, ჩვენთან ოპტიკური ელემენტები ვერ უძლებენ ლაზერული სხივის მოქმედებას და იქნებ იღონოთ რამეო?!



ილონეს, რა თქმა უნდა, 2.5-ჯერ გაიზარდა შესაბამისი მასალის სიმტკიცე. ამიტომაც იყო, რომ მეორედაც აქეთ მოაპყრეს მზერა იოფანელებმა (ИОФ АН), მაშინ, როცა ერთი, ჩვეულებრივად არასტაბილური, მაგრამ მეტად ღირებული ლაზერული ცენტრი “მოერჯულებინათ” ქართველებსა და ორიგინალური გზით მიეღწიათ მისი მდგრადობისთვის რადიაციულ კრისტალშია, მაგრამ დრომ შეუშალა ხელი ამ თანამშრომლობასა.

იმპერიის აკადემია კი ფიქრობდა ალბათ: ამას რად უნდა ჩვენი აკადემია, ისედაც მაგარიანო, თორემ მოსწონდა, თქმა არ უნდა, ანდრონიკაშვილისა და მისი თანაგუნდელების საქმიანობა; თავსაც იწონებდა ამით.

იმპერიასაც ნუ დავუკარგავთ ყველაფერს – ზედმეტი მომჭირნეობით (აკი, ყველაფერი ნორმირებული იყო იმ ქვეყანაში და ნიჭის ნიველირებასაც ცდილობდნენ!), მაგრამ მაინც იმეტებდა ჯილდოებსა, ანუ აღიარებდა შენს საქმეს: ერთხელ სტალინის პრემიით დააჯილდოვა ანდრონიკაშვილი (1952 წ.); მეორედ, სტალინი რომ აღარ იყო – სახელმწიფო პრემიითა (1978 წ.). აქვე დავუმატოთ სახელმწიფო პრემია (1977 წ.) და იმპერიის უმაღლესი ჯილდო – ლენინის პრემია (1970 წ.), მიღებული ანდრონიკაშვილის თანამშრომლებისა და მოწაფეების მიერ მისივე ძალისხმევით. და ეს ყველაფერი 30 წლიანი დაუღალავი შრომის შედეგად (აქ მხოლოდ იმპერიისა და “პერიფერიული” ინსტიტუტის დამოკიდებულებაზე ვამახვილებთ ყურადღებას, თორემ სანიმუშო შედეგები სხვაც იყო და დაელჯილდოვებინა კიდევ საქართველოს მთავრობას მათი ავტორებიცა. მათ შორის ისინიც, ახალ თაობას რომ ქმნიდნენ ინსტიტუტში და თავის ნიჭიერებით უკვე მოესწროთ მაღალი დონის შედეგების მიღება).

ანდა დროს როგორ გაუსწრო ანდრონიკაშვილმა დაბალტემპერატურული რადიაციული მასალათმცოდნეობის დაფუძნებით – მყარი სხეულების კვლევისთვის კოსმოსური გარემო რომ შეექმნა რეაქტორის არხშია. უფრო სწორედ, დროს კი არ გაუსწრო, არამედ დროზე შექმნა (გავიხსენოთ ის წლები – ადამიანი უკვე სტარტზეა კოსმოსში გასაფრენად!). ეს სხვები ჩამორჩნენ დროსა, მარცხითა, თუ სხვა მიზეზითა. იქნებ ისევ იმ გამოცემაში ჩაგვხვდება: «В 1961 создал первую в нашей стране низкотемпературную петлю оригинальной конструкции, что дает возможность облучать в ядерном реакторе различные вещества при температурах, близких к абсолютному нулю». ინსტიტუტი კი, ეს მართლაც უნიკალური მოვლენა ქართულ სინამდვილეში, ყოველივე ამის განხორციელებისთვის შრომის ორდენით იქნა დაჯილდოებული (1969 წ.).

აკადემიის მესვეურები ყველაფერს ხედავდნენ, რა თქმა უნდა, და თავს იწონებდნენ-მეთქი, აღვნიშნე. შეიქმნა კიდევ მყარი სხეულების რადიაციული ფიზიკის საპრობლემო საბჭო იმპერიულ მეცნიერებათა აკადემიაში და ანდრონიკაშვილსა და მის მოწაფეებს ჩააბარეს მისი ხელმძღვანელობაც (თავმჯდომარე, მოადგილე, სწავლული მდივანი). ხოლო უკვე ორდენით პატივცემული ინსტიტუტი, ამ საბჭოს საბაზისო ინსტიტუტად დასახელდა და, ამგვარად, იმპერიის 150 ინსტიტუტს უნდა ჩასდგომოდა თავშია. ცოტაც და ორი ათეული წელი წინამძღოლობდნენ ქართველები მეცნიერების ამ დარგსა იმპერიული მასშტაბებითა – იმდენი, რამდენიც იარსება ამ მეტად პრესტიჟულმა საბჭომ. შემდგომ იმპერიაც ჩამოინგრა და ყველა დაადგა თავ-თავიანთ გზასა.

ისე, კატერინას შექმნილ აკადემიას რას გადავეკიდე, როცა ჩვენ ვერ ვუვლით ამ განძსა ამ გაღატაკებულ ყოფაში და ხელში გვადნება ინსტიტუტი ყინულის



ლოლუასავითა. მის კედლებს შემორჩენილი თანდათან ვერხვით მარადისობის კანონითა და ისიც გაქრება, თუ არ ვიღონეთ რაიმე საგანგებოდ ... .

დგება ჟამი, როცა დრო ჩაერევა ხოლმე ამა თუ იმ მოვლენისა თუ პიროვნების შეფასებაში. ხშირად – ააყირავებს კიდეც წარსულის დალაგებულსა. უფრო მეტად მაშინ, როცა მარადისობა ვერ გუობს დადგენილ წესრიგსა. ანდრონიკაშვილს თუ შედარებით მოკრძალებული ადგილი მიუჩინეს ადრე მეცნიერების ქურუმებმა, ახლა მისი ფასი იზრდება გამეტებითა; იზრდება ისევ იმ კამკამა ექსპერიმენტითა (The New PHYSICS for the Twenty-First Century. Ed. G. Fraser, Cambridge, 2009). საუკუნიდან საუკუნეში, რომ გადასულა და მომავალშიც გადავა წარმატებითა.

ასე იცის დრომა!

და ბოლოს:

“We were deeply impressed by the vigorous and purposeful research work organized by you and your colleagues and the spirited educational activities at the University of Tbilisi, and we hope in both these fields for a close co-operation between the scientists in our two countries comparable in size and which have so much in common in aspirations and traditions.” – წერდა ქართული შთაბეჭდილებებით აღსავსე (1961 წ.) ღმერთკაცი (ნილს ბორი) ელევთერ ანდრონიკაშვილს ... .

ჩვენც აქ შევჩერდეთ!

ამ დალოცვილ მიწაზე დაბადებული რამ გაგაოცოს?!

არც არაფერმა! რაცა ვთქვი, იმიტომ ვთქვი, რომ უნდა მეთქვა.

P.S. მეფე მოკვდა! გაუმარჯოს მეფეს!

ე. ანდრონიკაშვილის ფიზიკის ინსტიტუტი მოკვდა!

გაუმარჯოს ელევთერ ანდრონიკაშვილის (სახელობის!) ფიზიკის ინსტიტუტს!

ნეტაი, ახალმა აჯობოს ძველსა!

აჯობებს და ძველების ღვაწლიც გაბრწყინდება ახალ ეპოქაშია.

2015 წ.

მინაწერი:

ამ წერილის საბოლოო ვარიანტზე მუშაობისას ავტორმა დიდი დახმარება მიიღო, რჩევითა თუ მოწოდებული მასალით, ქალბატონ ლია ზამთარაძისგან, რომელიც წარმოადგენს ელევთერ ანდრონიკაშვილის ფიზიკის ინსტიტუტის ღირსეულ მემკვიდრეს.

ავტორისთვის გარკვეული სტიმულის მომცემი იყო პროფ. ჯ. ჩქარეულის სიტყვა, თქმული ელევთერ ანდრონიკაშვილის იუბილეზე (საქართველოს მეცნიერებათა აკადემია, 2010 წლის 25 დეკემბერი) და ამჟამინდელი მხარდაჭერა.

ულრმესი მადლობა მათ.

**მე-2 საერთაშორისო კონფერენცია  
“არაორგანული მასალათმცოდნეობის  
თანამედროვე ტექნოლოგიები და მეთოდები”**

2015 წლის 20–24 აპრილს საქართველოში, თბილისში, ჩატარდა მე-2 საერთაშორისო კონფერენცია “არაორგანული მასალათმცოდნეობის თანამედროვე ტექნოლოგიები და მეთოდები”, რომელიც მიემდგვნა ფერდინანდ თავაძის მეტალურგიისა და მასალათმცოდნეობის ინსტიტუტის დაარსების 70-ე წლისთავს.

თავად იუბილარ ინსტიტუტთან ერთად კონფერენციის ორგანიზატორები იყვნენ საქართველოს ეკონომიკისა და მდგრადი განვითარების სამინისტრო, საქართველოს მეცნიერებათა ეროვნული აკადემია და საქართველოს სახელმწიფო სამხედრო-ტექნიკური ცენტრი “დელტა”. კონფერენცია ფინანსურად მხარდაჭერილი იქნა შოთა რუსთაველის ეროვნული სამეცნიერო ფონდის გრანტით.

მუშაობდა საორგანიზაციო კომიტეტი შემდეგი შემადგენლობით: თავმჯდომარე – გიორგი თავაძე (საქართველო); მდივანი – თამარ ბაძოშვილი (საქართველო); წევრები – მიხეილ ალიმოვი (რუსეთი), ალექსი ბერნერი (ისრაელი), ალექსანდრე ბურჯანაძე (საქართველო), არჩილ გაჩეჩილაძე (საქართველო), ელაზარ გუტმანასი (ისრაელი), ონურალფ იუჯელი (თურქეთი), გიორგი ონიაშვილი (საქართველო), ბორის პატონი (უკრაინა), ირაკლი ჟორდანიას (საქართველო), ალექსანდრე სიჩოვი (რუსეთი), ვალერი სკოროხოდი (უკრაინა), არჩილ ფრანგიშვილი (საქართველო), ალექსანდრე შტეინბერგი (აშშ), უჩა ძოძუაშვილი (საქართველო), ჯუმბერ ხანთაძე (საქართველო) და ავთანდილ ხვადაგიანი (საქართველო).



**გიორგი თავაძე  
(საქართველო)**



**ლეონიდ ჩერნიშოვი  
(უკრაინა)**



**ელაზარ გუტმანასი  
(ისრაელი)**



**ორესტ ივასიშინი  
(უკრაინა)**



**ალექსი ბერნერი  
(ისრაელი)**



**ოსკობ ცინცაძე  
(საქართველო)**

კონფერენცია გაიხსნა საქართველოს მეცნიერებათა ეროვნულ აკადემიაში ფერდინანდ თავაძის მეტალურგიისა და მასალათმცოდნეობის ინსტიტუტის 70-ე წლისთავსადმი მიძღვნილი საიუბილეო სხდომით, რომელსაც თავმჯდომარეობდა აკადემიის პრეზიდენტი აკად. გიორგი კვესიტაძე.



საიუბილეო სხდომის გახსნა

ინსტიტუტის დირექტორმა აკად. გიორგი თავაძემ გააკეთა მოხსენება თემაზე: "ინსტიტუტის წარსული, აწმყო და მომავალი". მოგონებებით ინსტიტუტის ისტორიიდან გამოვიდა დოქტ. იოსებ ცინცაძე. უცხოელი სტუმრები – მ. ალიმოვი (რუსეთი), ა. ბერნერი (ისრაელი), ე. გუტმანასი (ისრაელი), ო. ივასიშინი (უკრაინა), ე. ლევაშოვი (რუსეთი), ზ. მანსუროვი (ყაზახეთი), ვ. სიდორეცი (უკრაინა) და ლ. ჩერნიშევი (უკრაინა) – მიესალმენ კონფერენციას და ინსტიტუტს მიულოცეს მისი იუბილე. სიტყვით, აგრეთვე, გამოვიდნენ საქართველოს მთელი რიგი მნიშვნელოვანი სამეცნიერო ცენტრების ხელმძღვანელები: გ. ბოკუჩავა, თ. ნატრიაშვილი, გ. ტატიშვილი, ნ. ჩიხრაძე, ვ. ციციშვილი და ა. ხვადაგიანი.

შესვენების შემდეგ გაიმართა პლენარული სხდომა.



კონფერენციის მონაწილეები



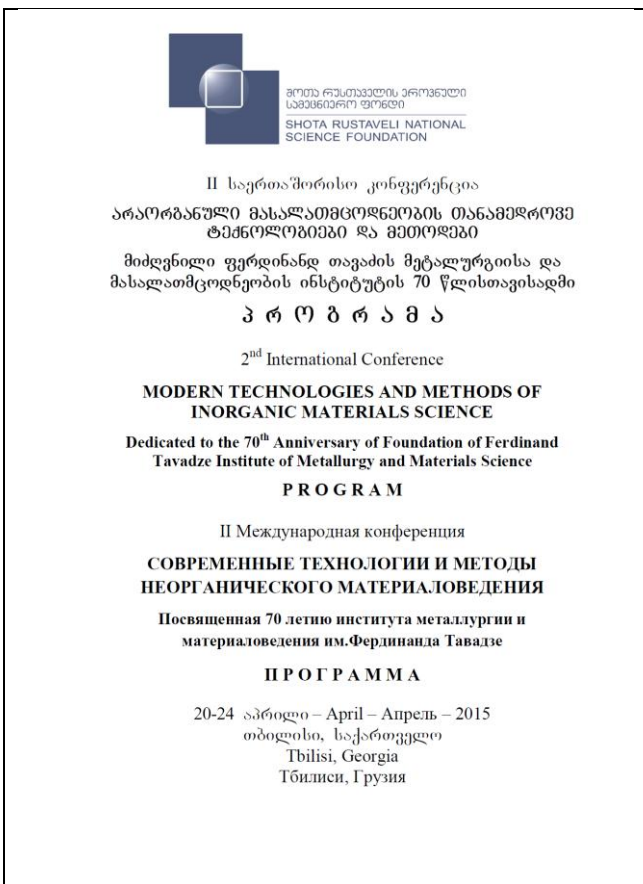
სხდომათა დარბაზში



დღის მეორე ნახევრიდან კონფერენცია გაგრძელდა სასტუმრო “ვერე პალასში”. საერთო ჯამში კონფერენციაზე წარმოდგენილ იქნა ოცდაათამდე ზეპირი და დაახლოებით ამდენივე პოსტერული მოხსენება. თემატიკა უაღრესად მრავალფეროვანი იყო: ფხვნილოვანი მეტალურგია, თვითგავრცელებადი მაღალტემპერატურული სინთეზი, ელექტროდაფენა, მრავალკომპონენტური სისტემების თერმოდინამიკა, ნანომასალების მიღება და გამოკვლევა, ნახევრადგამტარების ტექნოლოგია, მასალების სინთეზირების ქიმიური მეთოდები და ა.შ.

ქართველ მეცნიერებთან ერთად, თავიანთი მოხსენებები წარმოადგინეს კოლეგებმა თურქეთიდან, ისრაელიდან, რუსეთიდან, უკრაინიდან და ყაზახეთიდან.

პროგრამაში ჩართული მოხსენებების უმრავლესობა სტატიების სახით კონფერენციის დაიბეჭდა მოხსენებათა კრებულში (სარედაქციო ჯგუფი: ხელმძღვანელი – ჯ. ხანთაძე, წევრები – ლ. თავაძე, დ. რამაზაშვილი და ლ. ჩხარტიშვილი), რომელიც გადაეცათ მონაწილეებს.

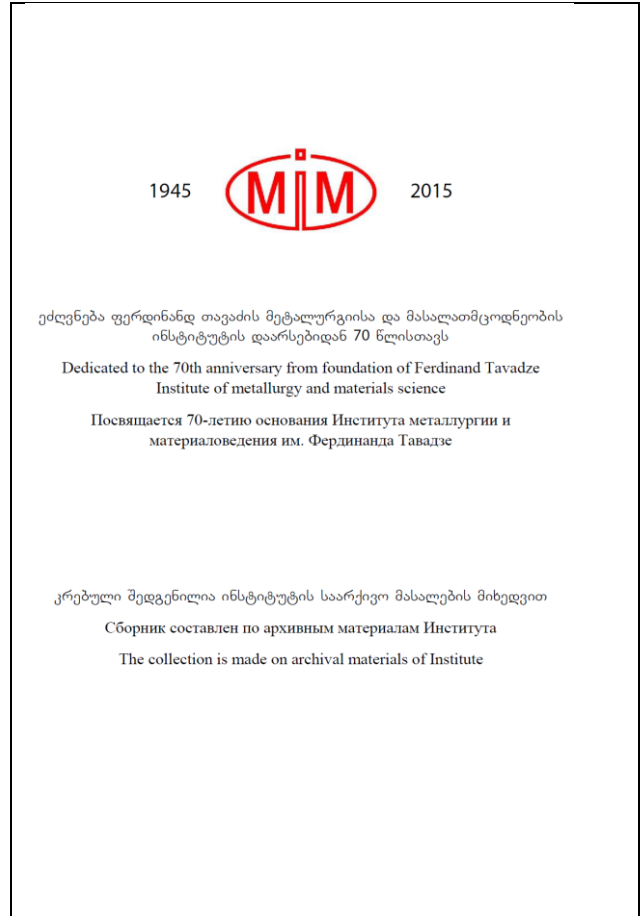


პროგრამის გარეკანი



მოხსენებათა კრებულის გარეკანი

გამოიცა ფერდინანდ თავაძის მეტალურგიისა და მასალათმცოდნეობის ინსტიტუტის 70-ე წლისთავისადმი მიძღვნილი საიუბილეო ბუკლეტი უზვადაა ილუსტრირებული და მოგვითხრობს საქართველოში მეტალურგიის განვითარების შესახებ, საკუთრივ ინსტიტუტის ისტორიაზე, მის დღევანდელ დღეზე და სამომავლო პერსპექტივებზე. ამ საინტერესო ბუკლეტის ეგზემპლარები ასევე დაურიგდათ კონფერენციის მონაწილეებს.



**საიუბილეო ბუკლეტის გარეკანი და მიძღვნის გვერდი**

ორგანიზატორებმა კონფერენციის მონაწილეებს საინტერესო სოციალური პროგრამა შესთავაზეს: საქართველოს ეროვნული მუზეუმის ოქრის ფონდის დათვალიერება, ტურები თბილისში და მცხეთაში, გალა-ბანკეტი.

მონაწილეები ერთხმად აღნიშნავენ ჩატარებული კონფერენციის მაღალ სამეცნიერო დონეს და მის შესანიშნავ ორგანიზებას. ამიტომაც მიიღეს დადგენილება, რომ არაორგანული მასალათმცოდნეობის თანამედროვე ტექნოლოგიებისა და მეთოდებისადმი მიძღვნილი კონფერენციები რეგულარულად, ყოველ სამ წელიწადში ერთხელ, გაიმართოს თბილისში, საქართველოში.

*ოთარ ცაგარეიშვილი*

2015 წლის 30 აპრილი

**მმსკ 2015: მოწინავე და ნანო მასალების  
საერთაშორისო კონფერენცია და გამოფენა**

მიმდინარე წელს გამართულ მთელ რიგ ნანოფორუმთა შორის ერთ-ერთი ყველაზე მნიშვნელოვანი უდავოდ არის მმსკ 2015 – მოწინავე და ნანომასალების საერთაშორისო კონფერენცია და გამოფენა (ოტავა, ონტარიო, კანადა 2015 წლის 10–12 აგვისტო). ღონისძიების ორგანიზატორი იყო IAEMM – ენერჯის, მინერალებისა და მასალების საერთაშორისო აკადემია (ემმსა), საკონსულტაციო ფორმასთან Fi Mat Con (მეტალურგიული კონსულტაცია, წვრილმარცვლოვანი ტექნოლოგია, ტექნოლოგიების გადაცემა), და გამომცემლობასთან Smart Pub – Open Access ერთად.



**კონფერენციის ლოგო**

კონფერენცია ჩატარდა სასტუმროს “ქორთიარდ მარიოტი ოტავა დაუნთაუნი” საკონფერენციო დარბაზებში; აქვე იყო გამოფენილი უახლესი გამოზომი აპარატურა ნანომასალათმცოდნეობისათვის. კონფერენციის მონაწილეების საზეიმო მიღებაც ამავე სასტუმროს ბისტროში გაიმართა.



**ორგანიზატორები  
გამოფენის მონაწილეები**

გაერთიანებულ სხდომებთან ერთად მუშაობა მიმდინარეობდა 7 სექციაში, რომელთა თემატიკაც მოიცავდა მოწინავე და ნანომასალათმცოდნეობის პრაქტიკულად ყველა წამყვან მიმართულებას:

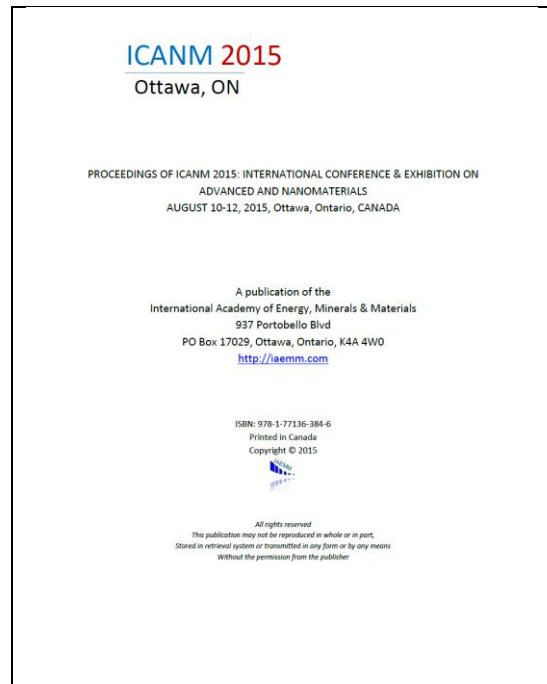
- მოწინავე და ნანომასალები: მიღება და გამოყენება;
- ფუნქციონალური მოწინავე და ნანომასალები;
- კომპოზიტები, პოლიმერები და ჰიბრიდული მასალები;
- ნანომედიცინა, ნანობიოტექნოლოგია, გარემო და ნანოტოქსიკოლოგია;
- ნანოდასტრუქტურებული მასალების მექანიკური ყოფაქცევა;
- მასალის მოდელირება, შეფასება, სიმულირება და ოპტიმიზება; და
- ნახშირბადის ნანომილაკები და გრაფენი.



კონფერენციის მოკლე სტატისტიკა ასეთია. წაკითხულ იქნა 53 ზეპირი მოხსენება (8 მოწვეული, 3 პლენარული და 42 სექციური) და ჩატარდა 2 პოსტერული სესია საერთო ჯამში 41 სტენდური მოხსენებით. ამრიგად, კონფერენციაზე სულ წარმოდგენილი იქნა 94 მოხსენება. ამ მოხსენებათა 300-ზე მეტი თანაავტორი მსოფლიოს 27 ქვეყანას (ავსტრალია, ალჟირი, ამერიკის შეერთებული შტატები, ახალი ზელანდია, ბრაზილია, გაერთიანებული არაბული საემიროები, დიდი ბრიტანეთისა და ჩრდილოეთ ირლანდიის გაერთიანებული სამეფო, ესპანეთი, იაპონია, ინდოეთი, ირანი, ისრაელი, კანადა, კონგოს დემოკრატიული რესპუბლიკა, მექსიკა, ნორვეგია, პოლონეთი, სამხრეთ კორეა, საუდის არაბეთი, საფრანგეთი, საქართველო, ტაივანი, ტაილანდი, უნგრეთი, ჩეხეთის რესპუბლიკა, ჩილე და ჩინეთი) წარმოადგენდა.



პროგრამის გარეკანი



ელექტრონულად გამოცემული მასალების სატიტულო გვერდი

დაიბეჭდა კონფერენციის პროგრამა, ხოლო მასალები ელექტრონულად გამოქვეყნდა. წინამდებარე ჟურნალი (ნანომეცნიერებებისა და ნანოტექნოლოგიების საერთაშორისო ჟურნალი Nano Studies) კონფერენციის ჟურნალი იყო. ამიტომ, რომ მის 2015 წლის გამოშვებებში (# 11 და # 12) იბეჭდება წარმოდგენილი მოხსენებების ნაწილი, რომელთაც მნმსკ 2015-ის სარედაქციო ჯგუფმა ფერ-რეცენზირება ჩაუტარა,

საქართველოდან მნმსკ 2015-ში მონაწილეობდა საქართველოს ტექნიკური უნივერსიტეტის საინჟინრო ფიზიკის დეპარტამენტის პროფესორი ლევან ჩხარტიშვილი. კონფერენციაზე პროფ. ლ. ჩხარტიშვილის გამგზავრება წილობრივად დაფინანსდა შოთა რუსთაველის ეროვნული სამეცნიერო ფონდის სამოგზაურო გრანტით და კონფერენციის მთავარი ორგანიზატორის (ემმსა-ის) მიერ. მან წარმოდგინა ორი მოხსენება, შესაბამისად, ზეპირი და სასტენდო:

- ლ. ჩხარტიშვილი, რ. ბეკერი. ბორის მცირე კლასტერების ატომური მუხტები და დიპოლური მომენტი; და
- ლ. ჩხარტიშვილი, დ. ჯიშიაშვილი, ზ. შიოლაშვილი, ნ. მახათაძე, ა. ჯიშიაშვილი, ბ. ბუაძე. ტემპერატურაზე დამოკიდებული მორფოლოგიური ცვლილებები ნანომავთულებში InP-ის ფუძეზე.



ლ. ჩხარტიშვილი (საქართველო) გამოდისზეპირიმოხსენებით



ლ. ჩხარტიშვილის (საქართველო) პოსტერული მოხსენება სტენდზე

გარდა ამისა, ლ. ჩხარტიშვილი იყო პლენარული და ორი სექციური (მასალის მოდელირება, შეფასება, სიმულირება და ოპტიმიზება; და ნახშირბადის ნანომილაკები და გრაფენი) სხდომის თავმჯდომარე. იგი მონაწილეობდა, როგორც კონფერენციის (ეროვნული და საერთაშორისო) საორგანიზაციო და სამეცნიერო კომიტეტის წევრი.



პლენარულ სხდომაზე  
ექტიტო საინოს (კანადა)  
წარადგენს ჯაზ პალ ბადიალი  
(დიდი ბრიტანეთი)



სექციის სხდომაზე  
თავმჯდომარეობს  
ჰოსსეინ ამინიანი  
(კანადა)



ლ. ჩხარტიშვილი (საქართველო) და ჰ. ამინიანი (კანადა)



თანაავტორები შესვენებისას: რ. ბეკერი (აშშ) და ლ. ჩხარტიშვილი (საქართველო)





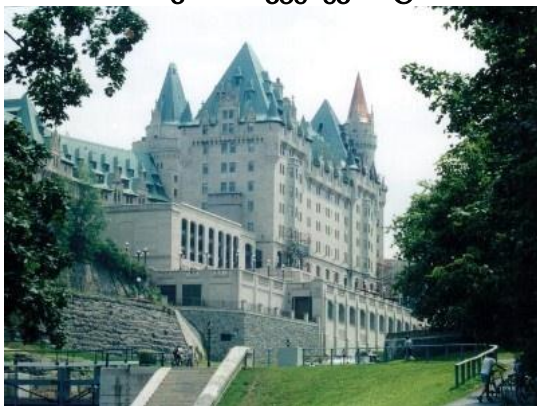
კონფერენციის მიმდინარეობისას ლევან ჩხარტიშვილმა მრავალი მნიშვნელოვანი შეხვედრა გამართა საზღვარგარეთელ კოლეგებთან. განსაკუთრებით აღსანიშნავია შეხვედრები კონფერენციის ერთ-ერთ ორგანიზატორთან – საკონსულტაციო ფირმის Fi Mat Con პრეზიდენტთან დოქტ. ჰოსსეინ ამინიანთან (ოტავა, კანადა), რომელიც აქტიურად მუშაობს ნანომასალების დარგში მიღწეული მეცნიერული შედეგების კომერციალიზაციის მიმართულებით, და საკუთარ თანაავტორთან რიკ ბეკერთან (ბორის კლასტერული მეტამასალები, კლასტერულ მეცნიერებათა ინსტიტუტი, იფსვიჩი, მასაჩუსეტსი, აშშ), რომელიც წამყვანი ექსპერიმენტატორია ბორის ნანომასალების დარგში.



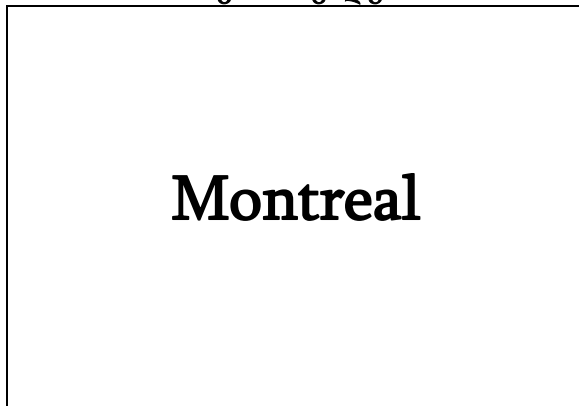
მმსკ 2013: კვებეკ-სიტი



მმსკ 2014: კალგარი



მმსკ 2015: ოტავა



მმსკ 2016: მონრეალი

დასკვნის სახით შეიძლება ითქვას, რომ მოწინავე და ნანომასალების საერთაშორისო კონფერენცია და გამოფენა (ოტავა, ონტარიო, კანადა 2015 წლის 10–12 აგვისტო) ძალზე მნიშვნელოვანი ფორუმი იყო ნანომასალების მიღების, კვლევისა და ტექნოლოგიებში მათი გამოყენებების დარგში მიღწეული შედეგების გაზიარებისათვის. იმის გამო, რომ მთავარი ორგანიზატორის ემმსა-ის შტაბ-ბინა კანადიაშია განლაგებული, მმსკ-ები 2013 წლიდან მოყოლებული ამ ქვეყნის სხვადასხვა ქალაქში იმართება. ეს ტრადიცია არც მომავალ წელს დაირღვევა – გადაწყდა, რომ მმსკ 2016-ს მონრეალი უმასპინძლებს.

*ლევან ჩხარტიშვილი*

2015 წლის 25 სექტემბერი

ISSN 1987-8826